Tungsten skarn deposits from the Canadian Cordillera: paleogeographic and geochemical controls on ore distribution

by

Vanessa Melodie Elongo

A thesis submitted in partial fulfillment of the requirements for the degree of

Doctor of Philosophy

Department of Earth and Atmospheric Sciences

University of Alberta

Abstract

Tungsten is a critical metal. Critical metals are strategic metals with associated economic, social, energy, geostrategic and environmental issues. As a result, the need to monitor and to secure local supplies of critical elements, including tungsten, has become a strategic priority for many countries. The Canadian Cordillera hosts one of the largest tungsten-producing provinces in North America. Tungsten mineralization in the Cordillera occurs mostly as skarns, which are calc-silicate rocks resulting from the hydrothermal alteration of carbonate rocks by fluids exsolved from an intrusive body. The most significant among the tungsten deposits known in the Canadian Cordillera as well as in the North American Cordillera broadly, include the Cantung and Mactung skarn deposits. Because of their major tungsten endowments, these deposits provide an ideal framework to study the parameters that govern tungsten mineralization.

In this dissertation, (1) we evaluate the paragenesis and mineral compositions in tungsten deposits from the Canadian Cordillera to determine the parameters that control the distribution of high-grade tungsten mineralization locally. (2) We constrain the magmatic sources of ore fluids in these deposits and the effects of fluid-rock interaction on the mineralization process and geochemical signatures in the Canadian Cordillera. And (3) we further evaluate the geochemical and paleogeographic controls responsible for the irregular distribution of tungsten in the North American Cordillera.

(1) The composition of minerals in tungsten skarn deposits from the Canadian Cordillera are indicative of reduced fluids, which is characteristic of high-grade tungsten deposits. We document that the main tungsten-bearing mineral in these deposits, scheelite ($CaWO_4$), precipitated throughout the entire evolution of the hydrothermal alteration but peaked at different stages for different deposits. Also, the preferential distribution of scheelite at the deposit scale was controlled

by parameters such as the permeability and porosity of the host rock. (2) Strontium isotopes and chemical variations in the host rocks reflect fluid-rock interaction processes. Although the geochemical variability of the host rock precludes quantification of chemical exchange between ore fluids and host rock, the distribution of the ore within preferential areas in the host rock suggests a lithologic control on the tungsten mineralization. In addition, strontium isotope data indicates that crust-derived fluids, likely from the granitoids adjacent to the deposits, are the main contributors to the ore fluids. (3) Geochemical fingerprinting using neodymium isotopes reveals that the ore fluids that precipitated tungsten in the North American Cordillera are specifically associated with source materials of Mesoarchean to Paleoproterozoic average age. We propose that tungsten enrichment in the North American Cordillera is the product of intense weathering of the supercontinents Columbia and Rodinia, followed by chemical transport and accumulation of tungsten-rich materials along the Ancient North American craton margin. Subsequent melting of these enriched sediments caused by orogenic heating produced reduced melts that scavenged tungsten and formed the major tungsten deposits found today in North America.

Preface

This thesis is an original work by Vanessa Melodie Elongo, hereafter referred to as "the author". It is composed of three main chapters, in addition to the introductory and concluding chapters, based on the findings of the author's PhD research supervised by Dr. Pilar Lecumberri-Sanchez. This research project has been made possible through funding from the NSERC Discovery Grant to Pilar Lecumberri-Sanchez, Polar Continental Shelf to Hendrik Falck, Targeted Geosciences Initiative from Natural Resources Canada to Pilar Lecumberri-Sanchez, and Northwest Territories Geological Survey contribution agreements. Dr. Pilar Lecumberri-Sanchez and Hendrik Falck were responsible for field work and sample collection for this project. Some of the samples used for this project were donated by Ehsan Salmabadi and Dr. Kenneth Hickey. Each chapter has significantly benefited from editorial and scientific input from the project supervisor, Dr. Pilar Lecumberri-Sanchez, and other co-authors listed below. Some of the thin sections used in this research were made by Mark Labbe and Walter Harley at the University of Alberta, and others were commercially made outside the university.

Chapter 1 (Introduction) is an original work produced by the author for this thesis.

Chapter 2 has been published in ORE GEOLOGY REVIEWS as: "Elongo, V., Lecumberri-Sanchez, P., Legros, H., Falck, H., Adlakha, E., & Roy-Garand, A. (2020). *Paragenetic constraints on the Cantung, Mactung and Lened tungsten skarn deposits, Canada: implications for grade distribution.* Ore Geology Reviews, 125, 103677". Petrographic analysis was performed by the author, aided by Hélène Legros. Microprobe data acquisition and processing was made possible with the help of Andrew Locock. Data interpretation was performed by the author and Pilar Lecumberri-Sanchez. The first draft of this manuscript was written by the author and all co-authors collaborated in the preparation of subsequent versions of the manuscript.

A modified version of **Chapter 3** will be submitted to MINERALIUM DEPOSITA as: "Elongo, V., Lecumberri-Sanchez, P., Falck, H., Legros, H., Sarkar, C., Pearson, D.G., Creaser, R.A., Zehnder, L., Li, G., & Adlakha, E. *Tracking fluid-rock interaction and element sources in tungsten skarn deposits of the Canadian Tungsten Belt*". Hélène Legros, Krystle Moore, Nathan Gerein and Adrien Vezinet assisted in sample preparation and preliminary work for this study. Rubidium-strontium isotope data were acquired at the University of Alberta with the help of Andy DuFrane, Chiranjeeb Sarkar, Rob Creaser and Graham Pearson. X-ray fluorescence analyses were performed by Lydia Zehnder at the Institute for Geochemistry and Petrology, ETH Zürich. Micro X-ray fluorescence data were acquired by Guanhua Li at the Key Laboratory of Deep Oil and Gas of China University of Petroleum. Data interpretation and primary discussions were performed by the author and Pilar Lecumberri-Sanchez. The first draft of this manuscript was written by the author. All co-authors collaborated in fruitful discussions and the preparation of subsequent versions of the manuscript.

Chapter 4 has been accepted for publication in GEOLOGY as: "Elongo, V., Lecumberri-Sanchez, P., Falck, H., Rasmussen, K., Robbins, L.J., Creaser, R., Luo, Y., Pearson, D.G., Sarkar, C., Adlakha, E., Palmer, M.C., Scott, J.M., Hickey, K., & Konhauser, K. *Ancient roots of tungsten in western North America*.". This chapter integrates the data produced in this study, and a compilation of literature data. Data compilation was performed by the author. Krystle Moore, Hélène Legros, Adrien Vezinet and Nathan Gerein assisted in sample preparation and preliminary work for this study. Samarium-neodymium isotope data were acquired at the University of Alberta with the help of Yan Luo, Chiranjeeb Sarkar, Andy DuFrane, Rob Creaser and Graham Pearson. Preliminary data analysis was performed by the author, Pilar Lecumberri-Sanchez, Graham Pearson and Kirsten Rasmussen. The first version of this manuscript was written by the author and Pilar Lecumberri-Sanchez. All co-authors contributed valuable ideas to the manuscript and subsequent data analysis, interpretation and writing, review and editing of the manuscript.

Chapter 5 (Conclusions) is an original work produced by the author for this thesis.

Dedication

To my father, Felix Elongo

You believed in me and wanted me to get all the great things life has to offer, and beyond.

I know this comes a little late, but I hope I still have made you proud.

Dad, you are my inspiration; you are my way!

To my mother, Sophie Clementine Goura

Mom, you are the strongest and sweetest person I have known.

If I am able to be even a quarter of the beautiful soul that you were, I can consider my life successful.

Acknowledgments

So many people are to thank for help designing and bringing this project to fruition. The following list is far from being exhaustive, and I apologize for not being able to list all those people because of the two-page limit of this section. To my family, friends, colleagues, and all mentors, I am grateful for all your contributions and acknowledge that I would not be writing this thesis without your multifaceted contributions.

First, I would like to thank my supervisor Dr. Pilar Lecumberri-Sanchez for giving me the opportunity to pursue this PhD research. I was very lucky to be her first PhD student and to benefit from her incredible knowledge. I am deeply grateful for her patience and guidance throughout this journey. Her kindness and constant support really contributed to my joyful experience. – Pilar, keep being awesome!

Second, I would like to thank Hendrik Falck. Hendrik has been very supportive, always enthusiastic and has contributed in so many ways to this project. His dedication and his willingness to assist wherever and whenever needed really are exceptional.

This work was supported by funding from the Natural Sciences and Engineering Resources Canada Discovery grant, Northwest Territories Geological Survey contribution agreements, Targeted Geosciences Initiative from Natural Resources Canada GC-130028S and the Polar Continental Shelf Program to Pilar Lecumberri-Sanchez. This project was also facilitated by the logistical and in-kind support from North American Tungsten Ltd. – Thank you very much, this work would not have been possible without your numerous contributions!

Much of this work would not have been possible without the help of many colleagues and collaborators from the University of Alberta. Thanks to Hélène Legros for always helping whenever needed in the lab. Thanks to Mark Labbe and Walter Harley for their help with thin sections and various equipment in the Headhouse. Thanks to Andrew Locock for his huge help with microprobe data collection and processing. Thanks to Yan Luo, Chiranjeeb Sarkar, Andy DuFrane, Rob Creaser and Graham Pearson for the samarium-neodymium and rubidium-strontium isotope data acquisition. Thanks to Andy DuFrane for his help with collecting LA-ICPMS data. Thanks to Krystle Moore for helping in the clean lab. Thanks to Adrien Vezinet for helping in the separation of my scheelite grains. Thanks to Igor Jakab for his help in the DIF lab and my numerous IT issues. Thanks to Nathan Gerein for his assistance with the SEM. Thank you to Lydia Zehnder from ETH Zürich, for performing the XRF analyses. And finally, thanks to Guanhua Li for acquiring the Micro XRF data at the China University of Petroleum.

I would like to thank my candidacy exam committee members: Pilar Lecumberri-Sanchez, Graham Pearson, Erin Adlakha, Andrew Locock and Karlis Muehlenbachs. Through their questions and comments, they helped me realize some important points that I needed to work on in order to conduct a successful PhD research project. Also, thank you to my PhD defense committee members: Pilar Lecumberri-Sanchez, Graham Pearson, Hendrik Falck, Matthieu Harlaux, Andrew Locock and Sasha Wilson and for taking the time to read through my thesis. I am looking forward to your questions and comments on this work as I know they will significantly help improve it.

Also, thanks to Pilar and to Dr. Matthew Steele-MacInnis for putting together such amazing research groups. The two Mineral Deposits research groups combined really formed an awesome crew! I am thankful for all your feedback when preparing my different presentations, for your questions about my data and for our fruitful discussions. Thanks a lot for the great time spent together at our regular group meetings, the Faculty Club, our barbecue parties and others.

Shoutout to my favorite *French crew*!!! Your presence was such a relief from the start of my PhD. I will always be grateful for your love and support during this journey.
Same goes to my *ladies*; you are amazing and have provided me with so much joy and fun time! To my other friends at the UofA, thanks for the welcoming environment, for the laughs, for all the good vibes; thanks for everything. Buddies, you have created memories that I will cherish forever.

Huge thank you to my family for believing in me and providing constant support since the beginning of time. They have invested in my future -in so many ways- and I hope that this accomplishment makes them proud. Dear family, your love is everything!!!

Thank you to my partner, Benhy. Your unconditional love and support have helped me way more than you think. You were there for me when I was at my lowest, encouraged and supported me in the completion of this work. I am so grateful to have you in my life and, knowing that I can always count on you means the world to me. -You are my rock!

And above all, thanks to the Creator!

Table of contents

List of tables

List of figures

Chapter 1: Introduction

1.1. Tungsten and tungsten skarn deposits

Tungsten is a metal used in a wide variety of sectors to make wear-resistant materials and heavy metal alloys used by petroleum, mining, construction, and metalworking industries. Tungsten is further used in lighting, electronic, electrical, welding and heating applications. In the last few years, tungsten has been classified a critical metal meaning that (1) it is essential to our modern life and economy, (2) it has no viable substitutes, and (3) its supply is at high risk and may be disrupted (Union, 2014; Fortier et al., 2018). With increasing applications in technology, the demand for tungsten is constantly on the rise. The supply of the current and future demand in tungsten relies on the discovery of new tungsten deposits, which relies upon our understanding of all the processes that lead to the concentration of tungsten ores. Hence, understanding all parameters involved in the genesis of tungsten deposits is critical to the future of all the sectors depending on tungsten supplies.

Tungsten skarn deposits exhibit higher grades than other tungsten deposits and constitute the main source of tungsten (Werner et al., 1998). Skarns are calc-silicate rocks which form in or at the contact with carbonate rocks, as a result of their interaction with hydrothermal fluids exsolved from a magma (Meinert, 1992). Specifically, tungsten skarn deposits are usually associated with calc-alkalic magmatism in orogenic belts (Meinert, 1992). In North America, the most important tungsten resources occur as skarns, and are located in the Canadian Cordillera (Dick & Hodgson, 1982).

1.2. Geology of the Canadian Cordillera

The Canadian Cordillera is the northern expression of the North American Cordillera, an orogen westerly along North America. The Canadian Cordillera covers the most part of Yukon and British Columbia Territories, the southwest part of the Northwest Territories and southwest Alberta in Canada (Fig 1.1). The North American Cordillera formed from the amalgamation of several terranes (Fig 1.1) on the western part of the Ancient North American basement, subsequent to the breakup of Rodinia supercontinent 750Ma ago (Gordey and Anderson, 1993; Ray, 2013). The Cordillera comprises accretionary complexes, oceanic arcs, pericratonic terranes, craton margin sedimentary rocks and ocean-floor rocks (Monger and Nokleberg, 1996; Nelson and Colpron, 2007; Ray, 2013). The amalgamation of those terranes was accompanied by extensive magmatism, displaying a wide range of compositions. Alkaline to sub- alkaline, I-type arc-related and S-type derived from crustal melts occur in the Cordillera and are associated with numerous mineralization types (Fig. 1.1; Hart, 1997; Driver et al., 2000; Hart et al., 2004; Ray, 2013). The westward pile of sedimentary rocks of mid-Proterozoic to mid-Jurassic age deposited along the continental margin of western North America is referred to as the “miogeocline” (Gordey and Anderson, 1993). The Canadian Cordillera miogeocline comprises late Precambrian to Middle Devonian deep shelf clastic rocks of the Selwyn Basin (Fig. 1.2), its northeastern coeval shallow shelf Mackenzie platform, and the Siluro-Devonian carbonate-clastic shelf called Cassiar platform. This sequence was followed by late Devonian to early Carboniferous turbiditic clastics and early Carboniferous to Triassic shallow water clastics, chert and carbonates (Gordey and Anderson, 1993). These units were subsequently deformed into a northeastward thin-skinned fold and thrust belt throughout the Mesozoic, caused by compressional deformation, with variably oblique dextral movement of the subducting oceanic plate relative to the Ancient North American craton margin (Price and

Carmichael, 1986; Gabrielse and Yorath, 1991; Gordey and Anderson, 1993). The dextral movement was accommodated by transpressional faults, mainly the Denali Fault and the Tintina Fault (Fig. 1.2) that were active from the Cretaceous to Eocene (Gabrielse et al., 2006).

More than 1000 skarns are known in the Canadian Cordillera, most of them bearing economic minerals (Fig. 1.1) ranging from small occurrences to large deposits and varying in age from Pre-Middle Triassic to Eocene-Oligocene (Ray, 2013). Three major periods of skarn development are recorded and are related to major plutonic episodes:

1/The first occurred during the Early to mid-Jurassic and is responsible of the formation of over half of the skarns in the cordillera. This plutonism of alkalic and calc-alkalic I-type (Ray, 2013) is related to subducting oceanic crust (Armstrong, 1988) and resulted in most of the Au, Fe and Cu skarns, and many of the Cu-Mo and Cu-Au porphyry deposits in the region (Preto, 1972; Preto et al., 1979; Dawson et al., 1991; Ray, 2013).

2/The second plutonic episode occurred during the Cretaceous. It is a syn to post-accretion magmatism, comprising several events that are related either to arc magmatism associated with subduction along the western margin of North America or back-arc magmatism associated with partial melting of the continental crust (Rasmussen, 2013). This magmatism, either I- or S-type depending on locations, reached its paroxysm in mid-Cretaceous and is responsible for most of the W and Sn skarns and some Cu skarns in the region (Ray, 2013).

Among the mid-Cretaceous plutonic belts found in the region, the innermost, the Tombstone-Tungsten Belt (Fig. 1.2) is of interest in this study. The Tombstone-Tungsten Belt comprises more than 100 plutons, numerous dykes and sills, grouped in three plutonic suites in the basis of their distribution and lithological similarities: Tombstone, Mayo and Tungsten (Fig. 1.2; Hart et al., 2004). These three plutonic suites show different characteristics and metallogeny. The Tombstone suite (94-89 Ma; Rasmussen, 2013) comprises dominantly coarse-grained alkali feldspar syenite to quartz syenite plutons associated with Au-Cu-Bi and U-Th-F mineralization. The Mayo suite (98-93 Ma; Rasmussen, 2013) consists mainly of medium- to fine-grained monzonite to granodiorite plutons associated with lamprophyres, porphyritic granitic dykes, aplites and pegmatites, and is associated with Au-Bi-Te, W, As and Ag-Pb mineralization. The Tungsten suite (98-95 Ma; Rasmussen, 2013) consists of medium-grained granite to monzogranite plutons with associated pegmatites, aplites and greisens and is related to W and Cu-Zn-Mo mineralization (Hart et al., 2004). The Tungsten suite intrusions and associated tungsten deposits form the "Canadian Tungsten Belt" (Fig. 1.2).

3/The third plutonic episode occurred in the Eocene-Oligocene and was related to transtensional movements and melting of the Ancestral North America Craton and its platform sediments (Woodsworth et al., 1991). This magmatism resulted in only a few number of Pb-Zn, Fe, Cu(-Au) and W skarns (Ray et al., 1995; Ray et al., 2002; Ray, 2013).

1.3. Research objectives and outline of the dissertation

The objective of this PhD research is to constrain the parameters that controlled known tungsten mineralization in the Canadian Cordillera, with the aim to determine the critical parameters that can be applicable on a broader scale to other major tungsten endowments in the world. In North America, the most important tungsten resources are in the Canadian Tungsten Belt and include the Cantung (3.8 Mt at 0.97% WO_3) and Mactung (33 Mt at 0.88% WO_3) deposits (Fig. 1.2; Dick & Hodgson, 1982; Government of Northwest Territories, 2016). The Lened deposit (Fig. 1.2) is a higher-grade tungsten deposit but lower tonnage (0.9 Mt at 1.0% WO_3) than Cantung and Mactung (Government of Northwest Territories, 2016). Because of their significant tungsten endowment, these deposits provide an ideal framework to study the parameters that govern tungsten mineralization. However, throughout this dissertation, emphasis will be put on the higher tonnage Cantung and Mactung deposits.

The largest proportion of tungsten resources in the world occur in skarns (Werner et al., 1998). Previous studies have shown that skarn mineral compositions and assemblages can provide information on their environment of formation and the redox conditions prevailing during skarn development, from which skarns can be classified in reduced or oxidized types (e.g., Kwak, 1986; Einaudi et al., 1981; Meinert, 1992; Nakano et al, 1994). The redox state is an important parameter because oxidized tungsten skarns are reported to be generally lower grade than reduced tungsten skarns due to reduced environments favoring the extraction of tungsten from the magma to the hydrothermal fluid (Candela, 1992). Constraining specific alteration stages at which peaks in tungsten concentrations are observed aids exploration and metallurgy, as well as contribute to more comprehensive genetic models. Therefore, establishing the paragenesis of the tungsten deposits in the study area, and the redox state of the system through mineral chemistry was the starting point towards a better understanding of the genesis of these tungsten deposits. These points will be addressed in **Chapter 2** of this thesis.

Fluid-rock interaction has been inferred as being decisive for tungsten mineralization (e.g., Lecumberri-Sanchez et al., 2017). However, the source of ore fluids in tungsten systems remains controversial. Tungsten deposits are commonly proposed to be related to crust-derived felsic magmas (Einaudi et al., 1981; Wang et al., 2010; Schmidt et al., 2012; Song et al., 2014; Legros et al., 2019; Sun et al., 2019; Zhu et al., 2019). However, mantle-derived mafic magmas have also been encountered in association with many high-grade tungsten deposits such as the Panasqueira deposit in Portugal (Burnard & Polya, 2004) or the Xihuashan deposit in China (Wei et al., 2019) among others. The occurrence of these potential mafic sources raises the question of the role of mafic magmas in the process of the formation of high-grade tungsten deposits and specifically if they are capable of enhancing the endowment of tungsten. The effects of fluid-rock interaction and the association of tungsten mineralization with crust- or mantle-derived materials are therefore crucial for a clearer understanding of the processes responsible for economic concentrations of tungsten. These points will be addressed in **Chapter 3** of this thesis. Strontium isotopes and element budget (major and trace element variations) are used for this purpose.

Despite a similar tectonic setting across the North American Cordillera, the distribution of tungsten deposits is highly irregular, and major tungsten deposits are located in narrow areas only (e.g., the Canadian Tungsten Belt, Fig. 1.2). Besides the tectonic controls and their associated magmatism, other parameters must then be responsible for the geographical distribution of tungsten mineralization. The factors that control tungsten endowment and distribution across the North American Cordillera are addressed in **Chapter 4** of this thesis. Neodymium isotopes, zircon saturation temperatures and oxidation state of magmatic rocks associated with tungsten deposits, as well as basement rock data are used for this purpose.

A summary of all the findings of this PhD research and future research directions are provided in **Chapter 5** of this thesis.

1.4. References

Armstrong, R. L., & Clark, S. P. (1988). Mesozoic and early Cenozoic magmatic evolution of the Canadian Cordillera. Geological Society of America Special Paper, 218, 55-91.

Burnard, P. G., & Polya, D. A. (2004). Importance of mantle derived fluids during granite associated hydrothermal circulation: He and Ar isotopes of ore minerals from Panasqueira. Geochimica et Cosmochimica Acta, 68(7), 1607-1615.

Candela, P. A. (1992). Controls on ore metal ratios in granite-related ore systems: an experimental and computational approach. Earth and Environmental Science Transactions of the Royal Society of Edinburgh, 83(1-2), 317-326.

Dawson, K.M., Panteleyev, A., Sutherland Brown, A., and Woodsworth. G.J. (1991). Regional metallogeny (Chapter 19). In Geology of the Cordilleran Orogeny in Canada. (H. Gabrielse and C.J. Yorath, eds.). Geological Survey of Canada, Geology of Canada 4, p. 707-768.

Dick, L. A., & Hodgson, C. J. (1982). The MacTung W-Cu (Zn) contact metasomatic and related deposits of the northeastern Canadian Cordillera. Economic Geology, 77(4), 845-867.

Driver, L. A., Creaser, R. A., Chacko, T., & Erdmer, P. (2000). Petrogenesis of the Cretaceous Cassiar batholith, Yukon–British Columbia, Canada: Implications for magmatism in the North American Cordilleran interior. Geological Society of America Bulletin, 112(7), 1119-1133.

Einaudi, M. T. (1981). Skarn deposits. Economic Geology, 75, 317-391.

Fortier, S. M., Nassar, N. T., Lederer, G. W., Brainard, J., Gambogi, J., & McCullough, E. A. (2018). Draft critical mineral list—Summary of methodology and background information—US Geological Survey technical input document in response to Secretarial Order No. 3359 (No. 2018-1021). US Geological Survey.

Gabrielse, H., & Yorath, C. J. (1991). Geology of the Cordilleran orogen in Canada. Geological Society of America, Volume G2

Gabrielse, H., Murphy, D. C., Mortensen, J. K., Haggart, J. W., Enkin, R. J., & Monger, J. W. H. (2006). Cretaceous and Cenozoic dextral orogen-parallel displacements, magmatism, and paleogeography, north-central Canadian Cordillera. Paleogeography of the North American Cordillera: Evidence For and Against Large-Scale Displacements: Geological Association of Canada Special Paper, 46, 255-276.

Gordey, S. P., & Anderson, R. G. (1993). Evolution of the northern Cordilleran miogeocline, Nahanni map area (105I), Yukon and Northwest Territories. Geological Survey of Canada Memoir 428, 214p.

Government of Northwest Territories (2016). A Guide to Mineral Deposits in the Northwest Territories. https://www.iti.gov.nt.ca/sites/iti/files/mineraldeposites2-nocrops.pdf

Hart, C. J. R. (1997). A transect across Stikinia: Geology of the northern Whitehorse map area, southern Yukon Territory (105D13–16). Exploration and Geological Services Division, Yukon, Indian and Northern Affairs Canada Bulletin 8, 1–112.

Hart, C. J., Mair, J. L., Goldfarb, R. J., & Groves, D. I. (2004). Source and redox controls on metallogenic variations in intrusion-related ore systems, Tombstone-Tungsten Belt, Yukon Territory, Canada. Earth and Environmental Science Transactions of The Royal Society of Edinburgh, 95(1-2), 339-356.

Kwak, T. A. P. (1986). Fluid inclusions in skarns (carbonate replacement deposits). Journal of Metamorphic Geology, 4(4), 363-384.

Lecumberri-Sanchez, P., Vieira, R., Heinrich, C. A., Pinto, F., & Wälle, M. (2017). Fluid-rock interaction is decisive for the formation of tungsten deposits. Geology, 45(7), 579-582.

Legros, H., Richard, A., Tarantola, A., Kouzmanov, K., Mercadier, J., Vennemann, T., ... & Bailly, L. (2019). Multiple fluids involved in granite-related W-Sn deposits from the world-class Jiangxi province (China). Chemical Geology, 508, 92-115.

Meinert, L. D. (1992). Skarns and skarn deposits. Geoscience Canada, 19(4).

Monger, J. W., Nokleberg, W. J., Coyner, A. R., & Fahey, P. L. (1996). Evolution of the northern North American Cordillera: generation, fragmentation, displacement and accretion of successive North American plate-margin arcs. Geology and Ore Deposits of the American Cordillera. Geological Society of Nevada, 1133-1152.

Nakano, T., Yoshino, T., Shimazaki, H., & Shimizu, M. (1994). Pyroxene composition as an indicator in the classification of skarn deposits. Economic Geology, 89(7), 1567-1580.

Nelson, J. L. and Colpron, M. (2007). Tectonics and metallogeny of the Canadian and Alaskan Cordillera, 1.8 Ga to present, in Goodfellow, W. D., ed., Mineral Deposits of Canada: A Synthesis of Major Deposit Types, District Metallogeny, the Evolution of Geological Provinces, and Exploration Methods: Mineral Deposit Division, Geological Association of Canada, Special Publication 5, p. 755-791.

Preto, V. A. G. (1972). Geology of Copper Mountain, BC Dept. of Mines and Petroleum Resources. Bulletin, 59.

Preto, V. A., Osatenko, M. J., McMillan, W. J., & Armstrong, R. L. (1979). Isotopic dates and strontium isotopic ratios for plutonic and volcanic rocks in the Quesnel Trough and Nicola Belt, south–central British Columbia. Canadian Journal of Earth Sciences, 16(9), 1658-1672.

Price, R. A., & Carmichael, D. M. (1986). Geometric test for Late Cretaceous-Paleogene intracontinental transform faulting in the Canadian Cordillera. Geology, 14(6), 468-471.

Rasmussen, K.L. (2013) The timing, composition, and petrogenesis of syn- to post-accretionary magmatism in the northern Cordilleran miogeocline, eastern Yukon and southwestern Northwest Territories. Ph.D. Thesis, University of British Columbia, Vancouver, British Columbia, Canada, 788 pp.

Ray, G. E. (2013). A review of skarn in Canadian Cordillera. British Columbia Ministry of Energy and Mines, British Columbia Geological Survey Open File, 8, 50.

Schmidt, S., Geo, P., & Hutten, W. (2012). From Deposit to Concentrate: The Basis of Tungsten Mining. Part 1: Project Generation and Project Development. International Tungsten Industry Association Newsletter June.

Song, G., Qin, K., Li, G., Evans, N. J., & Chen, L. (2014). Scheelite elemental and isotopic signatures: Implications for the genesis of skarn-type W-Mo deposits in the Chizhou Area, Anhui Province, Eastern China. American Mineralogist, 99(2-3), 303-317.

Sun, K., Chen, B., & Deng, J. (2019). Ore genesis of the Zhuxi supergiant W-Cu skarn polymetallic deposit, South China: Evidence from scheelite geochemistry. Ore Geology Reviews, 107, 14-29.

Union, I. (2014). Communication from the Commission to the European Parliament, the Council, the European Economic and Social Committee and the Committee of the Regions. A new skills agenda for europe. Brussels.

Wang, X., Ni, P., Jiang, S., Zhao, K., & Wang, T. (2010). Origin of ore-forming fluid in the Piaotang tungsten deposit in Jiangxi Province: Evidence from helium and argon isotopes. Chinese Science Bulletin, 55(7), 628-634.

Wei, W. F., Hu, R. Z., Bi, X. W., Jiang, G. H., Yan, B., Yin, R. S., & Yang, J. H. (2019). Mantle-derived and crustal He and Ar in the ore-forming fluids of the Xihuashan granite-associated tungsten ore deposit, South China. Ore Geology Reviews, 105, 605-615.

Wei, W. F., Hu, R. Z., Bi, X. W., Jiang, G. H., Yan, B., Yin, R. S., & Yang, J. H. (2019). Mantle-derived and crustal He and Ar in the ore-forming fluids of the Xihuashan granite-associated tungsten ore deposit, South China. Ore Geology Reviews, 105, 605-615.

Zhu, Lü-Yun, et al. "Origin of the Shangfang Tungsten Deposit in the Fujian Province of Southeast China: Evidence from Scheelite Sm–Nd Geochronology, H–O Isotopes and Fluid Inclusions Studies." Minerals 9.11 (2019): 713.

1.5. Figures

Figure 1.1. Simplified terrane map of the Canadian Cordillera, showing locations of significant skarn mineralization. Modified from Ray (2013).

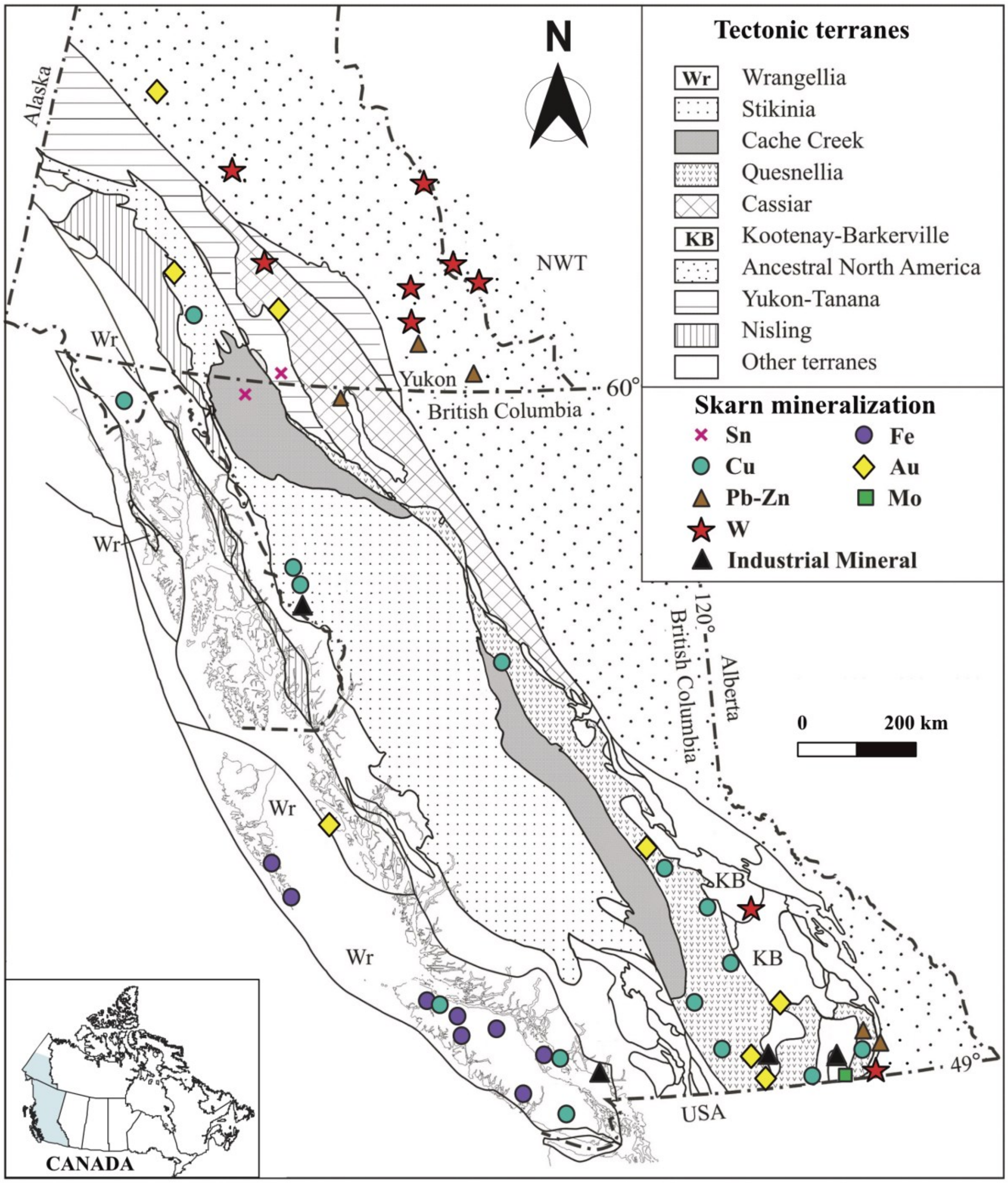

Figure 1.2. Regional map showing the geographical distribution of the mid-Cretaceous plutonic suites, including the location of the Tombstone-Tungsten Belt comprising the Tombstone, Mayo and Tungsten suites, and the location of the Cantung, Mactung and Lened deposits (modified from Hart et al., 2004). The grey-shaded area represents the Selwyn Basin. The Tungsten suite intrusions and associated tungsten deposits form the "Canadian Tungsten Belt".

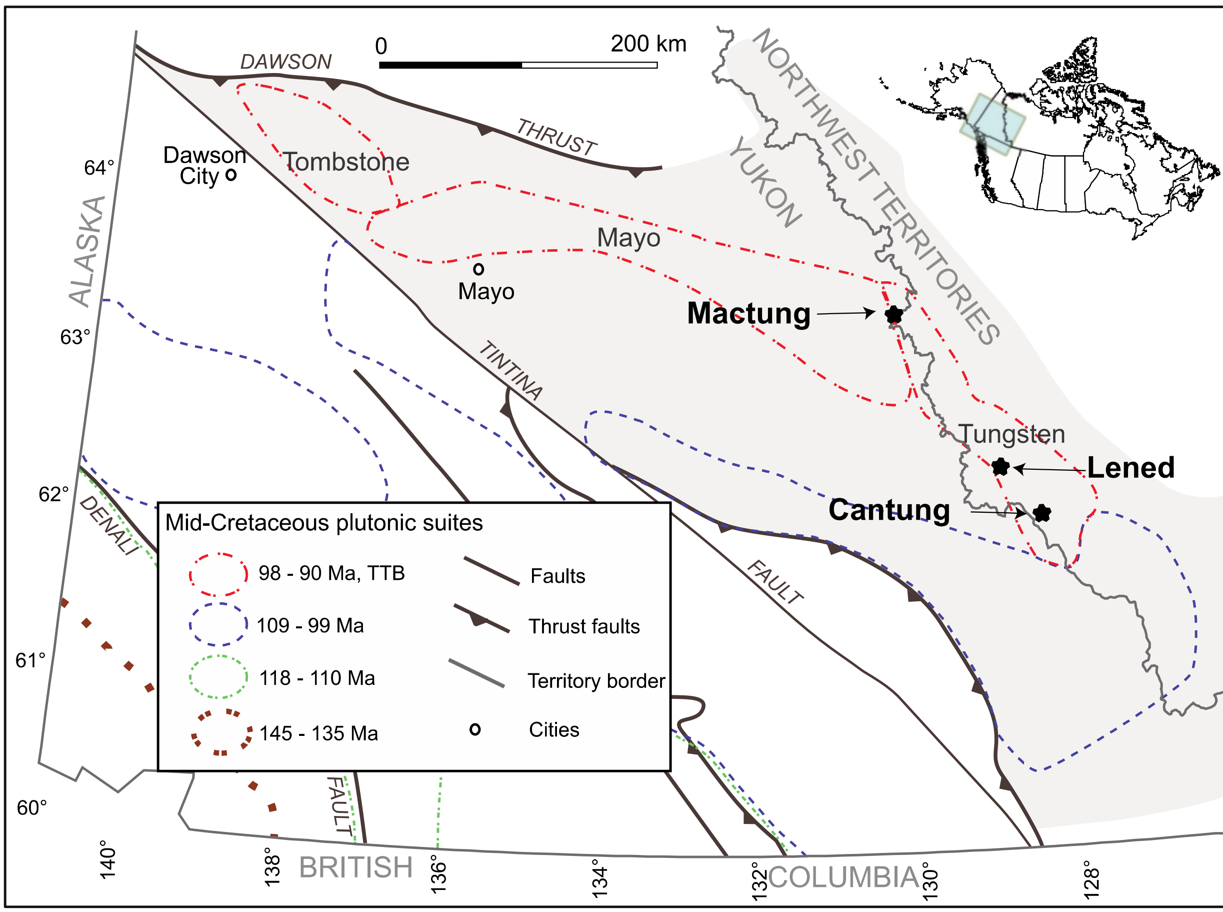

Chapter 2: Paragenetic constraints on the Cantung, Mactung and Lened tungsten skarn deposits, Canada: implications for grade distribution

Abstract

The Cantung, Mactung, and Lened W skarn deposits located in Northwest Territories and Yukon of Canada are part of a large metallogenic belt that contains all major tungsten deposits in western North America. In this study, we evaluate the paragenesis and mineral compositions in these deposits to determine the parameters that control the distribution of high-grade W mineralization in these skarn deposits.

The mineral compositions of the Cantung, Mactung and Lened deposits are indicative of reduced fluids (grossular-rich garnet + hedenbergite-rich pyroxene + abundant pyrrhotite), which is characteristic of high-grade W deposits. Local mineral assemblages indicative of oxidizing conditions are observed at Lened, the smallest of the deposits, but are interpreted to be induced by sporadic barite-rich facies within the host rock, and not by an oxidized fluid. Therefore, the redox state of the skarn does not necessarily lessen the exploration potential for the Lened deposit.

A correlation between high sulfide and scheelite ($CaWO_4$) contents at Cantung, Mactung and Lened has been reported previously and observed in this study. However, petrographic observations from this study show that scheelite and sulfides precipitated at different times. Scheelite crystallized throughout the entire history of skarn development but peaked at different stages for each deposit. In contrast, sulfides have mainly crystallized as late stage minerals postdating the silicates and scheelite. Variations in the host rock texture and porosity, and therefore

permeability, are proposed to be the main factor controlling scheelite-sulfide distribution. This control would be manifested such that areas of greater permeability focused fluid flow, which favored the precipitation of both scheelite and sulfides at different times in the history of the system.

2.1. Introduction

Cantung, Mactung and Lened are tungsten skarn deposits located in the eastern margin of the Selwyn Basin, close to the Yukon-Northwest Territories border, and are part of the only tungsten province in western North America. These three deposits share common features that have been described by Dick and Hodgson (1982): (i) they are located within the thermal aureoles of quartz-monzonite granitoids of Middle to Late Cretaceous age, and (ii) they are the product of the hydrothermal alteration of lower Paleozoic carbonate rocks. The tungsten-bearing mineral in the three deposits is scheelite ($CaWO_4$). Based on current resource estimates, Cantung (3.8 Mt at 0.97% WO_3) and Mactung (33 Mt at 0.88% WO_3) are larger deposits than Lened (0.9 Mt at 1.0% WO_3) (Government of Northwest Territories, 2016).

Previous studies (e.g. Dick and Hodgson, 1982; Mathieson and Clark, 1984) determined which minerals occur in each skarn facies (mineral associations) but did not establish which minerals precipitated in equilibrium in each facies (mineral assemblages) or the chronological order of crystallization of these mineral assemblages (paragenesis). Despite their similar characteristics and association with the same magmatic event and host rocks, the factors controlling the difference in size between Lened, Cantung and Mactung remain unclear.

This study proposes a detailed paragenetic sequence for the skarn facies recognized by Zaw and Clark (1978), Dick and Hodgson (1982) and Mathieson and Clark (1984) and provides new insight into their petrography and mineral chemistry to understand the controls on mineral associations (which minerals correlate with scheelite) and to evaluate the potential impact of the ore fluid redox state on the fertility of each deposit.

2.2. Regional geological setting

The Canadian Cordillera is the northern expression of the American Cordillera evolving along the western North American craton margin that formed during the breakup of Rodinia supercontinent at 750 Ma (Gordey and Anderson, 1983; Ray, 2013). The Cordillera includes several terranes that accreted against the western part of the ancient North American basement consisting of pericratonic terranes, oceanic arcs, accretionary complexes, craton margin sedimentary rocks and ocean-floor rocks (Monger and Nokleberg, 1996; Nelson and Colpron, 2007; Ray, 2013). Extensive and highly diverse magmatism accompanied and followed amalgamation of the terranes. Plutonic suites including alkaline to sub-alkaline, I-type arc-related and S-type derived from crustal melts are associated with various types of skarn ores (Hart, 1997; Driver et al., 2000; Hart et al., 2004; Ray, 2013; Rasmussen, 2013).

Over a thousand skarns ranging from small occurrences to large deposits are known in the Canadian Cordillera (Ray, 2013), and vary in age from Pre-Middle Triassic to Eocene-Oligocene. Three main periods of skarn development are recorded, related to major plutonic episodes during the i) Early to mid-Jurassic, ii) mid-Cretaceous and iii) Eocene-Oligocene (Ray, 2013). Among the mid-Cretaceous plutonic belts found in the region, the innermost Tombstone-Tungsten Belt (TTB) hosts tungsten resources with tonnages and grades significantly higher than most tungsten mines in the world (Einaudi and Burt, 1982). The TTB extends from the Alaska-Yukon border across Yukon and then southeast in the Northwest Territories (Fig. 2.1). The TTB comprises more than a hundred plutons and numerous dykes and sills that are grouped in three plutonic suites: Tombstone, Mayo and Tungsten (Fig. 2.1, Hart et al., 2004). The three plutonic suites show different lithologic characteristics and metallogeny. The Tombstone suite comprises dominantly coarse-grained alkali feldspar syenite to quartz syenite plutons associated with Au-Cu-Bi and U-Th-F mineralization. The Mayo suite consists mainly of medium- to fine-grained monzonite to granodiorite plutons with crosscutting lamprophyres, porphyritic granitic dykes, aplites and pegmatites and associated with Au-Bi-Te, W, As and Ag-Pb mineralization. The Tungsten suite consists of medium-grained granite to monzogranite plutons with associated pegmatites, aplites and greisens and is related to W and Cu-Zn-Mo mineralization (Hart et al., 2004), including the Cantung, Mactung and Lened deposits.

In the study area, two main contrasting facies were deposited during the evolution of the western North American craton from late Precambrian to Middle Devonian: deep-water shale, chert and sandstone on the southwest forming the Selwyn Basin, and coeval shallow water carbonates on the northeast in the Mackenzie Platform (Gordey and Anderson, 1993). This sequence was followed by late Devonian to early Carboniferous turbiditic clastics and early Carboniferous to Triassic shallow water clastics, chert and carbonates.

2.3. Local geologic setting

2.3.1. Cantung

The Cantung deposit is located in the eastern part of the Selwyn Basin in the Northwest Territories. The synclinally folded sedimentary rocks of the Flat River consist of a 6100 meters Upper Proterozoic to Upper Ordovician succession (Blusson, 1968) of sandstones, carbonates and shales. The four main units at Cantung are the “lower argillite” belonging to the Narchilla/Vampire

Formation, the “Swiss-Cheese” limestone (SCL), “Ore” limestone (OL) and “upper argillite” members of the Sekwi Formation (Fig. 2.2). The lower argillite (also referred to as the Footwall Argillite) is the oldest unit in the Cantung area, comprising in order of abundance slate, phyllite, siltstone and fine-grained quartzite with a thickness exceeding 2700 meters. The SCL consists of a 75 meters thick series of intercalated layers of siltstone and fine-grained limestone, which were compacted resulting in pods and lenses of limestone surrounded by a siltstone matrix, giving a "swiss cheese" aspect. The OL is a 100-meter-thick massive limestone that overlies conformably on the SCL. The OL consists generally of extremely pure calcite, with minor silt and argillite laminations and some coarse quartz sand, with dark and light grey to white layers. The upper argillite (also called Hanging-wall Argillite) is exposed only on the southwest side of the Flat River valley, thinning northwards and expanding southwards to a thickness of more than 700 meters of calcareous argillite, slate and shale, with local thin layers of limestone. The sequence is folded into a recumbent anticline plunging to the NE and intruded by the Mine Stock, a peraluminous S-type medium-grained biotite monzogranite (Mathieson and Clark, 1984; Fig. 2.2). The Mine Stock (101.15 ± 0.44 to 98.2 ± 0.4 Ma from U-Pb in zircons, Rasmussen et al., 2007) and its northern neighbor, the Circular Stock (96.7 ± 0.6 Ma from U-Pb in zircons; Rasmussen et al., 2011) are responsible for the contact metamorphism of sedimentary rocks at Cantung (Mathieson and Clark, 1984).

Two exoskarn orebodies have been described at Cantung: The Pit (open pit mining) and the E-zone (underground mining), and both are hosted in the OL and the SCL (Blusson, 1968; Zaw and Clark, 1978; Dick and Hodgson, 1982; Mathieson and Clark, 1984, Bowman et al., 1985, Yuvan, 2006, Fig. 2.2). The W-bearing mineral is scheelite, which is hosted in the skarnified SCL and OL as veins and disseminated occurrences.

2.3.2. Mactung

The stratigraphic succession at Mactung consists of variably metamorphosed pelites with interbedded carbonate units ranging from late Precambrian to late Ordovician designated alphanumerically: 1, 2B, 3C, 3D, 3E, 3F, 3G, 3H, and 4 (Dick and Hodgson, 1982; Fig. 2.3). The oldest outcropping unit (1) consists of a micaceous phyllite belonging to the Vampire Formation. The lower carbonate unit (2B) belongs to the Sekwi Formation. Unit 3C is a metapelitic unit belonging to the Hess River formation. The upper carbonate includes three distinct units (3D, 3E, 3F) that, in addition to dolostone (3G) and metapelitic (3H) units, belong to the Rabbitkettle Formation. Finally, Unit 4 consists of calcareous black shale and siliceous argillite belonging to the Duo Lake Formation (Gebru, 2017, Fischer et al., 2018). The sequence is isoclinally folded (Fig. 2.3).

The Mactung deposit is spatially associated with two cretaceous biotite quartz monzonite plutons: the Cirque Lake Stock also called Mactung North Pluton and the Rockslide Mountain Stock also called Mactung South Pluton. The skarn mineralization (97.5 ± 0.5 Ma from Re–Os in molybdenite, Selby et al., 2003) is coeval with the crystallization of the Cirque Lake Stock and the Rockslide Mountain Stock (97.6 ± 0.2 Ma from U-Pb in zircons, Gebru, 2017).

Mineralization at Mactung occurs as two W-bearing exoskarn orebodies hosted in the Lower carbonate (unit 2B, Sekwi Formation) and the Upper carbonate (units 3D, 3E and 3F, Rabbitkettle Formation) (Gebru, 2017; Fischer et al., 2018) with scheelite either disseminated in the skarns or in veins cutting the skarns.

2.3.3. Lened

The stratigraphic succession in the Lened area consists of rocks ranging from Late Proterozoic to the Devonian and is intruded by Cretaceous plutons. The oldest unit at Lened is the Late Proterozoic to Lower Cambrian Vampire Formation, consisting of phyllitic shale, siltstone, and very fine to fine- grained sandstone (Gordey and Anderson, 1993; Marshall et al., 2004). This formation is overlaid by the Cambro-Ordovician Rabbitkettle Formation which consists of dark grey, thin- to medium-bedded limestone with argillaceous to silty layers, and whitish grey dolomitic limestone to dark grey calcareous shaley siltstones (Gordey and Anderson, 1993; Marshall et al., 2004; Lake et al., 2017). Black shale, chert and sandstone conglomerate belonging to the Devono-Mississippian Portrait Lake Formation (Earn Group) have been thrust on top of the Rabbitkettle Formation along a fault contact (Gordey and Anderson, 1993; Marshall et al., 2004; Lake et al., 2017). The stratigraphic succession was intruded by the Lened pluton (Fig. 2.4), a two-mica Cretaceous monzogranite (97.5 ± 0.7 Ma, U-Pb in zircons, Rasmussen, 2013).

The Rabbitkettle Formation hosts the skarn orebodies and emerald-bearing quartz–carbonate veins. Tungsten mineralization at Lened is believed to be genetically related with the Lened pluton (Gordey and Anderson, 1993; Marshall et al., 2004; Lake et al., 2017). Mineralization is dominantly hosted by the Rabbitkettle Formation but also by the Lened pluton (Glover & Burson, 1987).

2.4. Materials and Methods

Ninety-seven samples from Cantung, forty-seven from Mactung and fifty-three from Lened were collected from outcrops and drill cores for the purpose of this study. Eighty-eight polished thin sections were made from these samples (forty-three from Cantung, twenty-two from Mactung and twenty-three from Lened). The samples were chosen to be representative of the unaltered rock-types and different skarn facies, while avoiding weathered rocks. Conventional petrographic methods, using an optical microscope with both transmitted and reflected light, were used for mineral identification and textural analysis to determine the mineral paragenesis.

The compositional variations of the dominant skarn minerals (garnet, pyroxene, amphibole, biotite and feldspars) in carbon-coated polished thin section was determined on an electron probe microanalyser (EPMA) [JEOL 8900 (TCP/IP Socket)] equipped with five tunable wavelength dispersive spectrometers at the Electron Microprobe Laboratory of the University of Alberta. Operating conditions include an accelerating voltage of 20 kV, beam current of 15 nA, and the beam diameter of 5 µm. Elements were acquired using analyzing crystals LIFH for Fe Kα and Mn Kα, PET for K Kα and Cr Kα, PETH for Ti Kα and Ca Kα, and TAP for Mg Kα, Na Kα, Al Kα and Si Kα. The standards were Alfa chromium oxide (for Cr), Rockport fayalite (Fe), 115900 labradorite (Ca), MTI Rutile (Ti), Frank Smith pyrope (Mg), Gore garnet (Si, Al), VA 131705 albite (Na), Itrongay sanidine (K), and Navegadora Mine spessartine-almandine (Mn).

For Ba-bearing phases, compositional analyses were acquired on a Cameca SX100/SXFive (TCP/IP Socket) EPMA equipped with five tunable wavelength dispersive spectrometers. Operating conditions used a beam energy of 15 kV, beam current of 20 nA, and the beam diameter of 5 µm at the Electron Microprobe Laboratory of the University of Alberta. Elements were acquired using analyzing crystals LLIF for Ba Lα, Fe Kα and Mn Kα, PET for Ti Kα, K Kα and Cr Kα, LPET for Ca Kα, Cl Kα and Sr Lα, LTAP for Si Kα, Al Kα, Mg Kα and Na Kα, and PC0 for F Kα. The standards were Alfa chromium oxide (for Cr), Wakefield diopside (Ca), Frank Smith pyrope (Mg), Itrongay sanidine (K and Si), Tugtupite (Cl and Na), Sanbornite, Fresno (Ba), SrTiO3 (Ti and Sr), Topaz (F), DUR Tephroite (Mn), Corundum (Al), and Elba 639 block Hematite (Fe).

The molar proportions of garnet end-members were calculated using the Microsoft Excel spreadsheet from Locock (2008). Pyroxenes were classified using WinPyrox program from Yavuz (2013) based on the standard International Mineralogical Association (IMA-88) nomenclature scheme. Amphiboles were classified using the Microsoft Excel spreadsheet from Locock (2014) and the results are presented on the calcic amphiboles classification diagram from Hawthorne et al. (2012).

2.5. Results

2.5.1. Facies and paragenesis

Cantung, Mactung and Lened show similar facies with comparable mineralogy and paragenesis. Two stages of skarn formation can be distinguished in the three deposits based on the dominant skarn minerals: the garnet-pyroxene stage and the pyroxene stage. The skarns are associated with an intense hydrosilicate alteration characterized by two main stages: an amphibole-rich stage and a biotite-rich stage. A late sulfide stage is also present.

The relative timing between the different stages is evidenced by the crosscutting relationships observed in drill core and outcrop (Fig. 2.5), and confirmed by replacement textures at the thin section scale. Garnet-pyroxene skarn is the earliest facies observed and is replaced by the pyroxene skarn at Cantung, Mactung and Lened. The garnet-pyroxene and pyroxene skarn facies are subsequently replaced and/or overprinted by the amphibole-rich facies, which is itself replaced by the biotite-rich facies (Fig. 2.5).

The textures, crystal sizes and accessory minerals of the different stages vary as a function of the host rock-type, even for a single deposit. Moreover, the crystallization sequence of minerals within the same facies and same deposit can vary slightly from a sample to another, highlighting a continued overlapping history. Despite this variation, there are some mineral associations and sequences that are similar between the three deposits. These are described below with particular emphasis on i) scheelite because of its economic importance, ii) sulfides because of their spatial correlation with scheelite (Dick and Hodgson, 1982), and iii) apatite and titanite because of their potential as chronometers and fluid tracers (Adlakha et al., 2018).

The paragenetic sequence summarizing the observations below is presented in Fig. 2.6. The mineralogy evolves from a prograde skarn stage consisting of the garnet-pyroxene and the pyroxene facies, to a retrograde hydrosilicate alteration stage represented by the amphibole-rich and the biotite-rich stages. These main stages are overprinted by a sulfide stage and followed by late replacement minerals.

2.5.1.1. Skarn facies

2.5.1.1.a. Garnet-pyroxene skarn

The main mineral in this skarn facies is garnet, with variable amounts of pyroxene and scheelite as other major minerals of comparable crystal size (mm-cm; Fig. 2.7 A, B) leading to an equigranular texture. Garnet at Cantung and Lened is mainly euhedral or subhedral and displays concentric zoning (Fig. 2.7 C, D), whereas garnet at Mactung is mostly subhedral (Fig. 2.7B). Scheelite is mostly µm-sized, euhedral or subhedral, and is either intergrown with garnet or in inclusions in both garnet and pyroxene (Fig. 2.7 B, C). Pyroxene is dominantly anhedral, occurs as overgrowths on both garnet and scheelite, and as replacement of garnet (Fig. 2.7 A, B, C), indicating that pyroxene postdates both garnet and scheelite. Scheelite, garnet and pyroxene often contain abundant µm-sized euhedral apatite inclusions; suggesting that apatite predates all of these minerals (Fig. 2.7F). Late garnet veinlets (garnet-pyrrhotite-calcite for Mactung) crosscut the garnet-pyroxene skarn at Cantung and Mactung. Garnet is commonly overgrown by euhedral µm-sized titanite. Late stage vesuvianite occurring as replacement of garnet is exclusive to this facies (Fig. 2.7H), being widespread in the OL (Cantung) and locally at Lened, but rare to absent in all other lithologies. At Cantung, mm-sized amphibole crystals replacing garnet and containing apatite, garnet and scheelite inclusions (Fig. 2.7J), suggest that amphibole postdates the aforementioned minerals.

Sulfides are generally not abundant in the garnet-pyroxene skarn. They consist mostly of µm - sized pyrrhotite intergrown with, or overgrown by, minor chalcopyrite and sphalerite. Sulfides are mostly anhedral and are present either in fractures or as replacement of all the silicates (Fig. 2.7A, C, E, F, I, J, L). Rare early sulfides occur in skarnified limestone pods in the SCL at Cantung, intergrown with garnet, as inclusions in pyroxene (Fig. 2.7C), and as overgrowths on garnet and scheelite (Fig. 2.7L). However, sulfides dominantly postdate the silicate phases in the garnet facies.

Scheelite at Mactung and Lened is not abundant in the garnet-pyroxene skarn and shows no obvious systematic distribution. At Cantung, scheelite can represent up to 15% (visual estimate) of the garnet-pyroxene skarn in the OL, where it is also coarser grained (up to 4mm).

2.5.1.1.b. Pyroxene skarn

The pyroxene skarn refers to the pyroxene-rich skarn assemblage that does not contain any garnet. In this assemblage, pyroxene is the main and sometimes exclusive mineral. Depending on the host rock, pyroxene is either fine-grained (µm to mm sized) or coarser (mm to cm sized). Pyroxene in this facies is mainly associated with scheelite. Scheelite is either euhedral or subhedral, mm to cm sized and either intergrown with (Fig. 2.8A, B), overgrown by (Fig. 2.8C), or as inclusions in pyroxene (Fig. 2.8C). Therefore, scheelite has a protracted crystallization history, precipitating prior to and synchronous with pyroxene. At Mactung, rare euhedral apatite inclusions are found in pyroxene but not in scheelite, suggesting that apatite formed between scheelite and pyroxene crystallization. Biotite in this facies is only found at Lened and can be abundant, as replacement of pyroxene in some samples (Fig. 2.8E). The biotite-bearing pyroxene facies is referred in this manuscript as the pyroxene-biotite facies and occurs only locally at Lened.

Sulfides can be abundant in the pyroxene facies and seem to correlate with scheelite (i.e., the scheelite content increases with the sulfide content). Sulfides in the three deposits are anhedral late-stage minerals, mostly present in fractures and consisting dominantly of pyrrhotite. Chalcopyrite and sphalerite are rare at Mactung. Chalcopyrite and pyrite are relatively abundant at Lened (Fig. 2.8F).

At Mactung, the pyroxene skarn is the most scheelite-rich facies (up to ~40% scheelite). Mineralization is especially well developed in finely layered host rock. In contrast, scheelite is scarce in this facies at Cantung. At Lened, scheelite content in pyroxene skarn is variable, but seems to correlate strongly with sulfide content and rock grain-size, such that sulfide-rich and fine-grained rocks contain higher scheelite content than sulfide-poor, coarse-grained rocks.

2.5.1.2. Hydrosilicate alteration facies

2.5.1.2.a. Amphibole-rich facies

Amphibole is the main mineral of this facies but can also occur as replacements of pyroxene in the pyroxene skarn (Lened) or garnet in the garnet-pyroxene skarn (Cantung-Fig. 2.7I). Amphibole crystals are µm-sized, euhedral, intergrown with and overgrown by subhedral µm-sized scheelite (Fig. 2.9A), or as overgrowths on euhedral scheelite (Fig. 2.9C). Euhedral and µm to mm-sized titanite inclusions in amphibole indicate that titanite pre-dates amphibole at Mactung. Scheelite also occur as inclusions in amphibole. The occurrence of scheelite inclusions in amphibole and amphibole inclusions in scheelite suggest that the two minerals are sub-coeval. Euhedral apatite inclusions in scheelite at Mactung suggest that apatite pre-dates scheelite. Biotite replacements of amphiboles and overgrowths on amphiboles (Fig. 2.9B) and scheelite indicate that biotite postdates both scheelite and amphibole.

Sulfides (pyrrhotite and rare chalcopyrite) are interstitial minerals, filling the voids between amphiboles, scheelite and biotite (Fig. 2.9A, B) and replacing amphibole (mostly at Mactung). This facies contains higher scheelite grade and more sulfides than other facies at Cantung, and has also high scheelite contents (up to 20% scheelite although not correlated with sulfides) at Mactung. The amphibole-rich facies is not well developed at Lened. Amphibole is anhedral and micron-sized. It occurs either with pyroxene inclusions in massive pyrrhotite in the reaction front of biotite-rich facies (Fig. 2.9D) or as a replacement product of pyroxene in the pyroxene skarn. Amphibole in the latter is replaced by pyrrhotite, manganaxinite (a Mn-Al-Ca borosilicate) and clinozoisite.

2.5.1.2.b. Biotite-rich facies

The biotite-rich facies consists of mainly biotite, quartz, apatite, sulfides, and rare plagioclase. This facies contains a significant proportion of quartz, especially at Cantung and Mactung. Biotite, quartz and apatite are µm to mm-sized, euhedral or subhedral and are intergrown or overgrown by each other (Fig. 2.10A, B), suggesting their co-precipitation. Biotite is sometimes partially altered to chlorite. Scheelite is up to 1mm in size and has an erratic distribution. It is either euhedral and overgrown by biotite, quartz and apatite (Fig. 2.10C) or anhedral and as overgrowths on apatite, quartz and biotite (Fig. 2.10D). Therefore, there are at least two generations of scheelite, one predating apatite, quartz and biotite and another generation postdating these minerals.

Sulfides are present as overgrowths on the other minerals in this facies (Fig. 2.10A, C, D) and can be abundant (Cantung, Lened) or rare (Mactung). At Mactung, late scheelite-sulfide veinlets crosscut the biotite-rich facies. In these veinlets, scheelite is euhedral/subhedral and intergrown with subhedral sulfides (Fig. 2.10F), suggesting a third generation of scheelite. Sulfide minerals consist of abundant pyrrhotite, chalcopyrite for the three deposits and rare sphalerite at Cantung. The sulfides are associated with minor native bismuth. Overall in this alteration facies, sulfide-rich samples have more scheelite than sulfide-poor samples.

At Cantung, in some cases, there is a transition from biotite-apatite-quartz-sulfide assemblage to a finer grained monomineralic assemblage of biotite only (Fig. 2.10E). At Lened, scheelite is widespread and is more abundant in this facies than in the others.

The biotite-rich facies is relatively rare at Mactung and Lened, whereas at Cantung it is very abundant.

2.5.1.3. Late stage replacements

Late stage replacements and overgrowths are common in all facies. Quartz, calcite, clinozoisite, chlorite, and rare plagioclase occur in all facies as anhedral overgrowths (Fig. 2.9C, D), interstitial precipitates (Fig. 2.8G), and/or replacements (Fig. 2.8A, 8C, 7H, 6J).

2.5.1.4. Mineralized plutons

At Lened, mineralization is not only hosted in sedimentary units but also in the Lened pluton. The hydrothermally altered Lened pluton consists of abundant plagioclase, with quartz, muscovite and titanite with ilmenite cores (Fig. 2.11 A, B). Accessory minerals include allanite and zircon. Scheelite and sulfides are present as hydrothermal alteration products. Scheelite is always anhedral, µm-sized and is present either in fractures or as replacement of titanite (Fig. 2.11 B, C). Sulfides are low in abundance but present in fractures (Fig. 2.11 A) and consist of pyrrhotite with minor chalcopyrite. The genetic relationship between scheelite and sulfides is not clear, as they do not occur together.

2.5.2. Skarn mineral compositions

Garnet at Cantung, Mactung and Lened consists mostly of solid solutions of grossular, spessartine, almandine and andradite, with small fractions of pyrope and schorlomite (Fig. 2.12, Table 2.1). Garnet at all three deposits is dominantly grossular (Fig. 2.12), with molar proportions ranging 39-85 % grossular for Cantung (n= 18), 50-81 % for Mactung garnet (n = 6), and 48-54 % for Lened (n = 7). Considering the compositional differences between early and late garnet within individual deposits, early disseminated garnet at Cantung and Mactung has a higher grossular component (44-62 % and 50-81%, respectively) than late garnet in veins (39-44 and 76%, respectively). The andradite mole fraction varies from 4 to 8% at Cantung, 8 to 14% at Mactung, and 0 to 7% at Lened. Pyrope and schorlomite fractions in the three deposits vary from 0 to less than 1% and 0 to 2% respectively. The compositional variation in garnet can be explained by extensive solid solution/substitution between grossular and spessartine+almandine, while the relative proportion of andradite is fairly similar between all garnets regardless of deposit and generation.

Pyroxene is a solid solution of diopside and hedenbergite (Table 2.2, Fig. 2.13). There is a relationship between the pyroxene composition and the type of skarn facies, especially at Mactung and Lened (Fig. 2.13A). At Cantung, pyroxene ranges from ferroan diopside to magnesian hedenbergite in composition (Di40-60; n = 12; Fig. 2.13A) independently of the host skarn facies. At Mactung and Lened, pyroxene from the garnet-pyroxene skarn is close to end-member hedenbergite (Di10-15 and Di12-20, respectively; n = 6 and 2, respectively) whereas those from the pyroxene skarn have mostly a magnesian-hedenbergite or ferroan-diopside composition (Di05-65 and Di25-70, respectively; n = 32 and 17, respectively). The range in data for Mactung and Lened pyroxene indicates that the pyroxene composition evolved from more Mg-rich to more Fe-rich throughout the paragenesis (Fig. 2.5). Note that the only diopsidic composition occurs in the pyroxene-biotite skarn at Lened (Di90-100; n = 19; Fig. 2.13A).

Amphibole at Mactung has a dominantly hornblende composition whereas amphibole from Cantung and Lened show extensive solid solution between hornblende and actinolite (Fig. 2.13B, 2.3). The composition of amphibole also varies among the different facies at Cantung. Amphibole composition in the garnet-(pyroxene) and the amphibole-biotite facies is highly variable ranging from actinolite/ferroactinolite to hornblende (Fig. 2.13B). Amphibole in the amphibole-rich facies is mostly actinolite (Fig. 2.13B).

The composition of mica varies between deposit and facies (Fig. 2.14 Table 2.4). Most Cantung, Mactung and Lened micas are solid solutions between phologopite and annite (Fig. 2.14). The composition of micas are narrow at Cantung and Lened (Phl50-72 and Phl60-65, respectively) whereas it is wider at Mactung, ranging from lower to higher phlogopite component (Phl33-68) (Fig. 2.14). At Lened, mica of the pyroxene-biotite facies exhibit solid solution between phlogopite and Ba-F-rich kinoshitalite (11-16 wt% Ba, ~3wt% F ; Table 2.4; Fig. 2.14).

The composition of feldspar at Mactung and Lened is mostly anorthitic (An72-96 and An90-98 respectively; Table 2.5; Fig. 2.15A) in all facies. At Cantung however, early feldspar in garnet-pyroxene skarn is anorthitic (An60-92), whereas late feldspar in biotite-rich facies is albitic (An0.6) (Fig. 2.15A). At Lened, feldspar from the pyroxene-biotite facies is Ba-rich (~36 wt% Ba on average; Table 2.1). Ba and Al substitute for K and Si in feldspar, reflecting solid solution between orthoclase ($KAlSi_3O_8$) and celsian ($BaAl_2Si_2O_8$; Fig. 2.15B).

Typical titanite, clinozoisite, vesuvianite and manganaxinite, do not show differences in composition as a function of the skarn facies (Table 2.6).

2.6. Discussion

2.6.1. Redox conditions of the Cantung, Mactung and Lened deposits

Skarn mineral compositions and assemblages provide information on their environment of formation and the redox conditions prevailing during skarn development, from which skarns can be classified in reduced (low fO_2, high Fe^{2+}) or oxidized (high fO_2, high Fe^{3+}) types (e.g. Kwak, 1986; Einaudi et al., 1981; Meinert, 1992; Nakano et al, 1994). Oxidized tungsten skarns are reported to be generally lower grade than reduced tungsten skarns because reduced environments favor the extraction of W from the magma to the hydrothermal fluid (Candela, 1992). The effect of oxygen fugacity on prograde skarn minerals is to produce hedenbergitic pyroxene and grossular-rich garnet in reduced environments, and diopsidic pyroxene, andraditic garnet and magnetite in oxidized environments (Kwak, 1994). In addition, sulfides like pyrrhotite tend to form in reduced environments while pyrite forms in more oxidized environments (Einaudi et al., 1981). The molybdenum content of scheelite is also used to decipher the oxidation state of deposits. As long as molybdenum is available in the fluid, oxidized environments favor the formation of Mo-bearing scheelite, whereas reduced environments form Mo-poor scheelite along with molybdenite, (Hsu and Galli, 1973; Hsu, 1977).

Calcic mineral assemblages dominate the Cantung, Mactung and Lened W skarn deposits. The grossular-rich garnet (>60 %) and hedenbergite-rich pyroxenes reported in this study are indicative of reduced skarns. The widespread occurrence of pyrrhotite and the absence of magnetite in the three deposits also support a reduced environment during skarn formation. In addition, molybdenite crystals, although rare, have been found at Cantung and Mactung and the bright blue fluorescence of scheelite suggests that it does not incorporate significant molybdenum (Mo-rich scheelite has a yellow fluorescence; Greenwood, 1943). This also supports a reduced environment. The only exception is Lened, where diopside-rich pyroxene and pyrite have been found in the local pyroxene-biotite facies (Fig. 2.13A) and are characteristic of oxidized skarns. Even though minerals indicative of oxidized environments can be locally found at Lened, overall, the mineral assemblages of the three deposits suggest reduced conditions.

The specific source of the mineralizing fluids remains unclear in Cantung and Mactung with some authors speculating that the fluids were at least partly derived from the nearby plutons (Dick and Hodgson, 1982) and other ones supporting exsolution from deep blind intrusions (Atkinson and Baker, 1986; Rasmussen et al., 2011). Plutons associated with Cantung, Mactung and Lened are reduced intrusions belonging to the ilmenite series (Rasmussen et al. 2011; Atkinson and Baker, 1986; Selby et al., 2003, Gordey and Anderson, 1983; Marshall et al., 2004; Lake et al., 2017). The presence of reduced skarns could indicate that the mineralizing fluids are in fact coming from the nearby intrusions or from a deeper system with similar oxidation state. Note, however, that the nature of the host rocks may also influence the oxidation state of the skarn during fluid-rock interaction.

2.6.1.1. Significance of oxidized facies at Lened

Diopside and pyrite are spatially related with Ba-bearing biotite and Ba-bearing feldspars (celsian) in the pyroxene-biotite facies at Lened, suggesting a relatively oxidized and Ba-rich local environment (Einaudi et al., 1981). The pyroxene-biotite facies is not widespread at the deposit scale (only two samples out of fifty-three in the study). The local oxidized conditions may be due to the interaction of rocks with an oxidized fluid (which would have implications for the mineralization potential of the fluid) or to local oxidized host rocks. The thrust fault contact above the Rabbitkettle Formation superimposes lithologies (e.g., black shale, chert and sandstone conglomerate, etc.; Gordey and Anderson, 1993; Marshall et al., 2004; Lake et al., 2017) that might have different redox states expressed in their mineralogy. At least one of these lithologies could therefore be oxidized, at least locally, which would explain the oxidized facies observed. Barite- and celsian-bearing metasediments are not uncommon in the Selwyn Basin; e.g. in the Tom and Jason deposit (Magnall et al., 2016); the Howards Pass deposit (Goodfellow et al., 1995), and the Vulcan deposit (Shanks et al., 1987).

Stream sediments in the Flat river portion of the Yukon-Northwest Territories range in composition from scheelite ± molybdenite to scheelite + cassiterite-bearing (Falck et al., 2015). The tin anomalies are associated with more oxidized plutons (e.g. Clea, northwest of Lened). The transition to cassiterite-bearing sediments occurs north of Cantung and is observed in streams proximal to Lened. Therefore, the potential for a relationship between oxidized facies at Lened and more oxidized plutons responsible for tin mineralization is explored below. The oxidized skarn facies at Lened could represent a transition from reduced to more oxidized plutons. However, the plutons outcropping in the area are not oxidized. As described above, oxidized conditions lead to pyroxenes of diopside composition, while reduced conditions lead to hedenbergite composition.

Even at Clea, which is related to a pluton more oxidized than Lened (Hart et al. 2004), pyroxene compositions range from Di0 to Di55 (Dick & Hodgson, 1982). In contrast, pyroxene in the oxidized facies at Lened is nearly pure diopside (Di90-100), but hedenbergite is also common in other areas within the same system. Therefore, we suggest that mineralizing fluids from the causative plutons were reduced at Lened and the distribution of oxidized skarn facies was controlled by the host rock. (Reduced magmatic fluid is consistent with the Lened pluton and the other reduced intrusions of the Tungsten suite (Kwak, 1987). The spatial correlation between minerals characteristic of oxidized skarns and Ba-bearing minerals supports the interpretation that the pyroxene-biotite facies formed from the metasomatism of a barite-bearing host rock.

2.6.2. Paragenetic evolution

2.6.2.1. Paragenetic relationship between facies, scheelite and sulfides

This study has shown through petrographic observations that scheelite precipitated throughout the entire history of skarn evolution and subsequent hydrosilicate alteration at Cantung, Mactung and Lened (Fig. 2.6). However, scheelite abundance peaked at different stages at each deposit: early in the pyroxene skarn at Mactung, in the amphibole-rich and biotite-rich facies at Cantung, and late in the biotite-rich facies at Lened.

Skarn deposits are typically characterized by two main stages following the contact metamorphism of the host rock: an early prograde anhydrous stage, which forms at high temperature, and a late retrograde hydrous stage, which forms at lower temperature (Einaudi et al., 1981; Kwak, 1986). The prograde stage at Cantung, Mactung and Lened is represented by the garnet-pyroxene and the pyroxene skarns and the retrograde stage is represented by the amphibole-rich and biotite-rich facies. In tungsten skarns, high grades are associated with the retrograde stage (Meinert, 1992) and scheelite generally occurs late in the paragenetic sequence (Kwak, 1994; e.g. Soloviev et al., 2020). However, at Cantung, Mactung and Lened, the highest scheelite grades are not necessarily associated with the retrograde hydrosilicate stage. The occurrence of scheelite in all stages but peaking in specific facies has also been noted in other deposits such as the Fujigatani Mine, Japan (Sato, 1980), the King Island mine, Australia (Kwak and Tan, 1981), the Salau deposit, France (Kwak, 1987) and the Sangdong deposit (Seo et al., 2017).

Sulfides in skarn deposits are most commonly associated with the retrograde assemblage, either with early amphibole (Kwak, 1986) or after the crystallization of amphibole-epidote and micas, prior to the crystallization of late carbonates (Kwak, 1994). Dick and Hodgson (1982) suggested that pyrrhotite is coeval with scheelite and amphibole in the amphibole-rich facies. However, the textural evidence for this interpretation was not presented in their study, nor observed in ours. Our observations do not support this timing relationship proposed by Dick and Hodgson (1982). In the amphibole-rich facies, sulfides are late and interstitial with respect to amphibole and scheelite and, in the biotite-rich facies sulfides are associated with late-stage scheelite that postdates biotite. The textural evidence from this study suggest that sulfides at Cantung, Mactung and Lened postdate the formation of silicate minerals. Sulfide coeval with garnet is locally found in the garnet-pyroxene facies at Cantung only. Considering that scheelite and sulfides are spatially correlated in some facies, the implications of this conclusion will be further discussed below.

2.6.2.2. Relationship between scheelite and sulfides

In this study, scheelite spatially associated with pyrrhotite was observed in the amphibole-rich facies at Cantung, the pyroxene facies at Mactung, and the biotite-rich facies at Lened. This is consistent with previous studies that indicated that scheelite is more abundant in pyrrhotite-rich facies (Dick and Hodgson, 1982; Mathieson and Clark, 1984). Despite their spatial association, scheelite precipitated throughout the entire evolution of the system and is not coeval with sulfides precipitation (Fig. 2.6). Although there is a timing discrepancy between the sulfides and scheelite, the similar spatial distribution of the minerals suggests that similar factors control where the minerals precipitated.

Several mechanisms can be responsible for both scheelite and pyrrhotite precipitation: cooling, depressurization, pH increase; and fluid-fluid and fluid-rock interactions (as they can trigger cooling and/or change in pH). While temperature and pressure changes can trigger both scheelite and sulfide precipitation (Gilbert et al., 1992; Wood & Samson, 2000; Rytuba, 1985; Heinrich & Candela, 2014), they are unlikely to change in a specific location without a host rock control (e.g., preferential fluid pathways). Precipitation reactions for scheelite and pyrrhotite (main sulfide present) are as follows:

Reaction 1. $HWO_4^- + Ca^{2+} = CaWO_4 + H^+$

Reaction 2. $FeCl_2 + HS^- = FeS + 2Cl^- + H^+$

These reactions show that pH controls the precipitation of scheelite and pyrrhotite. The carbonate host rock for the skarns has a high pH buffering capability that could favor the precipitation of both scheelite and pyrrhotite. This conclusion appears significant but the paragenesis suggests that, by the time sulfides precipitated, most of the carbonate had been altered to calc-silicates. Therefore, the pH buffering capacity of the rock would have been significantly reduced or lost.

Another factor that could cause both scheelite and sulfide precipitation is the availability of both Ca and Fe in the host rock, which could explain their correlation at least at the last stages. During the retrograde stage, replacement of pyroxene by amphibole can release some Ca, and sulfidation of pyroxene in reduced conditions can provide sufficient Fe to form abundant pyrrhotite (Burton et al., 1982; Gamble, 1982; Soloviev et al 2017). However, the reactions from which pyrrhotite is formed from sulfidation of pyroxene involves the formation of andradite and quartz together with pyrrhotite (Burton et al., 1982; Gamble, 1982), and that was not observed in our samples. Therefore, we consider that sulfidation of pyroxene, at least through that mechanism, may not be the process responsible for precipitation of pyrrhotite.

Building on this discussion, the first-order parameter controlling the distribution and spatial superposition of scheelite and pyrrhotite is probably not a chemical one but a physical one. A stratigraphic control relating mineralization to zones of higher permeability and porosity in the host rock is a plausible hypothesis and is reinforced by the preferential zones of skarn formation, as observed at Cantung (Fig. 2.16). The focusing of fluid flow would lead to locations where changes in pressure, temperature and chemistry are more likely to occur, causing precipitation of scheelite and sulfides at different times through chemical processes that may differ.

2.7. Summary

The mineral compositions at Cantung, Mactung and Lened W skarn deposits indicate their precipitation from a reduced ore-forming fluid. Reduced skarns tend to form large tungsten deposits, suggesting that the oxidation state of the fluid is not a barrier towards the fertility of these systems. The occurrence of local oxidized skarns at Lened is interpreted to represent barite-bearing metasediments and are therefore not indicative of the potential W grade of Lened.

In this study, we show conclusive textural evidence that scheelite has a protracted crystallization history, forming throughout the entire skarn evolution (prograde stage) and later hydrosilicate alteration (retrograde stage). In contrast, sulfides crystallized at the very end of the history of the system, overprinting all skarn and subsequent hydrosilicate alteration stages. This new data challenges previous studies that suggested that scheelite precipitation is contemporaneous with sulfides at the beginning of the retrograde stage.

Considering that scheelite and pyrrhotite are spatially related but not coeval, the potential reasons for their spatial relationship have been evaluated. We suggest that the spatial relationship between scheelite and sulfides is controlled by the permeability and porosity of the host rock. The distribution of sulfides and scheelite is therefore proposed to be stratigraphically controlled and likely correlated with preferential fluid pathways, either primary in origin or generated through fluid rock interaction in cleaner or coarser grained limestones.

2.8. Acknowledgments

This work was supported by NSERC Discovery Grant to Pilar Lecumberri-Sanchez, Polar Continental Shelf to Hendrik Falck, Northwest Territories Geological Survey contribution agreements for 2018-2019 and 2019-2020. This work would not have been possible without the access to Cantung facilitated by NorthAmerican Tungsten Corporation Ltd. Thank you to Andrew Locock at University of Alberta for his support with data collection and interpretation at the electron microprobe. We give thanks to Ehsan Salmabadi, Carlin Lentz, and Ken Hickey for helpful discussions.

2.9. References

Adlakha, E., Hanley, J., Falck, H., Boucher, B. (2018) The origin of mineralizing hydrothermal fluids recorded in apatite chemistry at the Cantung W-Cu skarn deposit, NWT, Canada. Eur. J. Mineral., 30, 1095-1113

Archibald, D. A., Clark, A. H., Farrar, E., & Zaw, U. K. (1978). Potassium–argon ages of intrusion and scheelite mineralization, Cantung, Tungsten, Northwest Territories. Canadian Journal of Earth Sciences, 15(7), 1205-1207.

Atkinson, D., & Baker, D.J. (1986). Recent developments in the geologic understanding of Mactung. Mineral Deposits of the Northern Cordillera. Canadian Institute of Mining, Metallurgy and Petroleum, 37, 234-244.

Blusson, S. L. (1968). Geology and tungsten deposits near the headwaters of Flat River, Yukon Territory and southwestern district of Mackenzie, Canada (Vol. 67, No. 22). Department of Energy, Mines and Resources.

Bowman, J. R., Covert, J. J., Clark, A. H., & Mathieson, G. A. (1985). The CanTung E Zone scheelite skarn orebody, Tungsten, Northwest Territories; oxygen, hydrogen, and carbon isotope studies. Economic Geology, 80(7), 1872-1895.

Brown, P. E., & Essene, E. J. (1985). Activity variations attending tungsten skarn formation, Pine Creek, California. Contributions to Mineralogy and Petrology, 89(4), 358-369.

Burton, J. C., & Taylor, L. A. (1982). The fO_2-T and $f\,S_2$-T stability relations of hedenbergite and of hedenbergite-johannsenite solid solutions. Economic Geology, 77(4), 764-783.

Candela, P. A. (1992). Controls on ore metal ratios in granite-related ore systems: an experimental and computational approach. Earth and Environmental Science Transactions of the Royal Society of Edinburgh, 83(1-2), 317-326.

Candela, P. A., & Bouton, S. L. (1990). The influence of oxygen fugacity on tungsten and molybdenum partitioning between silicate melts and ilmenite. Economic Geology, 85(3), 633-640.

Chappell, B. W., & White, A. J. R. (1992). I-and S-type granites in the Lachlan Fold Belt. Earth and Environmental Science Transactions of the Royal Society of Edinburgh, 83(1-2), 1-26.

Cummings, W. W., & Bruce, D. E. (1977). Canada Tungsten–Change to underground mining and description of mine-mill procedures. Canada Mining and Metallurgy Bulletin, 70, 94-101.

Dick, L. A., & Hodgson, C. J. (1982). The Mactung W-Cu (Zn) contact metasomatic and related deposits of the northeastern Canadian Cordillera. Economic Geology, 77(4), 845-867.

Driver, L. A., Creaser, R. A., Chacko, T., & Erdmer, P. (2000). Petrogenesis of the Cretaceous Cassiar batholith, Yukon–British Columbia, Canada: Implications for magmatism in the North American Cordilleran interior. Geological Society of America Bulletin, 112(7), 1119-1133.

Dubessy, J., Ramboz, C., Nguyen-Trung, C., Cathelineau, M., Charoy, B., Cuney, M., ... & Weisbrod, A. (1987). Physical and chemical controls (fO2, T, pH) of the opposite behaviour of U and Sn-W as examplified by hydrothermal deposits in France and Great-Britain, and solubility data. Bulletin de Minéralogie, 110(2), 261-281.

Einaudi, M. T. (1981). Skarn deposits. Economic Geology, 75, 317-391.

Einaudi, M. T., & Burt, D. M. (1982). Introduction; terminology, classification, and composition of skarn deposits. Economic Geology, 77(4), 745-754.

Falck, H (2015). Geochemical, Mineralogical and Indicator Mineral Data for Stream Silt Sediment, Heavy Mineral Concentrates and Waters, Flat River area Northwest Territories, (part of NTS 95E, 105H and 105I). NWT Open Report 2015-002.

Fischer, B.J., Martel, E., and Falck, H., (2018). Geology of the Mactung tungsten skarn and area – Review and 2016 field observations; Northwest Territories Geological Survey, NWT Open File 2018-02, 84 pages and appendices.

Gamble, Robert P. "An experimental study of sulfidation reactions involving andradite and hedenbergite." Economic Geology 77.4 (1982): 784-797.

Gebru, A. L. (2017). Petrogenesis of Granitoids in the Vicinity of the Mactung Tungsten Skarn Deposit, NE Yukon-Northwest Territories: Characterization of Skarn Mineralization and Causative Plutons through Geological, Petrochemical, Mineralogical, and Geochronological Analysis. UnPub PhD Thesis University of New Brunswick, New Brunswick, Canada.

Gibert, F., Moine, B., Schott, J., & Dandurand, J. L. (1992). Modeling of the transport and deposition of tungsten in the scheelite-bearing calc-silicate gneisses of the Montagne Noire, France. Contributions to Mineralogy and Petrology, 112(2-3), 371-384.

Glover, J.K. & Burson, M.J. (1987): Geology of the Lened tungsten skarn deposit, Logan Mountains, Northwest Territories. Canadian Institute of Mining, Metallurgy and Petroleum, Special Volume 37, 255-265.

Goodfellow, W. D., Cecile, M. P., & Leybourne, M. I. (1995). Geochemistry, petrogenesis, and tectonic setting of lower Paleozoic alkalic and potassic volcanic rocks, Northern Canadian Cordilleran Miogeocline. Canadian Journal of Earth Sciences, 32(8), 1236-1254.

Gordey, S. P., Anderson, R. G. (1993). Evolution of the northern Cordilleran miogeocline, Nahanni map area (105I), Yukon and Northwest Territories. Geological Survey of Canada Memoir 428, 214p.

Government of Northwest Territories (2016). A Guide to Mineral Deposits in the Northwest Territories. https://www.iti.gov.nt.ca/sites/iti/files/mineraldeposites2-nocrops.pdf

Greenwood, R. (1943). Effect of chemical impurities on scheelite fluorescence. Economic Geology 38 (1), 56-64.

Hart, C. J. R. (1997). A transect across Stikinia: Geology of the northern Whitehorse map area, southern Yukon Territory (105D13–16). Exploration and Geological Services Division, Yukon, Indian and Northern Affairs Canada Bulletin 8, 1–112.

Hart, C. J., Mair, J. L., Goldfarb, R. J., & Groves, D. I. (2004). Source and redox controls on metallogenic variations in intrusion-related ore systems, Tombstone-Tungsten Belt, Yukon Territory, Canada. Earth and Environmental Science Transactions of The Royal Society of Edinburgh, 95(1-2), 339-356.

Hawthorne, F. C., Oberti, R., Harlow, G. E., Maresch, W. V., Martin, R. F., Schumacher, J. C., & Welch, M. D. (2012). Nomenclature of the amphibole supergroup. American Mineralogist, 97(11-12), 2031-2048.

Heinrich, C. A., & Candela, P. A. (2014). Fluids and ore formation in the Earth's crust. In Treatise on Geochemistry (Second Edition) (Vol. 13, pp. 1-28). Elsevier.

Hsu, L. C. (1977). Effects of oxygen and sulfur fugacities on the scheelite-tungstenite and powellite-molybdenite stability relations. Economic Geology, 72(4), 664-670.

Hsu, L. C., & Galli, P. E. (1973). Origin of the scheelite-powellite series of minerals. Economic Geology, 68(5), 681-696.

Ishihara, S. (1977). The magnetite-series and ilmenite-series granitic rocks. Mining Geology, 27(145), 293-305.

Kwak, T. A. (1994). Hydrothermal alteration in carbonate-replacement deposits. Geol. Assoc. Canada, Short Course Notes, 11, 381-402.

Kwak, T. A. P. (1986). Fluid inclusions in skarns (carbonate replacement deposits). Journal of Metamorphic Geology, 4(4), 363-384.

Kwak, T. A. P. (1987). W-Sn skarn deposits and related metamorphic skarns and granitoids. Amsterdam: Elsevier.

Kwak, T. A. P., & Tan, T. H. (1981). The geochemistry of zoning in skarn minerals at the King Island (Dolphin) mine. Economic Geology, 76(2), 468-497.

Lake, D. J., Groat, L. A., Falck, H., Mulja, T., Cempírek, J., Kontak, D., Marshall, D., Giuliani, G., & Fayek, M. (2017). Genesis of emerald-bearing quartz veins associated with the Lened W-skarn mineralization, Northwest Territories, Canada. The Canadian Mineralogist, 55(4), 561-593.

Locock, A. J. (2008). An Excel spreadsheet to recast analyses of garnet into end-member components, and a synopsis of the crystal chemistry of natural silicate garnets. Computers & Geosciences, 34(12), 1769-1780.

Locock, A. J. (2014). An Excel spreadsheet to classify chemical analyses of amphiboles following the IMA 2012 recommendations. Computers & Geosciences, 62, 1-11.

Magnall, J. M., Gleeson, S. A., Stern, R. A., Newton, R. J., Poulton, S. W., & Paradis, S. (2016). Open system sulphate reduction in a diagenetic environment–Isotopic analysis of barite (δ34S and δ18O) and pyrite (δ34S) from the Tom and Jason Late Devonian Zn–Pb–Ba deposits, Selwyn Basin, Canada. Geochimica et Cosmochimica Acta, 180, 146-163.

Marshall, D. D., Groat, L. A., Falck, H., Giuliani, G., & Neufeld, H. (2004). The Lened Emerald prospect, Northwest Territories, Canada: Insights from fluid inclusions and stable isotopes, with implications for northern Cordilleran Emerald. The Canadian Mineralogist, 42(5), 1523-1539.

Mathieson, G. A., & Clark, A. H. (1984). The Cantung E Zone scheelite skarn orebody, Tungsten, Northwest Territories; a revised genetic model. Economic Geology, 79(5), 883-901.

Meinert, L. D. (1992). Skarns and skarn deposits. Geoscience Canada, 19(4).

Monger, J. W., Nokleberg, W. J., Coyner, A. R., & Fahey, P. L. (1996). Evolution of the northern North American Cordillera: generation, fragmentation, displacement and accretion of successive North American plate-margin arcs. Geology and Ore Deposits of the American Cordillera. Geological Society of Nevada, 1133-1152.

Morimoto, N. (1988). Nomenclature of pyroxenes. Mineralogy and Petrology, 39(1), 55-76.

Nachit, H., Ibhi, A., Abia, E. H., & Ohoud, M. B. (2005). Discrimination between primary magmatic biotites, reequilibrated biotites and neoformed biotites. Comptes Rendus Geoscience, 337(16), 1415-1420.

Nakano, T., Yoshino, T., Shimazaki, H., & Shimizu, M. (1994). Pyroxene composition as an indicator in the classification of skarn deposits. Economic Geology, 89(7), 1567-1580.

Nelson, J. L. and Colpron, M. (2007). Tectonics and metallogeny of the Canadian and Alaskan Cordillera, 1.8 Ga to present, in Goodfellow, W. D., ed., Mineral Deposits of Canada: A Synthesis of Major Deposit Types, District Metallogeny, the Evolution of Geological Provinces, and Exploration Methods: Mineral Deposit Division, Geological Association of Canada, Special Publication 5, p. 755-791.

Newberry, R.J. (1998). W- And Sn-Skarn Deposits: A 1998 Status Report. In Mineralized Intrusion Related Skarn Systems (D.R. Lentz, ed.). Mineralogical Association of Canada Short Course Series, Mineralogical Association of Canada, Quebec City, Quebec (289–335).

Rasmussen, K. L., Lentz, D. R., Falck, H., & Pattison, D. R. (2011). Felsic magmatic phases and the role of late-stage aplitic dykes in the formation of the world-class Cantung Tungsten skarn deposit, Northwest Territories, Canada. Ore Geology Reviews, 41(1), 75-111.

Rasmussen, K. L., Mortensen, J. K., Falck, H., & Ullrich, T. D. (2007). The potential for intrusion-related mineralization within the South Nahanni River MERA area, Selwyn and Mackenzie Mountains, Northwest Territories. Mineral and Energy Resource Assessment of the Greater Nahanni Ecosystem Under Consideration for the Expansion of the Nahanni National Park Reserve, Northwest Territories. Edited by DF Wright, D. Lemkow and JR Harris. Geological Survey of Canada, Open File, 5344, 203-278.

Rasmussen, K.L. (2013) The timing, composition, and petrogenesis of syn- to post-accretionary magmatism in the northern Cordilleran miogeocline, eastern Yukon and southwestern Northwest Territories. Ph.D. Thesis, University of British Columbia, Vancouver, British Columbia, Canada, 788 pp.

Ray, G. E. (2013). A review of skarn in Canadian Cordillera. British Columbia Ministry of Energy and Mines, British Columbia Geological Survey Open File, 8, 50.

Rytuba, J. J. (1985). Geochemistry of hydrothermal transport and deposition of gold and sulfide minerals in Carlin-type gold deposits. US Geological Survey Bulletin, 1646, 27-34.

Sato, K. (1980). Tungsten skarn deposit of the Fujigatani mine, southwest Japan. Economic Geology, 75(7), 1066-1082.

Selby, D., Creaser, R. A., Heaman, L. M., & Hart, C. J. (2003). Re-Os and U-Pb geochronology of the Clear Creek, Dublin Gulch, and Mactung deposits, Tombstone Gold Belt, Yukon, Canada: absolute timing relationships between plutonism and mineralization. Canadian Journal of Earth Sciences, 40(12), 1839-1852.

Seo, J. H., Yoo, B. C., Villa, I. M., Lee, J. H., Lee, T., Kim, C., & Moon, K. J. (2017). Magmatic–hydrothermal processes in Sangdong W–Mo deposit, Korea: Study of fluid inclusions and ^{39}Ar–^{40}Ar geochronology. Ore Geology Reviews, 91, 316-334.

Shanks, W. C., Woodruff, L. G., Jilson, G. A., Jennings, D. S., Modene, J. S., & Ryan, B. D. (1987). Sulfur and lead isotope studies of stratiform Zn-Pb-Ag deposits, Anvil Range, Yukon; basinal brine exhalation and anoxic bottom-water mixing. Economic Geology, 82(3), 600-634.

Shimazaki, H. I. D. E. H. I. K. O. (1980). Characteristics of skarn deposits and related acid magmatism in Japan. Economic Geology, 75(2), 173-183.

Soloviev, S. G., Kryazhev, S. G., & Dvurechenskaya, S. S. (2020). Geology, mineralization, and fluid inclusion characteristics of the Agylki reduced tungsten (W-Cu-Au-Bi) skarn deposit, Verkhoyansk fold-and-thrust belt, Eastern Siberia: tungsten deposit in a gold-dominant metallogenic province. Ore Geology Reviews, 103452.

Tischendorf, G., Forster, H. J., Gottesmann, B., & Rieder, M. (2007). True and brittle micas: composition and solid-solution series. Mineralogical Magazine, 71(3), 285-320.

Wang, Y., Wang, K., & Konare, Y. (2018). N 2-rich fluid in the vein-type Yangjingou scheelite deposit, Yanbian, NE China. Scientific reports, 8(1), 5662.

Wesolowski, D., Drummond, S. E., Mesmer, R. E., & Ohmoto, H. (1984). Hydrolysis equilibria of tungsten (VI) in aqueous sodium chloride solutions to 300. degree. C. Inorganic Chemistry, 23(8), 1120-1132.

White, A. J. R., Chappell, B. W., & Cleary, J. R. (1974). Geologic setting and emplacement of some Australian Palaeozoic batholiths and implications for intrusive mechanisms. Pacific Geology, 8, 159-171.

White, A. J., & Chappell, B. W. (1977). Ultrametamorphism and granitoid genesis. Tectonophysics, 43(1-2), 7-22.

Wise, H. M. (1974). Geological report and map of the Lened tungsten prospect, District of Mackenzie, NWT. NWT Assessment Report 080309.

Wood, S. A., & Samson, I. M. (2000). The hydrothermal geochemistry of tungsten in granitoid environments: I. Relative solubilities of ferberite and scheelite as a function of T, P, pH, and m NaCl. Economic Geology, 95(1), 143-182.

Yavuz, F. (2013). WinPyrox: A Windows program for pyroxene calculation classification and thermobarometry. American Mineralogist, 98(7), 1338-1359.

Yuvan, J. (2006). Fluid inclusion and oxygen isotope studies of high-grade quartz-scheelite veins at the Cantung Mine, Northwest Territories, Canada: products of a late-stage magmatic-hydrothermal event (Doctoral dissertation, University of Missouri-Columbia).

Zaw, U. K., & Clark, A. H. (1978). Fluoride-hydroxyl ratios of skarn silicates, Cantung E-zone scheelite orebody, Tungsten, Northwest Territories. The Canadian Mineralogist, 16(2), 207-221.

2.10. Tables

Table 2.1. Representative microprobe data of garnet from Cantung, Mactung and Lened sorted by early (disseminated) garnet and late (vein) garnet. All the garnets are from the garnet-pyroxene skarn facies. Oxide values are in wt%.

	Cantung			**Mactung**			**Lened**
	Early		Late	Early		Late	Early
SiO_2	38.21	37.60	37.20	36.78	37.72	37.61	37.79
TiO_2	0.75	0.30	0.40	0.54	0.35	0.19	0.17
Al_2O_3	19.99	19.99	20.24	19.68	18.82	18.29	20.23
Cr_2O_3	ND	ND	ND	0.01	ND	0.03	ND
FeO	4.29	8.76	12.29	14.52	6.22	7.14	14.48
MnO	0.07	11.55	13.52	6.77	1.31	1.28	8.09
MgO	0.13	0.09	0.18	0.02	0.00	0.00	0.03
CaO	36.03	21.54	16.36	20.74	34.69	34.31	19.93
Na_2O	ND	ND	ND	ND	0.01	ND	ND
K_2O	ND	ND	ND	ND	ND	ND	ND
TOTAL	99.47	99.83	100.19	99.07	99.13	98.85	100.72
End members %							
Grossular	85.32	51.87	39.29	48.93	80.51	77.27	48.16
Spessartine	0.00	25.65	30.27	15.22	0.60	2.18	17.89
Almandine	0.00	12.66	21.81	24.42	0.00	0.00	25.24
Andradite	10.72	7.76	5.85	8.36	14.09	17.13	7.10
Pyrope	0.49	0.35	0.71	0.08	0.00	0.00	0.12
Schorlomite-Al	2.15	0.89	1.19	1.63	1.02	0.56	0.50
Formula based on 12 O							
Z site							
Si	2.917	2.958	2.950	2.927	2.911	2.917	2.960
Al	0.083	0.042	0.050	0.073	0.089	0.083	0.040
Sum Z	3.000	3.000	3.000	3.000	3.000	3.000	3.000
Y site							
Al	1.716	1.811	1.842	1.773	1.623	1.589	1.828
Fe^{3+}	0.280	0.196	0.161	0.234	0.425	0.470	0.191
Sum Y	1.996	2.007	2.002	2.007	2.048	2.059	2.020
X site							
Ca	2.947	1.815	1.390	1.768	2.869	2.851	1.673
Fe^{2+}	0.006	0.380	0.654	0.733	0.023	0.007	0.757
Mn	0.005	0.770	0.908	0.457	0.086	0.084	0.537
Ti	0.043	0.018	0.024	0.033	0.020	0.011	0.010

Table 2.1. (continued)

Mg	0.015	0.011	0.021	-	-	-	-
Sum X	3.016	2.993	2.998	2.990	2.998	2.953	2.977

ND: not detected.

Table 2.2. Representative microprobe data of pyroxene from Cantung, Mactung and Lened sorted by skarn facies. Oxide values are in wt%.

	Cantung			Mactung			Lened		
	Garnet-pyroxene skarn		Pyroxene skarn	Garnet-pyroxene skarn	Pyroxene skarn		Garnet-pyroxene skarn	Pyroxene skarn	Pyroxene-biotite skarn
SiO_2	51.08	52.70	52.34	48.01	49.24	51.37	48.58	52.29	55.20
TiO_2	0.10	0.05	0.10	0.13	0.14	0.07	0.10	0.08	0.08
Al_2O_3	0.20	0.14	0.26	0.43	0.48	0.22	0.20	0.26	0.11
Cr_2O_3	0.01	0.00	0.02	0.01	0.01	0.00	0.00	0.00	0.00
FeO	14.36	10.31	12.65	25.87	23.29	13.53	24.04	11.98	0.62
MnO	2.20	0.12	0.12	2.01	1.41	1.17	2.82	1.72	0.07
MgO	8.24	11.64	10.35	1.11	3.48	9.02	1.57	9.95	18.16
CaO	23.44	25.24	24.83	22.54	22.64	24.56	23.11	24.48	25.57
Na_2O	0.08	0.07	0.08	0.07	0.11	0.05	0.05	0.07	ND
K_2O	0.01	ND	0.01	ND	0.01	ND	ND	0.02	ND
TOTAL	99.71	100.27	100.76	100.19	100.81	100.00	100.47	100.85	99.83
Classification	**Mg-Hd** [a]	**Fe-Di** [b]	**Fe-Di** [b]	**Hd** [c]	**Mg-Hd** [a]	**Fe-Di** [b]	**Hd** [c]	**Fe-Di** [b]	**Di** [d]
End members %									
Wollastonite	51.3	51.64	51.18	52.34	50.85	52.38	53.74	51.86	49.63
Enstatite	25.09	33.14	29.68	3.59	10.88	26.76	5.08	29.33	49.04
Ferrosilite	23.61	15.22	19.14	44.07	38.28	20.86	41.18	18.81	1.33
Formula based on 6 O									
Z site									
Si	1.987	1.986	1.982	1.962	1.965	1.979	1.971	1.985	1.996
Al	0.009	0.006	0.012	0.021	0.023	0.010	0.010	0.012	0.005
Sum Z	1.996	1.992	1.994	1.982	1.987	1.989	1.981	1.997	2.000
Y site									
Ti	0.003	0.001	0.003	0.004	0.004	0.002	0.003	0.002	0.002
Cr	-	-	0.001	-	-	-	-	-	-
Fe^{3+}	0.018	0.025	0.024	0.053	0.049	0.032	0.046	0.019	-
Fe^{2+}	0.450	0.300	0.377	0.831	0.729	0.404	0.770	0.361	0.019
Mn	0.073	0.004	0.004	0.070	0.048	0.038	0.097	0.055	0.002
Mg	0.478	0.654	0.584	0.068	0.207	0.518	0.095	0.563	0.979
Sum Y	1.020	0.984	0.992	1.025	1.036	0.994	1.011	1.001	1.002
X site									
Ca	0.977	1.019	1.008	0.987	0.968	1.014	1.005	0.996	0.990
Na	0.006	0.005	0.006	0.006	0.009	0.004	0.004	0.005	-
K	0.001	-	0.001	-	0.001	-	-	0.001	-

Table 2.2. (continued)

Sum X	0.983	1.024	1.014	0.992	0.977	1.017	1.009	1.002	0.990

ND: not detected. [a] **Magnesian hedenbergite;** [b] **Ferroan diopside;** [c] **Hedenbergite;** [d] **Diopside.**

Table 2.3. Representative microprobe data of amphibole from Cantung, Mactung and Lened sorted by facies. Oxide values are in wt%.

	Cantung					Mactung	Lened	
	Garnet-pyroxene skarn		**Amphibole-rich facies**	**Amphibole –biotite facies**		**Amphibole-rich facies**	**Amphibole-rich facies**	
SiO_2	43.01	48.95	49.44	48.61	51.52	40.03	55.2	45.84
TiO_2	0.22	0.23	0.10	0.27	0.28	0.60	0.08	0.32
Al_2O_3	9.47	4.48	3.07	7.46	3.15	11.38	0.88	6.12
Cr_2O_3	ND	ND	ND	ND	0.02	0.02	ND	ND
FeO	24.80	23.73	22.78	16.21	16.45	28.80	14.72	26.72
MnO	1.15	1.42	1.29	0.72	0.95	1.01	0.75	1.74
MgO	4.98	6.97	8.95	11.86	12.38	2.20	13.42	4.22
CaO	11.81	11.97	10.93	11.52	12.12	11.21	12.21	11.54
Na_2O	0.80	0.35	0.57	0.99	0.36	0.90	0.13	0.56
K_2O	0.81	0.33	0.23	0.77	0.27	1.08	0.07	0.50
H_2O (calculated)	1.90	1.97	1.96	2.03	2.03	1.85	2.06	1.90
TOTAL	98.95	100.40	99.32	100.44	99.52	99.09	99.52	99.46
Classification	**Fhb** [a]	**Fac** [b]	**Fac** [b]	**Mhb** [c]	**Act** [d]	**Fhb** [a]	**Act** [d]	**Fhb** [a]
Formula based on 23 O								
T site								
Si	6.705	7.606	7.500	7.105	7.594	6.357	8.021	7.162
Al	1.295	0.394	0.500	0.895	0.406	1.643	0.151	0.838
Sum T	8.000	8.000	8.000	8.000	8.000	8.000	8.021	8.000
C site								
Fe^{2+}	2.808	2.691	2.507	1.720	1.889	3.213	1.789	3.215
Mg	1.157	1.857	2.024	2.584	2.720	0.521	2.907	0.983
Fe^{3+}	0.426	0.135	0.383	0.262	0.140	0.611	-	0.277
Mn^{2+}	0.139	0.134	0.026	0.014	0.078	0.092	0.092	0.199
Al	0.445	0.166	0.049	0.391	0.140	0.488	0.151	0.289
Ti	0.026	0.017	0.011	0.030	0.031	0.072	0.009	0.038
Cr	-	-	-	-	0.002	0.003	-	-
Sum C	5.001	5.000	5.000	5.001	5.000	5.000	4.948	5.001
B site								
Ca	1.973	1.956	1.777	1.804	1.914	1.908	1.901	1.932
Mn^{2+}	0.013	0.020	0.140	0.075	0.040	0.043	-	0.032
Na	0.015	0.024	0.083	0.121	0.047	0.049	0.037	0.036
Sum B	2.001	2.000	2.000	2.000	2.001	2.000	1.938	2.000
A site								
Na	0.227	0.056	0.084	0.159	0.057	0.227	-	0.133

Table 2.3. (continued)

K	0.161	0.027	0.045	0.144	0.051	0.219	0.013	0.100
Sum A	0.388	0.083	0.129	0.303	0.108	0.446	0.013	0.233
Sum T, C, B, A	15.390	15.083	15.129	15.304	15.109	15.446	14.920	15.234
W site								
OH	2.000	2.000	2.000	2.000	2.000	2.000	2.000	2.000
Sum W	2.000	2.000	2.000	2.000	2.000	2.000	2.000	2.000
O (non-W)	22.000	22.000	22.000	22.000	22.000	22.000	22.000	22.000

ND: not detected. [a] Ferro-hornblende; [b] Ferro-actinolite; [c] Magnesio-hornblende; [d] Actinolite.

Table 2.4. Representative microprobe data of micas from Cantung, Mactung and Lened sorted by facies. Oxide values are in wt%.

	Cantung		Mactung	Lened	
	Biotite-rich facies	**Amphibole-biotite facies**	**Biotite-rich facies**	**Biotite-rich facies**	**Pyroxene-biotite skarn**
SiO_2	39.30	36.36	35.83	38.39	27.86
TiO_2	0.33	1.71	1.55	0.52	2.34
Al_2O_3	14.44	15.54	16.08	14.04	20.83
Cr_2O_3	0.00	0.00	0.01	0.00	0.00
FeO	12.26	20.31	24.99	16.58	5.24
MnO	0.85	0.48	0.50	0.43	0.09
MgO	16.74	11.32	7.30	15.11	20.33
SrO	NA	NA	NA	NA	ND
BaO	NA	NA	NA	NA	17.01
CaO	ND	0.05	0.03	ND	ND
Cl	NA	NA	NA	NA	0.06
F	NA	NA	NA	NA	1.60
Na_2O	0.11	0.08	0.17	0.07	0.33
K_2O	10.02	9.56	9.14	9.75	4.01
H_2O (calculated)	4.01	3.90	3.83	3.96	0.63
TOTAL	98.06	99.31	99.43	98.84	100.35
End members %					
Annite	29.12	50.15	65.76	38.10	10.60
Phlogopite	70.88	49.85	34.24	61.90	73.28
Kinoshitalite	0.00	0.00	0.00	0.00	16.12
Formula					
T site					
Si	2.940	2.792	2.802	2.904	2.198
Al	1.060	1.208	1.198	1.096	1.802
Sum T	4.000	4.000	4.000	4.000	4.000
C site					
Al	0.213	0.198	0.284	0.156	0.136
Ti	0.019	0.099	0.091	0.029	0.139
Cr	0.000	0.000	0.000	0.000	0.000
Fe	0.767	1.304	1.634	1.049	0.346
Mn	0.054	0.031	0.033	0.028	0.006
Mg	1.867	1.296	0.851	1.704	2.391
Sum C	2.919	2.929	2.893	2.965	3.018
A site					
Ca	0.000	0.004	0.003	0.000	0.003

Table 2.4. (continued)

Ba	0.000	0.000	0.000	0.000	0.526
Na	0.016	0.011	0.026	0.010	0.050
K	0.956	0.936	0.912	0.941	0.403
Sum A	0.972	0.951	0.942	0.951	0.982
W site					
OH	2.000	2.000	2.000	2.000	0.345
F	-	-	-	-	1.595
Cl	-	-	-	-	0.060
Sum W	2.000	2.000	2.000	2.000	2.000
O (non-W)	11	11	11	11	11

ND: not detected; NA: not analyzed.

Table 2.5. Representative microprobe data of feldspars from Cantung, Mactung and Lened sorted by facies. Oxide values are in wt%.

	Cantung				Mactung	Lened			
	Garnet-pyroxene skarn		**Amphibole-biotite facies**	**Biotite-rich facies**	**Biotite-rich facies**	**Garnet-pyroxene skarn**	**Pyroxene skarn**	**Pyroxene-biotite skarn**	**Mineralized pluton**
SiO_2	44.49	45.68	56.36	66.94	42.76	43.60	43.80	30.96	42.71
TiO_2	0.05	0.06	0.06	0.05	0.07	0.07	0.06	ND	0.07
Al_2O_3	35.60	34.45	27.25	19.85	36.65	35.96	35.94	26.94	35.88
Cr_2O_3	ND	ND	ND	0.01	0.03	ND	ND	ND	ND
FeO	0.13	0.17	0.31	0.52	0.14	0.03	0.14	0.01	0.05
MnO	ND	ND	ND	ND	0.01	ND	ND	0.01	ND
MgO	ND	0.01	0.03	0.01	ND	ND	0.01	ND	ND
SrO	NA	NA	NA	NA	NA	NA	NA	0.12	NA
BaO	NA	NA	NA	NA	NA	NA	NA	41.61	NA
CaO	18.88	17.58	8.98	0.12	19.98	19.57	19.64	ND	19.91
Na_2O	0.85	1.64	6.31	10.84	0.34	0.80	0.49	0.10	0.32
K_2O	0.02	0.03	0.16	0.67	0.04	0.01	0.01	0.04	0.02
TOTAL	100.02	99.63	99.46	99.01	100.01	100.04	100.09	99.78	98.95
End members %									
Anorthite	92.35	85.40	43.61	0.59	96.85	93.11	95.61	-	97.06
Albite	7.56	14.42	55.46	95.54	2.94	6.85	4.35	1.23	2.85
Orthoclase	0.09	0.18	0.93	3.88	0.21	0.04	0.04	0.29	0.09
Celsian	-	-	-	-	-	-	-	98.48	-
Formula based on 8 O									
T site									
Si	2.050	2.104	2.541	2.966	1.975	2.007	2.021	1.965	1.995
Al	1.934	1.870	1.448	1.037	1.995	1.952	1.955	2.015	1.975
Sum T	3.984	3.974	3.990	4.003	3.970	3.959	3.976	3.980	3.969
A site									
Ca	0.932	0.868	0.434	0.006	0.988	0.966	0.971	-	0.996
Na	0.076	0.147	0.552	0.931	0.030	0.071	0.044	0.013	0.029
K	0.001	0.002	0.009	0.038	0.002	-	-	0.003	0.001
Ba	-	-	-	-	-	-	-	1.035	-
Fe	0.005	0.006	0.012	0.019	0.006	0.001	0.005	-	0.002
Ti	0.002	0.002	0.002	0.002	0.002	0.002	0.002	-	0.002
Mg	-	0.001	0.002	-	-	-	0.001	-	-
Cr	-	-	-	-	0.001	-	-	-	-
Mn	-	-	-	-	-	-	-	0.001	-
Sum A	1.016	1.025	1.010	0.996	1.030	1.040	1.024	1.052	1.031[1]

ND: not detected. NA: not analyzed.

Table 2.6. Representative microprobe data of titanite, clinozoisite, vesuvianite and manganaxinite from Cantung, Mactung and Lened. Oxide values are in wt%.

	Titanite			Clinozoisite			Vesuvianite			Manganaxinite	
	Cantung	Mactung	Lened	Cantung	Mactung	Lened	Cantung	Mactung	Lened	Lened	
SiO_2	31.53	30.82	30.80	38.69	38.58	38.47	38.70	36.46	39.06	41.64	42.16
TiO_2	31.88	31.62	31.12	0.06	0.18	0.18	0.07	0.26	0.13	0.11	0.07
Al_2O_3	5.71	5.00	6.28	30.51	29.46	31.54	20.83	17.82	20.54	18.16	18.23
Cr_2O_3	ND	0.02	ND	ND	ND	ND	ND	ND	ND	ND	ND
FeO	0.47	0.75	0.06	4.22	5.28	3.19	3.11	3.54	3.37	6.06	6.01
MnO	0.05	0.08	0.06	0.19	0.28	1.04	0.10	0.06	0.15	6.14	6.25
MgO	0.00	0.04	0.00	0.07	0.16	0.03	0.06	1.54	0.05	0.58	0.54
CaO	28.79	29.14	29.40	24.72	24.61	23.75	36.96	36.45	37.07	19.63	19.90
Na_2O	0.36	ND	ND	ND	ND	ND	ND	0.03	ND	ND	ND
K_2O	ND	ND	ND	ND	ND	ND	ND	ND	ND	ND	ND
TOTAL	98.79	97.48	97.72	98.46	98.55	98.20	99.83	96.16	100.37	92.32	93.16

ND: not detected.

2.11. Figures

Figure 2.1. Regional map showing the geographical distribution of the mid-Cretaceous plutonic suites, including the location of the Tombstone-Tungsten Belt (TTB) comprising the Tombstone, Mayo and Tungsten suites, and the location of the Cantung, Mactung and Lened deposits. Modified from Hart et al. (2004).

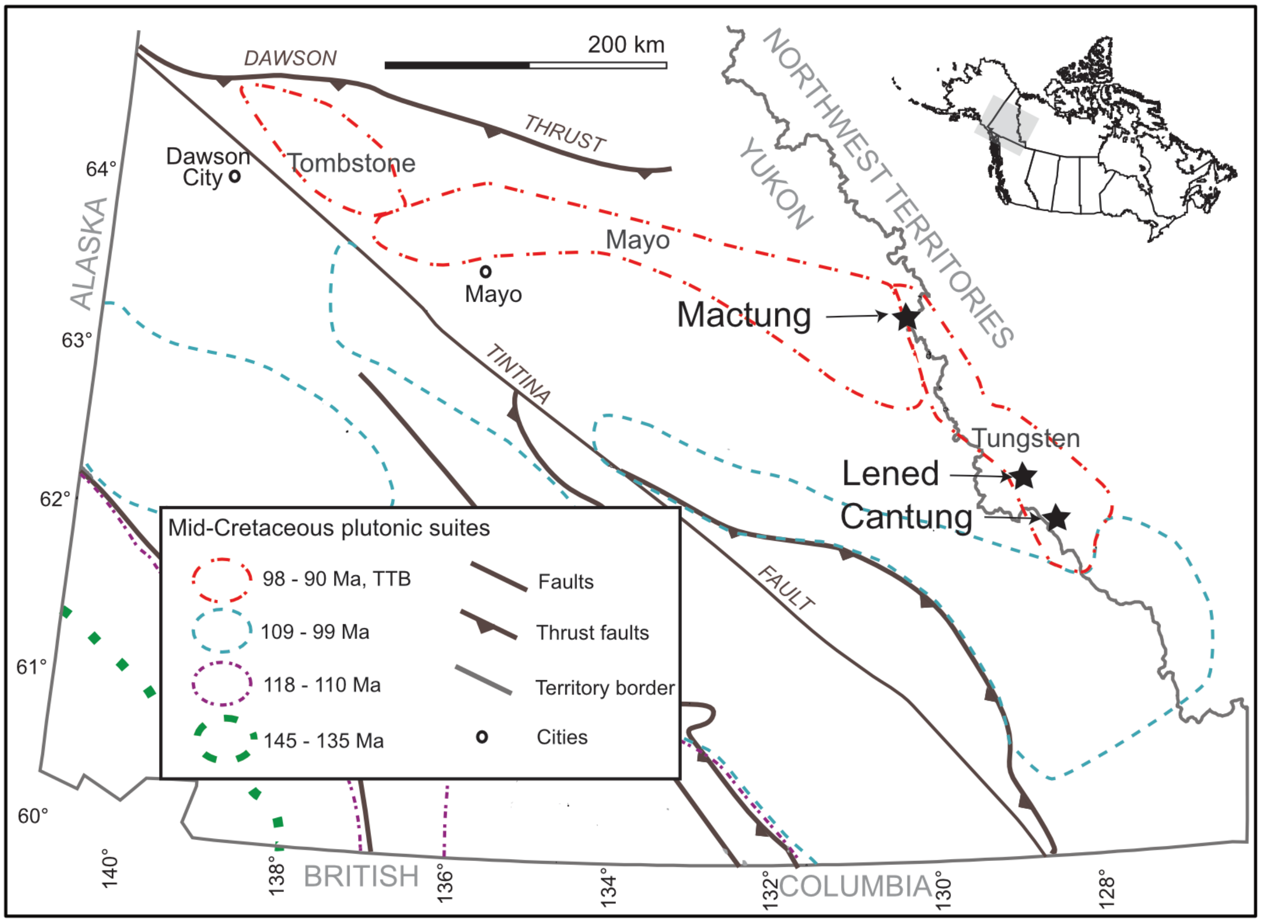

Figure 2.2. Local geology of the Cantung deposit. A/ Surface geology of the Cantung mine (modified after Blusson, 1968). B/ Geological cross-section through the Cantung deposit, looking west (modified from Cummings and Bruce, 1977).

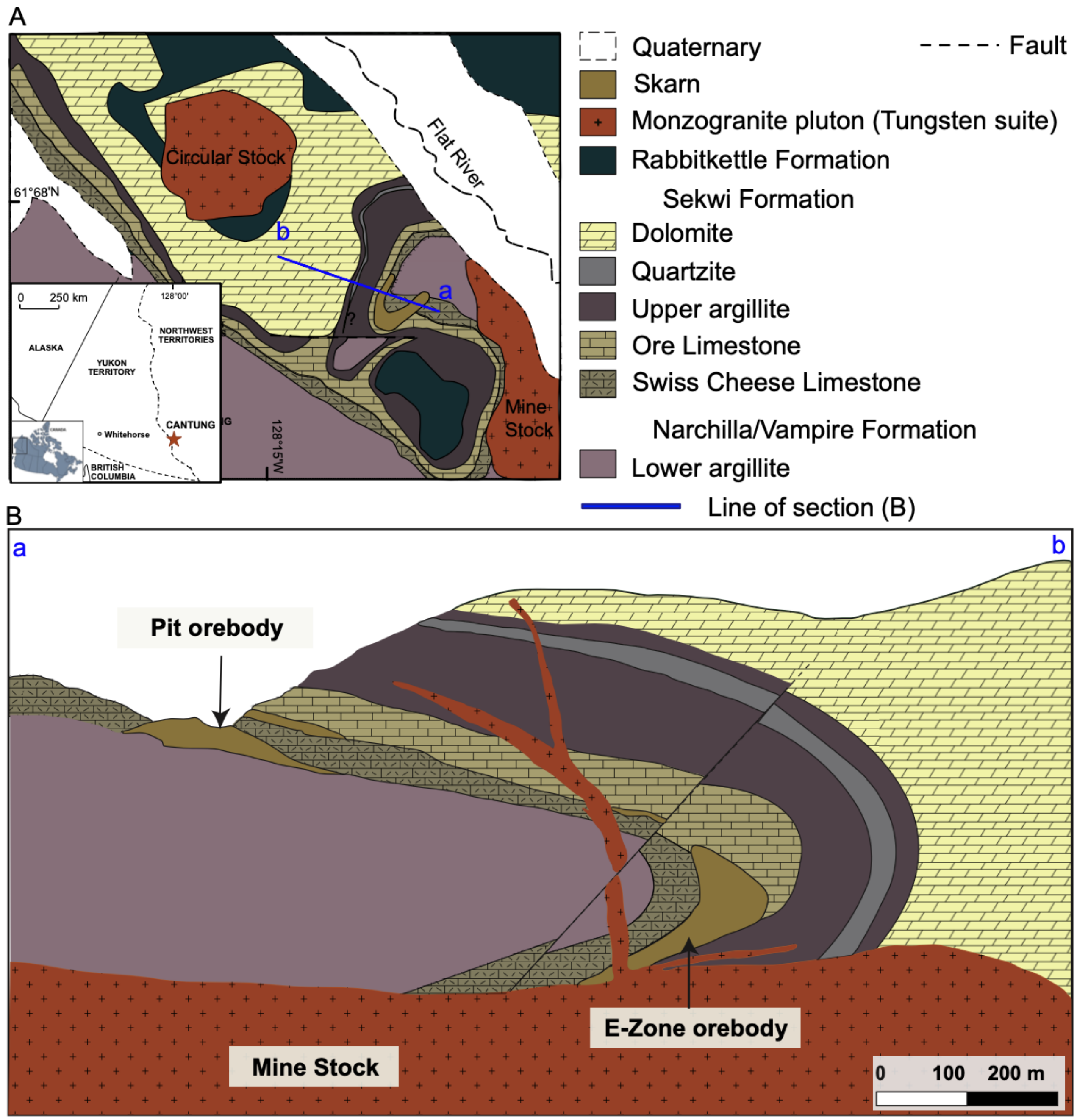

Figure 2.3. Local geology of the Mactung deposit. A/ Surface geology of the Mactung mine (modified after Gebru, 2017). B/ Geological cross-section through the Mactung deposit (modified from Gebru, 2017 and Fischer et al., 2018). Mineralization (shaded areas) is hosted in the Upper carbonate skarn (units 3D, 3E, 3F) and in the Lower carbonate skarn (unit 2B).

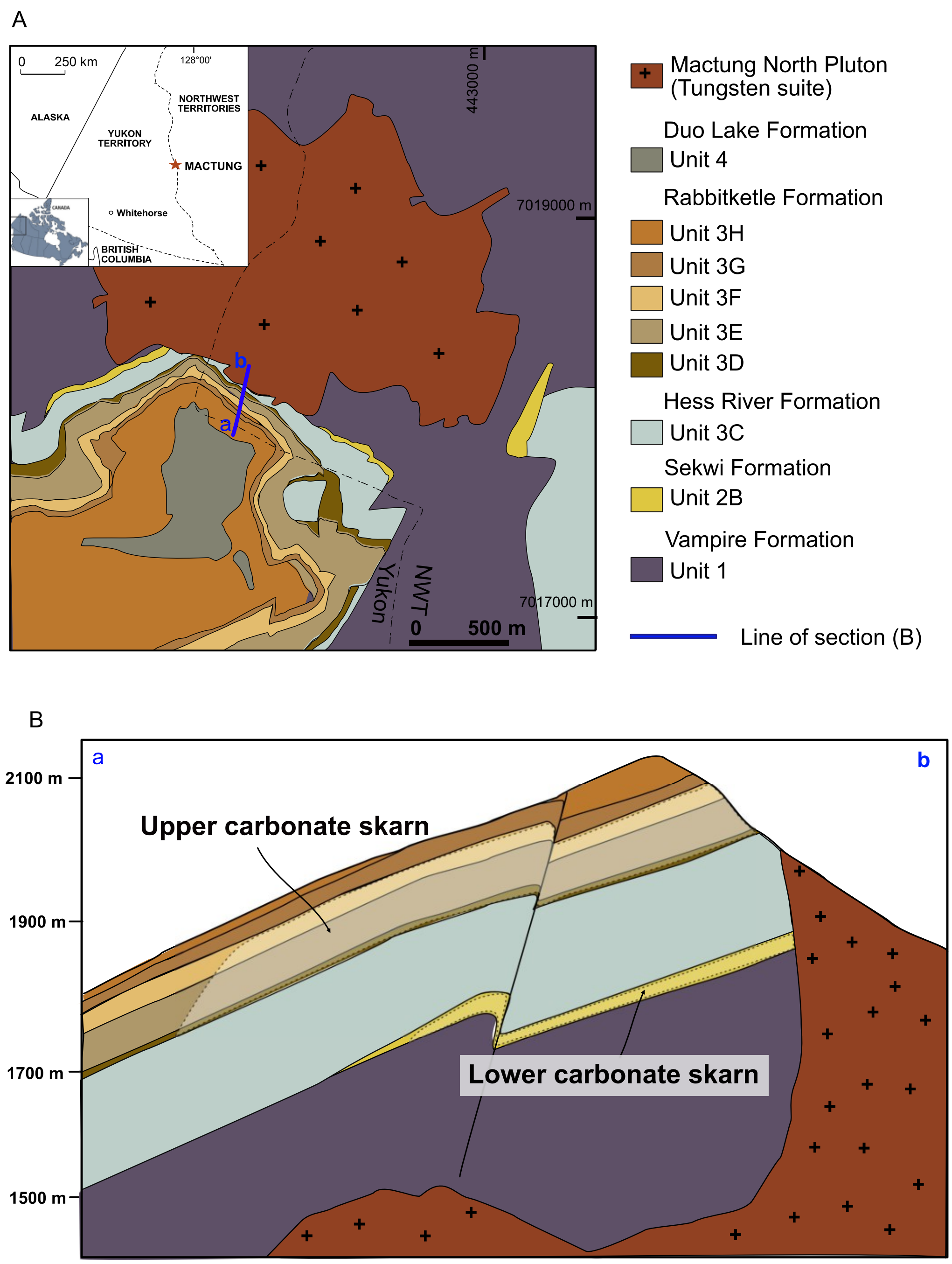

Figure 2.4. Local geology of the Lened deposit. A/ Surface geology of the Lened deposit (modified from Lake et al., 2017 and Wise, 1974). B/ Cross section through the Lened Ridge, redrafted from Wise (1974).

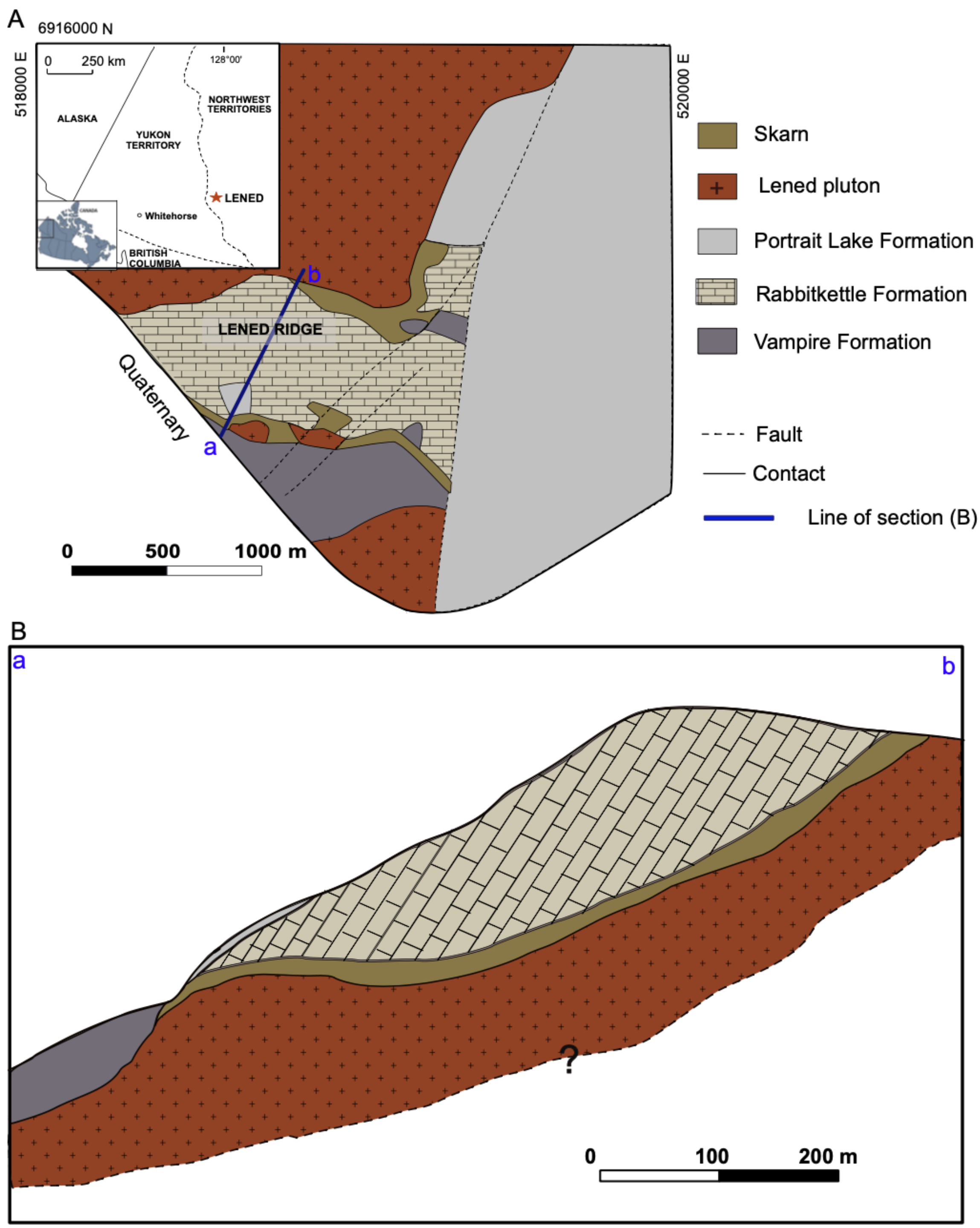

Figure 2.5. Hand sample showing replacement and overprinting relationships between different facies at Cantung. The early garnet skarn (pink areas) is partially replaced by the amphibole-rich hydrosilicate alteration assemblage (blue-green areas), which is itself replaced and overprinted by the biotite-rich hydrosilicate alteration assemblage (brown areas).

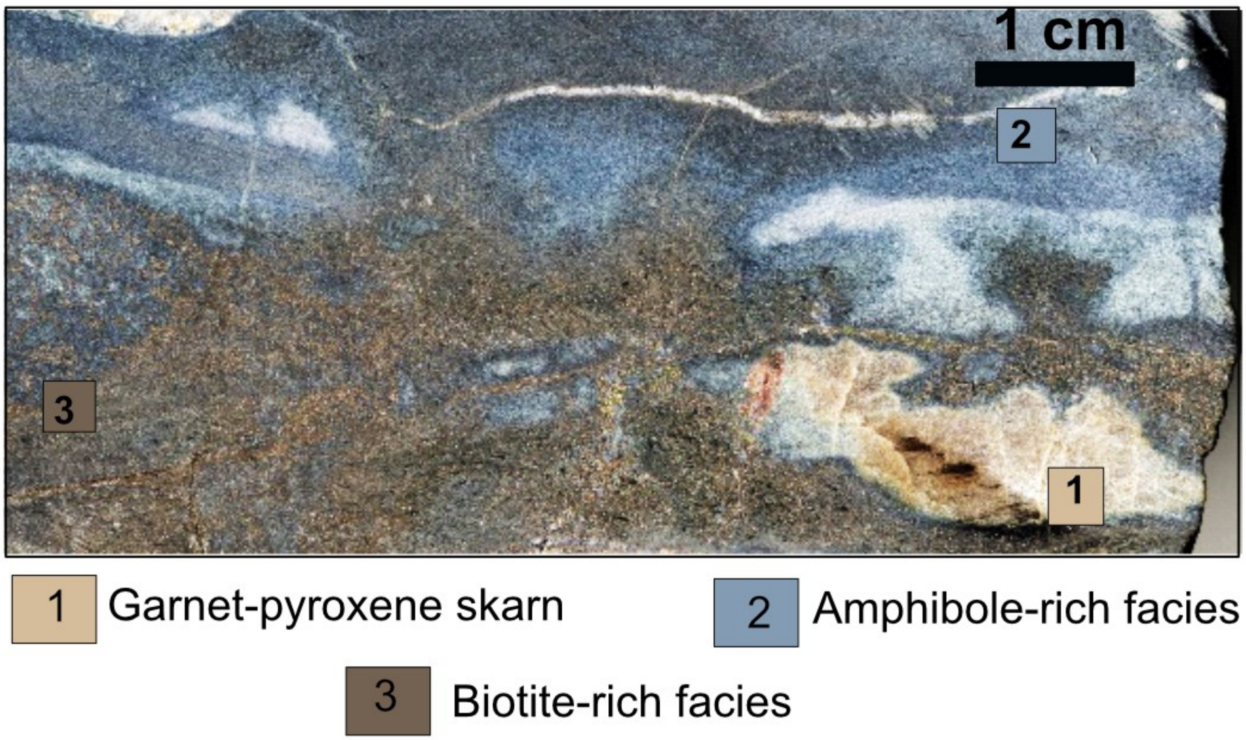

Figure 2.6. Paragenetic sequence of Cantung, Mactung and Lened. The evolution of mineralogy in the skarns through time is grouped in a prograde stage including the garnet-pyroxene and the pyroxene skarn stages, followed by a retrograde hydrosilicate stage including the amphibole-rich and biotite-rich facies. These two main stages precede a sulfide stage, followed by late replacement minerals. The wider the line, the more abundant the mineral. Dotted lines mean the minerals continuously crystallized.

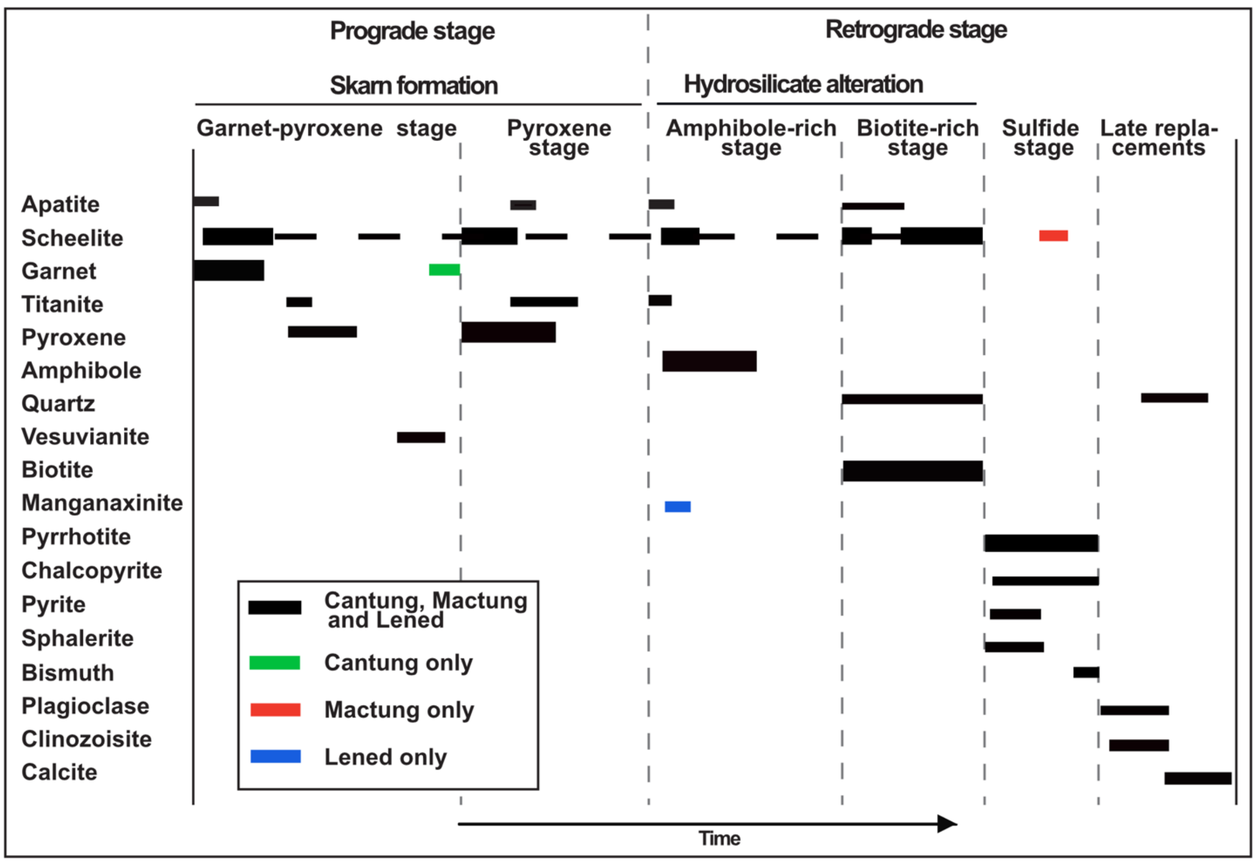

Figure 2.7. (*Next page*) Thin-section photographs showing different assemblages of the garnet-pyroxene skarn. A, B, D, F, G, I, J and L are plane-polarized transmitted light images; E, H and K are cross-polarized transmitted light images. A- (Mactung) Garnet (Grt) partially replaced and overgrown by pyroxene (Px) with subhedral scheelite (Scl) grains overgrown by both garnet (Grt) and pyroxene (Px); B- (Mactung) Subhedral scheelite (Scl) inclusions in anhedral garnet (Grt). Scheelite (Scl) and garnet (Grt) are overgrown by pyroxene (Px); C- (Cantung) Euhedral garnet (Grt) intergrown with, and overgrown by, euhedral sulfides (Sul). Euhedral sulfide (Sul) and scheelite (Scl) are also inclusions in a pyroxene (Px) crystal that surrounds garnet (Grt); D- (Lened) Euhedral zoned garnet (Grt) with some zones replaced by calcite (Cal) and quartz (Qtz); E- (Lened) Euhedral and subhedral pyroxene (Px) crystals with scheelite (Scl) inclusions. Pyroxene (Px) is incompletely replaced by vesuvianite (Ves) and calcite (Cal); F- (Cantung) Apatite (Ap) inclusions in garnet (Grt) and scheelite (Scl). Scheelite (Scl) is overgrown by garnet (Grt). Garnet (Grt) is replaced by pyroxene (Px). G- (Lened) Garnet (Grt) overgrown by calcite (Cal). Calcite (Cal) inclusions occur in early euhedral titanite (Ttn). H- (Lened) Garnet (Grt) replaced by quartz (Qtz), calcite (Cal), vesuvianite (Ves) and pyroxene (Px); I- (Cantung) Garnet (Grt), with apatite inclusions, replaced by amphibole; J- (Cantung) Euhedral apatite (Ap) and subhedral scheelite (Scl) inclusions in amphibole (Amp). Amphibole (Amp) replaces garnet (Grt); K- (Lened) Pyroxene (Px) being replaced by quartz (Qtz), calcite (Cal) and clinozoisite (Czo) and overgrown by quartz (Qtz) and calcite (Cal); L- (Cantung) Garnet (Grt) and scheelite (Scl) replaced by fine-grained pyroxene (Px). Coarse-grained pyroxene (Px) occurs as overgrowths on garnet (Grt) and scheelite (Scl). Sulfides occur as overgrowths on and partially replace garnet (Grt) and pyroxene (Px).

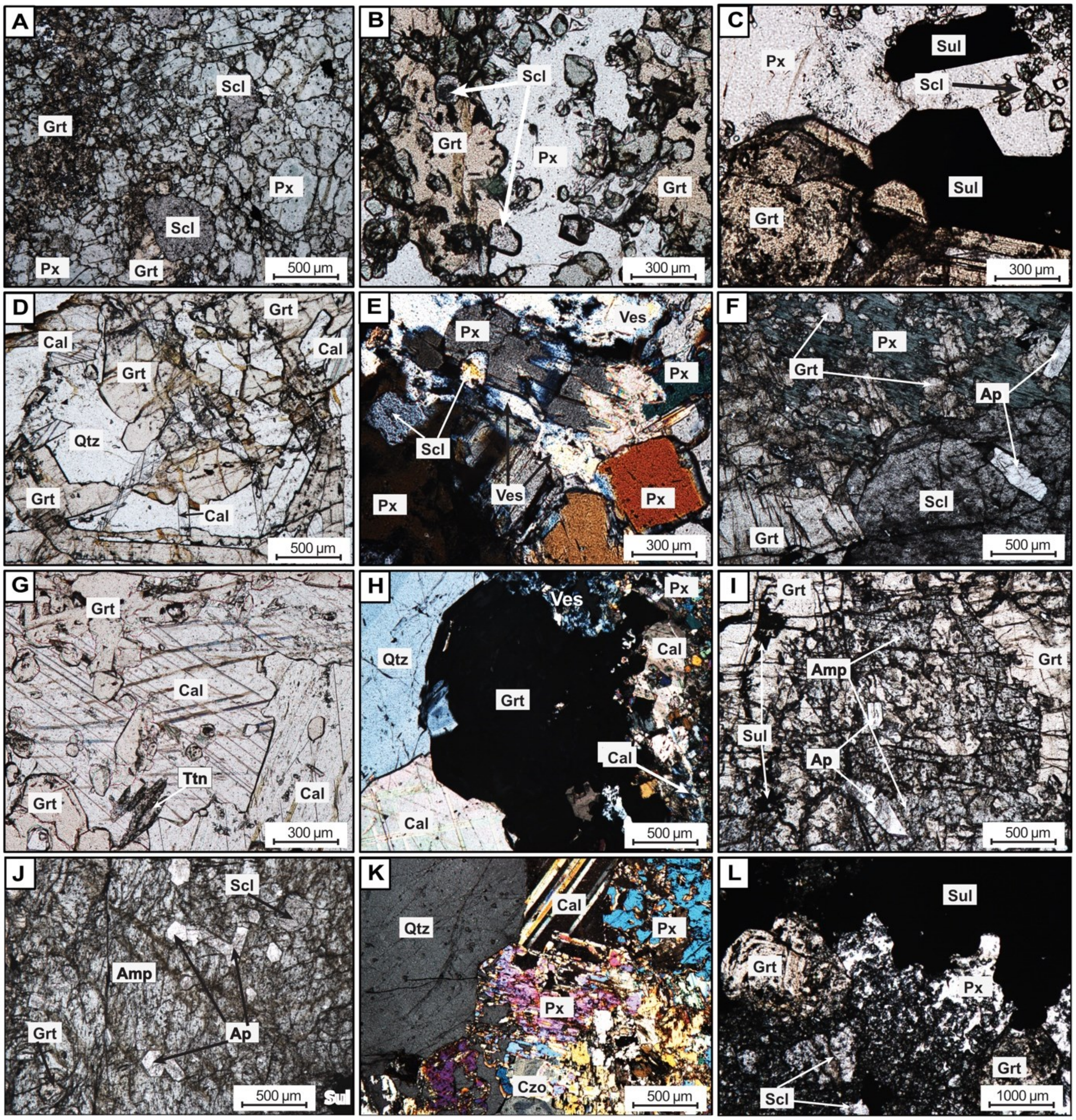
A
Scl
Grt
Px
Scl
Px
Grt
500 µm
B
Scl
Grt
Px
Grt
300 µm
C
Sul
Px
Scl
Sul
Grt
300 µm
D
Grt
Cal
Cal
Grt
Qtz
Grt
Cal
500 µm
E
Ves
Px
Px
Scl
Ves
Px
Px
300 µm
F
Px
Grt
Ap
Scl
Grt
500 µm
G
Grt
Cal
Ttn
Grt
Cal
300 µm
H
Ves
Px
Qtz
Cal
Grt
Cal
Cal
500 µm
I
Grt
Grt
Amp
Sul
Ap
500 µm
J
Scl
Amp
Grt
Ap
500 µm
K
Qtz
Cal
Px
Px
Czo
500 µm
L
Sul
Grt
Px
Grt
Scl
1000 µm

Figure 2.8. Thin-section photographs showing different assemblages of the pyroxene skarn. A, B, C and E are plane-polarized transmitted light images, D is a cross-polarized transmitted light image and F is a plane-polarized reflected light image. A- (Lened) Euhedral/subhedral scheelite (Scl) intergrown with to overgrown by pyroxene (Px) generating vugs filled by quartz (Qtz), calcite (Cal) and sulfide (Sul)s; B- (Cantung) Subhedral scheelite (Scl) intergrown with pyroxene (Px) replaced by calcite (Cal); C-(Mactung) Scheelite (Scl) intergrown to overgrown by pyroxene (Px). Pyroxene (Px) is overgrown by titanite (Ttn), overgrown by plagioclase (Pl). and replaced by plagioclase (Pl) and quartz (Qtz); D- (Mactung) Euhedral pyroxene (Px) in pyroxene (Px) + scheelite (Scl)+ plagioclase (Pl) aggregrate overgrown and replaced by quartz (Qtz), calcite (Cal), clinozoisite (Czo) and sulfides (Sul); One of the euhedral labelled pyroxene (Px) is extinct; E- (Lened) Biotite (Bt) overgrowing and replacing pyroxene (Px). Sulfides (Sul) along cleavage planes may replace, crosscut or occur as inclusions in biotite (Bt). Quartz (Qtz) and calcite (Cal) overgrowths on biotite (Bt). F- (Lened) Pyrite (Py), pyrrhotite (Po) and chalcopyrite (Cp) replacing and overgrowing pyroxene (Px).

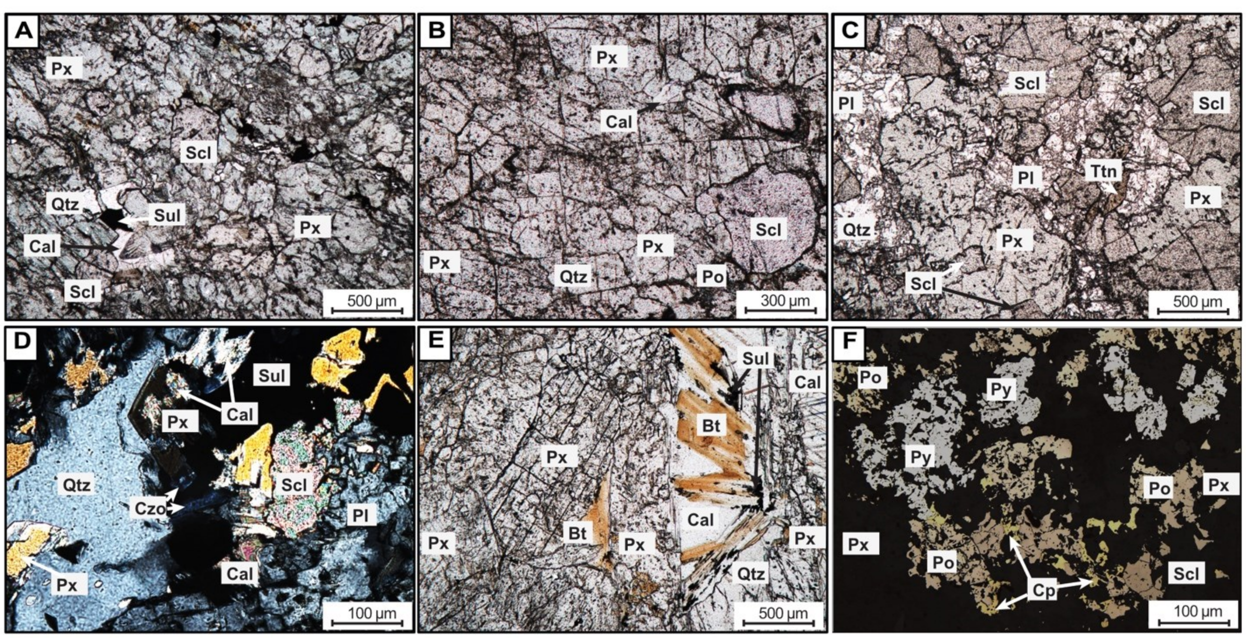

Figure 2.9. Thin-section photographs showing different assemblages of the amphibole-rich facies. All the images are plane-polarized transmitted light images. A- (Cantung) Euhedral amphibole (Amp) overgrown by euhedral scheelite (Scl). Open space fillings and amphibole (Amp) replacements consist of sulfides (Sul); B- (Cantung) Amphibole (Amp) overgrown and replaced by biotite (Bt), and locally replaced by sulfide (Sul); C- (Mactung) Euhedral scheelite (Scl) (with apatite (Ap) inclusions) overgrown by amphibole (Amp), which is replaced by plagioclase (Pl) and quartz (Qtz); D-(Lened) Amphibole (Amp), with pyroxene (Px) inclusions, in massive sulfide (Sul) at the contact with the biotite (Bt) skarn.

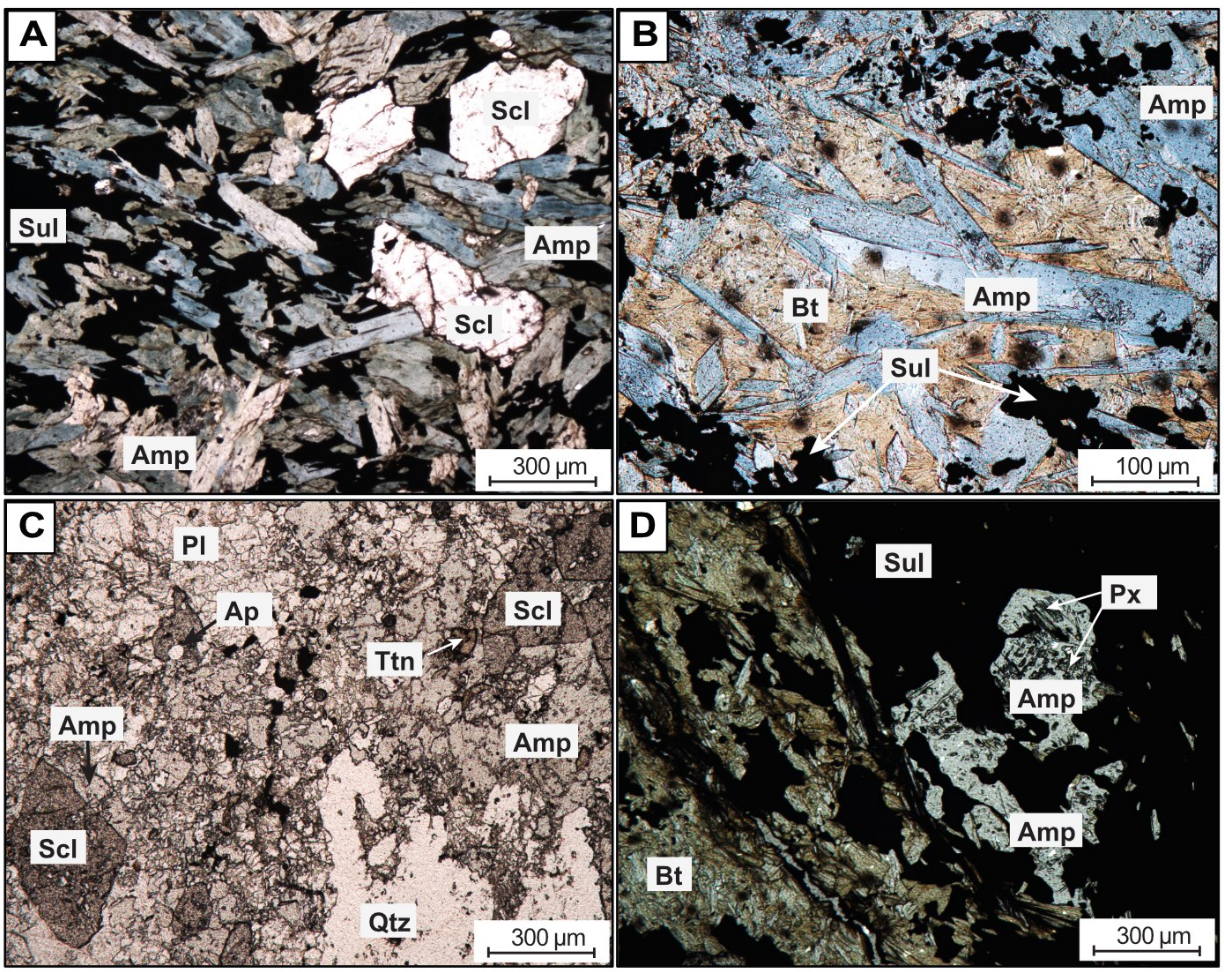

Figure 2.10. Thin-section photographs showing different assemblages of the biotite-rich facies. A, B, C and E are plane-polarized transmitted light images, D is a back-scattered image and F is plane-polarized reflected light image. A- (Cantung) Biotite (Bt), quartz (Qtz) and apatite (Ap) replaced and/or crosscut by sulfide (Sul); B- Biotite (Bt) overgrown and replaced by quartz (Qtz) containing apatite (Ap) inclusions; C- (Lened) Euhedral scheelite (Scl) overgrown by euhedral quartz (Qtz) containing inclusions of apatite (Ap) and biotite (Bt). Quartz (Qtz) and biotite (Bt) overgrown by sulfide (Sul); D- (Cantung) Euhedral apatite (Ap) and biotite (Bt) overgrown by scheelite (Scl) and sulfides (Sul); E- (Cantung) Transition from fine-grained biotite (Bt) skarn to coarser grained biotite-sulfides with biotite (Bt) overgrown by sulfides (Sul); F- (Mactung) Subhedral scheelite (Scl) and sulfides (Sul) in a veinlet crosscutting the biotite-rich facies.

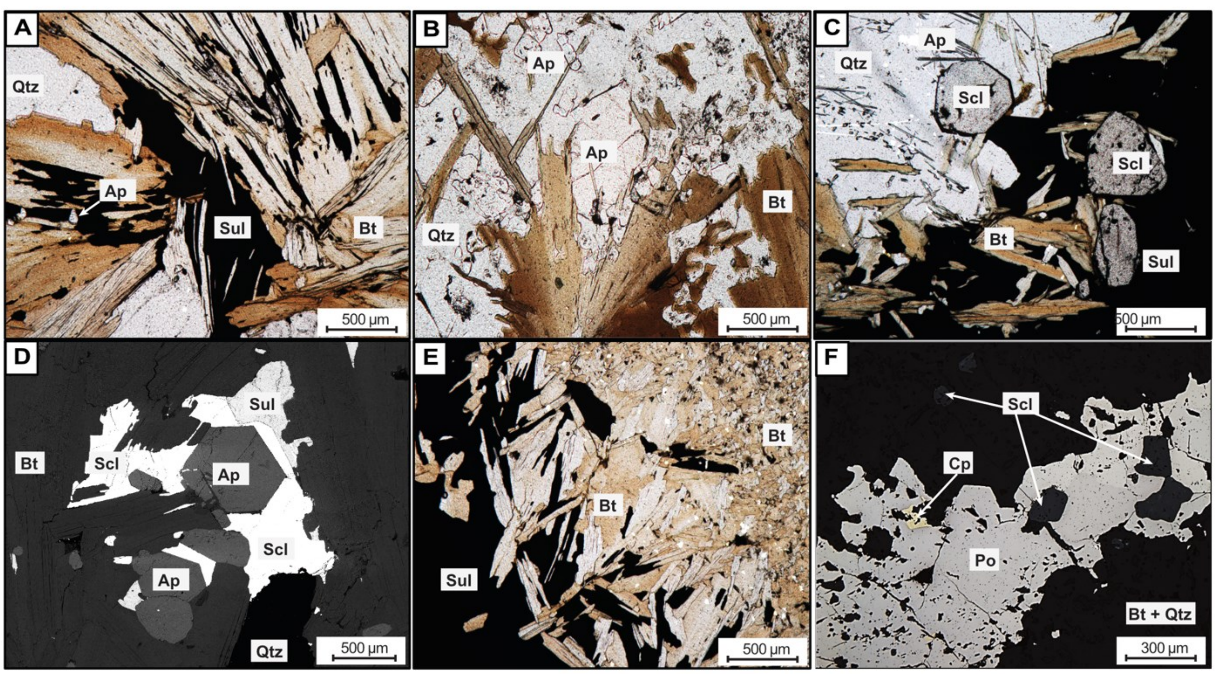

Figure *2*.11. Thin-section photographs showing different assemblages of the pluton-hosted skarn from Lened. A is a cross-polarized transmitted light images; B and C are back-scattered electron images. Muscovite, plagioclase (Pl), quartz (Qtz) and titanite (Ttn) are the primary minerals of the pluton; scheelite (Scl) and sulfides (Sul) are hydrothermal minerals. A- Magmatic quartz (Qtz), plagioclase (Pl) and muscovite cut off by sulfide (Sul) veinlets; B- Ilmenite replaced by titanite (Ttn) + scheelite (Scl) assemblage; C- Ilmenite replaced by titanite (Ttn) + scheelite (Scl) assemblage.

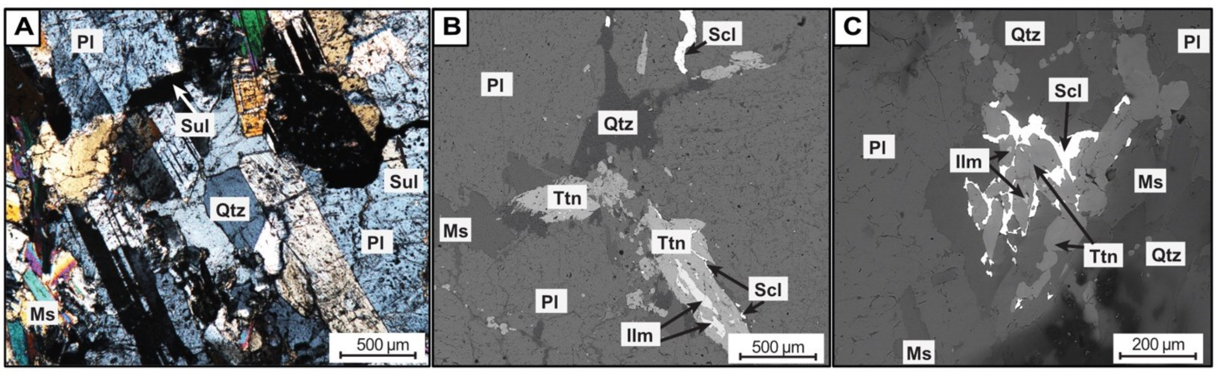

Figure 2.12. Garnet composition: grossular-andradite-(spessartine + almandine) ternary plot. All garnets are from the garnet-pyroxene skarn facies.

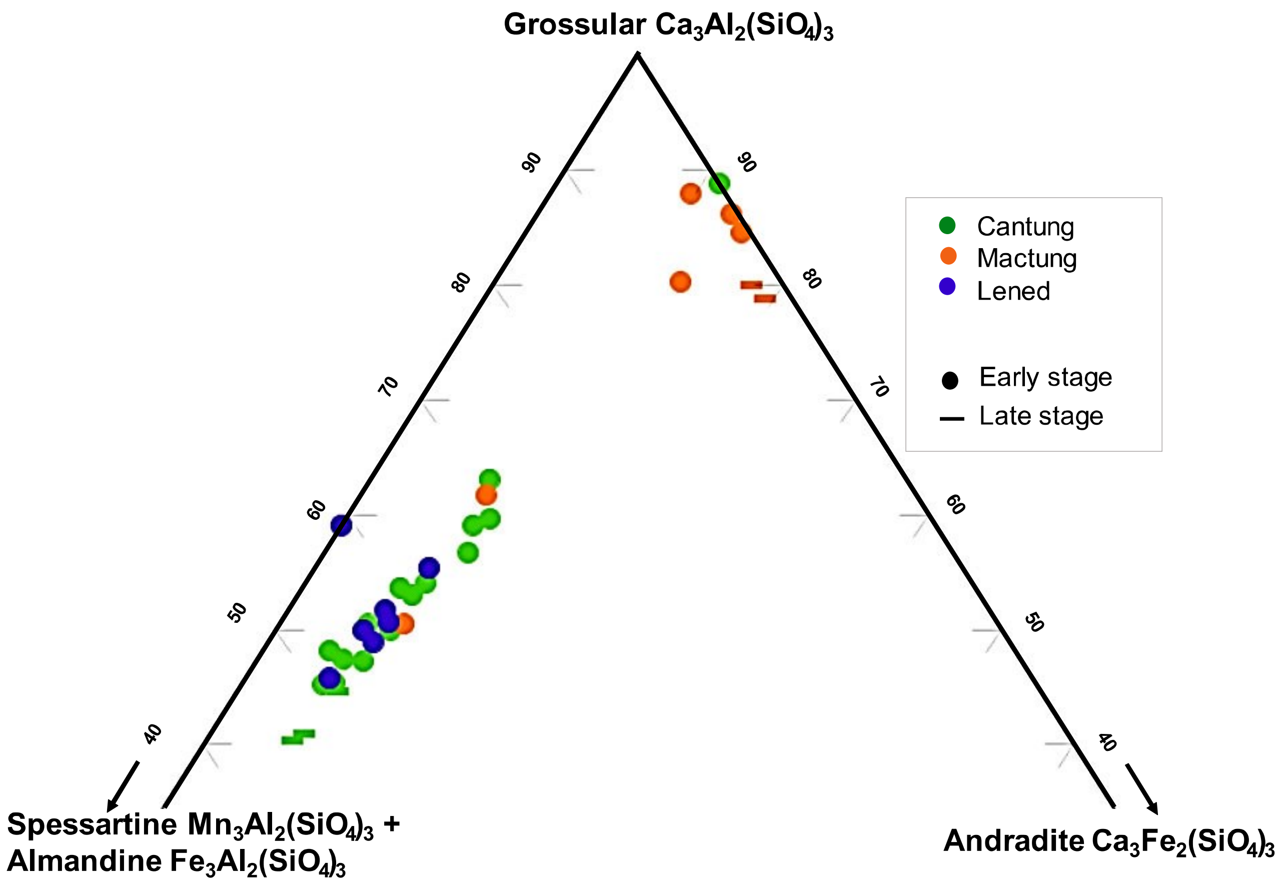

Figure 2.13. Pyroxene and amphibole classification. A/ Wollastonite–enstatite–ferrosilite classification diagram for pyroxenes (after Morimoto et al. 1988); B/ Calcic amphibole classification diagram (after Hawthorne et al., 2012).

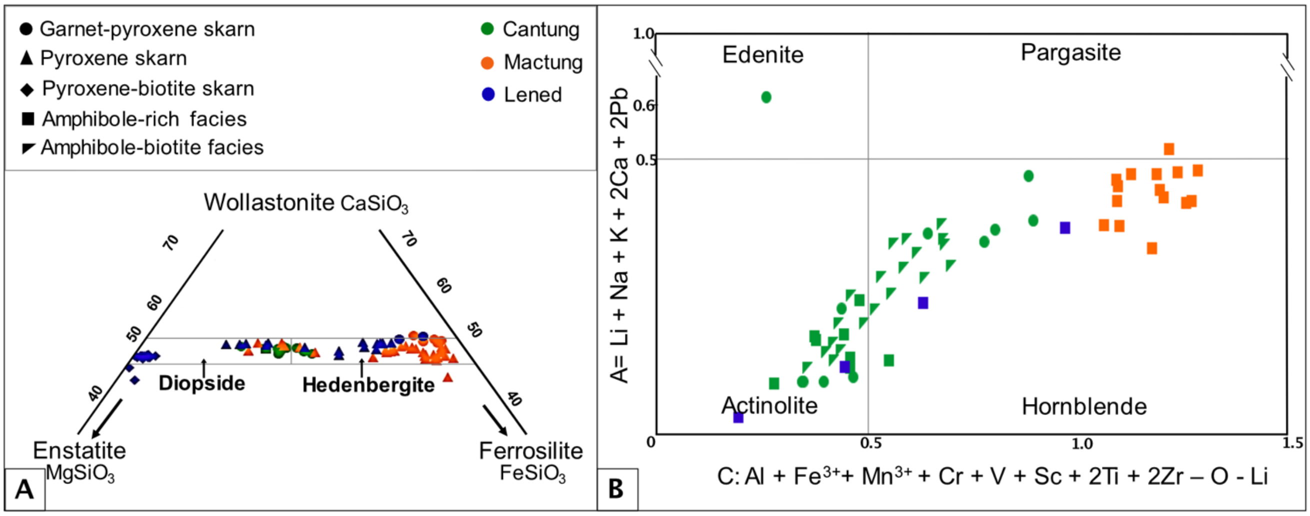

Figure 2.14. Mica classification diagram based on their Fe, Mg and Ba content. Diagram from Tischendorf et al. (2007).

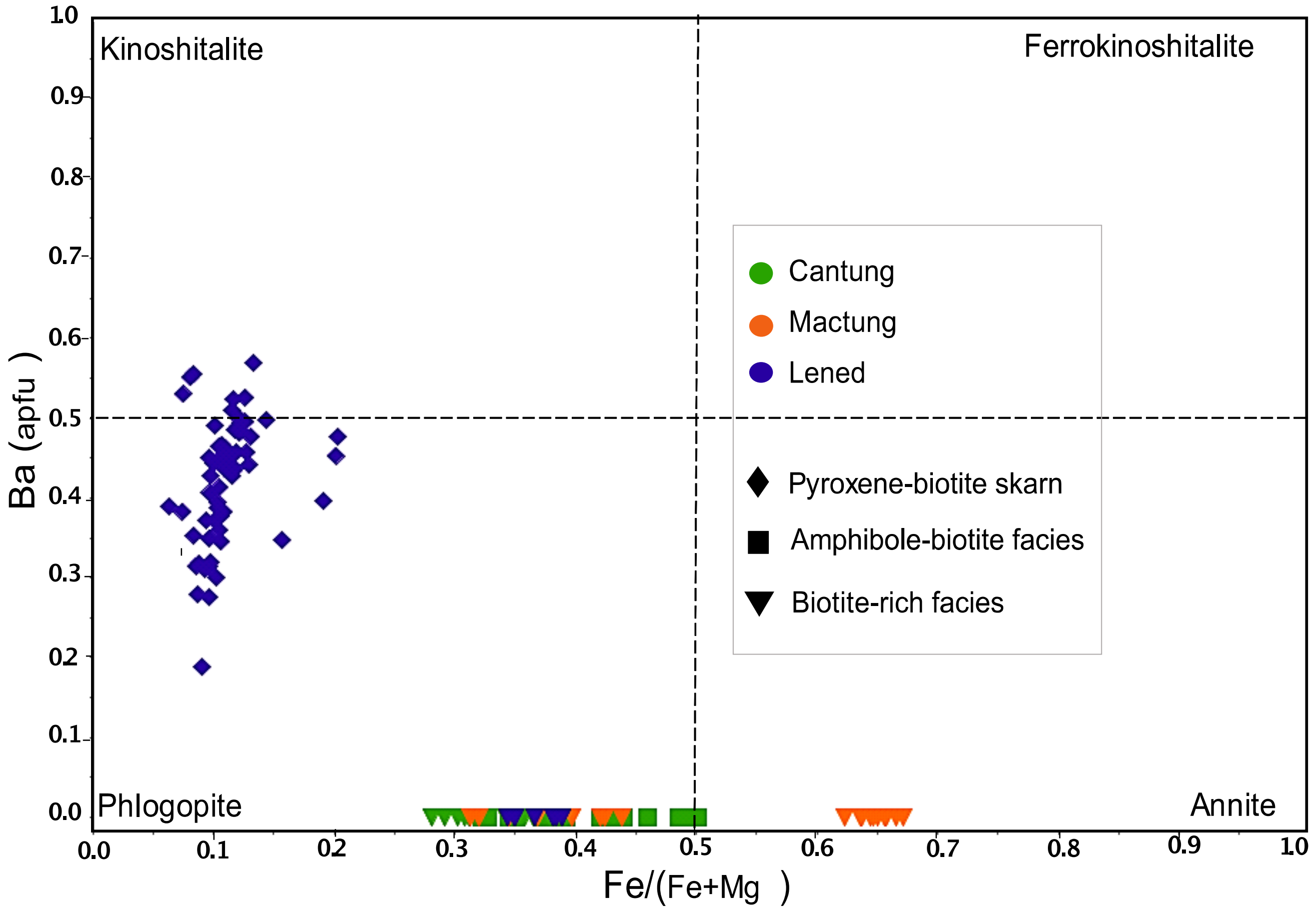

Figure 2.15. A/ Ba-free feldspar classification diagram. Note the trend from an anorthitic composition in the garnet-pyroxene skarn to an albitic composition in the biotite-rich through the amphibole-biotite facies at Cantung. B/ Ba-bearing feldspar classification diagram based on Ba, K and Na substitution.

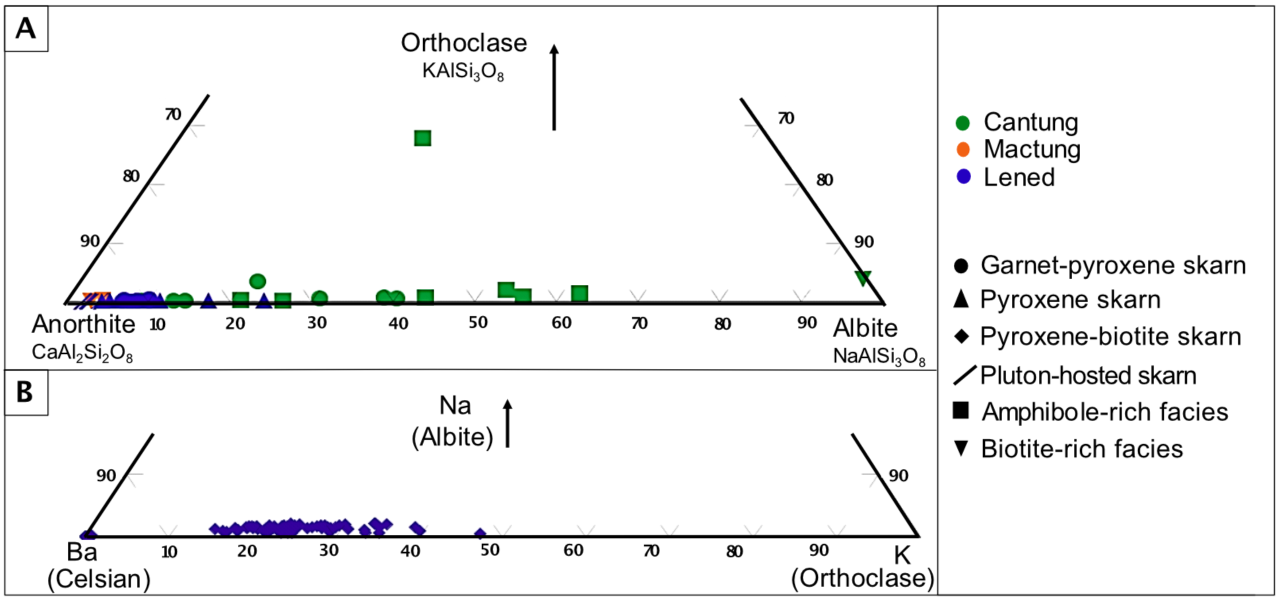

Figure 2.16. Cross-section through the Cantung E-zone orebody showing the distribution of the skarn facies and later alteration assemblages. Modified from Mathieson and Clark (1984).

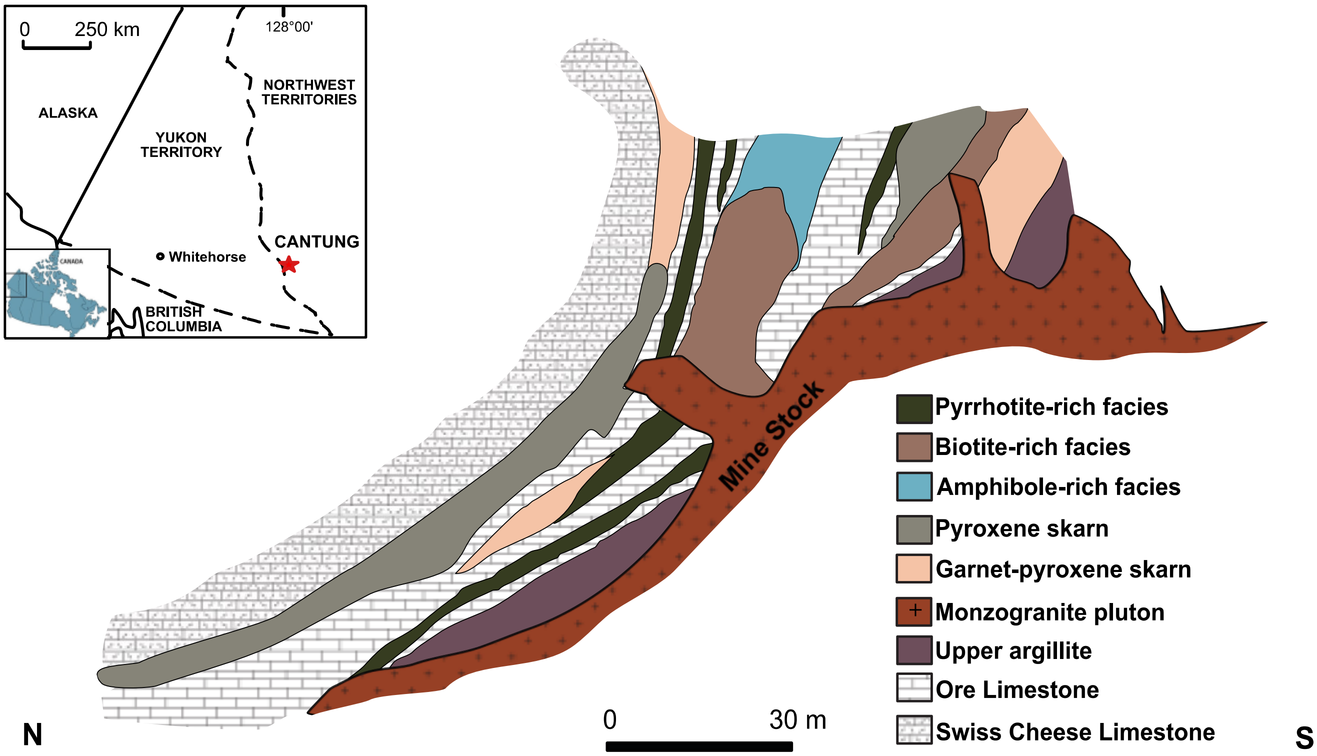

Chapter 3: Tracking fluid-rock interaction and element sources in tungsten skarn deposits of the Canadian Tungsten Belt

Abstract

Cantung and Mactung are two tungsten skarns in the Canadian Cordillera and the two largest tungsten deposits in western North America. These deposits are hosted in locally skarnified carbonate units, and spatially associated with granitoids from the mid-Cretaceous Tungsten suite. The tungsten mineralization occurs as scheelite ($CaWO_4$). The strontium isotopic signatures of scheelite and all intrusive rocks from Cantung and Mactung display a crustal signature, compatible with the common association of tungsten deposits with crustally-derived rocks. Furthermore, strontium isotopes and chemical variations of the carbonate host rocks track fluid-rock interaction and provide constraints on the genesis of the deposits. At Cantung, the strontium isotopic signatures of granitoids and local sedimentary units generally overlap, making interpretations about fluid source ambiguous. However, the least altered signatures suggest a primary input from the Cantung granitoids to the original chemistry of the ore fluid. At Mactung, the strontium isotopic signature of scheelite is dependent on the host lithology and displays an intermediate composition between that of the host lithology and the local granitoids, providing evidence of fluid-rock interaction. Fluid-rock interaction is further supported by enrichment of skarnified limestones in elements of magmatic origin. While abundant textural, geochemical, and isotopic evidence support extensive fluid-rock interaction, quantification of element gains and losses in this system has not

been possible due to the combination of high geochemical variability of the original host rock and pervasive textural overprinting of the skarnified samples.

3.1. Introduction

Tungsten is a critical resource essential to our modern life and economy. It is used to make wear-resistant materials, carbides, steel, and other heavy metal alloys used by construction, mining, petroleum, metalworking, aerospace industries, and in many other electronic and electrical applications. However, tungsten has no viable substitutes and is at a high risk of supply disruption (Union, 2014; Fortier et al., 2018). The highly localized nature of tungsten worldwide, with about sixty percent of the world reserves located in China, an additional nine percent in Canada, and seven percent in Russia (U.S. Geological Survey, 2017 & 2020), is one of the main contributing factors to tungsten being a critical resource. Therefore, constraining the genesis and evolution of tungsten deposits is of interest to determine the global and regional prospectivity for this critical resource. Skarns represent one of the most important types of tungsten deposits and exhibit higher grades than other tungsten deposits, with scheelite ($CaWO_4$) being the tungsten-bearing mineral most commonly mined in these deposits (Werner et al., 1998). Mineralized skarns are traditionally considered to be the result of interaction between a magmatic fluid and carbonate rocks (Meinert, 1992) and provide an ideal setting to determine how the element and isotopic budget of a fluid varies as it migrates through a highly reactive rock.

Tungsten skarn deposits form in or at the contact with carbonate rocks, and are typically associated with calc-alkalic magmatism in orogenic belts (Meinert, 1992). Extensive work has been done in skarn systems to infer their genesis, their relationship with magmatic activity, their age, the source of ore fluids and metals, and fluid pathways (e.g., Shimazaki, 1980; Kato, 1999; Kamvong and

Zaw, 2009; Rasmussen and Mortensen, 2013; Mollai et al., 2014; Adlakha et al., 2018; Legros et al., 2020). Radiogenic isotopes (including Samarium-neodymium and Rubidium-strontium systematics) are increasingly used in this regard in whole rocks, and in gangue and ore minerals. Since scheelite does not incorporate significant amounts of rubidium, a radiogenic contribution to the strontium isotopic signature of scheelite is unlikely. Therefore, the strontium isotopic signature of scheelite reflects the signature of the fluid at the time of precipitation.

In this study, $^{87}Sr/^{86}Sr$ was measured on scheelite and local country rocks from the high grade/tonnage Cantung and Mactung tungsten skarn deposits from the Canadian Tungsten Belt, to constrain (1) the potential sources of ore fluids, (2) the potential effects of fluid-rock interaction on the composition of ore fluids and country rocks, and (3) the magmatic sources in the study area and their affiliation to the crust or the mantle. Comparison between the strontium isotopic signature of scheelite and that of the local lithologies is used to determine which of the local reservoirs may have played a role on the chemistry of the ore fluids. To test whether the reaction of the ore fluids with the country rocks could also be reflected on the chemistry of the country rocks, we examined the chemical variation of the limestone units hosting the skarn deposits, as a function of degree and stage of alteration by the ore fluids.

3.2. Geological setting

3.2.1. Regional geology

Cantung and Mactung are two tungsten deposits located in the Selwyn Basin within the Canadian Cordillera. The Canadian cordillera had a protracted evolution which started during the Neoproterozoic with the breakup of the Rodinia supercontinent (ca. 750 Ma ago) and continued with the formation of the Laurentia craton (Gordey and Anderson, 1993; Monger and Price, 2002;

Ray, 2013). The divergent setting during the Neoproterozoic transitioned to a convergent setting in the Devonian causing the subduction of the Panthalassa ocean basin under the Laurentian margin (Monger and Price, 2002). Progressive amalgamation of magmatic arcs into the Laurentian margin formed the Canadian Cordillera (Monger and Price, 2002). Extensive magmatism accompanied and followed the amalgamation of these different parts of the Cordillera during the mid-Cretaceous. This magmatism encompasses several plutonic suites with large variations in composition, including alkaline to sub-alkaline, and arc-related to crust-derived (Driver et al., 2000; Hart, 1997; Hart et al., 2004; Rasmussen, 2013; Ray, 2013).

During the evolution of the Canadian Cordillera from late Precambrian to Middle Devonian, two main sedimentary facies were deposited in the study area: deep-water shale, chert and sandstone on the southwest forming the Selwyn Basin, and coeval shallow-water carbonates on the northeast in the Mackenzie platform (Gordey and Anderson, 1993). This sequence is overlaid with late Devonian to early Carboniferous turbiditic clastics and early Carboniferous to Triassic shallow-water clastics, chert and carbonates (Gordey and Anderson, 1993).

The Tombstone-Tungsten Belt (TTB) is a plutonic belt within the broader Selwyn plutonic suite associated with mid-Cretaceous magmatism and extending over 700 km from Central Yukon to the southeast of Northwest Territories (Fig. 3.1). The TTB comprises the Tombstone, Mayo and Tungsten suites (Fig. 3.1; Hart et al, 2004). The Tungsten plutonic suite consists of granite to monzogranite plutons with associated pegmatites, aplites and rare lamprophyre dykes (Hart et al., 2004, Gordey and Anderson, 1993) and is derived from a sedimentary crustal source (Hart et al, 2004). The Tungsten plutonic suite is associated with major tungsten deposits including the Cantung and Mactung deposits in the Selwyn Basin (Fig. 3.1).

3.2.2. Local geology

The Cantung and Mactung deposits are skarn deposits located in the eastern part of the Selwyn Basin close the Yukon-Northwest Territories border (Fig. 3.1). The two deposits are very similar in terms of mineralogy and paragenesis (Elongo et al., 2020). A prograde stage of skarn formation consists of a garnet-pyroxene skarn facies followed by a pyroxene skarn facies; and is overprinted by a retrograde alteration stage starting with an amphibole-rich facies followed by a biotite-rich facies (Elongo et al., 2020). Finally, these stages are further overprinted by a sulfide stage followed by late quartz-sulfides veins. The main tungsten-bearing mineral found in these deposits is scheelite. Scheelite is either disseminated in the different prograde and retrograde facies or associated with sulfides and quartz-sulfides veins and is paragenetically associated with all stages of skarnification.

3.2.2.1.The Cantung deposit

The Cantung tungsten skarn deposit is located in the Northwest Territories, Canada, and is hosted in Upper Proterozoic to Upper Ordovician sedimentary rocks (Blusson, 1968). Four sedimentary units are found at Cantung: the "Lower Argillite" belonging to the Narchilla/Vampire formation, the "Swiss-Cheese Limestone", the "Ore Limestone", and the "Upper Argillite" belonging to the Sekwi formation (Fig. 3.2). The entire sedimentary sequence is folded into a recumbent anticline that was later intruded by the Mine Stock pluton, a medium-grained monzogranite (Mathieson and Clark, 1984; Fig. 3.2) belonging to the Tungsten suite of granitoids. A few dykes are also present locally, crosscutting the sedimentary sequence and the Mine Stock pluton as well. Dykes consist of fine-grained monzogranites, aplitic alkali feldspar granites, and kersantitic lamprophyres (Mathieson and Clark, 1984).

Tungsten mineralization at Cantung occurs in two exoskarn orebodies (the Pit orebody and the E-Zone orebody) hosted in the Swiss-Cheese Limestone and the Ore Limestone. The Ore Limestone is a fine-grained limestone with minor dolomite, and the Swiss-Cheese Limestone consists of impure limestone irregularly interbedded with dolomitic siltstone (Blusson, 1968). The relationship between the Mine Stock monzogranite and tungsten mineralization at Cantung remains debated, although its emplacement is associated with contact metamorphism of the sedimentary sequence hosting the Cantung skarn deposit (Mathieson and Clark, 1984). The Mine Stock pluton (98.2 ± 0.4 Ma from U-Pb in zircon, Rasmussen, 2013) shows in fact only local evidence of hydrothermal alteration (Mathieson and Clark, 1984) or fluid saturation. Furthermore, there is no evidence for extensive magmatic fractionation in the Mine Stock pluton, which is a common characteristic of magmatic sources for tungsten mineralization (Rasmussen et al., 2011). Late-stage aplitic dykes are extensively altered and are inferred to be syn-mineralization (Rasmussen et al., 2011) or predate mineralization and act as fluid flow conduits (Adlakha et al., 2018). Mineralization at Cantung ranges in age from ~103 to 93 Ma (Re–Os in molybdenite, Appendix A/Table A.1; and Lentz, 2020).

3.2.2.2.The Mactung deposit

The Mactung tungsten skarn deposit is located in Yukon, Canada, and is hosted in an isoclinally folded sedimentary sequence consisting of units ranging in age from late Precambrian to late Ordovician (Dick and Hodgson, 1982). From older to younger, these units are: the Vampire formation (unit 1), the Sekwi formation (unit 2B), the Hess River formation (unit 3C), the Rabbitkettle formation (units 3D, 3E, 3F, 3G and 3H) and the Duo Lake formation (unit 4, Fig. 3.3; Gebru, 2017; Fischer et al., 2018). Tungsten mineralization at Mactung occurs in two exoskarn orebodies (the Lower and Upper carbonate skarns) hosted in the carbonate rich units within Sekwi and Rabbitkettle formations (units 2B, 3D, 3E and 3F; Dick and Hodgson, 1982; Gebru, 2017; Fischer et al., 2018). Unit 2B consists dominantly of fine-grained limestone and clastics with interbedded slump breccias and units 3D, 3E and 3F consist of intercalated beds of limestone, shale, mudstone and siltstone (Atkinson and Baker, 1986).

Two biotite quartz monzonite plutons belonging to the Tungsten suite are spatially associated with the Mactung deposit: the Cirque Lake Stock also called Mactung North Pluton and the Rockslide Mountain Stock also called Mactung South Pluton (Atkinson and Baker, 1986). Porphyritic, aplitic and pegmatitic dykes also occur at the vicinity of the Mactung deposit. The Cirque Lake Stock was initially proposed as the source of the ore fluids at Mactung because of its spatial association with the Mactung mineralization. However, that relationship was challenged because of the weak hydrothermal alteration around the Cirque Lake Stock, the lack of mineralization in the carbonate units at the direct contact with the Cirque Lake Stock, and the lack of correlation between veins and alteration types in the Cirque Lake Stock and that of the mineralized zones (Atkinson and Baker, 1986). Nonetheless, recent studies have shown that the tungsten skarn mineralization at Mactung (97.5 ± 0.5 Ma from Re–Os in molybdenite, Selby et al., 2003) is coeval with the emplacement of the Cirque Lake Stock and the Rockslide Mountain Stock (97.6 ± 0.2 Ma from U-Pb in zircon, Gebru, 2017).

3.3. Materials and methods

3.3.1. Rock composition

3.3.1.1. Rubidium and strontium concentrations

Whole rock samples representative of the local lithologies at Cantung and Mactung (Table 3.1) were selected to determine their rubidium and strontium content, prior to strontium isotopic analyses. Samples were examined in thin sections through transmitted and reflected light microscopy and Scanning Electron Microscopy (SEM) and unaltered samples were selected for whole rock analyses and ground in a shatter box using an alumina mill.

Whole rock powders were analyzed for their Rb and Sr content through solution ICP-MS. For limestone samples, 200 mg of powder were dissolved in 10 mL of 8N HNO_3 and for all other samples, 200 mg of powder were dissolved in 8mL of 29N HF and 2mL of 16 HNO_3. The mixtures were dried on a hot plate at 130°C overnight, then 5 mL of 12N HCL and 5 mL of 16N HNO_3 were subsequently added, then the solutions were heated at 130°C overnight until completely dried. Finally, 10 mL 8N HNO_3 was added, and the solutions heated at 130°C for 2 hours. Prior to analysis, 0.1 mL of HNO_3, 0.1 mL internal standards (In, Bi, and Sc) and 8.8 ml DI H_2O were added to 1 mL of each solution. The solutions were analyzed using a Perkin Elmer's Elan 6000 ICP-MS at the CCIM-ICP MS facility of the University of Alberta, with a RF power of 1300 W, in dual detector mode, auto lens on and 4 points calibration curves. The flow rate was about 1 mL/minute, dwell times were 10 ms for Sr and 20 ms for Rb and integration times were 350 ms for Sr and 700 ms for Rb. The final results are the average of 3 replicates, with 35 sweeps/replicate.

3.3.1.2.Strontium isotopic composition

Whole rock samples representative of the local lithologies at Cantung and Mactung (Table 3.1) were selected to determine their strontium isotopic signatures.

Limestone sample powders were dissolved in 6N HCl and all other samples in a HF-HNO_3 mixture, in sealed PFA Teflon vessels for 5 days at 150°C on a hotplate. After digestion, the solutions were evaporated to dryness overnight and residues were dissolved in 2.5N HCl. Separation of Sr was carried out following conventional cation-exchange techniques using 0.75N HCl, oxalic acid:HCl mix, and 2.5N HCl (0.75N and 2.5N HCl only for limestone samples). Whole rock dissolution and Sr fraction separation was performed at the Crustal Re-Os Geochronology Laboratory at the University of Alberta. Sr isotopes were measured using a Nu Plasma™ multi-collector inductively coupled plasma mass spectrometer (MC-ICP-MS) at CCIM-ICPMS facility at the University of Alberta. Sr isotopic abundances were normalized for variable mass fractionation to a value of 0.1194 for $^{86}Sr/^{88}Sr$ and using the exponential law. The $^{87}Rb/^{86}Sr$ ratios are calculated using whole-rock Rb and Sr abundances, together with the $^{87}Sr/^{86}Sr$ ratio (Table 3.1).

3.3.1.3. Lithogeochemistry

Whole rock samples of unaltered and altered limestone from Cantung and Mactung (Appendix A/Table A.2) were selected to determine the variation of the chemical composition of limestone as a function of degree of hydrothermal alteration and paragenetic stage at Cantung and Mactung. Unaltered and altered limestone from Cantung are all sampled from the impure Swiss-Cheese limestone (refer to section 3.2.2.1). At Mactung however, due to the inability to find unaltered samples and samples from all alteration facies within the same unit, different units were sampled. The selected unaltered limestone sample is from unit 3E, the host unit for the garnet-pyroxene skarn sample is unconstrained, the amphibole-rich facies sample is from unit 3F, and the biotite-rich facies sample is from unit 2B. These units are heterogeneous and consist of a mixture of limestone and clastic rocks (refer to section 3.2.2.2). Although these units are lithologically similar, local lithological differences might result in significant geochemical differences between the samples being compared.

Approximately 150 g of sample was crushed, powdered (to ~ 100 microns) in an agate mill, dried overnight at 105°C, then 8 g of powder was mixed with 2 g of fluxana wax in a 30 mL glass vial. One plexiglass ball was then added, and the mixture was homogenized on a mill for 8 minutes with 17 U/s (rotations per second). The mixture was subsequently pressed for one minute at 450 bars using a steel hydraulic press. The resulting pressed pellet was then used to obtain whole rock composition. The analyses were performed at the Institute for Geochemistry and Petrology, ETH Zürich, using a wave-length dispersive X-ray fluorescence (XRF) spectrometer PANalytical AXIOS equipped with five diffraction crystals. The elements analyzed include ten major elements (SiO_2, TiO_2, Al_2O_3, Fe_2O_3, MnO, MgO, CaO, Na_2O, K_2O, P_2O_5) and thirty-five trace elements (Ag, As, Ba, Cd, Ce, Cl, Co, Cr, Cs, Cu, F, Ga, Hf, La, Nb, Nd, Ni, Pb, Rb, S, Sb, Sc, Sn, Ta, Sr, Th, U, V, W, Y, Zn, Zr, Mo, Br, and Bi). Results were calibrated using the following reference materials: AGV-2-T-wax, AN-G-T-wax, BCR-2-T-wax, BHVO-2-T-wax, BIR-1a-T-wax, CD-1-T-wax, DTS-2b-T-wax, G2-T-wax, GSS-4-T-wax, KC-1-T-wax, MA-1-T-wax, MA-N-T-wax, MAG-1-T-wax, MP-1-T-wax, MP-1a-T-wax, MP-1b-T-wax, MRG-1-T-wax, NIM-D-T-wax, NIM-G-T-wax, NIM-L-T-wax, NIM-P-T-wax, NIM-S-T-wax, PCC-1-T-wax, PTC-1-T-wax, PTC-1b-T-wax, PTM-1-T-wax, QLO-2-T-wax, RGM-2-T-wax, SCO-1-T-wax, SDC-1-T-wax, SiO_2-T-wax, SU-1-T-wax, SU-1b-T-wax, SY-3-T-wax, UM-1-T-wax, UM-2-T-wax, and UM-4-T-wax. The reported error for XRF analysis of powder-wax pellets is ~ 5 % for major and trace elements. The enrichment and depletion of elements in the alteration facies from XRF data have been calculated based on a normalization to Zr (immobile element) and using an unaltered sample of limestone as reference.

In addition, four samples of hydrothermally altered limestone from the Cantung deposit were selected to complement the evaluation of the chemical reaction of the ore fluids with the country rocks, using specifically areas that are altered rather than powdered bulk samples. They include one sample from the garnet-pyroxene skarn facies, two samples from the pyroxene skarn facies, and one sample from the amphibole-rich facies. Elements including Si, Al, Fe, Mg, Ca, Mn, Mo, Sn and W were examined by micro X-ray fluorescence (micro-XRF) using a Bruker M4 Tornado micro-XRF at the Key Laboratory of Deep Oil and Gas of China University of Petroleum. Analyses were performed with a scanning resolution of 30 μm, a pixel time of 5 ms, a current of 600 μA and a voltage of 50 kV. Other instrument settings were kept as default. The data obtained through this method have a high spatial resolution, but are qualitative and only provide the relative distribution of the detected elements. Moreover, due to the limited number of samples and the fact that analyses are restricted to the surface of small sample areas only, the results may not be representative of the entire deposits. However, the results can provide general trends of chemical variations.

3.3.2. Scheelite composition

Two types of scheelite grains from Cantung and Mactung (Table 3.2) were selected in this study to determine their strontium isotopic signatures. The first type aims to capture the geochemistry of the fluid least modified by interaction with the carbonate units and includes scheelite hosted in lithologies located stratigraphically below the skarn bodies (argillites and granitoids). The second type aims to capture progressive stages of evolution within the skarn bodies and therefore includes scheelites hosted in different skarn facies and subsequent alteration facies. Prior to analysis, chemical homogeneity/heterogeneity in scheelite was examined in thin section through cathodoluminescence (CL) imaging at the Scanning Electron Microscope Laboratory at the

University of Alberta using a Zeiss EVO LS15 Scanning Electron Microscope. In the CL images, no evidence of plastic deformation was observed in scheelite (see Appendix A/ Fig. A1), suggesting that no deformation-induced redistribution of elements occured.

3.3.2.1. Rubidium and strontium concentrations

Concentrations of Rb and Sr were obtained by LA-ICPMS analyses on thin sections in a Thermo Scientific ICAP-Q quadrupole ICPMS coupled to a New Wave UP-213 Nd YAG laser ablation system at the CCIM-ICPMS facility of the University of Alberta using spot sizes of 25 or 30µm. Analyses were run on transects perpendicular to growth zones in individual scheelite grains and the final results presented are an average of concentrations obtained along transects for each grain. No matrix-matched standard is currently available for scheelite, therefore NIST 612 was used as an external standard cycled prior to and at the end of each sample analysis and after every 8 or 10 spot analyses. Calcium (^{43}Ca) was used as internal standard assuming a stoichiometric composition for scheelite with Ca 13.92 weight %. Data reduction was carried out using Igor Pro and Iolite software.

3.3.2.2. Strontium isotopic composition

Scheelite grains were separated at the SELFRAG laboratory of the Canadian Centre for Isotopic Microanalysis (CCIM) at the University of Alberta, handpicked under a binocular microscope under shortwave ultraviolet light, then powdered using an agate mortar and pestle. Scheelite dissolution and Sr fraction separation were performed at the Crustal Re-Os Geochronology Laboratory of the University of Alberta following the procedure described by Kempe et al. (2001). Sr isotopes analyses were carried out using a Nu Plasma™ multi-collector inductively coupled plasma mass spectrometer (MC-ICP-MS) at CCIM-ICPMS facility at the University of Alberta. Sr isotopic abundances were normalized for variable mass fractionation to a value of 0.1194 for $^{86}Sr/^{88}Sr$ and using the exponential law.

3.4. Results

3.4.1. Rb-Sr concentrations and Sr isotope compositions

The rubidium concentrations in whole rocks from Cantung and Mactung are highly variable, with 0.2 to 3.9 ppm in limestones, and 92.6 to 230 ppm in the other lithologies (Table 3.1). Strontium concentrations in whole rocks range between 30.4 and 387.8 ppm with the lowest concentration in argillites and the highest in the lamprophyre from Cantung (Table 3.1). The rubidium concentration in scheelite from Cantung and Mactung is below detection limit (0.04ppm) and strontium concentrations are between 24 and 77ppm (Table 3.2).

The present day $^{87}Sr/^{86}Sr$ values ($^{87}Sr/^{86}Sr_0$) of wholes rocks at Cantung and Mactung are also highly variable (0.71580 to 0.79373, Table 3.1). Due to the very low (or non-existant) rubidium content of scheelite, the present-day $^{87}Sr/^{86}Sr$ values are similar to their initial ratios at ~97Ma (Table 3.2). The present day $^{87}Sr/^{86}Sr$ values ($^{87}Sr/^{86}Sr_0$) of scheelite overlap with the range of whole rock values but are significantly narrower (0.71290 to 0.73070 at Cantung and 0.72143 to 0.74981 at Mactung respectively). The highest $^{87}Sr/^{86}Sr_0$ values are recorded in scheelite hosted in argillite units and the lowest in scheelite from amphibole-rich facies for both Cantung and Mactung (Table 3.2). At Cantung, scheelite sampled below the skarn bodies (scheelite hosted in quartz vein and in Lower Argillite) have $^{87}Sr/^{86}Sr_0$ values similar to the Mine Stock granitoid and aplite dyke (Tables 3.1 and 3.2).

3.4.2. Rock major and trace element composition

Whole rock composition of unaltered and altered limestone from Cantung and Mactung display variable major and trace element compositions without clear systematics (Appendix A/Table A.2) which we consider to be not-interpretable likely due to sampling issues as discussed below.

The results of the micro-XRF analyses are reported as elemental intensity maps highlighting the main elements present in the examined samples, their distribution, and relative amounts (Fig. 3.4 and Appendix A/Fig. A.2). The least altered regions of the samples (Fig. 3.4 and Appendix A/Fig. A.2) are characterized by high calcium and silicon content, and lack of tungsten, iron, and manganese. Tungsten, iron, and manganese are present only in the highly altered sections of the samples.

3.5. Discussion

3.5.1. Magmatic sources in the Canadian Tungsten Belt

Granitic magmas are commonly proposed as the metal source of tungsten deposits (Wang et al., 2010 ; Legros et al., 2019 ; Sun et al., 2019 ; Song et al., 2014 ; Zhu et al., 2019). The relationship between crustally-derived granitoids and tungsten fertility is supported by noble gases, Sr, Nd, O and H isotopic compositions and trace elements data of sulfides, scheelite, wolframite, quartz and whole rock in the Sanin and Kitakami belts (Ishara, 1977), the Canadian Tungsten Belt (Hart et al., 2004), the Bolivian Tin Belt (Sato, 2012) and in the circum-Japan Sea Region (Sato, 2004). The reduced nature of crustal sedimentary source rocks and high fractionation of the magma in these locations is considered to enhance the mobilization and enrichment of tungsten (Sato, 2012; Romer and Kroner, 2016), and a tungsten pre-enrichment of the granite source and/or specific temperatures of crustal melting further favor tungsten fertility (Romer and Kroner, 2015, 2016; Yuan et al., 2019). Granitoids from the Cantung and Mactung deposits are isotopically evolved (initial $^{87}Sr/^{86}Sr$ ($^{87}Sr/^{86}Sr_t$) values of 0.719-0.721 and 0.736-0.739 respectively, Table 3.1), which is consistent with a crustal origin of the granitoids also supported by previous O, S, Nd and Sr isotope data (Rasmussen, 2013; Gebru, 2017).

While granitoids are broadly accepted to play a role in tungsten deposits, the role of the mantle in tungsten deposit fertility remains debated as either a potential supply of volatiles and heat necessary to fuel the hydrothermal system and/or to induce crustal melting, or a supply of mantle-derived fluids mixed with crustal material during their ascension. The involvement of mantle fluids has been proposed in tungsten deposits in Iberia (Burnard & Polya, 2004), the Nanling region (Hu et al., 2012, Xiaofeng et al., 2016, Hsieh et al., 2008, Wei et al., 2019) and the Canadian Tungsten Belt (Adlakha et al.2018), and is based on noble gases, Sr and Nd isotope data of sulfides and scheelite, melt inclusions and whole rock compositions. At Cantung and Mactung, lamprophyres are the only rocks with potential to be mantle-derived. However, the Cantung lamprophyre dyke is of kersantitic nature and has an isotopically evolved signature ($^{87}Sr/^{86}Sr_t$ = 0.714). Other lamprophyre dykes in the Selwyn Basin also have evolved Sr signatures with $^{87}Sr/^{86}Sr_{100}$ of 0.714 to 0.721 (Rasmussen, 2013 ; Mair et al., 2011). A crustal source for the lamprophyres or crustal contamination of a mafic magma during ascent would explain these Sr isotopic signatures (Rock, 1987). Therefore, at Cantung and Mactung there is no lithologic or isotopic evidence for mantle input into the outcropping granitoids and local lamprophyres are unlikely to represent regional mantle input. While mantle heat contribution upon crustal thinning cannot be discarded, we propose that the geochemical budget at Cantung and Mactung is only associated with crustal-derived materials.

3.5.2. Source of Sr in the ore fluids at Cantung and Mactung

At Cantung, the Sr isotopic compositions of scheelite at the time of scheelite formation (~97 Ma) display different patterns when compared to that of the host rocks (Fig. 3.5A, Tables 3.1 and 3.2). Scheelite sampled below the skarn bodies (scheelite from quartz vein and Lower Argillite) have $^{87}Sr/^{86}Sr_{97Ma}$ values similar to the Mine Stock monzogranite and related aplite dyke (Fig. 3.5A). This signature might represent the least altered signature of the ore fluid since no interaction with the highly reactive limestones occurred. These results therefore support a primary input from the Cantung granitoids source melt to the original chemistry of the ore fluid. The $^{87}Sr/^{86}Sr_{97Ma}$ of scheelite hosted in the pyroxene and biotite facies indicates a dominant contribution from the limestone. Scheelite hosted in the Upper Argillite unit has a Sr signature compatible with variable contributions from the argillite, limestone and/or Cantung granitoids. Significantly, one sample hosted in the amphibole-rich facies has $^{87}Sr/^{86}Sr_{97Ma}$ out of the compositional range of the local lithologies (closest to that of the lamprophyre dyke, Fig. 3.5A) suggesting an unidentified source of strontium to the system.

The Sr isotopic compositions of scheelite at Mactung provide clear indication of fluid-rock interaction. The Sr isotopic composition of scheelite at time of formation (~97 Ma) represents an intermediate composition between the main intrusive bodies and the lithologies in which those scheelites are hosted (Fig. 3.5B, Tables 3.1 and 3.2). All limestone-hosted scheelites have an intermediate $^{87}Sr/^{86}Sr_{97Ma}$ composition between the compositions of limestone and the Mactung granitoids, and all argillite-hosted scheelites have an intermediate $^{87}Sr/^{86}Sr_{97Ma}$ composition between the compositions of argillites with the Mactung granitoids. These results therefore support an input from the Mactung granitoids source melt and either the limestone or the argillite units depending on which lithology hosts scheelite.

3.5.3. Fluid-rock interaction and implications for tungsten mineralization

The effects of fluid-rock interaction can be evaluated comparing the whole rock geochemical composition of unaltered host rock with that of altered facies (Appendix A/Table A.3 and Fig. A.3). The lack of systematics in the results obtained (Appendix A/ Fig. A.3) is likely related with the heterogeneous nature of the original lithology. The Swiss-Cheese Limestone consists of impure limestone interbedded with siliciclastics in variable proportions. In order to compare whole rock geochemistry from unaltered and altered rocks, the samples selected have to, within reason, have the same original geochemical signature (i.e., have variability of geochemical composition that can be captured in the samples analyzed). Furthermore, in order to constrain the geochemical evolution of the system, the sample also has to represent a single skarn facies. The intermingling of silicate and carbonate facies in the original lithologies implies that samples commonly have variable ratios of silicate-rich to carbonate-rich rock. In pervasively skarnified samples, the original ratio of carbonate to silicate lithologies gets obscured. Therefore, the geochemical trends obtained in this portion of the study are likely to represent variable contributions from the geochemical variability on the original lithology plus geochemical overprinting by a hydrothermal fluid. Due to the spatial distribution of skarn facies, samples that are representative of a single facies and at the same time representative of the average geochemistry of that facies were not available for this study. Given the inherent challenges of using whole rock composition to determine element budget contribution from the fluid, microXRF maps were used towards assessing those contributions qualitatively. Having noted this significant shortcoming, rubidium, cesium and potassium (Appendix A/ Fig. A.3 A, B, E & F) are systematically and progressively enriched in skarnified facies. This enrichment is consistent with a hydrothermal origin and the tendency of lithophile and highly incompatible elements to preferentially remain in the melt and being exsolved at late stages of fractional crystallization (Hulsbosch et al. 2016; Audétat, 2019). These results are in accordance with those from fluid inclusions in scheelite and quartz from the Cantung deposit reported by Legros et al. (2020), in which rubidium, cesium and potassium were some of the elements identified in the ore fluid least affected by interaction with the country rocks. Chemical variations are also detectable in ore-bearing hand samples from the Swiss-Cheese Limestone (Fig. 3.4). The ore-bearing samples display variably altered regions, likely resulting from the textural and mineralogical variability within the Swiss-Cheese Limestone. The sample from the pyroxene skarn facies (Fig. 3.4A) includes least altered regions consisting of quartz, plagioclase, chlorite, clinozoisite, and fine-grained pyroxene, and highly altered regions consist dominantly of coarser-grained pyroxene, pyrrhotite and scheelite. The sample from the amphibole-rich facies (Fig. 3.4B) includes least altered regions consisting of muscovite, quartz, plagioclase, calcite and minor biotite, and highly altered regions consisting of amphibole, pyrrhotite, scheelite, with lesser pyrite, quartz, and plagioclase. The least altered regions of these samples are systematically richer in siliciclastics and likely correspond to the siliciclastic-rich regions of the original Swiss-Cheese limestone. The highly altered regions of the samples most likely correspond to the carbonate-rich regions. The distribution of elements in the geochemical maps (Fig. 3.4 and Appendix A/ Fig. A.2) is compatible with the mineralogy observed. The least altered regions have a high calcium and silicon content, and lack tungsten (contained in scheelite), iron (mostly contained in pyrrhotite) and manganese, whereas the highly altered sections are rich in those elements. The chemical variability of the original host rock hinders the quantification of chemical exchange between the ore fluid and the host rock. However, the preferential distribution of ore minerals in the carbonate-rich regions of the Swiss-Cheese Limestone suggests a lithologic control in the precipitation of scheelite (e.g., Elongo et al., 2020), supporting the fluid-rock interaction process previously inferred.

3.6. Conclusion

The strontium isotopic signatures of scheelite and all intrusive rocks from Cantung and Mactung are purely crustal, discarding a direct mantle contribution to the composition of the ore fluids. Strontium isotopes and chemical variations of host rocks at Cantung and Mactung track fluid-rock interaction and provide constraints on the genesis of the deposits. At Cantung, the strontium isotopic signatures of scheelite are dominantly compatible with contributions from the local lithologies, with the least altered signatures suggesting a primary input from the Cantung granitoids to the chemistry of the ore fluid. In addition, one skarn-hosted scheelite has lower $^{87}Sr/^{86}Sr$ than any of the local lithologies suggesting that an additional strontium contributor has not been identified in this study. At Mactung, strontium isotopic signatures of scheelite display an intermediate composition between the compositions of the Mactung granitoids and the scheelite host lithologies (either argillite or limestone), probably reflecting a mixing, and providing a proxy for fluid-rock interaction. During fluid-rock interaction, elements of clear magmatic origin (Rb, Cs, K) were added to the carbonate host rocks by the ore fluids. The geochemical variability of the original host rock and pervasive skarnification preclude quantifying element gains and losses in this study. However, element distribution maps suggest a lithologic control on the tungsten mineralization, also evidencing the effect of fluid-rock interaction.

3.7. Acknowledgements

This work was supported by NSERC Discovery Grant to Pilar Lecumberri-Sanchez, Polar Continental Shelf to Hendrik Falck, Northwest Territories Geological Survey contribution agreements for 2018-2019 and 2019-2020. We thank NorthAmerican Tungsten Corporation Ltd. for giving us access to the Cantung mine and facilitating our field work there. Thank you to Krystle Moore, Andy DuFrane, Adrien Vezinet and Nathan Gerein from the University of Alberta for their great contribution in this work, helping in sample preparation and analysis, and for fruitful discussions. Thank you to Ehsan Salmabadi and Ken Hickey for valuable discussions and for donating some of the samples used in this study.

3.8. References

Adlakha, E., Hanley, J., Falck, H., & Boucher, B. (2018). The origin of mineralizing hydrothermal fluids recorded in apatite chemistry at the Cantung W–Cu skarn deposit, NWT, Canada. European Journal of Mineralogy, 30(6), 1095-1113.

Atkinson, D., & Baker, D.J. (1986). Recent developments in the geologic understanding of Mactung. Mineral Deposits of the Northern Cordillera. Canadian Institute of Mining, Metallurgy and Petroleum, 37, 234-244.

Audétat, A. (2019). The metal content of magmatic-hydrothermal fluids and its relationship to mineralization potential. Economic Geology, 114(6), 1033-1056.

Bell, K., Anglin, C. D., & Franklin, J. M. (1989). Sm-Nd and Rb-Sr isotope systematics of scheelites: Possible implications for the age and genesis of vein-hosted gold deposits. Geology, 17(6), 500-504.

Blusson, S. L. (1968). Geology and tungsten deposits near the headwaters of Flat River, Yukon Territory and southwestern district of Mackenzie, Canada (Vol. 67, No. 22). Department of Energy, Mines and Resources.

Brugger, J., Maas, R., Lahaye, Y., McRae, C., Ghaderi, M., Costa, S., Lambert, D., Bateman, R., & Prince, K. (2002). Origins of Nd–Sr–Pb isotopic variations in single scheelite grains from Archaean gold deposits, Western Australia. Chemical Geology, 182(2-4), 203-225.

Burnard, P. G., & Polya, D. A. (2004). Importance of mantle derived fluids during granite associated hydrothermal circulation: He and Ar isotopes of ore minerals from Panasqueira. Geochimica et Cosmochimica Acta, 68(7), 1607-1615.

Chivas, A. R., Andrew, A. S., Sinha, A. K., & O'Neil, J. R. (1982). Geochemistry of a Pliocene–Pleistocene oceanic-arc plutonic complex, Guadalcanal. Nature, 300(5888), 139-143.

DePaolo, D. J., & Wasserburg, G. J. (1976). Nd isotopic variations and petrogenetic models. Geophysical Research Letters, 3(5), 249-252.

Dick, L. A., & Hodgson, C. J. (1982). The Mactung W-Cu (Zn) contact metasomatic and related deposits of the northeastern Canadian Cordillera. Economic Geology, 77(4), 845-867.

Driver, L. A., Creaser, R. A., Chacko, T., & Erdmer, P. (2000). Petrogenesis of the Cretaceous Cassiar batholith, Yukon–British Columbia, Canada: Implications for magmatism in the North American Cordilleran interior. Geological Society of America Bulletin, 112(7), 1119-1133.

Elongo, V., Lecumberri-Sanchez, P., Legros, H., Falck, H., Adlakha, E., & Roy-Garand, A. (2020). Paragenetic constraints on the Cantung, Mactung and Lened tungsten skarn deposits, Canada: Implications for grade distribution. Ore Geology Reviews, 125, 103677.

Fischer, B.J., Martel, E., and Falck, H., (2018). Geology of the Mactung tungsten skarn and area – Review and 2016 field observations; Northwest Territories Geological Survey, NWT Open File 2018-02, 84 pages and appendices.

Fortier, S. M., Nassar, N. T., Lederer, G. W., Brainard, J., Gambogi, J., & McCullough, E. A. (2018). Draft critical mineral list—Summary of methodology and background information—US Geological Survey technical input document in response to Secretarial Order No. 3359 (No. 2018-1021). US Geological Survey.

Gebru, A. L. (2017). Petrogenesis of Granitoids in the Vicinity of the Mactung Tungsten Skarn Deposit, NE Yukon-Northwest Territories: Characterization of Skarn Mineralization and Causative Plutons through Geological, Petrochemical, Mineralogical, and Geochronological Analysis. UnPub PhD Thesis University of New Brunswick, New Brunswick, Canada.

Gordey, S. P., & Anderson, R. G. (1993). Evolution of the northern Cordilleran miogeocline, Nahanni map area (105I), Yukon and Northwest Territories. Geological Survey of Canada Memoir 428, 214.

Hart, C. J. R. (1997). A transect across Stikinia: Geology of the northern Whitehorse map area, southern Yukon Territory (105D13–16). Exploration and Geological Services Division, Yukon, Indian and Northern Affairs Canada Bulletin 8, 1–112.

Hart, C. J., Mair, J. L., Goldfarb, R. J., & Groves, D. I. (2004). Source and redox controls on metallogenic variations in intrusion-related ore systems, Tombstone-Tungsten Belt, Yukon Territory, Canada. Earth and Environmental Science Transactions of The Royal Society of Edinburgh, 95(1-2), 339-356.

Hsieh, P. S., Chen, C. H., Yang, H. J., & Lee, C. Y. (2008). Petrogenesis of the Nanling Mountains granites from South China: constraints from systematic apatite geochemistry and whole-rock geochemical and Sr–Nd isotope compositions. Journal of Asian Earth Sciences, 33(5-6), 428-451.

Hu, R. Z., Bi, X. W., Jiang, G. H., Chen, H. W., Peng, J. T., Qi, Y. Q., ... & Wei, W. F. (2012). Mantle-derived noble gases in ore-forming fluids of the granite-related Yaogangxian tungsten deposit, Southeastern China. Mineralium Deposita, 47(6), 623-632.

Hulsbosch, N., Boiron, M. C., Dewaele, S., & Muchez, P. (2016). Fluid fractionation of tungsten during granite–pegmatite differentiation and the metal source of peribatholitic W quartz veins: Evidence from the Karagwe-Ankole Belt (Rwanda). Geochimica et Cosmochimica Acta, 175, 299-318.

Ishihara, S. (1977). The magnetite-series and ilmenite-series granitic rocks. Mining Geology, 27(145), 293-305.

Kamvong, T., & Zaw, K. (2009). The origin and evolution of skarn-forming fluids from the Phu Lon deposit, northern Loei Fold Belt, Thailand: evidence from fluid inclusion and sulfur isotope studies. Journal of Asian Earth Sciences, 34(5), 624-633.

Kato, Y. (1999). Rare Earth Elements as an Indicator to Origins of Skarn Deposits: Examples of the Kamioka Zn-Pb and Yoshiwara-Sannotake Cu (–Fe) Deposits in Japan. Resource Geology, 49(4), 183-198.

Kempe, U., Belyatsky, B., Krymsky, R., Kremenetsky, A., & Ivanov, P. (2001). Sm–Nd and Sr isotope systematics of scheelite from the giant Au (–W) deposit Muruntau (Uzbekistan): implications for the age and sources of Au mineralization. Mineralium Deposita, 36(5), 379-392.

Kozlik, M., Gerdes, A., & Raith, J. G. (2016). Strontium isotope systematics of scheelite and apatite from the Felbertal tungsten deposit, Austria–results of in-situ LA-MC-ICP-MS analysis. Mineralogy and Petrology, 110(1), 11-27.

Lecumberri-Sanchez, P., Vieira, R., Heinrich, C. A., Pinto, F., & Wälle, M. (2017). Fluid-rock interaction is decisive for the formation of tungsten deposits. Geology, 45(7), 579-582.

Legros, H., Lecumberri-Sanchez, P., Elongo, V., Laurent, O., Falck, H., Adlakha, E., & Chelle-Michou, C. (2020). Fluid evolution of the Cantung tungsten skarn, Northwest Territories, Canada: Differentiation and fluid-rock interaction. Ore Geology Reviews, 103866.

Legros, H., Richard, A., Tarantola, A., Kouzmanov, K., Mercadier, J., Vennemann, T., ... & Bailly, L. (2019). Multiple fluids involved in granite-related W-Sn deposits from the world-class Jiangxi province (China). Chemical Geology, 508, 92-115.

Lentz, C. (2020). Genesis of Gold Mineralization at the Cantung W-Cu skarn deposit, N.W.T. MSc Thesis, University of New Brunswick, New Brunswick, Canada

Mair, J. L., Farmer, G. L., Groves, D. I., Hart, C. J., & Goldfarb, R. J. (2011). Petrogenesis of postcollisional magmatism at Scheelite Dome, Yukon, Canada: evidence for a lithospheric mantle source for magmas associated with intrusion-related gold systems. Economic Geology, 106(3), 451-480.

Mathieson, G. A., & Clark, A. H. (1984). The Cantung E Zone scheelite skarn orebody, Tungsten, Northwest Territories; a revised genetic model. Economic Geology, 79(5), 883-901.

Meinert, L. D. (1992). Skarns and skarn deposits. Geoscience Canada.

Mollai, H., Pe-Piper, G., & Dabiri, R. (2014). Genetic relationships between skarn ore deposits and magmatic activity in the Ahar region, Western Alborz, NW Iran. Geologica Carpathica, 65(3), 209-227.

Monger, J. W., Nokleberg, W. J., Coyner, A. R., & Fahey, P. L. (1996). Evolution of the northern North American Cordillera: generation, fragmentation, displacement and accretion of successive North American plate-margin arcs. Geology and Ore Deposits of the American Cordillera. Geological Society of Nevada, 1133-1152

Monger, J., & Price, R. (2002). The Canadian Cordillera: geology and tectonic evolution. CSEG Recorder, 27(2), 17-36.

Rasmussen, K. L., & Mortensen, J. K. (2013). Magmatic petrogenesis and the evolution of (F: Cl: OH) fluid composition in barren and tungsten skarn-associated plutons using apatite and biotite compositions: Case studies from the northern Canadian Cordillera. Ore Geology Reviews, 50, 118-142.

Rasmussen, K. L., Lentz, D. R., Falck, H., & Pattison, D. R. (2011). Felsic magmatic phases and the role of late-stage aplitic dykes in the formation of the world-class Cantung Tungsten skarn deposit, Northwest Territories, Canada. Ore Geology Reviews, 41(1), 75-111.

Rasmussen, K.L. (2013) The timing, composition, and petrogenesis of syn- to post-accretionary magmatism in the northern Cordilleran miogeocline, eastern Yukon and southwestern Northwest Territories. Ph.D. Thesis, University of British Columbia, Vancouver, British Columbia, Canada, 788 pp.

Ray, G. E. (2013). A review of skarn in Canadian Cordillera. British Columbia Ministry of Energy and Mines, British Columbia Geological Survey Open File, 8, 50

Rock, N. M. (1987). The nature and origin of lamprophyres: an overview. Geological Society, London, Special Publications, 30(1), 191-226.

Romer, R. L., & Kroner, U. (2015). Sediment and weathering control on the distribution of Paleozoic magmatic tin–tungsten mineralization. Mineralium Deposita, 50(3), 327-338.

Romer, R. L., & Kroner, U. (2016). Phanerozoic tin and tungsten mineralization—tectonic controls on the distribution of enriched protoliths and heat sources for crustal melting. Gondwana Research, 31, 60-95.

Sato, K. (2012). Sedimentary Crust and Metallogeny of Granitoid Affinity: Implications from the Geotectonic Histories of the Circum-J apan S ea Region, Central A ndes and Southeastern Australia. Resource Geology, 62(4), 329-351.

Sato, K., Kovalenko, S. V., Romanovsky, N. P., Nedachi, M., Berdnikov, N. V., & Ishihara, T. (2004). Crustal control on the redox state of granitoid magmas: tectonic implications from the granitoid and metallogenic provinces in the circum-Japan Sea Region. Earth and Environmental Science Transactions of The Royal Society of Edinburgh, 95(1-2), 319-337.

Scanlan, E. J., Scott, J. M., Wilson, V. J., Stirling, C. H., Reid, M. R., & Le Roux, P. J. (2018). In situ 87Sr/86Sr of scheelite and calcite reveals proximal and distal fluid-rock interaction during orogenic W-Au mineralization, Otago Schist, New Zealand. Economic Geology, 113(7), 1571-1586.

Selby, D., Creaser, R. A., Heaman, L. M., & Hart, C. J. (2003). Re-Os and U-Pb geochronology of the Clear Creek, Dublin Gulch, and Mactung deposits, Tombstone Gold Belt, Yukon, Canada: absolute timing relationships between plutonism and mineralization. Canadian Journal of Earth Sciences, 40(12), 1839-1852

Shimazaki, H. I. D. E. H. I. K. O. (1980). Characteristics of skarn deposits and related acid magmatism in Japan. Economic Geology, 75(2), 173-183.

Song, G., Qin, K., Li, G., Evans, N. J., & Chen, L. (2014). Scheelite elemental and isotopic signatures: Implications for the genesis of skarn-type W-Mo deposits in the Chizhou Area, Anhui Province, Eastern China. American Mineralogist, 99(2-3), 303-317.

Sun, K., & Chen, B. (2017). Trace elements and Sr-Nd isotopes of scheelite: Implications for the W-Cu-Mo polymetallic mineralization of the Shimensi deposit, South China. American Mineralogist, 102(5), 1114-1128.

Sun, K., Chen, B., & Deng, J. (2019). Ore genesis of the Zhuxi supergiant W-Cu skarn polymetallic deposit, South China: Evidence from scheelite geochemistry. Ore Geology Reviews, 107, 14-29.

U.S. Geological Survey, 2017, Mineral commodity summaries 2017: U.S. Geological Survey, 202 p., https://doi.org/10.3133/70180197.

U.S. Geological Survey, 2020, Mineral commodity summaries 2020: U.S. Geological Survey, 200 p., https://doi.org/10.3133/mcs2020.

Union, I. (2014). Communication from the Commission to the European Parliament, the Council, the European Economic and Social Committee and the Committee of the Regions. A new skills agenda for europe. Brussels.

Voicu, G., Bardoux, M., Stevenson, R., & Jebrak, M. (2000). Nd and Sr isotope study of hydrothermal scheelite and host rocks at Omai, Guiana Shield: implications for ore fluid source and flow path during the formation of orogenic gold deposits. Mineralium Deposita, 35(4), 302-314.

Wang, X., Ni, P., Jiang, S., Zhao, K., & Wang, T. (2010). Origin of ore-forming fluid in the Piaotang tungsten deposit in Jiangxi Province: Evidence from helium and argon isotopes. Chinese Science Bulletin, 55(7), 628-634.

Wei, W. F., Hu, R. Z., Bi, X. W., Jiang, G. H., Yan, B., Yin, R. S., & Yang, J. H. (2019). Mantle-derived and crustal He and Ar in the ore-forming fluids of the Xihuashan granite-associated tungsten ore deposit, South China. Ore Geology Reviews, 105, 605-615.

Werner, A. B., Sinclair, W. D., & Amey, E. B. (1998). International Strategic Mineral Issues Summary Report--tungsten (No. 930). US Government Printing Office.

Xiaofeng, L., Cheng, H., Chunzeng, W., & Lifa, W. (2016). Genesis of the Huangshaping W–Mo–Cu–Pb–Zn polymetallic deposit in Southeastern Hunan Province, China: Constraints from fluid inclusions, trace elements, and isotopes. Ore Geology Reviews, 79, 1-25.

Yuan, S., Williams-Jones, A. E., Romer, R. L., Zhao, P., & Mao, J. (2019). Protolith-related thermal controls on the decoupling of Sn and W in Sn-W metallogenic provinces: Insights from the Nanling region, China. Economic Geology, 114(5), 1005-1012.

Zhu, Lü-Yun, et al. "Origin of the Shangfang Tungsten Deposit in the Fujian Province of Southeast China: Evidence from Scheelite Sm–Nd Geochronology, H–O Isotopes and Fluid Inclusions Studies." Minerals 9.11 (2019): 713.

3.9. Tables

Table 3.1. Initial, present time and at 97 Ma whole rock strontium isotope composition for lithologies from the Cantung and Mactung deposits. The "t" indice represents the initial value (at the time t of formation) and "0" the present-day value. For lithologies with large ranges for age, the age t (Ma) used to calculate the Sr isotope ratios is an average of the age range. MS= Mine Stock, MNP=Mactung North Pluton, MSP= Mactung South Pluton, OL=Ore Limestone, SCL=Swiss-Cheese Limestone. Refer to the local geology section for details about the different units.

Deposit	Sample name	Lithology	Rb (ppm)	Sr (ppm)	$^{87}Sr/^{86}Sr_0$	2 SE on $^{87}Sr/^{86}Sr_0$	$^{87}Rb/^{86}Sr$	Age t (Ma)	$^{87}Sr/^{86}Sr_t$	$^{87}Sr/^{86}Sr_{97Ma}$	Lithology age range (Ma)	Age reference
Cantung	S12-39 913	Granitoid (MS #1)	172	173	0.72500	0.00001	2.88	98.2	0.72098	0.72103	98.2 ± 0.4	Rasmussen (2013)
	S13-06 666.5-668	Granitoid (MS #2)	147	164	0.72343	0.00001	2.60	98.2	0.71981	0.71985	98.2 ± 0.4	Rasmussen (2013)
	18-CA-11	Aplite	193.0	204.0	0.72404	0.00002	2.74	97.3	0.72025	0.72026	97.3 ±0.3	Rasmussen (2013)
	18-CA-37	Lamprophyre	166.1	387.8	0.71580	0.00002	1.24	96.7	0.71409	0.71409	96.7 ± 0.8	Rasmussen (2013)
	U2535 96-96.5	Limestone (OL)	3.9	154.4	0.72646	0.00003	0.07	525	0.72591	0.72636	541-509	Blusson (1968)
	18-CA-05	Limestone (SCL)	0.5	77.2	0.72317	0.00002	0.02	525	0.72303	0.72314	541-509	Blusson (1968)
	U2602-140	Argillite (Upper)	92.6	56.4	0.79373	0.00005	4.79	525	0.75788	0.78713	541-509	Blusson (1968)
	18-CA-10	Argillite (Lower)	230.3	111.4	0.73962	0.00002	6.00	582	0.68985	0.73136	635-529	Blusson (1968)
Mactung	18-MA-13	Granitoid (MSP)	176	122	0.74540	0.00002	4.19	97.6	0.73959	0.73963	97.6 ± 0.2	Gebru (2017)
	18-MA-03	Granitoid (MNP)	138	82	0.74302	0.00001	4.89	97.6	0.73624	0.73629	97.6 ± 0.2	Gebru (2017)
	MS05-146 123.4-123.6	Limestone (Unit 3F)	0.3	63.7	0.71790	0.00002	0.01	490	0.71780	0.71788	497-485.4	Gordey and Anderson (1993)
	MS146 122.0	Limestone (Unit 3F)	0.2	50.3	0.71664	0.00003	0.01	490	0.71654	0.71662	497-485.4	Gordey and Anderson (1993)
	MS161 322-322.3 A	Argillite (Unit 1)	133.8	150.6	0.76775	0.00002	2.59	582	0.74629	0.76419	635-529	Gordey and Anderson (1993)
	MS177 86.2-86.3	Argillite (Unit 1)	178.8	30.4	0.79136	0.00003	17.15	582	0.64900	0.76771	635-529	Gordey and Anderson (1993)
	18-MA-10	Argillite (Unit 1)	165.1	63.5	0.76690	0.00003	7.57	582	0.70407	0.75646	635-529	Gordey and Anderson (1993)

Table 3.2. Strontium isotope composition at present time and at 97 Ma for scheelite hosted in different facies at the Cantung and Mactung deposits. The "0" indice in the isotope ratios represents the present-day value. DL= detection limit (DL=0.04ppm for Rb). OL=Ore Limestone, SCL=Swiss-Cheese Limestone. Refer to the local geology section for details about the different units.

Deposit	**Sample name**	**Host lithology/facies**	**Rb (ppm)**	**Sr (ppm)**	$^{87}Sr/^{86}Sr_0$	**2 SE on** $^{87}Sr/^{86}Sr_0$	$^{87}Sr/^{86}Sr_{97Ma}$
Cantung	18-CA-50c	Quartz vein in Mine Stock pluton	<DL	50	0.72252	0.00002	0.72252
	18-CA-50r	Quartz vein in Mine Stock pluton	<DL	50	0.72346	0.00002	0.72346
	18-CA-47	Garnet-pyroxene skarn (OL)	<DL	35	0.71543	0.00002	0.71543
	18-CA-31a	Pyroxene skarn (SCL)	<DL	55	0.72637	0.00002	0.72637
	18-CA-29b	Amphibole-rich facies (SCL)	<DL	53	0.71290	0.00003	0.71290
	18-CA-28	Biotite-rich facies (OL)	<DL	77	0.72514	0.00002	0.72514
	18-CA-10	Argillite (Lower)	<DL	60	0.72280	0.00003	0.72280
	18-CA-51	Argillite (Upper)	<DL	50	0.73070	0.00001	0.73070
Mactung	18-MA-02	Garnet-pyroxene skarn (Unit 3E)	<DL	57	0.72646	0.00002	0.72646
	MS231 60-60.3	Pyroxene skarn (Unit 3E)	<DL	30	0.72464	0.00002	0.72464
	MS161 185.6-185.9	Amphibole-rich facies (Unit 3F)	<DL	60	0.72143	0.00002	0.72143
	MS161 322-322.3 A	Argillite (Unit 1)	<DL	24	0.74981	0.00001	0.74981

3.10. Figures

Figure 3.1. Regional map showing the geographical distribution of the mid-Cretaceous plutonic suites, including the location of the Tombstone-Tungsten Belt comprising the Tombstone, Mayo and Tungsten suites, and the location of the Cantung and Mactung deposits (modified from Hart et al., 2004). The grey-shaded area represents the Selwyn Basin.

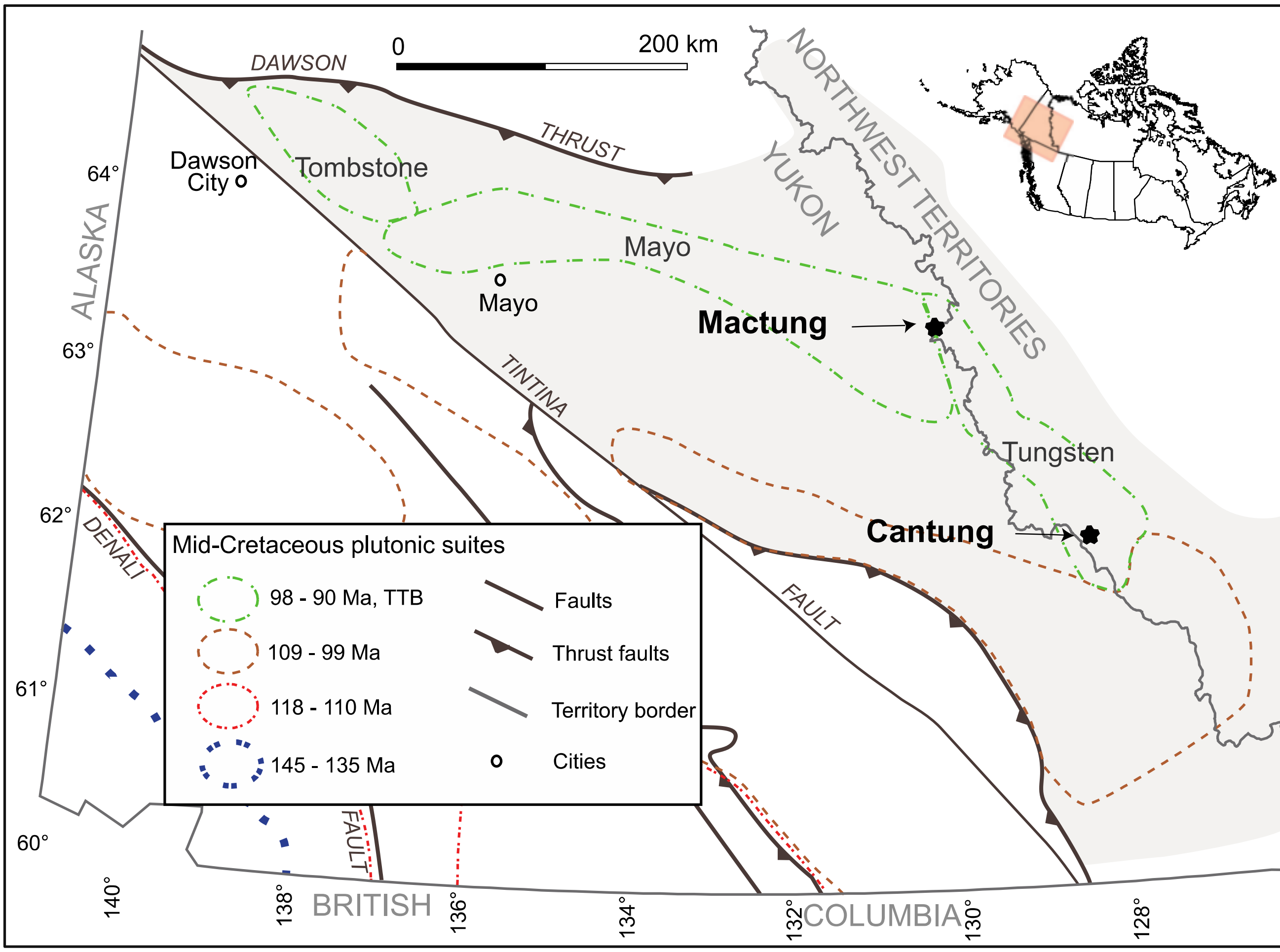

Figure 3.2. Local geology of the Cantung deposit. A/ Surface geology of the Cantung deposit (modified after Blusson, 1968). B/ Geological cross-section through the Cantung deposit, looking west (modified from Cummings and Bruce, 1977).

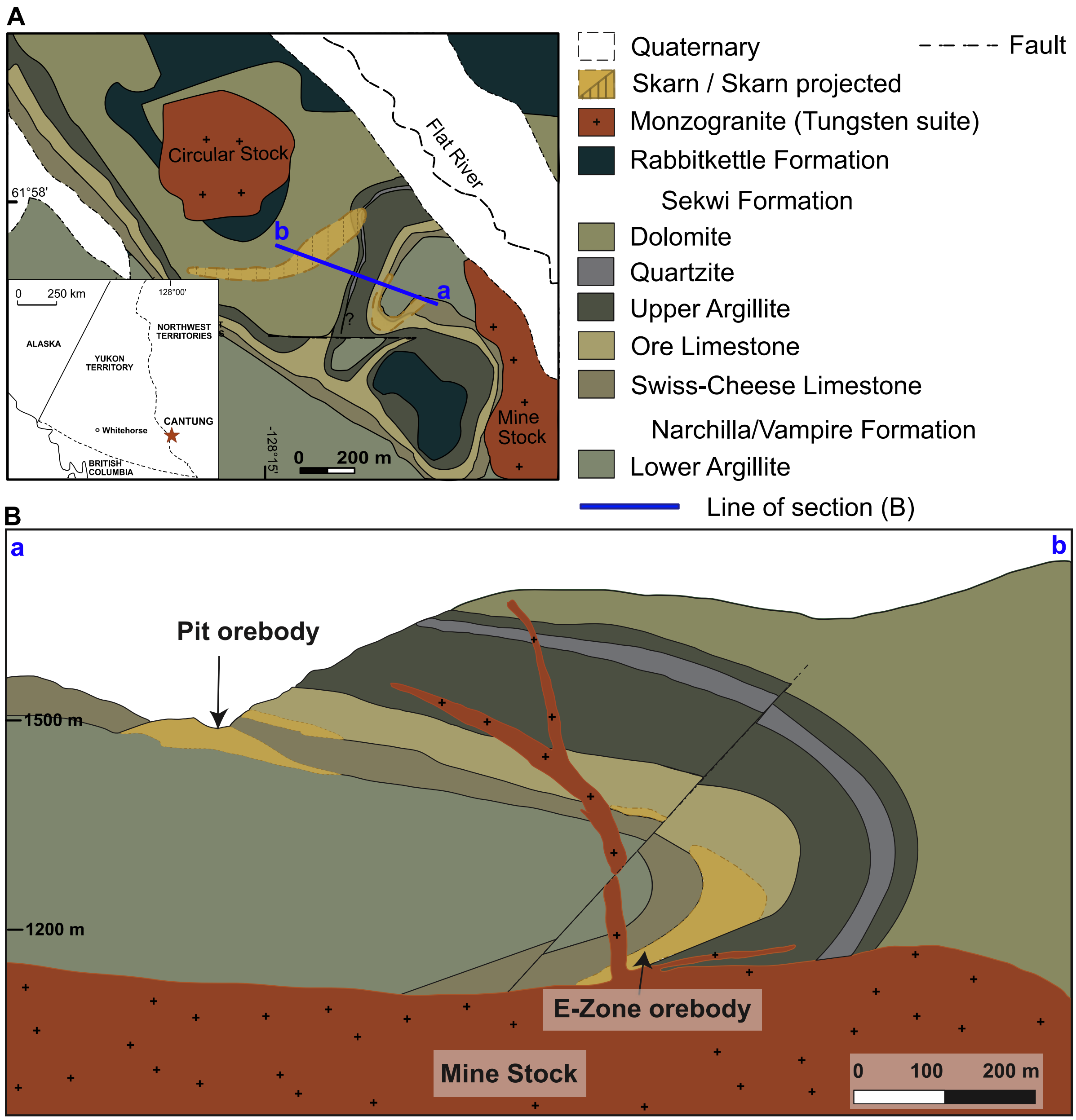

Figure 3.3. Local geology of the Mactung deposit. A/ Surface geology of the Mactung deposit (modified after Gebru, 2017). B/ Geological cross-section through the Mactung deposit (modified from Gebru, 2017 and Fischer et al., 2018). Mineralization (shaded areas) is hosted in the Lower carbonate skarn (unit 2B) and in the Upper carbonate skarn (units 3D, 3E, 3F).

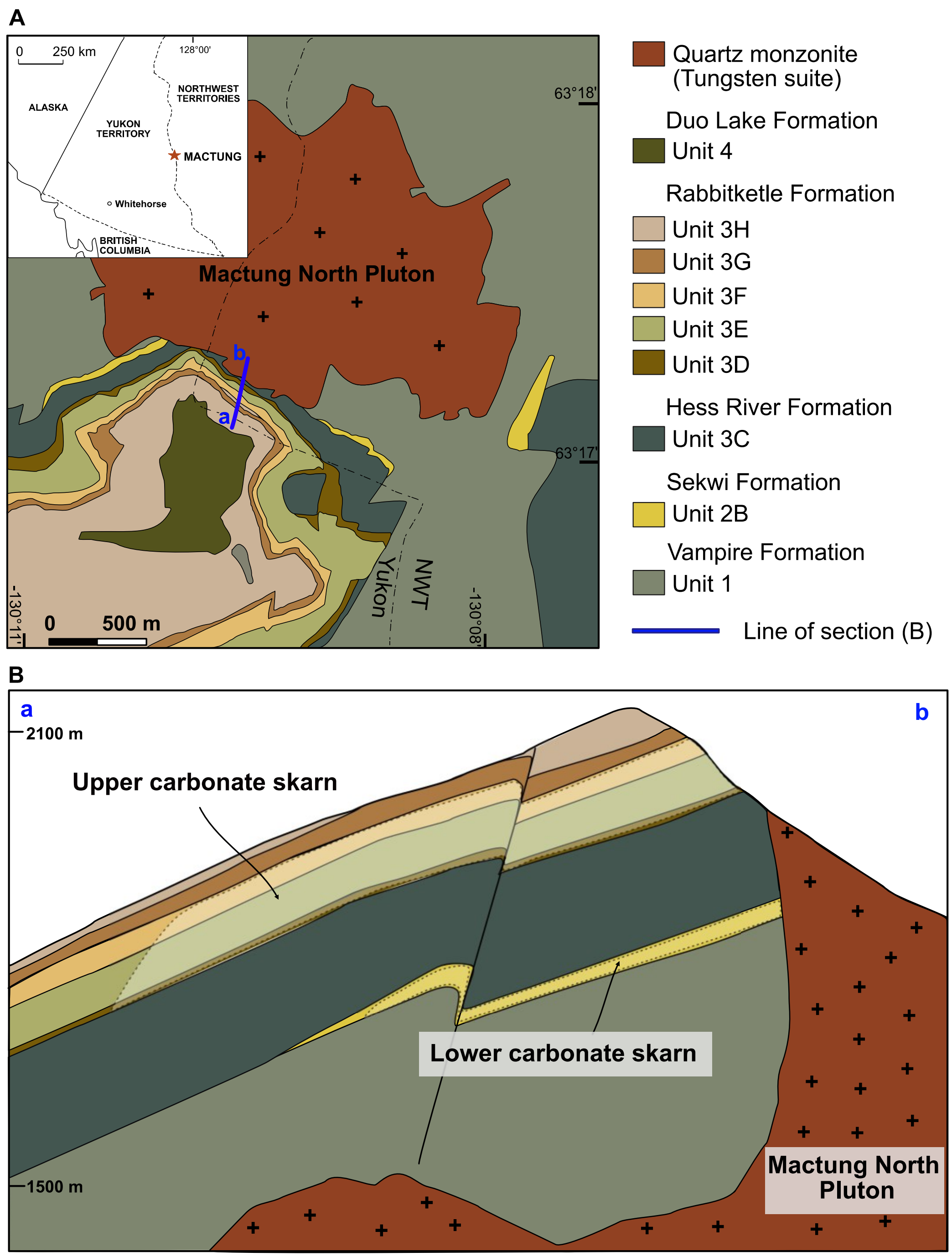

Figure 3.4. Micro-XRF elemental intensity maps showing intensity of Ca, Si, W, Fe and Mn for two representative core samples (A & B) of the impure Swiss-Cheese Limestone from the Cantung deposit. Photographs at the top of each column represent the core samples under natural light before elemental mapping. A/ Pyroxene skarn facies sample, with least altered regions consisting of quartz, plagioclase, chlorites, clinozoisite, and pyroxene, and highly altered regions consisting dominantly of pyroxene, pyrrhotite and scheelite. B/ Amphibole-rich facies sample, with least altered regions consisting of muscovite, quartz, plagioclase, calcite and minor biotite, and highly altered regions consisting of amphibole, pyrrhotite, scheelite, and lesser quartz, plagioclase and pyrite. The least altered regions have a high calcium and silicon content, and lack tungsten, iron, and manganese. The highly altered regions are rich in tungsten, iron and manganese.

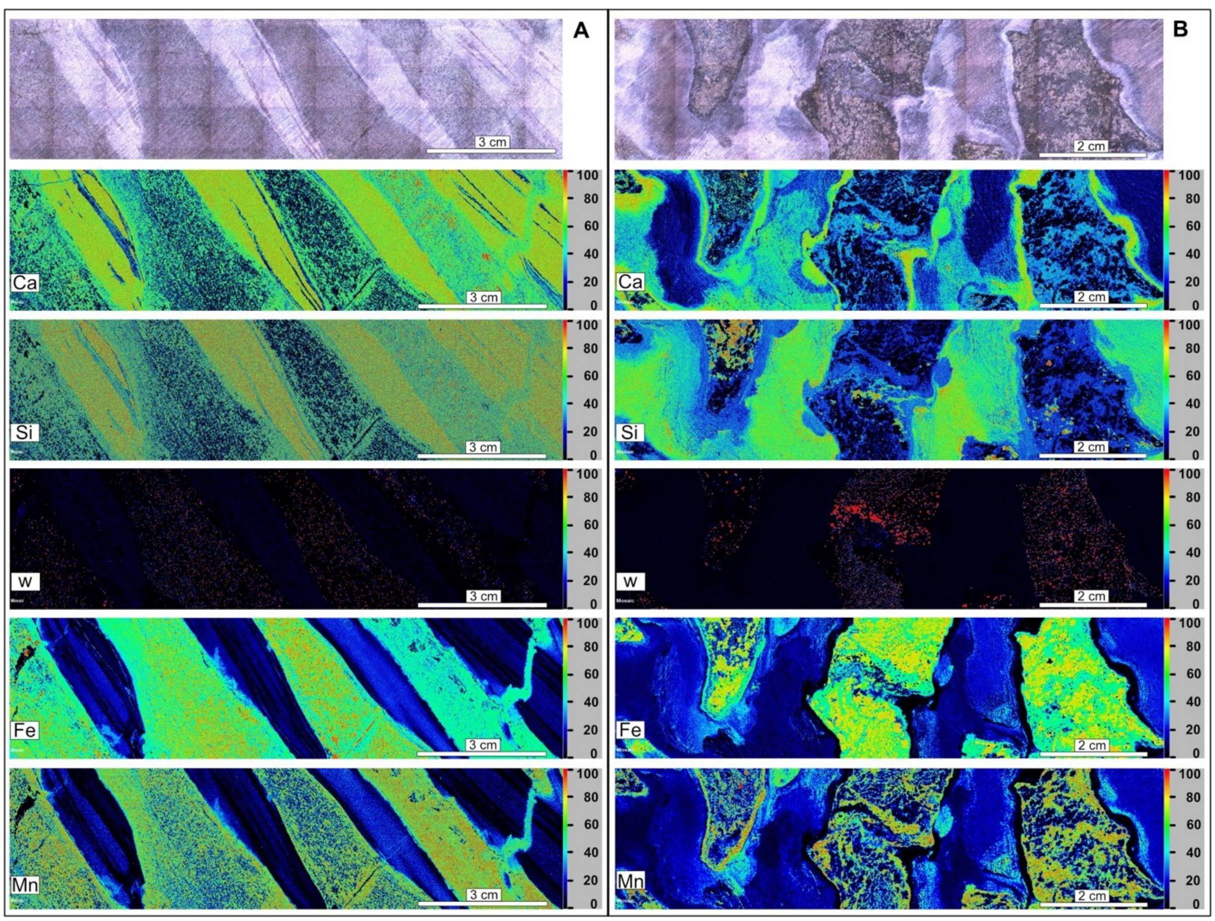

Figure 3.5. $^{87}Sr/^{86}Sr$ isotope composition at 97 Ma for whole rocks and scheelite hosted in different facies, from A/ the Cantung deposit and B/ the Mactung deposit. Whole rock data have been age-corrected to 97 Ma, the approximate time of scheelite formation at Cantung and Mactung. Squares represent whole rock data and circle represent scheelite data from different hosts. The average $^{87}Sr/^{86}Sr_{97Ma}$ of Mid-Ocean Ridge Basalts (MORB) is also indicated for reference. *OL= Ore Limestone; SCL=Swiss-Cheese Limestone.*

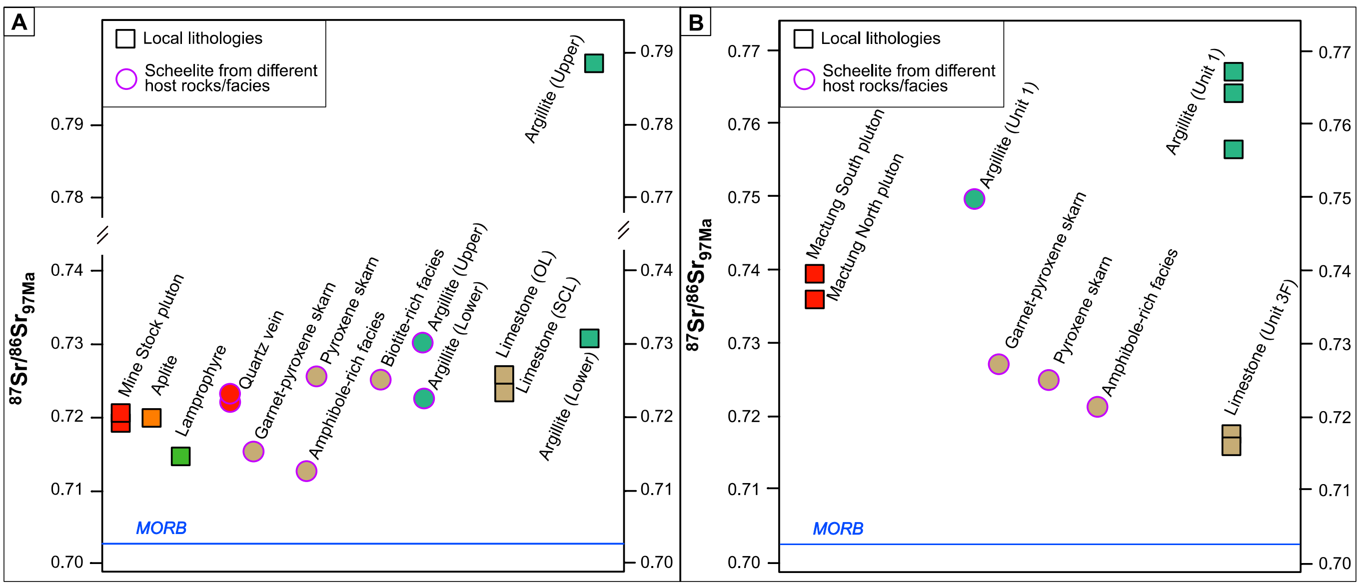

Chapter 4: Ancient roots of tungsten in western North America

Abstract

The highly irregular and localized distribution of tungsten deposits worldwide constitutes a supply challenge for basic industries such as steel and carbides. Over Earth's history, tungsten has preferentially accumulated at paleocontinental margins formed during the breakup of supercontinents. Later crustal thickening of these paleogeographic regions and the magmas they produce are associated with large tungsten districts. However, all the largest tungsten deposits in the modern North American Cordillera, which preserves over three billion years of geologic record in a paleocontinental margin with abundant crustal magmatism, are limited to the narrow Canadian Tungsten Belt in northwestern Canada. Here, we use neodymium isotopic compositions of scheelite ($CaWO_4$) from the Canadian Tungsten Belt and the paleogeographic distribution of tungsten deposits in the North American Cordillera to constrain the factors that control tungsten distribution. We document that tungsten is specifically associated with materials that, on average, were derived from the mantle during the Mesoarchean to Paleoproterozoic. Weathering and erosion of the supercontinents Columbia and Rodinia favored pre-enrichment of tungsten in sediments. The orogenic heating of pre-enriched sediments produced reduced melts capable of efficiently scavenging tungsten, and formed the largest deposits in North America.

4.1. Introduction

Tungsten is a key strategic metal for modern society used in alloys due to its hardness, density, and high temperature resistance, with highly localized production, and with no current substitutes (European Commission, 2020). Recent disruptions in supply chains have drawn attention to the strategic need to secure local supplies of critical elements (Guan et al., 2020). In this context, identifying locations prospective for critical elements, such as tungsten, is a global priority (European Commission, 2020; Simandl et al., 2021). The tungsten cycle over Earth's history has been affected by supercontinent assembly and breakup (Romer and Kroner, 2016), the evolution of early life (Kletzin and Adams, 1996), and crustal melting and differentiation (Candela and Bouton, 1990). Therefore, determining how/if current tungsten distribution relates to paleogeography, the evolution of early life, and source rock characteristics is of high scientific and economic interest.

The factors that control tungsten distribution can be best identified in a province with diverse paleogeography and geology that also hosts various degrees of tungsten enrichment. The North American Cordillera has long been a tectonically active region beneath which the age of the crustal lithosphere extends back to the Archean-Paleoproterozoic (Whitmeyer and Karlstrom, 2007). Despite a favorable tectonic setting across the Cordillera, the economically most significant tungsten mineralization is focused along the narrow Canadian Tungsten Belt (CTB), defined by peraluminous intrusions that host two of the largest tungsten deposits in the world (Figs. 4.1 and 4.2). The Cordillera therefore provides an ideal region to evaluate which factors control tungsten distribution.

4.2. Neodymium as a tracer of source materials

Current continents, including North America, are a mosaic of multiple paleogeographic provinces that have migrated, assembled and disassembled over geologic time. The regional neodymium isotopic composition (εNd) can be a proxy for either the age (depleted mantle model age, T_{DM}) at which the crust differentiated from the mantle or the average age (T_{DM}) of a mixture of materials derived from the mantle at different times (Arndt and Goldstein, 1987). Therefore, εNd and T_{DM} are used in this manuscript towards fingerprinting paleogeographic provinces, but not towards defining absolute ages of formation of crust. Crustal materials derived from the same paleogeographic provinces or from the same mixture of materials from different provinces follow a comparable evolution of εNd versus time (e.g., provinces with Grenvillian, Paleoproterozoic and Archean T_{DM}, Fig. 4.3). The εNd and T_{DM} of tungstate minerals in tungsten deposits can therefore provide an indirect proxy to characterize the source(s) of tungsten in mineralized systems.

The initial values of εNd in intrusive rocks at the time of formation (εNd_t) reach a minimum landward from subduction trenches that reflects the homogenized isotopic signature of the underlying crustal basement (Chapman et al., 2017). The εNd_t of landward Cretaceous intrusive rocks in Yukon (Fig. 4.1, a-a') reaches a minimum of -17 (Morris and Creaser, 2008), which is consistent with sources derived dominantly from materials with Archean to Paleoproterozoic T_{DM}. In Arizona (Fig. 4.1, b-b'), εNd_t of Mesozoic to Cenozoic intrusive rocks reaches a landward minimum of -10 with a natural variability of approximately 2 epsilon units (Chapman et al., 2017), reflecting materials with an average Proterozoic T_{DM}.

4.3. Geologic context

The CTB is the most important tungsten metallogenic province within the North American Cordillera (Figs. 4.1 and 4.2). The CTB consists of mid-Cretaceous peraluminous intrusions (Rasmussen et al., 2011) hosted in Neoproterozoic to Devonian pelitic, carbonaceous and calcareous sedimentary units that were deposited along the ancestral western margin of North America in the Selwyn Basin (Gordey and Anderson, 1993; Hart et al., 2004). Farther east, the oldest shallow shelf equivalents of the Selwyn Basin include the Paleoproterozoic Wernecke, the

Meso/Neoproterozoic Mackenzie Mountains, and the Cambrian Windermere supergroups in the Mackenzie Platform, but their extent beneath the Selwyn Basin is unknown (Gordey and Anderson, 1993). The CTB hosts deposits of comparable size and grade to other world-class tungsten deposits (Werner et al., 2014). Most notable, the CTB includes one of the top ten historic producers of tungsten worldwide (the Cantung deposit; Fig. 4.2a) and currently the greatest reserves in North America (the Mactung deposit; Fig. 4.2b), as well as numerous additional tungsten deposits (Werner et al., 2014; Karl et al., 2020). Tungsten mineralization in the CTB occurs dominantly as scheelite in skarns, which are hydrothermal mineral deposits hosted in calc-silicate rocks (detailed local geology in Appendix B.1).

4.4. Results

Depleted mantle model ages (T_{DM}) dominantly between 3.1 and 1.5 Ga (Appendix B/Tables B.1, B.2 & B.3) and strongly negative εNd_t mainly between -20 to -15 (Fig. 4.3) in scheelites from both the Mactung and Cantung deposits demonstrate that mineralization in the CTB is sourced from crustal materials with a Mesoarchean to mid-Paleoproterozoic average age. Neoproterozoic to Cambrian sedimentary units and Cretaceous intrusive rocks analyzed in this study have isotopic signatures that are similar to those of scheelite at the time of their formation (Fig. 4.3). In this context, the scheelite Nd isotopic signatures reflect a mixture of the source and the Neoproterozoic to Cambrian host rocks to the mineralization (e.g., Scanlan et al., 2018), with the Nd signature of scheelite closer to that of its main Nd contributor.

The compiled isotopic and geographic evidence shows that the largest tungsten deposits in the North American Cordillera have a source of Mesoarchean to Paleoproterozoic T_{DM} (Fig. 4.1 and 4.3). In the North American Cordillera, tungsten tonnages approaching those of the CTB are only found at the Andrew deposit in the Tungsten Hills District (TDH) of southern California and Nevada (Karl et al.,2020). The TDH consists dominantly of Upper Jurassic granite and quartz diorite intruded in Paleozoic sandstone, shale and limestone that are variably metamorphosed (Lemmon, 1941). The T_{DM} of the crust in the TDH is 2.3 to 2 Ga and mineralization is associated with peraluminous granites that have $\varepsilon Nd_t < -16$ (Bennet and DePaolo, 1987). This early Paleoproterozoic signature likely reflects a dominant Nd contribution from the underlying Archean Mojave Block (Fig. 4.1) or materials derived from it. Similarly, the richest tungsten deposit in Idaho (the CuMo deposit) is related to the Atlanta lobe of the Idaho Batholith, a metaluminous granite with Mesoarchean to Paleoproterozoic T_{DM}, unlike other Sierran equivalents (Gaschnig et al., 2011).

4.5. Discussion

The new and compiled data presented here demonstrate that large tonnage tungsten deposits throughout the North American Cordillera are sourced from materials that have a Mesoarchean to Paleoproterozoic average age. Additional geological parameters required to form tungsten deposits include the association with peraluminous and reduced intrusions, and their exposure at the Earth's surface (Candela and Bouton, 1990; Barton, 1996).

Peraluminous melts can result from low melt/rock ratios in the crust that optimize the ability of a melt to either scavenge or accumulate incompatible elements such as tungsten (Cerny et al., 2005). The lowest melt/rock ratios occur when a melt is extracted at low temperature (<700°C) because minerals that accumulate tungsten in the source rocks melt at relatively low temperatures (Yuan et al., 2019). As tungsten is more compatible with minerals present in oxidized lithologies than in reduced lithologies, reduced melts are more effective than oxidized melts at scavenging tungsten (Candela and Bouton, 1990), limiting the ability of oxidized melts to extract tungsten.

In the North American Cordillera, peraluminous plutons were emplaced as an extensive semi-continuous belt (Chapman et al., 2017). The most tungsten-fertile regions of the peraluminous belt have temperatures of melt extraction consistently above 800°C based on zircon saturation temperatures (Fig. 4.4). Therefore, at the Cordillera scale, the temperature of melt extraction is not the primary limiting factor for tungsten mineralization. Reduced intrusive rocks in the CTB, as indicated by the ratio of reduced to oxidized iron, are associated with the largest tungsten deposits (Fig. 4.4) and smaller deposits are associated with less reduced magmas in the Mojave block (Fig. 4.4). Finally, tungsten occurrences are most commonly exposed where the amount of exhumation ranges between 4 and 8 km (mineralization depth; Barton, 1996) but within this range large tungsten systems are only found in the CTB. In summary, the major tungsten deposits in the North American Cordillera are specifically associated with reduced peraluminous magmas derived from sediments with Mesoarchean to Paleoproterozoic T_{DM}.

4.6. Implications

The association between tungsten mineralization and sources of Mesoarchean to Paleoproterozoic average T_{DM} in western North America has important implications for tungsten exploration, and links paleogeographic observations with the geochemical cycling of redox-sensitive elements in ancient Earth. Stable supercontinents lead to extensive periods of chemical weathering that particularly favor tungsten enrichment in continental crust (Romer and Kroner, 2016). The reason for this enrichment is that tungsten is dominantly hosted in minerals with low solubility in surface water (e.g., rutile; Cave et al., 2017). Leaching of other elements through chemical weathering and minimal mechanical transport increases the tungsten concentration in the residual sediment (Romer and Kroner, 2016). Continental breakup then leads to the deposition of tungsten-rich refractory minerals along the passive margin by erosion of the weathered interior of the continent (e.g., Fig. 4.1; Romer and Kroner, 2015). Tungsten enrichment through this process in Atlantic North America and Europe was likely associated with the breakup of the supercontinent Gondwana (Romer and Kroner, 2016). In the North American Cordillera—including the CTB— the isotopic results and paleogeographic context suggest instead a more likely association with the breakup of the supercontinents Columbia and Rodinia. Specifically, between 2.3 and 2.2 Ga, continent evolution went through a quiescent period in terms of magmatism, orogeny and passive margin sedimentation which was followed by the assembly of the supercontinent Columbia between 2.1 and 1.8 Ga (Spencer et al., 2018). The period between 1.8 Ga to 0.8 Ga marks a period of tectonic stability, during which Columbia did not completely disassemble and when the paleogeographic relationships within western North America did not change significantly (Tang et al., 2021). The stratigraphic record of this period within the Canadian Cordillera is represented by the Paleo/Mesoproterozoic Wernecke and Mackenzie Mountains supergroups, both interpreted to have been deposited in epicratonic basins (Gordey and Anderson, 1993). Deposition of the Windermere Supergroup marked the end of this period of tectonic stability (Tang et al., 2021) and the onset of the breakup of Rodinia at the end of the Neoproterozoic (e.g., Moynihan et al., 2019). Paleogeographically, the western edge of North America remained part of a supercontinent from 2.2 to 0.8 Ga, providing an extended quiescent period to enrich tungsten in weathered Archean to Proterozoic crust. Subsequent erosion of these materials during the breakup of Rodinia (Neoproterozoic to early Paleozoic) would have allowed their transport and redeposition as the passive margin sediments that are spatially and isotopically associated with tungsten mineralization in the CTB. Additionally, some paleogeographic reconstructions place the Cathaysia block, the top tungsten producing province worldwide and host to the tungsten-enriched Neoproterozoic Shuangqiaoshan Group in China (Huang and Jiang, 2014), contiguous to the western edge of Laurentia prior to the breakup of Rodinia (Li et al., 2008). The Mesoarchean to Paleoproterozoic was further a dynamic period in Earth's history, characterized by the rise of oxygenic photosynthesis and attendant changes in redox cycling in surface environments (Lyons et al., 2014), as well as continental emergence (Tang et al., 2021). The role of such fundamental changes in pre-enriching tungsten in sediments remains an under constrained topic.

Our data combined with this synthesis suggest that the distribution of much of the tungsten ore deposits in the North American Cordillera was controlled by the Columbian-Rodinian supercontinent cycle and its effects on the concentration of tungsten-enriched reduced source rocks—with a Mesoarchean to Paleoproterozoic average age—along the continental margin.

4.7. Acknowledgments

Kevin Ansdell and an anonymous reviewer for thoughtful comments that helped improve this manuscript. Ehsan Salmabadi for donating some of the samples used in this study. Krystle Moore, Andy DuFrane, Hélène Legros, Adrien Vezinet and Nathan Gerein from University of Alberta for assistance with sample preparation and/or analysis. Polar Continental Shelf Program and North American Tungsten for logistical and in-kind support. Funding from Northwest Territories Geological Survey contribution agreements (PLS), Targeted Geosciences Initiative from Natural Resources Canada GC-130028S (PLS), Natural Sciences and Engineering Resources Canada Discovery grant (PLS) and the Polar Continental Shelf Program.

4.8. References

Arndt, N. T., & Goldstein, S. L. (1987). Use and abuse of crust-formation ages. Geology, 15(10), 893-895.

Barton, M. D. (1996). Granitic magmatism and metallogeny of southwestern North America. Earth and Environmental Science Transactions of the Royal Society of Edinburgh, 87(1-2), 261-280.

Bennett, V. C., & DePaolo, D. J. (1987). Proterozoic crustal history of the western United States as determined by neodymium isotopic mapping. Geological Society of America Bulletin, 99(5), 674-685.

Blusson, S. L. (1968). Geology and tungsten deposits near the headwaters of Flat River, Yukon Territory and southwestern district of Mackenzie, Canada (Vol. 67, No. 22). Department of Energy, Mines and Resources

Estève, C., Audet, P., Schaeffer, A. J., Schutt, D. L., Aster, R. C., & Cubley, J. F. (2020). Seismic evidence for craton chiseling and displacement of lithospheric mantle by the Tintina fault in the northern Canadian Cordillera. Geology, 48(11), 1120-1125.

Candela, P. A., & Bouton, S. L. (1990). The influence of oxygen fugacity on tungsten and molybdenum partitioning between silicate melts and ilmenite. Economic Geology, 85(3), 633-640.

Cave, B.J., Pitcairn, I.K., Large, R.R., Thompson, J.M. and Johnson, S.C. (2017) A metamorphic mineral source for tungsten in the turbidite-hosted orogenic gold deposits of the Otago Schist, New Zealand. Mineralium Deposita, 52, 515-537.

Cerny, P., Blevin, P. L., Cuney, M., & London, D. (2005). Granite-related ore deposits. Economic Geology, 100, 337-370.

Chapman, J. B., Ducea, M. N., Kapp, P., Gehrels, G. E., & DeCelles, P. G. (2017). Spatial and temporal radiogenic isotopic trends of magmatism in Cordilleran orogens. Gondwana Research, 48, 189-204.

European Commission (2020). Study on the EU's list of Critical Raw Materials. https://rmis.jrc.ec.europa.eu/uploads/CRM_2020_Report_Final.pdf

Gaschnig, R. M., Vervoort, J. D., Lewis, R. S., & Tikoff, B. (2011). Isotopic evolution of the Idaho batholith and Challis intrusive province, northern US Cordillera. Journal of Petrology, 52(12), 2397-2429.

Gebru, A. L. (2017). Petrogenesis of Granitoids in the Vicinity of the Mactung Tungsten Skarn Deposit, NE Yukon-Northwest Territories: Characterization of Skarn Mineralization and Causative Plutons through Geological, Petrochemical, Mineralogical, and Geochronological Analysis. Unpublished PhD Thesis University of New Brunswick, New Brunswick, Canada.

Gordey, S. P., & Anderson, R. G. (1993). Evolution of the northern Cordilleran miogeocline, Nahanni map area (105I), Yukon and Northwest Territories. Geological Survey of Canada Memoir 428, 214p.

Guan, D., Wang, D., Hallegatte, S., Davis, S. J., Huo, J., Li, S., Bai, Y., Lei, T., Xue, Q., Coffman, D'M., Cheng, D., Chen, P., Liang, X., Xu, B., Lu, Xiaosheng, Wang, S., Hubacek, K., & Gong, P. (2020). Global supply-chain effects of COVID-19 control measures. Nature Human Behaviour, 4(6), 577-587.

Hart, C. J., Mair, J. L., Goldfarb, R. J., & Groves, D. I. (2004). Source and redox controls on metallogenic variations in intrusion-related ore systems, Tombstone-Tungsten Belt, Yukon Territory, Canada. Earth and Environmental Science Transactions of The Royal Society of Edinburgh, 95(1-2), 339-356.

Huang, L.C., Jiang, S.Y. (2014) Highly fractionated S-type granites from the giant Dahutang tungsten deposit in Jiangnan Orogen, Southeast China: geochronology, petrogenesis and their relationship with W-mineralization. Lithos, 202, 207-226.

Karl, N. A., Burger, T. R., Knudsen, M. H., Long, L. D., Reyes, K. R., & TA Schmeda, G. (2020). Tungsten deposits in the United States (ver. 2.0, August 2020). U.S. Geological Survey data release, https://doi.org/10.5066/P97NJLI4.

Lemmon, D. M. (1941). Tungsten Deposits in the Tungsten Hills, Inyo County, California. US Government Printing Office.

Lyons, T. W., Reinhard, C. T., & Planavsky, N. J. (2014). The rise of oxygen in Earth's early ocean and atmosphere. Nature, 506(7488), 307-315.

Kletzin, A., & Adams, M. W. (1996). Tungsten in biological systems. FEMS Microbiology Reviews, 18(1), 5-63.

Li, Z. X., Bogdanova, S., Collins, A. S., Davidson, A., De Waele, B., Ernst, R. E., ... & Vernikovsky, V. (2008). Assembly, configuration, and break-up history of Rodinia: a synthesis. Precambrian research, 160(1-2), 179-210.

Morris, G. A., & Creaser, R. A. (2008). Correlation of mid-Cretaceous granites with source terranes in the northern Canadian Cordillera. Canadian Journal of Earth Sciences, 45(3), 389-403.

Moynihan, D. P., Strauss, J. V., Nelson, L. L. & Padget, C. D. (2019). Upper Windermere Supergroup and the transition from rifting to continent-margin sedimentation, Nadaleen River area, northern Canadian Cordillera. GSA Bulletin (2019) 131 (9-10): 1673–1701. https://doi.org/10.1130/B32039.1.

Rasmussen, K. L., Lentz, D. R., Falck, H., & Pattison, D. R. (2011). Felsic magmatic phases and the role of late-stage aplitic dykes in the formation of the world-class Cantung Tungsten skarn deposit, Northwest Territories, Canada. Ore Geology Reviews, 41(1), 75-111.

Romer, R. L., & Kroner, U. (2015). Sediment and weathering control on the distribution of Paleozoic magmatic tin–tungsten mineralization. Mineralium Deposita, 50(3), 327-338.

Romer, R. L., & Kroner, U. (2016). Phanerozoic tin and tungsten mineralization—tectonic controls on the distribution of enriched protoliths and heat sources for crustal melting. Gondwana Research, 31, 60-95.

Scanlan, E.J., Scott, J.M., Wilson, V.J., Stirling, C.H., Reid M.R., Le Roux, P.J. (2018) In situ 87Sr/86Sr of scheelite and calcite reveals proximal and distal fluid-rock interaction during orogenic W-Au mineralization, Otago schist, New Zealand. Economic Geology, 113(7), 1571-1586.

Simandl, L., Simandl, G. J., & Paradis, S. (2021). Economic Geology Models 5. Specialty, Critical, Battery, Magnet and Photovoltaic Materials: Market Facts, Projections and Implications for Exploration and Development. Geoscience Canada: Journal of the Geological Association of Canada/Geoscience Canada: journal de l'Association Géologique du Canada, 48(2), 73-92.

Spencer, C. J., Murphy, J. B., Kirkland, C. L., Liu, Y., & Mitchell, R. N. (2018). A Palaeoproterozoic tectono-magmatic lull as a potential trigger for the supercontinent cycle. Nature Geoscience, 11(2), 97-101.

Tang, M., Chu, X., Hao, J. & Shen, B. (2021) Orogenic quiescence in Earth's middle age. Science, 371, 728-731.

Werner, A.B.T., Sinclair, W.D., and Amey, E.B., 2014, International strategic mineral issues summary report—Tungsten (ver. 1.1, November 2014): U.S. Geological Survey Circular 930–O, 74 p., https://pubs.usgs.gov/circ/0930/o/. [Supersedes version 1.0 published in 1998; revisions in 2014 by John H. DeYoung, Jr., and Kim B. Shedd.]

Whitmeyer, S. J., & Karlstrom, K. E. (2007). Tectonic model for the Proterozoic growth of North America. Geosphere, 3(4), 220-259.

Yuan, S., Williams-Jones, A. E., Romer, R. L., Zhao, P., & Mao, J. (2019). Protolith-related thermal controls on the decoupling of Sn and W in Sn-W metallogenic provinces: Insights from the Nanling region, China. Economic Geology, 114(5), 1005-1012.

4.9. Figures

Figure 4.1. (***Next page***) Distribution of tungsten deposits in the North American Cordillera and their relationship to basement rocks from literature compilation. Tungsten deposits are classified by size with 1 (Cantung) and 2 (Mactung) representing two of the largest deposits in North America. The two largest tungsten provinces are identified and further enlarged and labeled in Fig. 4.4. The basement domains are drafted from Whitmeyer and Karlstrom (2007), with the "Mackenzie craton + Canadian shield" field from Esteve et al. (2020) considered to be ancient (cold) crust based in geophysical data and separated by a brown dashed line. The white areas are regions where the basement is unconstrained. Trends in Nd isotopic composition are for Mesozoic to Cenozoicigneous rocks and are constructed from data from Morris and Creaser (2008) and Chapman et al. (2017). Details on data plotted are provided in Appendix B.4. Map projection: NAD 83 / UTM.

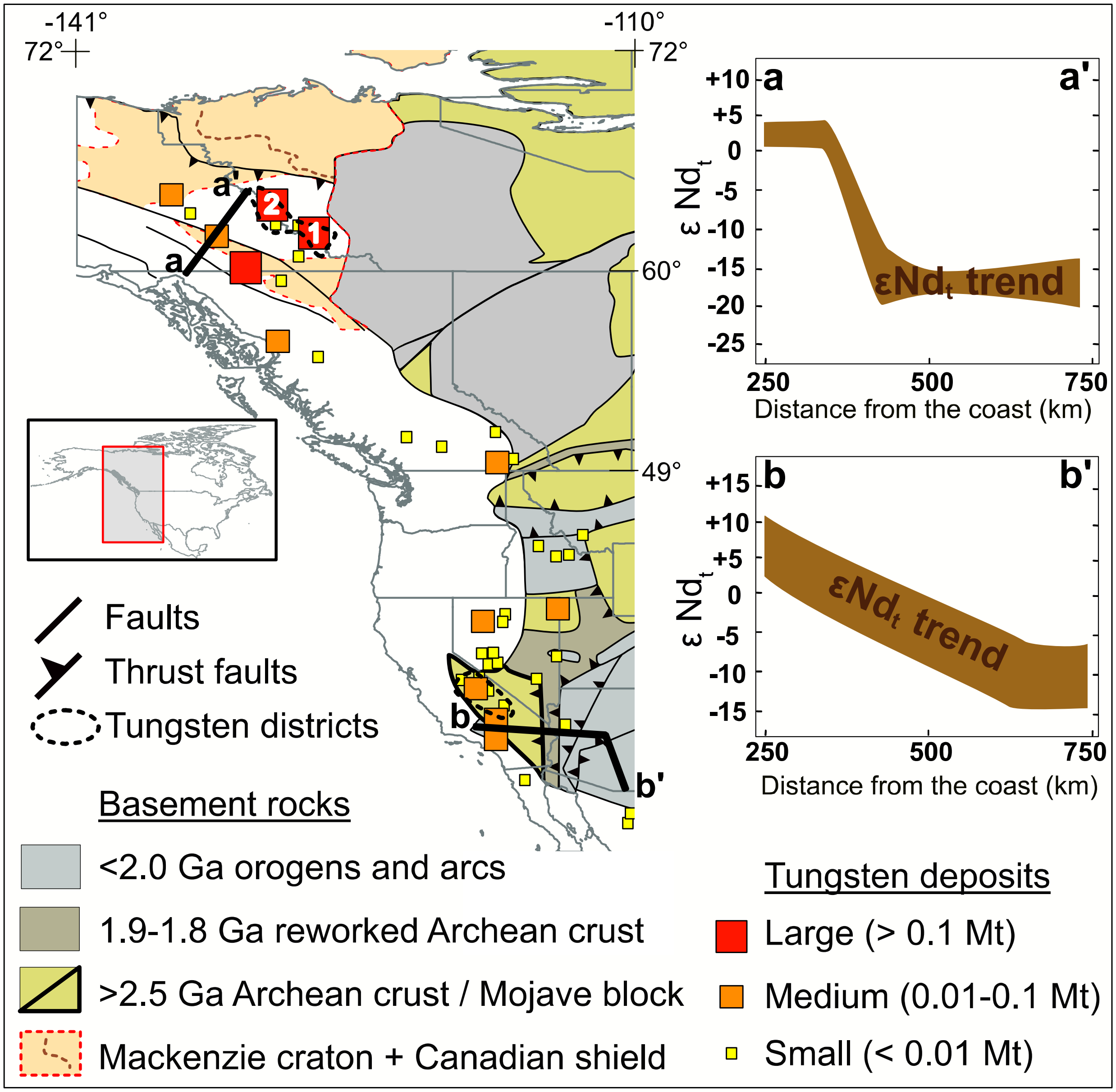
-141°
72°
-110°
72°
60°
49°
a
a'
b
b'
1
2
+10
+5
0
-5
-10
-15
-20
-25
ε Nd_t
εNd_t trend
250
500
750
Distance from the coast (km)
+15
+10
+5
0
-5
-10
-15
Faults
Thrust faults
Tungsten districts
Basement rocks
<2.0 Ga orogens and arcs
1.9-1.8 Ga reworked Archean crust
>2.5 Ga Archean crust / Mojave block
Mackenzie craton + Canadian shield
Tungsten deposits
Large (> 0.1 Mt)
Medium (0.01-0.1 Mt)
Small (< 0.01 Mt)

Figure 4.2. Location of the Canadian Tungsten Belt (CTB) and geologic maps of the Cantung (a) and Mactung (b) deposit areas. Geologic maps are modified from Blusson (1968) and Gebru (2017), respectively.

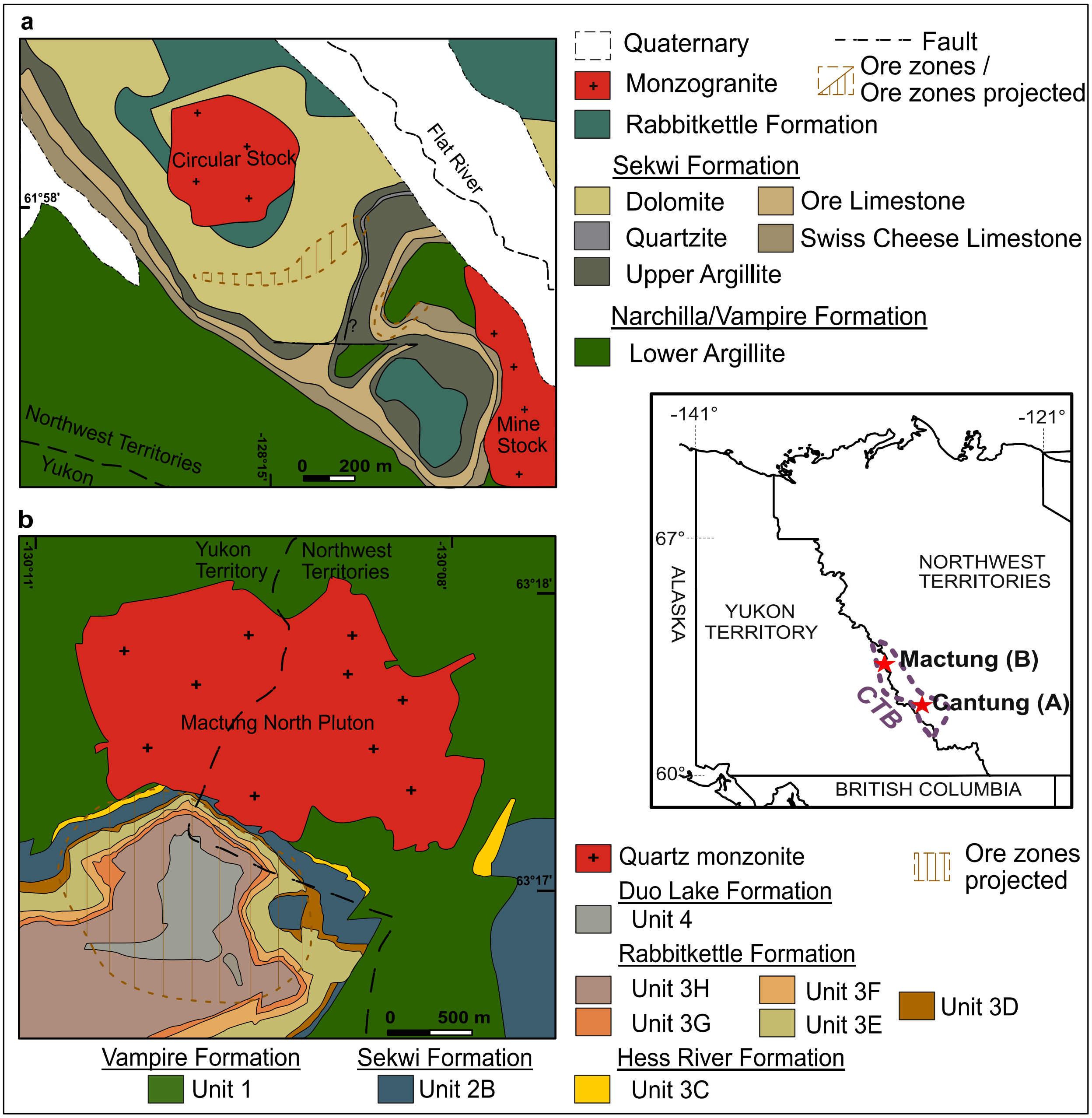

Figure 4.3. εNd at time of formation (t) for scheelite, and local and regional lithologies in the Canadian Cordillera. Triangles and diamonds represent data compiled from the literature, and squares and circles are data acquired in this study. The trends correspond to the εNd evolution of North American crust with Grenville, Paleoproterozoic and Archean T_{DM} respectively; Grenville data obtained south of the Mojave Block (Bennet and DePaolo, 1987). Sampling and methodology for this study are provided in Appendices B.2 & B.3; data and sources are provided in Appendix B.4. Data acquired in this study are also presented in Figure B.1 (Appendix B) and in Tables B.2 & B.3 (Appendix B).

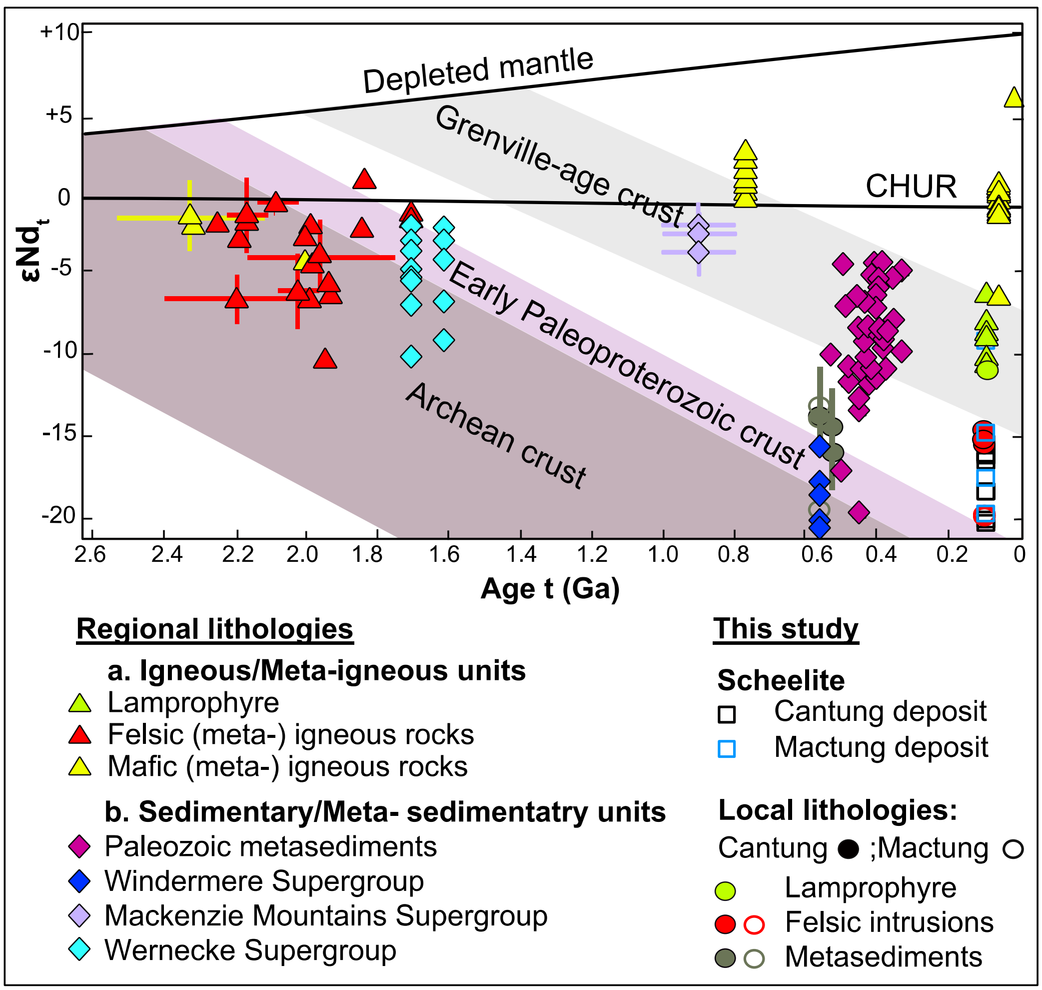

Figure 4.4. Oxidation state (OS) and zircon saturation temperatures (ZST) of peraluminous granites in the Canadian Tungsten Belt (a & b) and Tungsten Hills District of Nevada/California (c & d). Basement rocks and tungsten deposit symbols as in Figure 1. OS data are based on FeO/Fe_2O_3 whole rock ratios. Pie charts represent the relative frequency of OS and ZST obtained from whole rock in specific plutons. Original sources are provided in Appendix B.4 and in Table B.4 (Appendix B).

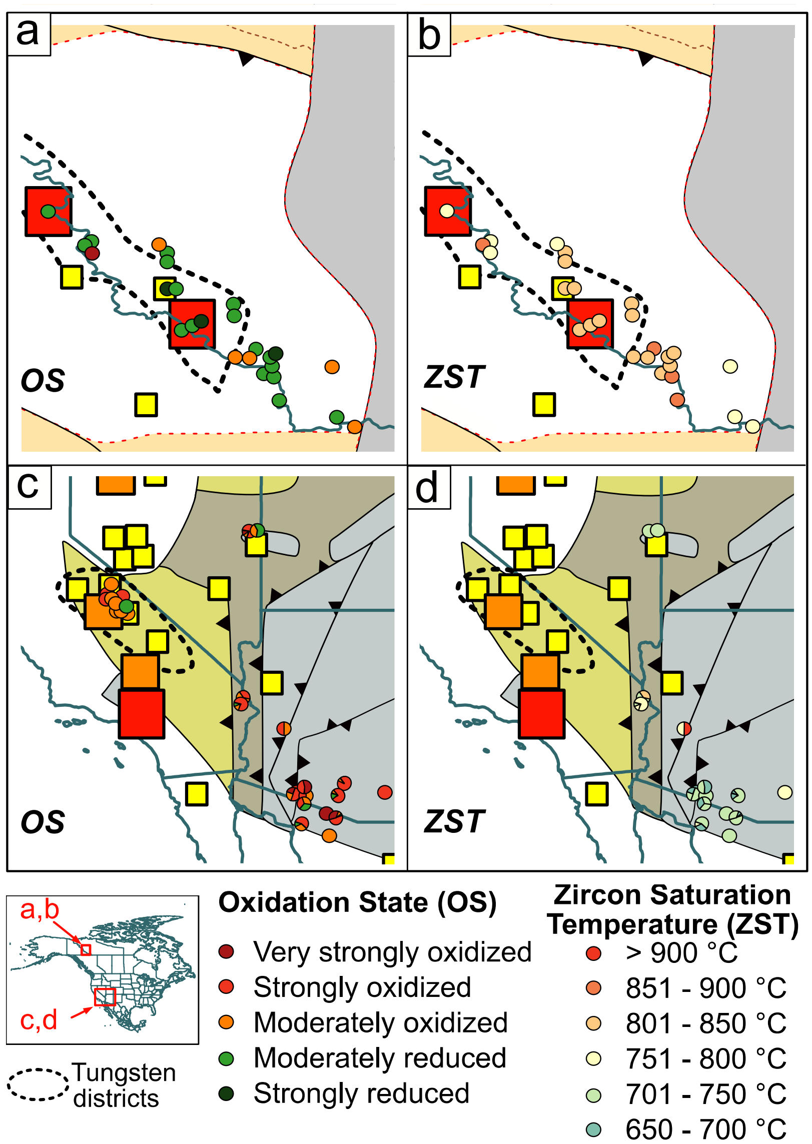

Chapter 5: Conclusions

5.1. Summary

This PhD research aimed to constrain the parameters that control major tungsten mineralization in the Canadian Cordillera, and to distinguish the most prominent parameters that can be applicable to other major tungsten endowments in the entire North American Cordillera.

This study showed that the high-grade tungsten skarn deposits from the Canadian Cordillera have a mineralogy that is indicative of a reduced environment of formation, which is compatible with previous studies that demonstrated that reduced environments tend to form the most significant tungsten deposits. Additionally, this study provided textural evidence that the main tungsten-bearing mineral, scheelite $CaWO_4$, although occurring at all stages of hydrothermal alteration, had peaks of precipitation at specific stages depending on the deposit. Also, the preferential distribution of scheelite within the host rock was controlled by the permeability and porosity of the host rock. Furthermore, strontium isotopes and chemical variations of host rocks at the Cantung and Mactung deposits in the Canadian Cordillera provide a proxy for fluid-rock interaction in these tungsten skarn systems. The preferential distribution of scheelite only in the carbonate-rich regions of the originally impure host rock suggests a lithologic control in the precipitation of scheelite, and highlights the decisive effect of fluid-rock interaction in the genesis of the deposits. Strontium isotopes further support a contribution from both the adjacent granitoids and the country rocks to the ore fluids and suggest the involvement of crust-derived fluids only. Therefore, the interaction of the ore fluids, most likely exsolved from the adjacent crust-derived intrusive bodies, with the country rocks is responsible for the tungsten mineralization at the Cantung and Mactung deposits.

Finally, data from this study, combined with data from previous studies, suggest that the distribution of much of the tungsten deposits in the North American Cordillera is related to the breakup of the Columbia and Rodinia supercontinents, and their associated reduced tungsten-rich sediments sourced from materials of Mesoarchean to Paleoproterozoic average age. Subsequent orogenesis provided the heat necessary to melt these reduced tungsten-rich sediments, forming melts that efficiently extracted tungsten and eventually formed the largest tungsten deposits found in the Canadian Cordillera and in North America.

Scheelite-bearing skarn systems are a major global source of tungsten and their genesis requires the interaction of a crust-derived fluid with limestone-rich rocks. The composition of skarn minerals reflects the redox state of the system. The redox state of the large deposits from the Canadian Cordillera is consistent with reduced magmas being more efficient than oxidized magmas at extracting tungsten from the source rock. The source rocks from which the tungsten-rich melts originate are critical as they control first order parameters such as the primary total tungsten content and the redox state of these melts, which in turn controls the efficiency of tungsten extraction. In the case of the North American Cordillera, Mesoarchean to Paleoproterozoic basement rocks seem to be the best targets for large tungsten endowments. Future exploration for tungsten skarn resources in the Cordillera could be guided by basement rocks of that age and derived magmatism.

Strontium and neodymium isotopes have proven to be effective at tracking fluid-rock interactions and fluid sources in tungsten skarns from the Canadian Cordillera. These methods can be effectively applied not only to other tungsten skarn deposits but also to other deposit types.

5.2. Future directions

The Canadian Cordillera provides an ideal framework to study the genesis and hydrothermal evolution of tungsten-rich systems. Further investigations should focus on refining known genetic models, which will be valuable to the advancement of research on tungsten systems and to exploration for tungsten resources.

Despite the large numbers of studies that focused on tungsten deposits from the Canadian Cordillera, the source of magmatism associated with these deposits remains debated. A better understanding of the genesis of the granitoid magmas from which the ore fluids were sourced is crucial to a better understanding of these large tungsten deposits. This would not only benefit the advancement of research on tungsten deposits from the Canadian Cordillera but also other tungsten provinces in the world with a similar geologic context.

In addition, most studies that try to constrain the age of tungsten mineralization rely on the analysis of gangue minerals, which are not always coeval with the ore mineral. Moreover, most of these studies fail to capture the continuous and protracted history of precipation of the ore mineral, which is an important parameter in the understanding of the lifespan of these systems. Hence, the direct dating of tungsten-bearing minerals is key to the advancement of our knowledge of these tungsten systems. The development of more accurate and precise in situ dating techniques of tungsten minerals, with matrix-matched standards, is essential to reach that goal.

References

Abraham, A. C., Francis, D., & Polvé, M. (2001). Recent alkaline basalts as probes of the lithospheric mantle roots of the northern Canadian Cordillera. Chemical Geology, 175(3-4), 361-386.

Adlakha, E., Hanley, J., Falck, H., & Boucher, B. (2018). The origin of mineralizing hydrothermal fluids recorded in apatite chemistry at the Cantung W–Cu skarn deposit, NWT, Canada. European Journal of Mineralogy, 30(6), 1095-1113.

Archibald, D. A., Clark, A. H., Farrar, E., & Zaw, U. K. (1978). Potassium–argon ages of intrusion and scheelite mineralization, Cantung, Tungsten, Northwest Territories. Canadian Journal of Earth Sciences, 15(7), 1205-1207.

Armstrong, R. L., & Clark, S. P. (1988). Mesozoic and early Cenozoic magmatic evolution of the Canadian Cordillera. Geological Society of America Special Paper, 218, 55-91.

Arndt, N. T., & Goldstein, S. L. (1987). Use and abuse of crust-formation ages. Geology, 15(10), 893-895.

Atkinson, D., & Baker, D.J. (1986). Recent developments in the geologic understanding of Mactung. Mineral Deposits of the Northern Cordillera. Canadian Institute of Mining, Metallurgy and Petroleum, 37, 234-244.

Audétat, A. (2019). The metal content of magmatic-hydrothermal fluids and its relationship to mineralization potential. Economic Geology, 114(6), 1033-1056.

Barton, M. D. (1996). Granitic magmatism and metallogeny of southwestern North America. Earth and Environmental Science Transactions of the Royal Society of Edinburgh, 87(1-2), 261-280.

Bateman, P. C., Pakiser, L. C., & Kane, M. F. (1965). Geology and tungsten mineralization of the Bishop district, California, with a section on gravity study of Owens Valley and a section on seismic profile (No. 470). US Govt. Print. Off., 208p.

Bell, K., Anglin, C. D., & Franklin, J. M. (1989). Sm-Nd and Rb-Sr isotope systematics of scheelites: Possible implications for the age and genesis of vein-hosted gold deposits. Geology, 17(6), 500-504.

Bennett, V. C., & DePaolo, D. J. (1987). Proterozoic crustal history of the western United States as determined by neodymium isotopic mapping. Geological Society of America Bulletin, 99(5), 674-685.

Best, M. G., & Brimhall, W. H. (1974). Late Cenozoic alkalic basaltic magmas in the western Colorado Plateaus and the Basin and Range transition zone, USA, and their bearing on mantle dynamics. Geological Society of America Bulletin, 85(11), 1677-1690.

Blevin, P. L. (2004). Redox and compositional parameters for interpreting the granitoid metallogeny of eastern Australia: Implications for gold-rich ore systems. Resource Geology, 54(3), 241-252.

Blusson, S. L. (1968). Geology and tungsten deposits near the headwaters of Flat River, Yukon Territory and southwestern district of Mackenzie, Canada (Vol. 67, No. 22). Department of Energy, Mines and Resources.

Bowman, J. R., Covert, J. J., Clark, A. H., & Mathieson, G. A. (1985). The CanTung E Zone scheelite skarn orebody, Tungsten, Northwest Territories; oxygen, hydrogen, and carbon isotope studies. Economic Geology, 80(7), 1872-1895.

Brown, P. E., & Essene, E. J. (1985). Activity variations attending tungsten skarn formation, Pine Creek, California. Contributions to Mineralogy and Petrology, 89(4), 358-369.

Brugger, J., Maas, R., Lahaye, Y., McRae, C., Ghaderi, M., Costa, S., Lambert, D., Bateman, R., & Prince, K. (2002). Origins of Nd–Sr–Pb isotopic variations in single scheelite grains from Archaean gold deposits, Western Australia. Chemical Geology, 182(2-4), 203-225.

Burnard, P. G., & Polya, D. A. (2004). Importance of mantle derived fluids during granite associated hydrothermal circulation: He and Ar isotopes of ore minerals from Panasqueira. Geochimica et Cosmochimica Acta, 68(7), 1607-1615.

Burton, J. C., & Taylor, L. A. (1982). The fO_2-T and $f S_2$-T stability relations of hedenbergite and of hedenbergite-johannsenite solid solutions. Economic Geology, 77(4), 764-783.

Candela, P. A. (1992). Controls on ore metal ratios in granite-related ore systems: an experimental and computational approach. Earth and Environmental Science Transactions of the Royal Society of Edinburgh, 83(1-2), 317-326.

Candela, P. A., & Bouton, S. L. (1990). The influence of oxygen fugacity on tungsten and molybdenum partitioning between silicate melts and ilmenite. Economic Geology, 85(3), 633-640.

Cave, B.J., Pitcairn, I.K., Large, R.R., Thompson, J.M. and Johnson, S.C. (2017) A metamorphic mineral source for tungsten in the turbidite-hosted orogenic gold deposits of the Otago Schist, New Zealand. Mineralium Deposita, 52, 515-537.

Cerny, P., Blevin, P. L., Cuney, M., & London, D. (2005). Granite-related ore deposits. Economic Geology, 100, 337-370.

Chapman, J. B., Ducea, M. N., Kapp, P., Gehrels, G. E., & DeCelles, P. G. (2017). Spatial and temporal radiogenic isotopic trends of magmatism in Cordilleran orogens. Gondwana Research, 48, 189-204.

Chapman, J. B., Runyon, S. E., Shields, J., Lawler, B. L., Pridmore, C. J., Scoggin, S. H., Swaim, N.T., Trzinski, A.E., Wiley, H.N., Barth, A.P., & Haxel, G. B. (2021). The North American Cordilleran Anatectic Belt. Earth-Science Reviews, 215, 103576.

Chappell, B. W., & White, A. J. R. (1992). I-and S-type granites in the Lachlan Fold Belt. Earth and Environmental Science Transactions of the Royal Society of Edinburgh, 83(1-2), 1-26.

Chivas, A. R., Andrew, A. S., Sinha, A. K., & O'Neil, J. R. (1982). Geochemistry of a Pliocene–Pleistocene oceanic-arc plutonic complex, Guadalcanal. Nature, 300(5888), 139-143.

Cousens, B. L. (2007). Radiogenic isotope studies of Pb-Zn mineralization in the Howards Pass area, Selwyn Basin. Mineral and Energy Resource Potential of the Proposed Expansion to the Nahanni National Park Reserve, North Cordillera, Northwest Territories: Geological Survey of Canada, Open File, 5344, 14.

Cousens, B. L., & Bevier, M. L. (1995). Discerning asthenospheric, lithospheric, and crustal influences on the geochemistry of Quaternary basalts from the Iskut–Unuk rivers area, northwestern British Columbia. Canadian Journal of Earth Sciences, 32(9), 1451-1461.

Creaser, R. A., Erdmer, P., Stevens, R. A., & Grant, S. L. (1997). Tectonic affinity of Nisutlin and Anvil assemblage strata from the Teslin tectonic zone, northern Canadian Cordillera: Constraints from neodymium isotope and geochemical evidence. Tectonics, 16(1), 107-121.

Cummings, W. W., & Bruce, D. E. (1977). Canada Tungsten–Change to underground mining and description of mine-mill procedures. Canada Mining and Metallurgy Bulletin, 70, 94-101.

Dawson, K.M., Panteleyev, A., Sutherland Brown, A., and Woodsworth. G.J. (1991). Regional metallogeny (Chapter 19). In Geology of the Cordilleran Orogeny in Canada. (H. Gabrielse and C.J. Yorath, eds.). Geological Survey of Canada, Geology of Canada 4, p. 707-768.

DePaolo, D. J., & Wasserburg, G. J. (1976). Nd isotopic variations and petrogenetic models. Geophysical Research Letters, 3(5), 249-252.

Dick, L. A., & Hodgson, C. J. (1982). The Mactung W-Cu (Zn) contact metasomatic and related deposits of the northeastern Canadian Cordillera. Economic Geology, 77(4), 845-867.

Driver, L. A., Creaser, R. A., Chacko, T., & Erdmer, P. (2000). Petrogenesis of the Cretaceous Cassiar batholith, Yukon–British Columbia, Canada: Implications for magmatism in the North American Cordilleran interior. Geological Society of America Bulletin, 112(7), 1119-1133.

Dubessy, J., Ramboz, C., Nguyen-Trung, C., Cathelineau, M., Charoy, B., Cuney, M., ... & Weisbrod, A. (1987). Physical and chemical controls (fO2, T, pH) of the opposite behaviour of U and Sn-W as examplified by hydrothermal deposits in France and Great-Britain, and solubility data. Bulletin de Minéralogie, 110(2), 261-281.

Dudás, F. Ö., & Lustwerk, R. L. (1997). Geochemistry of the Little Dal basalts: continental tholeiites from the Mackenzie Mountains, Northwest Territories, Canada. Canadian Journal of Earth Sciences, 34(1), 50-58.

Einaudi, M. T. (1981). Skarn deposits. Economic Geology, 75, 317-391.

Einaudi, M. T., & Burt, D. M. (1982). Introduction; terminology, classification, and composition of skarn deposits. Economic Geology, 77(4), 745-754.

Elongo, V., Lecumberri-Sanchez, P., Legros, H., Falck, H., Adlakha, E., & Roy-Garand, A. (2020). Paragenetic constraints on the Cantung, Mactung and Lened tungsten skarn deposits, Canada: Implications for grade distribution. Ore Geology Reviews, 125, 103677.

Estève, C., Audet, P., Schaeffer, A. J., Schutt, D. L., Aster, R. C., & Cubley, J. F. (2020). Seismic evidence for craton chiseling and displacement of lithospheric mantle by the Tintina fault in the northern Canadian Cordillera. Geology, 48(11), 1120-1125.

European Commission (2020). Study on the EU's list of Critical Raw Materials. https://rmis.jrc.ec.europa.eu/uploads/CRM_2020_Report_Final.pdf

Falck, H (2015). Geochemical, Mineralogical and Indicator Mineral Data for Stream Silt Sediment, Heavy Mineral Concentrates and Waters, Flat River area Northwest Territories, (part of NTS 95E, 105H and 105I). NWT Open Report 2015-002.

Fischer, B.J., Martel, E., and Falck, H., (2018). Geology of the Mactung tungsten skarn and area – Review and 2016 field observations; Northwest Territories Geological Survey, NWT Open File 2018-02, 84 pages and appendices.

Fischer, B.J., Martel, E., and Falck, H., (2018). Geology of the Mactung tungsten skarn and area – Review and 2016 field observations; Northwest Territories Geological Survey, NWT Open File 2018-02, 84 pages and appendices.

Fisher, C. M., Vervoort, J. D., & DuFrane, S. A. (2014). Accurate Hf isotope determinations of complex zircons using the “laser ablation split stream” method. Geochemistry, Geophysics, Geosystems, 15(1), 121-139.

Force, E. R. (1997). Geology and mineral resources of the Santa Catalina Mountains, southeastern Arizona: A cross-sectional approach. Earth, Planets and Space, 57(8), 701-715.

Fortier, S. M., Nassar, N. T., Lederer, G. W., Brainard, J., Gambogi, J., & McCullough, E. A. (2018). Draft critical mineral list—Summary of methodology and background information—US Geological Survey technical input document in response to Secretarial Order No. 3359 (No. 2018-1021). US Geological Survey.

Gabrielse, H., & Yorath, C. J. (1991). Geology of the Cordilleran orogen in Canada. Geological Society of America, Volume G2.

Gabrielse, H., Murphy, D. C., Mortensen, J. K., Haggart, J. W., Enkin, R. J., & Monger, J. W. H. (2006). Cretaceous and Cenozoic dextral orogen-parallel displacements, magmatism, and paleogeography, north-central Canadian Cordillera. Paleogeography of the North American Cordillera: Evidence For and Against Large-Scale Displacements: Geological Association of Canada Special Paper, 46, 255-276.

Gamble, Robert P. "An experimental study of sulfidation reactions involving andradite and hedenbergite." Economic Geology 77.4 (1982): 784-797.

Garzione, C. N., Patchett, P. J., Ross, G. M., & Nelson, J. (1997). Provenance of Paleozoic sedimentary rocks in the Canadian Cordilleran miogeocline: a Nd isotopic study. Canadian Journal of Earth Sciences, 34(12), 1603-1618.

Gaschnig, R. M., Vervoort, J. D., Lewis, R. S., & Tikoff, B. (2011). Isotopic evolution of the Idaho batholith and Challis intrusive province, northern US Cordillera. Journal of Petrology, 52(12), 2397-2429.

Gebru, A. L. (2017). Petrogenesis of Granitoids in the Vicinity of the Mactung Tungsten Skarn Deposit, NE Yukon-Northwest Territories: Characterization of Skarn Mineralization and Causative Plutons through Geological, Petrochemical, Mineralogical, and Geochronological Analysis. Unpublished PhD Thesis University of New Brunswick, New Brunswick, Canada.

Gibert, F., Moine, B., Schott, J., & Dandurand, J. L. (1992). Modeling of the transport and deposition of tungsten in the scheelite-bearing calc-silicate gneisses of the Montagne Noire, France. Contributions to Mineralogy and Petrology, 112(2-3), 371-384.

Glover, J.K. & Burson, M.J. (1987): Geology of the Lened tungsten skarn deposit, Logan Mountains, Northwest Territories. Canadian Institute of Mining, Metallurgy and Petroleum, Special Volume 37, 255-265.

Goldstein, S. L., O'nions, R. K., & Hamilton, P. J. (1984). A Sm-Nd isotopic study of atmospheric dusts and particulates from major river systems. Earth and Planetary Science Letters, 70(2), 221-236.

Goodfellow, W. D., Cecile, M. P., & Leybourne, M. I. (1995). Geochemistry, petrogenesis, and tectonic setting of lower Paleozoic alkalic and potassic volcanic rocks, Northern Canadian Cordilleran Miogeocline. Canadian Journal of Earth Sciences, 32(8), 1236-1254.

Gordey, S. P., & Anderson, R. G. (1993). Evolution of the northern Cordilleran miogeocline, Nahanni map area (105I), Yukon and Northwest Territories. Geological Survey of Canada Memoir 428, 214p.

Government of Northwest Territories (2016). A Guide to Mineral Deposits in the Northwest Territories. https://www.iti.gov.nt.ca/sites/iti/files/mineraldeposites2-nocrops.pdf

Greenwood, R. (1943). Effect of chemical impurities on scheelite fluorescence. Economic Geology 38 (1), 56-64.

Guan, D., Wang, D., Hallegatte, S., Davis, S. J., Huo, J., Li, S., Bai, Y., Lei, T., Xue, Q., Coffman, D'M., Cheng, D., Chen, P., Liang, X., Xu, B., Lu, Xiaosheng, Wang, S., Hubacek, K., &

Gong, P. (2020). Global supply-chain effects of COVID-19 control measures. Nature Human Behaviour, 4(6), 577-587.

Hart, C. J. R. (1997). A transect across Stikinia: Geology of the northern Whitehorse map area, southern Yukon Territory (105D13–16). Exploration and Geological Services Division, Yukon, Indian and Northern Affairs Canada Bulletin 8, 1–112.

Hart, C. J., Mair, J. L., Goldfarb, R. J., & Groves, D. I. (2004). Source and redox controls on metallogenic variations in intrusion-related ore systems, Tombstone-Tungsten Belt, Yukon Territory, Canada. Earth and Environmental Science Transactions of The Royal Society of Edinburgh, 95(1-2), 339-356.

Hawthorne, F. C., Oberti, R., Harlow, G. E., Maresch, W. V., Martin, R. F., Schumacher, J. C., & Welch, M. D. (2012). Nomenclature of the amphibole supergroup. American Mineralogist, 97(11-12), 2031-2048.

Heinrich, C. A., & Candela, P. A. (2014). Fluids and ore formation in the Earth's crust. In Treatise on Geochemistry (Second Edition) (Vol. 13, pp. 1-28). Elsevier.

Hsieh, P. S., Chen, C. H., Yang, H. J., & Lee, C. Y. (2008). Petrogenesis of the Nanling Mountains granites from South China: constraints from systematic apatite geochemistry and whole-rock geochemical and Sr–Nd isotope compositions. Journal of Asian Earth Sciences, 33(5-6), 428-451.

Hsu, L. C. (1977). Effects of oxygen and sulfur fugacities on the scheelite-tungstenite and powellite-molybdenite stability relations. Economic Geology, 72(4), 664-670.

Hsu, L. C., & Galli, P. E. (1973). Origin of the scheelite-powellite series of minerals. Economic Geology, 68(5), 681-696.

Hu, R. Z., Bi, X. W., Jiang, G. H., Chen, H. W., Peng, J. T., Qi, Y. Q., ... & Wei, W. F. (2012). Mantle-derived noble gases in ore-forming fluids of the granite-related Yaogangxian tungsten deposit, Southeastern China. Mineralium Deposita, 47(6), 623-632.

Huang, L.C., Jiang, S.Y. (2014) Highly fractionated S-type granites from the giant Dahutang tungsten deposit in Jiangnan Orogen, Southeast China: geochronology, petrogenesis and their relationship with W-mineralization. Lithos, 202, 207-226.

Hulsbosch, N., Boiron, M. C., Dewaele, S., & Muchez, P. (2016). Fluid fractionation of tungsten during granite–pegmatite differentiation and the metal source of peribatholitic W quartz veins: Evidence from the Karagwe-Ankole Belt (Rwanda). Geochimica et Cosmochimica Acta, 175, 299-318.

Ishihara, S. (1977). The magnetite-series and ilmenite-series granitic rocks. Mining Geology, 27(145), 293-305.

Jacobsen, S. B., & Wasserburg, G. J. (1980). Sm-Nd isotopic evolution of chondrites. Earth and Planetary Science Letters, 50(1), 139-155.

John, B. E., & Wooden, J. (1990). Petrology and geochemistry of the metaluminous to peraluminous Chemehuevi Mountains Plutonic Suite, southeastern California. The Nature and Origin of Cordilleran Magmatism. Geological Society of America, Memoir, 174, 71-98.

Kamvong, T., & Zaw, K. (2009). The origin and evolution of skarn-forming fluids from the Phu Lon deposit, northern Loei Fold Belt, Thailand: evidence from fluid inclusion and sulfur isotope studies. Journal of Asian Earth Sciences, 34(5), 624-633.

Karl, N. A., Burger, T. R., Knudsen, M. H., Long, L. D., Reyes, K. R., & TA Schmeda, G. (2020). Tungsten deposits in the United States (ver. 2.0, August 2020). U.S. Geological Survey data release, https://doi.org/10.5066/P97NJLI4.

Kato, Y. (1999). Rare Earth Elements as an Indicator to Origins of Skarn Deposits: Examples of the Kamioka Zn-Pb and Yoshiwara-Sannotake Cu (–Fe) Deposits in Japan. Resource Geology, 49(4), 183-198.

Keith, S. B., & Reynolds, S. J. (1980). Geochemistry of Cordilleran metamorphic core complexes. Cordilleran metamorphic core complexes and their uranium favorability: US Department of Energy Open-File Report GJBX-256 (80), 321.

Kempe, U., Belyatsky, B., Krymsky, R., Kremenetsky, A., & Ivanov, P. (2001). Sm–Nd and Sr isotope systematics of scheelite from the giant Au (–W) deposit Muruntau (Uzbekistan): implications for the age and sources of Au mineralization. Mineralium Deposita, 36(5), 379-392.

Kletzin, A., & Adams, M. W. (1996). Tungsten in biological systems. FEMS Microbiology Reviews, 18(1), 5-63.

Kozlik, M., Gerdes, A., & Raith, J. G. (2016). Strontium isotope systematics of scheelite and apatite from the Felbertal tungsten deposit, Austria–results of in-situ LA-MC-ICP-MS analysis. Mineralogy and Petrology, 110(1), 11-27.

Kwak, T. A. (1994). Hydrothermal alteration in carbonate-replacement deposits. Geol. Assoc. Canada, Short Course Notes, 11, 381-402.

Kwak, T. A. P. (1986). Fluid inclusions in skarns (carbonate replacement deposits). Journal of Metamorphic Geology, 4(4), 363-384.

Kwak, T. A. P. (1987). W-Sn skarn deposits and related metamorphic skarns and granitoids. Amsterdam: Elsevier.

Kwak, T. A. P., & Tan, T. H. (1981). The geochemistry of zoning in skarn minerals at the King Island (Dolphin) mine. Economic Geology, 76(2), 468-497.

Lake, D. J., Groat, L. A., Falck, H., Mulja, T., Cempírek, J., Kontak, D., Marshall, D., Giuliani, G., & Fayek, M. (2017). Genesis of emerald-bearing quartz veins associated with the Lened W-skarn mineralization, Northwest Territories, Canada. The Canadian Mineralogist, 55(4), 561-593.

Lecumberri-Sanchez, P., Vieira, R., Heinrich, C. A., Pinto, F., & Wälle, M. (2017). Fluid-rock interaction is decisive for the formation of tungsten deposits. Geology, 45(7), 579-582.

Lee, D. E., & Van Loenen, R. E. (1971). Hybrid granitoid rocks of the southern Snake Range, Nevada (pp. 1-46). US Government Printing Office.

Lee, D. E., Kistler, R. W., Friedman, I., & Van Loenen, R. E. (1981). Two-mica granites of northeastern Nevada. Journal of Geophysical Research: Solid Earth, 86(B11), 10607-10616.

Legros, H., Lecumberri-Sanchez, P., Elongo, V., Laurent, O., Falck, H., Adlakha, E., & Chelle-Michou, C. (2020). Fluid evolution of the Cantung tungsten skarn, Northwest Territories, Canada: Differentiation and fluid-rock interaction. Ore Geology Reviews, 103866.

Legros, H., Richard, A., Tarantola, A., Kouzmanov, K., Mercadier, J., Vennemann, T., ... & Bailly, L. (2019). Multiple fluids involved in granite-related W-Sn deposits from the world-class Jiangxi province (China). Chemical Geology, 508, 92-115.

Lemmon, D. M. (1941). Tungsten Deposits in the Tungsten Hills, Inyo County, California. US Government Printing Office.

Lentz, C. (2020). Genesis of Gold Mineralization at the Cantung W-Cu skarn deposit, N.W.T. Unpublished MSc Thesis, University of New Brunswick, New Brunswick, Canada.

Li, Z. X., Bogdanova, S., Collins, A. S., Davidson, A., De Waele, B., Ernst, R. E., ... & Vernikovsky, V. (2008). Assembly, configuration, and break-up history of Rodinia: a synthesis. Precambrian research, 160(1-2), 179-210.

Locock, A. J. (2008). An Excel spreadsheet to recast analyses of garnet into end-member components, and a synopsis of the crystal chemistry of natural silicate garnets. Computers & Geosciences, 34(12), 1769-1780.

Locock, A. J. (2014). An Excel spreadsheet to classify chemical analyses of amphiboles following the IMA 2012 recommendations. Computers & Geosciences, 62, 1-11.

Luo, Y., Pearson, D.G., Scott, J., Palmer, M.C., Fisher, C.M., Sarkar, C., Vezinet, A., Lecumberri-Sanchez, P., 2019. Simultaneous In situ Analysis of Sm-Nd isotopes and Trace Elements in Scheelite by Laser Ablation Split Stream ICP-MS: Challenges and Emerging Approaches., 2019 North America laser ablation workshop, Austin, p. 34.

Lyons, T. W., Reinhard, C. T., & Planavsky, N. J. (2014). The rise of oxygen in Earth’s early ocean and atmosphere. Nature, 506(7488), 307-315.

Magnall, J. M., Gleeson, S. A., Stern, R. A., Newton, R. J., Poulton, S. W., & Paradis, S. (2016). Open system sulphate reduction in a diagenetic environment–Isotopic analysis of barite (δ34S and δ18O) and pyrite (δ34S) from the Tom and Jason Late Devonian Zn–Pb–Ba deposits, Selwyn Basin, Canada. Geochimica et Cosmochimica Acta, 180, 146-163.

Mair, J. L., Farmer, G. L., Groves, D. I., Hart, C. J., & Goldfarb, R. J. (2011). Petrogenesis of postcollisional magmatism at Scheelite Dome, Yukon, Canada: evidence for a lithospheric mantle source for magmas associated with intrusion-related gold systems. Economic Geology, 106(3), 451-480.

Markey, R., Stein, H. J., Hannah, J. L., Zimmerman, A., Selby, D., & Creaser, R. A. (2007). Standardizing Re–Os geochronology: a new molybdenite reference material (Henderson, USA) and the stoichiometry of Os salts. Chemical Geology, 244(1-2), 74-87.

Marshall, D. D., Groat, L. A., Falck, H., Giuliani, G., & Neufeld, H. (2004). The Lened Emerald prospect, Northwest Territories, Canada: Insights from fluid inclusions and stable isotopes, with implications for northern Cordilleran Emerald. The Canadian Mineralogist, 42(5), 1523-1539.

Mathieson, G. A., & Clark, A. H. (1984). The Cantung E Zone scheelite skarn orebody, Tungsten, Northwest Territories; a revised genetic model. Economic Geology, 79(5), 883-901.

Meinert, L. D. (1992). Skarns and skarn deposits. Geoscience Canada, 19(4).

Miller, C. F., McDowell, S. M., & Mapes, R. W. (2003). Hot and cold granites? Implications of zircon saturation temperatures and preservation of inheritance. Geology, 31(6), 529-532.

Mollai, H., Pe-Piper, G., & Dabiri, R. (2014). Genetic relationships between skarn ore deposits and magmatic activity in the Ahar region, Western Alborz, NW Iran. Geologica Carpathica, 65(3), 209-227.

Monger, J. W., Nokleberg, W. J., Coyner, A. R., & Fahey, P. L. (1996). Evolution of the northern North American Cordillera: generation, fragmentation, displacement and accretion of successive North American plate-margin arcs. Geology and Ore Deposits of the American Cordillera. Geological Society of Nevada, 1133-1152.

Monger, J., & Price, R. (2002). The Canadian Cordillera: geology and tectonic evolution. CSEG Recorder, 27(2), 17-36.

Morimoto, N. (1988). Nomenclature of pyroxenes. Mineralogy and Petrology, 39(1), 55-76.

Morris, G. A., & Creaser, R. A. (2003). Crustal recycling during subduction at the Eocene Cordilleran margin of North America: a petrogenetic study from the southwestern Yukon. Canadian Journal of Earth Sciences, 40(12), 1805-1821.

Morris, G. A., & Creaser, R. A. (2008). Correlation of mid-Cretaceous granites with source terranes in the northern Canadian Cordillera. Canadian Journal of Earth Sciences, 45(3), 389-403.

Moynihan, D. P., Strauss, J. V., Nelson, L. L. & Padget, C. D. (2019). Upper Windermere Supergroup and the transition from rifting to continent-margin sedimentation, Nadaleen River area, northern Canadian Cordillera. GSA Bulletin (2019) 131 (9-10): 1673–1701. https://doi.org/10.1130/B32039.1.

Nachit, H., Ibhi, A., Abia, E. H., & Ohoud, M. B. (2005). Discrimination between primary magmatic biotites, reequilibrated biotites and neoformed biotites. Comptes Rendus Geoscience, 337(16), 1415-1420.

Nakano, T., Yoshino, T., Shimazaki, H., & Shimizu, M. (1994). Pyroxene composition as an indicator in the classification of skarn deposits. Economic Geology, 89(7), 1567-1580.

Nelson, J. L. and Colpron, M. (2007). Tectonics and metallogeny of the Canadian and Alaskan Cordillera, 1.8 Ga to present, in Goodfellow, W. D., ed., Mineral Deposits of Canada: A Synthesis of Major Deposit Types, District Metallogeny, the Evolution of Geological Provinces, and Exploration Methods: Mineral Deposit Division, Geological Association of Canada, Special Publication 5, p. 755-791.

Newberry, R.J. (1998). W- And Sn-Skarn Deposits: A 1998 Status Report. In Mineralized Intrusion Related Skarn Systems (D.R. Lentz, ed.). Mineralogical Association of Canada Short Course Series, Mineralogical Association of Canada, Quebec City, Quebec (289–335).

Preto, V. A. G. (1972). Geology of Copper Mountain, BC Dept. of Mines and Petroleum Resources. Bulletin, 59.

Preto, V. A., Osatenko, M. J., McMillan, W. J., & Armstrong, R. L. (1979). Isotopic dates and strontium isotopic ratios for plutonic and volcanic rocks in the Quesnel Trough and Nicola Belt, south–central British Columbia. Canadian Journal of Earth Sciences, 16(9), 1658-1672.

Price, R. A., & Carmichael, D. M. (1986). Geometric test for Late Cretaceous-Paleogene intracontinental transform faulting in the Canadian Cordillera. Geology, 14(6), 468-471.

Rainbird, R. H., McNicoll, V. J., Theriault, R. J., Heaman, L. M., Abbott, J. G., Long, D. G. F., & Thorkelson, D. J. (1997). Pan-continental river system draining Grenville Orogen recorded by U-Pb and Sm-Nd geochronology of Neoproterozoic quartzarenites and mudrocks, northwestern Canada. The Journal of Geology, 105(1), 1-17.

Rasmussen, K. L., & Mortensen, J. K. (2013). Magmatic petrogenesis and the evolution of (F: Cl: OH) fluid composition in barren and tungsten skarn-associated plutons using apatite and biotite compositions: Case studies from the northern Canadian Cordillera. Ore Geology Reviews, 50, 118-142.

Rasmussen, K. L., Lentz, D. R., Falck, H., & Pattison, D. R. (2011). Felsic magmatic phases and the role of late-stage aplitic dykes in the formation of the world-class Cantung Tungsten skarn deposit, Northwest Territories, Canada. Ore Geology Reviews, 41(1), 75-111.

Rasmussen, K. L., Mortensen, J. K., Falck, H., & Ullrich, T. D. (2007). The potential for intrusion-related mineralization within the South Nahanni River MERA area, Selwyn and Mackenzie Mountains, Northwest Territories. Mineral and Energy Resource Assessment of the Greater Nahanni Ecosystem Under Consideration for the Expansion of the Nahanni National Park

Reserve, Northwest Territories. Edited by DF Wright, D. Lemkow and JR Harris. Geological Survey of Canada, Open File, 5344, 203-278.

Rasmussen, K.L. (2013) The timing, composition, and petrogenesis of syn- to post-accretionary magmatism in the northern Cordilleran miogeocline, eastern Yukon and southwestern Northwest Territories. Ph.D. Thesis, University of British Columbia, Vancouver, British Columbia, Canada, 788 pp.

Ray, G. E. (2013). A review of skarn in Canadian Cordillera. British Columbia Ministry of Energy and Mines, British Columbia Geological Survey Open File, 8, 50

Rock, N. M. (1987). The nature and origin of lamprophyres: an overview. Geological Society, London, Special Publications, 30(1), 191-226.

Romer, R. L., & Kroner, U. (2015). Sediment and weathering control on the distribution of Paleozoic magmatic tin–tungsten mineralization. Mineralium Deposita, 50(3), 327-338.

Romer, R. L., & Kroner, U. (2016). Phanerozoic tin and tungsten mineralization—tectonic controls on the distribution of enriched protoliths and heat sources for crustal melting. Gondwana Research, 31, 60-95.

Rytuba, J. J. (1985). Geochemistry of hydrothermal transport and deposition of gold and sulfide minerals in Carlin-type gold deposits. US Geological Survey Bulletin, 1646, 27-34.

Sato, K. (1980). Tungsten skarn deposit of the Fujigatani mine, southwest Japan. Economic Geology, 75(7), 1066-1082.

Sato, K. (2012). Sedimentary Crust and Metallogeny of Granitoid Affinity: Implications from the Geotectonic Histories of the Circum-J apan S ea Region, Central A ndes and Southeastern Australia. Resource Geology, 62(4), 329-351.

Sato, K., Kovalenko, S. V., Romanovsky, N. P., Nedachi, M., Berdnikov, N. V., & Ishihara, T. (2004). Crustal control on the redox state of granitoid magmas: tectonic implications from the granitoid and metallogenic provinces in the circum-Japan Sea Region. Earth and Environmental Science Transactions of The Royal Society of Edinburgh, 95(1-2), 319-337.

Scanlan, E. J., Scott, J. M., Wilson, V. J., Stirling, C. H., Reid, M. R., & Le Roux, P. J. (2018). In situ 87Sr/86Sr of scheelite and calcite reveals proximal and distal fluid-rock interaction during orogenic W-Au mineralization, Otago Schist, New Zealand. Economic Geology, 113(7), 1571-1586.

Schmidt, S., Geo, P., & Hutten, W. (2012). From Deposit to Concentrate: The Basis of Tungsten Mining. Part 1: Project Generation and Project Development. International Tungsten Industry Association Newsletter June.

Selby, D., & Creaser, R. A. (2004). Macroscale NTIMS and microscale LA-MC-ICP-MS Re-Os isotopic analysis of molybdenite: Testing spatial restrictions for reliable Re-Os age determinations, and implications for the decoupling of Re and Os within molybdenite. Geochimica et Cosmochimica Acta, 68(19), 3897-3908.

Selby, D., Creaser, R. A., Heaman, L. M., & Hart, C. J. (2003). Re-Os and U-Pb geochronology of the Clear Creek, Dublin Gulch, and Mactung deposits, Tombstone Gold Belt, Yukon, Canada: absolute timing relationships between plutonism and mineralization. Canadian Journal of Earth Sciences, 40(12), 1839-1852.

Seo, J. H., Yoo, B. C., Villa, I. M., Lee, J. H., Lee, T., Kim, C., & Moon, K. J. (2017). Magmatic–hydrothermal processes in Sangdong W–Mo deposit, Korea: Study of fluid inclusions and ^{39}Ar–^{40}Ar geochronology. Ore Geology Reviews, 91, 316-334.

Shanks, W. C., Woodruff, L. G., Jilson, G. A., Jennings, D. S., Modene, J. S., & Ryan, B. D. (1987). Sulfur and lead isotope studies of stratiform Zn-Pb-Ag deposits, Anvil Range, Yukon; basinal brine exhalation and anoxic bottom-water mixing. Economic Geology, 82(3), 600-634.

Shaw, A. L., & Guilbert, J. M. (1990). Geochemistry and metallogeny of Arizona peraluminous granitoids with reference to Appalachian and European occurrences. Ore-bearing granite systems: petrogenesis and mineralizing processes. Geological Society of America, Special Paper, 246, 317-356.

Shimazaki, H. I. D. E. H. I. K. O. (1980). Characteristics of skarn deposits and related acid magmatism in Japan. Economic Geology, 75(2), 173-183.

Simandl, L., Simandl, G. J., & Paradis, S. (2021). Economic Geology Models 5. Specialty, Critical, Battery, Magnet and Photovoltaic Materials: Market Facts, Projections and Implications for Exploration and Development. Geoscience Canada: Journal of the Geological Association of Canada/Geoscience Canada: journal de l'Association Géologique du Canada, 48(2), 73-92.

Sinclair, W D; Gonevchuck, G A; Korostelev, P G; Semenyak, B I; Rodlonov, S; Seltmann, R; Stemprok, M. (2011). World distribution of tin and tungsten deposits. Geological Survey of Canada, Open File 5482, https://doi.org/10.4095/287906

Sinclair, W D; Gonevchuk, G A; Korostelev, P G; Semenyak, B I; Rodionov, S M; Seltmann, R; Stemprok, M. (2014). Geological Survey of Canada, Open File 7688, https://doi.org/10.4095/295581

Smoliar, M. I., Walker, R. J., & Morgan, J. W. (1996). Re-Os ages of group IIA, IIIA, IVA, and IVB iron meteorites. Science, 271(5252), 1099-1102.

Soloviev, S. G., Kryazhev, S. G., & Dvurechenskaya, S. S. (2020). Geology, mineralization, and fluid inclusion characteristics of the Agylki reduced tungsten (W-Cu-Au-Bi) skarn deposit, Verkhoyansk fold-and-thrust belt, Eastern Siberia: tungsten deposit in a gold-dominant metallogenic province. Ore Geology Reviews, 103452.

Song, G., Qin, K., Li, G., Evans, N. J., & Chen, L. (2014). Scheelite elemental and isotopic signatures: Implications for the genesis of skarn-type W-Mo deposits in the Chizhou Area, Anhui Province, Eastern China. American Mineralogist, 99(2-3), 303-317.

Spencer, C. J., Murphy, J. B., Kirkland, C. L., Liu, Y., & Mitchell, R. N. (2018). A Palaeoproterozoic tectono-magmatic lull as a potential trigger for the supercontinent cycle. Nature Geoscience, 11(2), 97-101.

Sun, K., & Chen, B. (2017). Trace elements and Sr-Nd isotopes of scheelite: Implications for the W-Cu-Mo polymetallic mineralization of the Shimensi deposit, South China. American Mineralogist, 102(5), 1114-1128.

Sun, K., Chen, B., & Deng, J. (2019). Ore genesis of the Zhuxi supergiant W-Cu skarn polymetallic deposit, South China: Evidence from scheelite geochemistry. Ore Geology Reviews, 107, 14-29.

Tanaka, T., Togashi, S., Kamioka, H., Amakawa, H., Kagami, H., Hamamoto, T., ... & Kunimaru, T. (2000). JNdi-1: a neodymium isotopic reference in consistency with LaJolla neodymium. Chemical Geology, 168(3-4), 279-281.

Tang, M., Chu, X., Hao, J. & Shen, B. (2021) Orogenic quiescence in Earth’s middle age. Science, 371, 728-731.

Thériault, R. J., & Ross, G. M. (1991). Nd isotopic evidence for crustal recycling in the ca. 2.0 Ga subsurface of western Canada. Canadian Journal of Earth Sciences, 28(8), 1140-1147.

Thorkelson, D. J., Abbott, J. G., Mortensen, J. K., Creaser, R. A., Villeneuve, M. E., McNicoll, V. J., & Layer, P. W. (2005). Early and middle Proterozoic evolution of Yukon, Canada. Canadian Journal of Earth Sciences, 42(6), 1045-1071.

Thorkelson, D. J., Mortensen, J. K., Creaser, R. A., Davidson, G. J., & Abbott, J. G. (2001). Early Proterozoic magmatism in Yukon, Canada: constraints on the evolution of northwestern Laurentia. Canadian Journal of Earth Sciences, 38(10), 1479-1494.

Tischendorf, G., Forster, H. J., Gottesmann, B., & Rieder, M. (2007). True and brittle micas: composition and solid-solution series. Mineralogical Magazine, 71(3), 285-320.

U.S. Geological Survey, 2017, Mineral commodity summaries 2017: U.S. Geological Survey, 202 p., https://doi.org/10.3133/70180197.

U.S. Geological Survey, 2020, Mineral commodity summaries 2020: U.S. Geological Survey, 200 p., https://doi.org/10.3133/mcs2020.

Union, I. (2014). Communication from the Commission to the European Parliament, the Council, the European Economic and Social Committee and the Committee of the Regions. A new skills agenda for europe. Brussels.

Unterschutz, J. L., Creaser, R. A., Erdmer, P., Thompson, R. I., & Daughtry, K. L. (2002). North American margin origin of Quesnel terrane strata in the southern Canadian Cordillera: Inferences from geochemical and Nd isotopic characteristics of Triassic metasedimentary rocks. Geological Society of America Bulletin, 114(4), 462-475.

Villeneuve, M. E. (1993). Tectonic subdivision and U-Pb geochronology of the crystalline basement of the Alberta Basin, Western Canada (Vol. 447). Geological Survey of Canada.

Villeneuve, M. E., Thériault, R. J., & Ross, G. M. (1991). U–Pb ages and Sm–Nd signature of two subsurface granites from the Fort Simpson magnetic high, northwest Canada. Canadian Journal of Earth Sciences, 28(7), 1003-1008.

Voicu, G., Bardoux, M., Stevenson, R., & Jebrak, M. (2000). Nd and Sr isotope study of hydrothermal scheelite and host rocks at Omai, Guiana Shield: implications for ore fluid source and flow path during the formation of orogenic gold deposits. Mineralium Deposita, 35(4), 302-314.

Wang, X., Ni, P., Jiang, S., Zhao, K., & Wang, T. (2010). Origin of ore-forming fluid in the Piaotang tungsten deposit in Jiangxi Province: Evidence from helium and argon isotopes. Chinese Science Bulletin, 55(7), 628-634.

Wang, Y., Wang, K., & Konare, Y. (2018). N 2-rich fluid in the vein-type Yangjingou scheelite deposit, Yanbian, NE China. Scientific reports, 8(1), 5662.

Wasserburg, G. J., Jacobsen, S. B., DePaolo, D. J., McCulloch, M. T., & Wen, T. (1981). Precise determination of SmNd ratios, Sm and Nd isotopic abundances in standard solutions. Geochimica et Cosmochimica Acta, 45(12), 2311-2323.

Watson, E. B., & Harrison, T. M. (1983). Zircon saturation revisited: temperature and composition effects in a variety of crustal magma types. Earth and Planetary Science Letters, 64(2), 295-304.

Wei, W. F., Hu, R. Z., Bi, X. W., Jiang, G. H., Yan, B., Yin, R. S., & Yang, J. H. (2019). Mantle-derived and crustal He and Ar in the ore-forming fluids of the Xihuashan granite-associated tungsten ore deposit, South China. Ore Geology Reviews, 105, 605-615.

Werner, A. B., Sinclair, W. D., & Amey, E. B. (1998). International Strategic Mineral Issues Summary Report--tungsten (No. 930). US Government Printing Office.

Werner, A.B.T., Sinclair, W.D., and Amey, E.B., 2014, International strategic mineral issues summary report—Tungsten (ver. 1.1, November 2014): U.S. Geological Survey Circular 930–O, 74 p., https://pubs.usgs.gov/circ/0930/o/. [Supersedes version 1.0 published in 1998; revisions in 2014 by John H. DeYoung, Jr., and Kim B. Shedd.]

Wesolowski, D., Drummond, S. E., Mesmer, R. E., & Ohmoto, H. (1984). Hydrolysis equilibria of tungsten (VI) in aqueous sodium chloride solutions to 300. degree. C. Inorganic Chemistry, 23(8), 1120-1132.

White, A. J. R., Chappell, B. W., & Cleary, J. R. (1974). Geologic setting and emplacement of some Australian Palaeozoic batholiths and implications for intrusive mechanisms. Pacific Geology, 8, 159-171.

White, A. J., & Chappell, B. W. (1977). Ultrametamorphism and granitoid genesis. Tectonophysics, 43(1-2), 7-22.

Whitmeyer, S. J., & Karlstrom, K. E. (2007). Tectonic model for the Proterozoic growth of North America. Geosphere, 3(4), 220-259.

Wise, H. M. (1974). Geological report and map of the Lened tungsten prospect, District of Mackenzie, NWT. NWT Assessment Report 080309.

Wise, S. A., & Watters, R. L. (2011). Reference Material 8599 Henderson Molybdenite. National Institute of Standards and Technology, Report of Investigation, 30.

Wood, S. A., & Samson, I. M. (2000). The hydrothermal geochemistry of tungsten in granitoid environments: I. Relative solubilities of ferberite and scheelite as a function of T, P, pH, and m NaCl. Economic Geology, 95(1), 143-182.

Xiaofeng, L., Cheng, H., Chunzeng, W., & Lifa, W. (2016). Genesis of the Huangshaping W–Mo–Cu–Pb–Zn polymetallic deposit in Southeastern Hunan Province, China: Constraints from fluid inclusions, trace elements, and isotopes. Ore Geology Reviews, 79, 1-25.

Xie, L., Zhang, Y., Zhang, H., Sun, J., & Wu, F. (2008). In situ simultaneous determination of trace elements, U-Pb and Lu-Hf isotopes in zircon and baddeleyite. Chinese Science Bulletin, 53(10), 1565-1573.

Yavuz, F. (2013). WinPyrox: A Windows program for pyroxene calculation classification and thermobarometry. American Mineralogist, 98(7), 1338-1359.

Yuan, H. L., Gao, S., Dai, M. N., Zong, C. L., Günther, D., Fontaine, G. H., ... & Diwu, C. (2008). Simultaneous determinations of U–Pb age, Hf isotopes and trace element compositions of zircon by excimer laser-ablation quadrupole and multiple-collector ICP-MS. Chemical Geology, 247(1-2), 100-118.

Yuan, S., Williams-Jones, A. E., Romer, R. L., Zhao, P., & Mao, J. (2019). Protolith-related thermal controls on the decoupling of Sn and W in Sn-W metallogenic provinces: Insights from the Nanling region, China. Economic Geology, 114(5), 1005-1012.

Yuvan, J. (2006). Fluid inclusion and oxygen isotope studies of high-grade quartz-scheelite veins at the Cantung Mine, Northwest Territories, Canada: products of a late-stage magmatic-hydrothermal event (Doctoral dissertation, University of Missouri-Columbia).

Zaw, U. K., & Clark, A. H. (1978). Fluoride-hydroxyl ratios of skarn silicates, Cantung E-zone scheelite orebody, Tungsten, Northwest Territories. The Canadian Mineralogist, 16(2), 207-221.

Zhu, L. Y., Jiang, S. Y., Chen, R. S., & Ma, Y. (2019). Origin of the Shangfang Tungsten Deposit in the Fujian Province of Southeast China: Evidence from Scheelite Sm–Nd Geochronology, H–O Isotopes and Fluid Inclusions Studies. Minerals, 9(11), 713.

Appendices

Appendix A: Supplementary material to Chapter 3

A.1. Rhenium-Osmium geochronology of molybdenite from the Cantung deposit

Molybdenite crystals used for Re-Os geochronology are from a quartz-scheelite-tourmaline-molybdenite vein (sample 18-CA-50) cutting across the Mine Stock pluton at the Cantung deposit. Methods used for molybdenite analysis are described in detail by Selby & Creaser (2004). Preparation of a molybdenite mineral separate was made by metal-free crushing and sieving followed by magnetic and gravity concentration methods. The ^{187}Re and ^{187}Os concentrations in molybdenite were determined by isotope dilution mass spectrometry using Carius-tube, solvent extraction, anion chromatography and negative thermal ionization mass spectrometry techniques. For this work, a mixed double spike containing known amounts of isotopically enriched ^{185}Re, ^{190}Os, and ^{188}Os analysis was used (Markey et al., 2007). Isotopic analysis used a ThermoScientific Triton mass spectrometer by Faraday collector. Total procedural blanks for Re and Os are less than <3 picograms and 2 picograms, respectively, which are insignificant in comparison to the Re and Os concentrations in molybdenite. The Reference Material 8599 Henderson molybdenite (Markey et al., 2007) is routinely analyzed as a standard, and during the past 5 years returned an average Re-Os date of 27.78 ± 0.06 Ma (n=16), indistinguishable from the Reference Age Value of 27.66 ± 0.1 Ma (Wise and Watters, 2011). The ^{187}Re decay constant used is 1.666×10^{-11} year^{-1} (Smoliar et al, 1996). Mineral separation and Re-Os isotope investigations were performed at the Canadian Centre for Isotopic Microanalysis (CCIM), University of Alberta.

The molybdenite crystals analyzed yielded a Re-Os age of 94.6 ± 2.1 Ma (Table A.1). The age uncertainty is quoted at 2σ level, and includes all known analytical uncertainty, including a ~ 0.31% uncertainty in the decay constant of ^{187}Re.

Table A.1. Re-Os isotopic and age data of molybdenite from the Cantung deposit. Molybdenite crystals analyzed are from a quartz-scheelite-tourmaline-molybdenite vein cutting across the Mine Stock pluton at the Cantung deposit.

Sample name	**Re (ppm)**	**± 2σ on Re (ppm)**	**^{187}Re (ppm)**	**± 2σ on ^{187}Re (ppm)**	**^{187}Os (ppb)**	**± 2σ on ^{187}Os (ppm)**	**Model age (Ma)**	**± 2σ on model age (Ma)**
18-CA-50	2.344	0.007	1.473	0.004	2.324	0.051	94.6	2.1

Table A.2. XRF data for samples from the Cantung and Mactung deposits.

CANTUNG						MACTUNG				
Sample name	18-CA-05	18-CA-46	18-CA-31	18-CA-29	18-CA-22	Sample name	MS 234 198.1-198.4	18-MA-02	MS 161 185.6-185.9	MS 161 322-322.3 A2
Facies	Limestone	Garnet-pyroxene skarn	Pyroxene skarn	Amphibole-rich facies	Biotite-rich facies	Facies	Limestone	Garnet-pyroxene skarn	Amphibole-rich facies	Biotite-rich facies
SiO_2 (wt%)	27.5	30.0	27.4	29.3	31.0	SiO_2 (wt%)	40.8	35.5	33.5	64.10
TiO_2 (wt%)	0.7	0.1	0.0	0.0	0.3	TiO_2 (wt%)	0.4	0.1	0.6	0.72
Al_2O_3 (wt%)	8.7	5.8	0.5	1.5	7.4	Al_2O_3 (wt%)	4.4	3.8	7.5	14.93
Fe_2O_3 (wt%)	10.8	13.7	21.6	25.2	34.5	Fe_2O_3 (wt%)	16.5	20.0	16.4	2.37
MnO (wt%)	1.4	8.6	4.7	0.7	0.4	MnO (wt%)	1.0	1.7	0.9	0.02
MgO (wt%)	1.9	3.5	1.9	11.0	7.3	MgO (wt%)	1.6	0.6	1.1	1.32
CaO (wt%)	18.5	15.5	19.1	13.7	0.6	CaO (wt%)	18.7	20.6	19.5	3.47
Na_2O (wt%)	0.2	0.2	0.0	0.2	0.4	Na_2O (wt%)	0.2	0.0	0.3	1.46
K_2O (wt%)	0.1	0.0	0.0	0.2	4.2	K_2O (wt%)	0.0	0.0	0.0	4.44
P_2O5 (wt%)	0.2	0.2	0.0	0.1	0.2	P_2O5 (wt%)	1.3	0.5	0.3	0.05
Ag (ppm)	90.4	81.2	82.8	72.3	70.4	Ag (ppm)	73.4	80.1	75.6	68.70
As (ppm)	115.2	244.7	161.1	251.3	131.0	As (ppm)	144.0	276.8	474.1	79.50
Ba (ppm)	20.0	23.9	18.5	15.2	358.5	Ba (ppm)	18.9	20.3	32.0	1347.10
Cd (ppm)	5.7	30.2	22.1	15.8	36.3	Cd (ppm)	16.7	19.7	16.6	5.50
Ce (ppm)	87.1	10.4	0.9	15.2	40.9	Ce (ppm)	95.2	2.8	41.6	64.30
Cl (ppm)	45.0	26.7	30.5	94.5	142.4	Cl (ppm)	15.8	17.8	20.6	20.10
Co (ppm)	17.8	4.6	6.3	27.6	56.8	Co (ppm)	4.8	6.8	25.0	0.00
Cr (ppm)	384.9	339.1	75.2	36.4	106.4	Cr (ppm)	24.2	67.5	23.6	79.10
Cs (ppm)	3.7	0.0	8.8	0.0	99.4	Cs (ppm)	0.0	0.0	0.0	18.80
Cu (ppm)	61.8	22198.0	17.2	1250.2	5811.4	Cu (ppm)	18.2	592.7	224.4	44.40
F (ppm)	536.6	413.1	508.9	2737.8	6472.7	F (ppm)	899.2	1246.3	701.3	745.00
Ga (ppm)	56.0	44.4	16.7	30.6	35.0	Ga (ppm)	20.9	43.2	38.6	20.90
Hf (ppm)	12.2	0.0	5.9	5.3	0.0	Hf (ppm)	7.9	6.9	17.4	2.90
La (ppm)	32.9	13.2	4.6	10.0	20.5	La (ppm)	40.7	4.6	22.2	37.80
Nb (ppm)	24.3	18.5	8.6	11.8	52.2	Nb (ppm)	27.5	27.8	79.9	20.80
Nd (ppm)	42.4	4.6	2.1	0.0	16.4	Nd (ppm)	40.1	11.2	19.9	30.40
Ni (ppm)	8.0	0.0	0.0	0.0	0.0	Ni (ppm)	0.0	0.0	0.0	0.00
Pb (ppm)	36.4	0.0	1.9	0.0	2.6	Pb (ppm)	0.0	0.0	0.0	39.80
Rb (ppm)	8.4	12.1	17.0	13.9	512.5	Rb (ppm)	7.9	11.2	14.0	189.70

Table A.2. (continued)

S (ppm)	4955.9	63015.0	0.0	76852.5	163096.8	**S (ppm)**	17235.4	17379.2	19470.3	4492.20
Sb (ppm)	22.3	16.2	19.3	6.6	5.2	**Sb (ppm)**	13.0	13.5	4.9	0.00
Sc (ppm)	16.8	0.0	0.0	0.0	1.0	**Sc (ppm)**	2.8	0.0	0.0	14.40
Sn (ppm)	157.4	335.8	164.7	54.7	37.2	**Sn (ppm)**	51.5	133.7	51.7	0.00
Ta (ppm)	0.0	0.8	0.0	0.0	27.8	**Ta (ppm)**	0.0	0.0	0.0	2.70
Sr (ppm)	242.9	8.4	25.7	13.4	24.0	**Sr (ppm)**	84.4	18.1	182.7	140.50
Th (ppm)	18.6	53.9	118.4	11.7	531.3	**Th (ppm)**	0.7	12.1	12.5	21.30
U (ppm)	6.7	0.0	0.0	0.0	4.9	**U (ppm)**	0.0	0.0	0.0	1.90
V (ppm)	94.0	25.3	9.3	15.4	62.1	**V (ppm)**	98.6	53.4	170.8	82.30
W (ppm)	59.5	5850.6	1645.8	8362.5	25.3	**W (ppm)**	1983.9	7682.4	16627.6	24.20
Y (ppm)	43.9	15.8	3.1	11.8	10.7	**Y (ppm)**	44.6	15.9	36.6	22.90
Zn (ppm)	342.5	1203.9	905.6	200.0	782.5	**Zn (ppm)**	360.8	277.0	99.7	2.50
Zr (ppm)	269.9	191.6	25.8	21.7	37.9	**Zr (ppm)**	92.8	34.2	96.9	171.30
Mo (ppm)	0.0	2.0	0.0	32.4	6.6	**Mo (ppm)**	27.7	32.9	58.2	52.80
Br (ppm)	6.5	0.0	3.5	0.0	0.8	**Br (ppm)**	0.1	0.0	0.0	1.10
Bi (ppm)	2.1	124.0	311.8	19.7	1286.3	**Bi (ppm)**	1.6	26.7	0.0	11.38

Table A.3. Mass percent element enrichment and depletion of limestone in comparison to subsequent alteration facies at Cantung and Mactung. Concentration changes are normalized to Zr (immobile) element using the limestone as reference. *N/A=not applicable.*

CANTUNG						MACTUNG				
Sample name	**18-CA-05**	**18-CA-46**	**18-CA-31**	**18-CA-29**	**18-CA-22**	**Sample name**	**MS 234 198.1-198.4**	**18-MA-02**	**MS 161 185.6-185.9**	**MS 161 322-322.3 A2**
Facies	**Limestone**	**Garnet-pyroxene skarn**	**Pyroxene skarn**	**Amphibole-rich facies**	**Biotite-rich facies**	**Facies**	**Limestone**	**Garnet-pyroxene skarn**	**Amphibole-rich facies**	**Biotite-rich facies**
SiO_2	0.0	53.7	942.4	1226.2	702.6	**SiO_2**	0.0	136.0	-21.4	-14.9
TiO_2	0.0	-73.1	-66.7	-46.7	180.7	**TiO_2**	0.0	-13.4	29.7	-3.6
Al_2O_3	0.0	-5.4	-40.4	117.6	506.3	**Al_2O_3**	0.0	131.8	62.5	82.7
Fe_2O_3	0.0	78.9	1994.4	2809.4	2176.1	**Fe_2O_3**	0.0	227.2	-5.1	-92.2
MnO	0.0	796.3	3540.6	509.0	86.2	**MnO**	0.0	334.4	-19.0	-98.9
MgO	0.0	161.5	941.1	7187.8	2690.3	**MgO**	0.0	-0.4	-35.8	-54.8
CaO	0.0	17.8	979.2	818.7	-76.2	**CaO**	0.0	198.9	0.3	-89.9
Na_2O	0.0	30.4	34.0	809.7	1071.2	**Na_2O**	0.0	-52.0	50.7	382.9
K_2O	0.0	-78.7	375.5	2670.2	45185.5	**K_2O**	0.0	-32.2	145.4	14946.8
P_2O_5	0.0	7.9	13.2	163.8	599.8	**P_2O_5**	0.0	-1.4	-77.2	-97.9
Ag	0.0	26.5	858.2	894.7	454.6	**Ag**	0.0	196.1	-1.4	-49.3
As	0.0	199.2	1362.9	2613.2	709.8	**As**	0.0	421.6	215.3	-70.1
Ba	0.0	68.3	867.7	845.3	12665.1	**Ba**	0.0	191.4	62.1	3761.3
Cd	0.0	646.3	3956.0	3347.7	4435.2	**Cd**	0.0	220.1	-4.8	-82.2
Ce	0.0	-83.2	-89.2	117.1	234.4	**Ce**	0.0	-92.0	-58.2	-63.4
Cl	0.0	-16.4	609.0	2511.9	2153.5	**Cl**	0.0	205.7	24.9	-31.1
Co	0.0	-63.6	270.3	1828.6	2172.4	**Co**	0.0	284.4	398.8	-100.0
Cr	0.0	24.1	104.4	17.6	96.9	**Cr**	0.0	656.9	-6.6	77.1
Cs	0.0	-100.0	2388.1	-100.0	19031.5	**Cs**	#N/A	#N/A	#N/A	#N/A
Cu	0.0	50497.9	191.2	25061.4	66866.2	**Cu**	0.0	8736.6	1080.8	32.2
F	0.0	8.4	892.1	6245.9	8490.1	**F**	0.0	276.1	-25.3	-55.1
Ga	0.0	11.7	212.0	579.6	345.1	**Ga**	0.0	460.9	76.9	-45.8
Hf	0.0	-100.0	405.9	440.3	-100.0	**Hf**	0.0	137.0	110.9	-80.1
La	0.0	-43.5	46.3	278.0	343.7	**La**	0.0	-69.3	-47.8	-49.7
Nb	0.0	7.2	270.2	504.0	1429.8	**Nb**	0.0	174.3	178.3	-59.0
Nd	0.0	-84.7	-48.2	-100.0	175.4	**Nd**	0.0	-24.2	-52.5	-58.9
Ni	0.0	-100.0	-100.0	-100.0	-100.0	**Ni**	#N/A	#N/A	#N/A	#N/A
Pb	0.0	-100.0	-45.4	-100.0	-49.1	**Pb**	#N/A	#N/A	#N/A	#N/A
Rb	0.0	102.9	2017.2	1958.2	43348.8	**Rb**	0.0	284.7	69.7	1200.9
S	0.0	1691.1	-100.0	19187.6	23336.2	**S**	0.0	173.6	8.2	-85.9
Sb	0.0	2.3	805.4	268.1	66.1	**Sb**	0.0	181.8	-63.9	-100.0
Sc	0.0	-100.0	-100.0	-100.0	-57.6	**Sc**	0.0	-100.0	-100.0	178.6
Sn	0.0	200.5	994.6	332.2	68.3	**Sn**	0.0	604.4	-3.9	-100.0
Ta	#N/A	#N/A	#N/A	#N/A	#N/A	**Ta**	#N/A	#N/A	#N/A	#N/A
Sr	0.0	-95.1	10.7	-31.4	-29.6	**Sr**	0.0	-41.8	107.3	-9.8
Th	0.0	308.2	6559.2	682.4	20241.9	**Th**	0.0	4590.4	1610.2	1548.4
U	0.0	-100.0	-100.0	-100.0	420.8	**U**	#N/A	#N/A	#N/A	#N/A
V	0.0	-62.1	3.5	103.8	370.5	**V**	0.0	47.0	65.9	-54.8
W	0.0	13751.3	28836.3	174708.4	202.8	**W**	0.0	950.7	702.7	-99.3
Y	0.0	-49.3	-26.1	234.3	73.6	**Y**	0.0	-3.3	-21.4	-72.2
Zn	0.0	395.2	2666.0	626.3	1527.0	**Zn**	0.0	108.3	-73.5	-99.6

Table A.3. (continued)

Zr	0.0	0.0	0.0	0.0	0.0	**Zr**	0.0	0.0	0.0	0.0
Mo	#N/A	#N/A	#N/A	#N/A	#N/A	**Mo**	0.0	222.3	101.2	3.3
Br	0.0	-100.0	463.3	-100.0	-12.4	**Br**	0.0	-100.0	-100.0	495.9
Bi	0.0	8260.5	156038.4	11639.4	438408.1	**Bi**	0.0	4480.2	-100.0	290.4

Figure A.1. Representative Scanning Electron Microscope-Cathodoluminescence (SEM-CL) images of scheelite hosted in skarn samples from A/ the Cantung deposit and B/ the Mactung deposit.

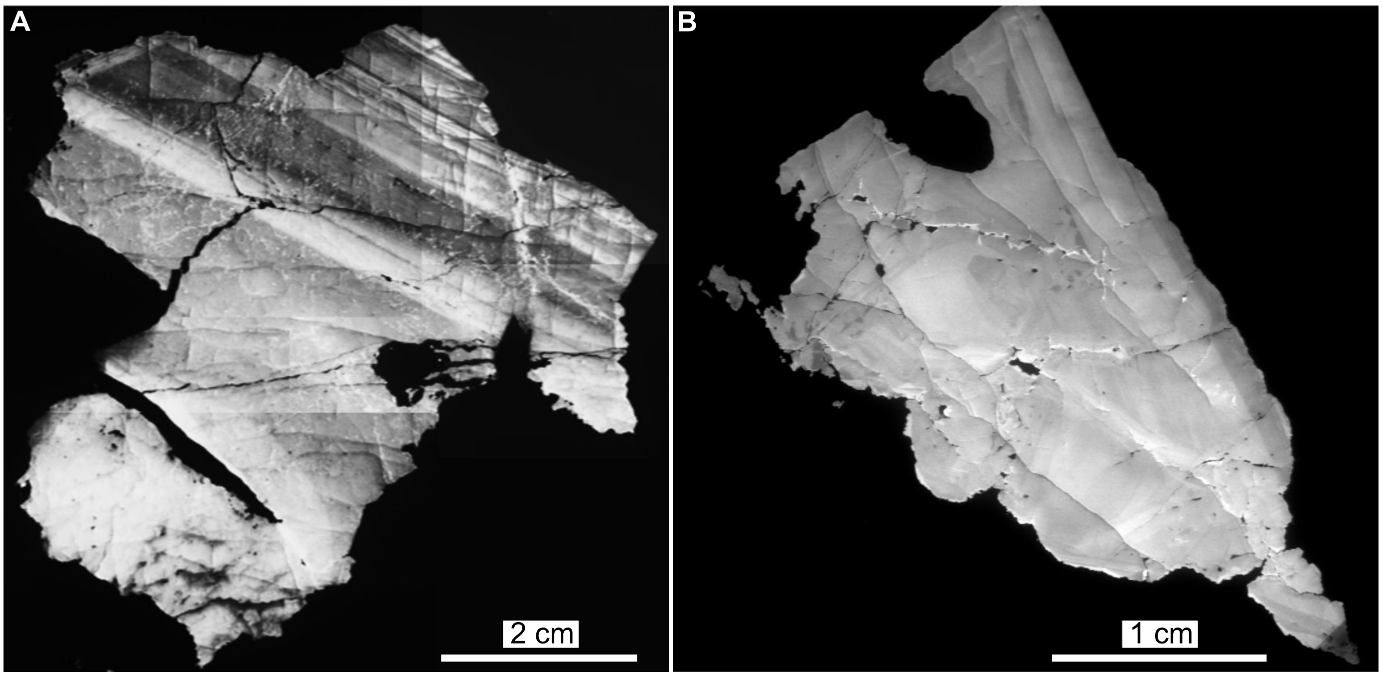

Figure A.2. (***Next page***) Micro-XRF elemental intensity maps showing the intensity of Ca, Si, W, Fe, Mn, Al, Mg, Mo and Sn for four samples of altered limestone from the Cantung deposit. Photographs at the top of each column represent the core samples under natural light before elemental mapping. The least altered regions have a high calcium and silicon content, and lack tungsten, iron, and manganese. The highly altered regions are rich in tungsten, iron and manganese. The distribution of elements in the geochemical maps is compatible with the mineralogy observed.

Sample V2791 33.5-34.5 (Pyroxene skarn facies): least altered regions consist of quartz, plagioclase, chlorites, clinozoisite, and pyroxene, and highly altered regions consist dominantly of pyroxene, pyrrhotite and scheelite.

Sample V2603 402-403 (Amphibole-rich facies): least altered regions consist of micas, quartz, plagioclase, calcite and minor biotite, and highly altered regions consist of amphibole, pyrrhotit

Sample U1841 342.5-343 (Pyroxene skarn facies): least altered regions consist of quartz, calcite, plagioclase, chlorites, clinozoisite, micas, pyroxene,and minor pyrrhotite, and highly altered regions consist of pyrrhotite, pyroxene, and minor scheelite, calcite, micas, chlorites, quartz, plagioclase and clinozoisite.e, scheelite, and lesser quartz, plagioclase and pyrite.

Sample 18-CA-05b (Garnet-pyroxene skarn facies): least altered regions consist dominantly of micas, chlorite, minor quartz, plagioclase, clinozoisite, and pyroxene, and highly altered regions consist dominantly of garnet, pyroxene, pyrrhotite, minor scheelite and vesuvianite, and occasional amphibole, quartz, plagioclase and titanite.

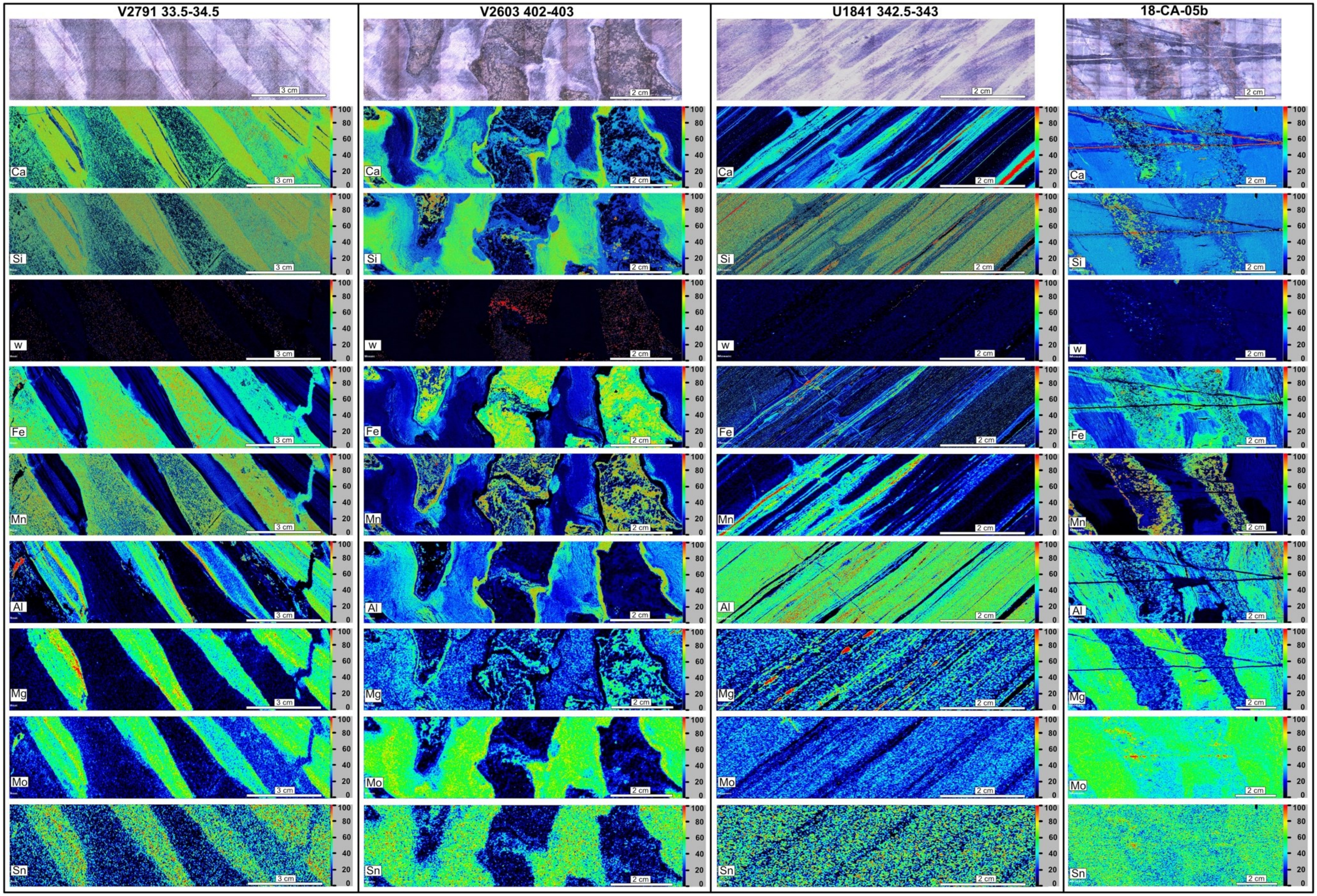
V2791 33.5-34.5
V2603 402-403
U1841 342.5-343
18-CA-05b
3 cm
2 cm
Ca
Si
W
Fe
Mn
Al
Mg
Mo
Sn
0
20
40
60
80
100

Figure A.3. Mass percent element enrichment and depletion of limestone in comparison to subsequent alteration facies at Cantung (A, C, E) and Mactung (B, D, F). Concentration changes are normalized to Zr (immobile) element using the limestone as reference. For Mactung, stage 2 (pyroxene skarn) composition was not determined in this study.

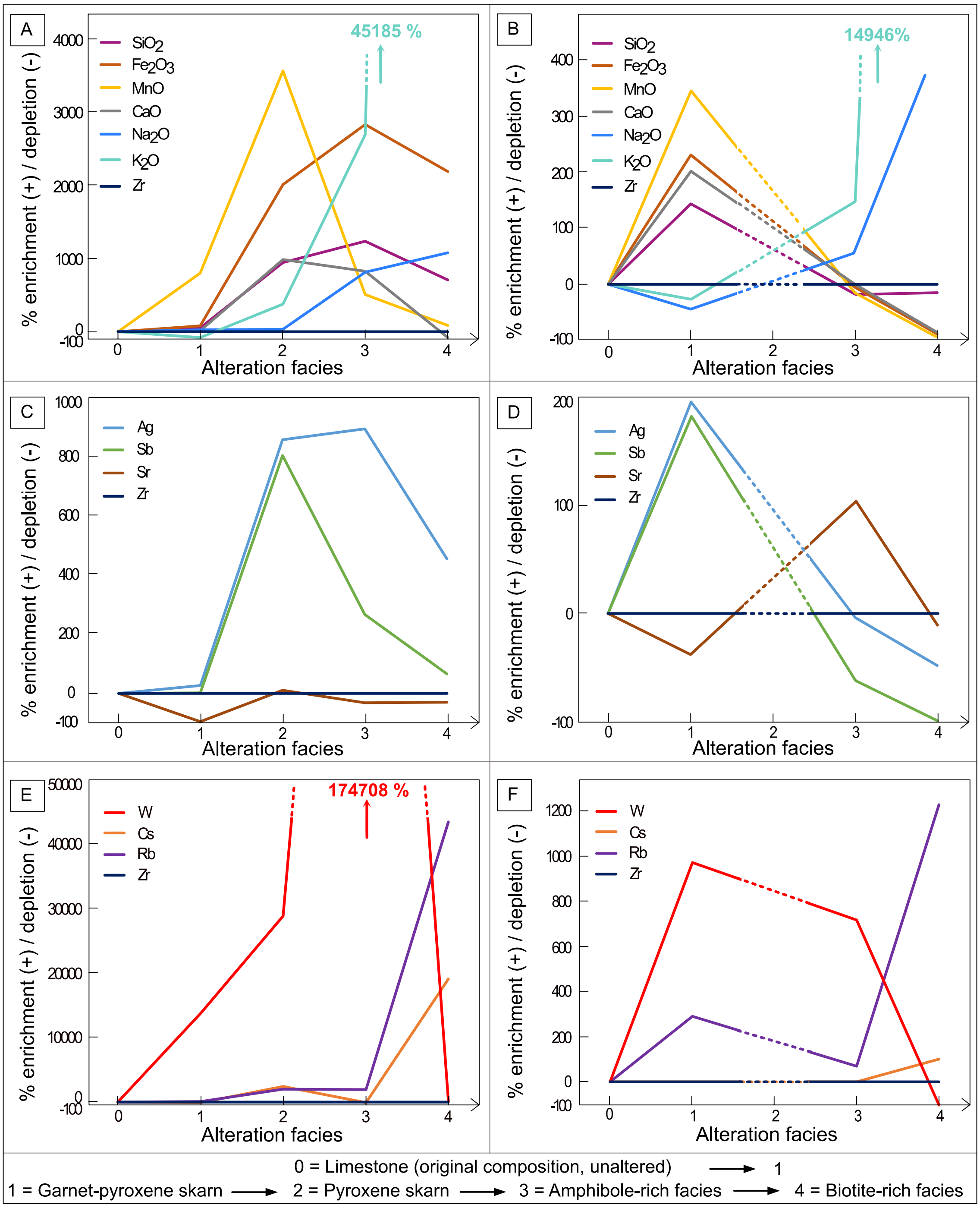

A.2. References

Markey, R., Stein, H. J., Hannah, J. L., Zimmerman, A., Selby, D., & Creaser, R. A. (2007). Standardizing Re–Os geochronology: a new molybdenite reference material (Henderson, USA) and the stoichiometry of Os salts. Chemical Geology, 244(1-2), 74-87.

Selby, D., & Creaser, R. A. (2004). Macroscale NTIMS and microscale LA-MC-ICP-MS Re-Os isotopic analysis of molybdenite: Testing spatial restrictions for reliable Re-Os age determinations, and implications for the decoupling of Re and Os within molybdenite. Geochimica et Cosmochimica Acta, 68(19), 3897-3908.

Smoliar, M. I., Walker, R. J., & Morgan, J. W. (1996). Re-Os ages of group IIA, IIIA, IVA, and IVB iron meteorites. Science, 271(5252), 1099-1102.

Wise, S. A., & Watters, R. L. (2011). Reference Material 8599 Henderson Molybdenite. National Institute of Standards and Technology, Report of Investigation, 30.

Appendix B: Supplementary material to Chapter 4

B.1: Detailed geology of the Cantung and Mactung deposits

Cantung and Mactung are two tungsten skarn deposits located in the eastern part of the Selwyn Basin close to the Yukon–Northwest Territories border. Cantung and Mactung show similar mineralogy and paragenetic evolution (Elongo et al., 2020). The mineralogy in the two deposits consists of a prograde skarn stage evolving from garnet-pyroxene to pyroxene facies; and an overprinting retrograde alteration stage evolving from the amphibole-rich facies to the biotite-rich facies (Elongo et al., 2020). These main stages are further overprinted by a sulfide stage followed by late quartz-sulfides veins. Scheelite is the main tungsten-bearing mineral and is either disseminated in the different facies or present in quartz and/or sulfides veins.

B.1.1. The Cantung deposit

The Cantung skarn deposit in the Northwest Territories is hosted in Upper Proterozoic to Upper Ordovician sedimentary rocks (Blusson, 1968). Four main sedimentary units from latest Precambrian to lower Cambrian age are present at Cantung: the "Lower Argillite" of the Narchilla/Vampire formation, and the "Swiss-Cheese" Limestone, the "Ore" Limestone, and "Upper Argillite" of the Sekwi formation. The sedimentary sequence is folded into a recumbent anticline and was intruded by the Mine Stock pluton, a monzogranite (Mathieson and Clark, 1984) belonging to the Tungsten suite. The Mine Stock (98.2 ± 0.4 Ma from U-Pb in zircon; Rasmussen, 2013) is associated with contact metamorphism of the sedimentary sequence hosting the Cantung skarn (Mathieson and Clark, 1984). Dykes locally crosscutting the Mine Stock pluton consist of fine-grained monzogranite, aplitic to porphyry alkali feldspar granite, and kersantitic lamprophyres (Mathieson and Clark, 1984).

The magmatic Mine Stock pluton is unlikely to be responsible for tungsten mineralization at Cantung. Despite its proximity to mineralization at Cantung, the Mine Stock pluton shows only local evidence of hydrothermal alteration (Mathieson and Clark, 1984) or fluid saturation. In contrast, dikes crosscutting the pluton are extensively altered suggesting that they could be associated with the fluid source or a fluid conduit. Furthermore, there is no evidence for extensive magmatic fractionation in the Mine Stock monzogranite, which is a common characteristic of magmatic sources for tungsten mineralization (Rasmussen et al., 2011). However, mineralization at Cantung ranges in age from ~103 to 96 Ma (Lentz, 2020), so while the upper portions of the Mine Stock pluton may not be the source of fluids and tungsten, magma, fluid and metals were likely derived from the same unexposed magma body at depth (Rasmussen et al., 2011).

B.1.2. The Mactung deposit

The Mactung skarn deposit in Yukon is hosted in an isoclinally folded succession of sedimentary units ranging in age from latest Precambrian to late Ordovician (Dick and Hodgson, 1982). From older to younger, these units correspond to the Vampire formation (locally unit 1), Sekwi formation (locally unit 2B), Hess River formation (locally unit 3C), the Rabbitkettle formation (locally units 3D, 3E, 3F, 3G and 3H) and the Duo Lake formation (locally unit 4 ; Gebru, 2017 ; Fischer et al., 2018). Tungsten mineralization at Mactung occurs in two exoskarn orebodies hosted in the carbonate rich units within Sekwi and Rabbitkettle formations (locally units 2B, 3D, 3E and 3F ; Dick and Hodgson, 1982; Gebru, 2017; Fischer et al., 2018).

Two biotite quartz monzonite plutons (and related porphyritic, aplitic and pegmatitic dykes) belonging to the Tungsten suite are spatially associated with the Mactung deposit: the Cirque Lake Stock (also called Mactung North Pluton) and the Rockslide Mountain Stock (also called

Mactung South Pluton; Atkinson and Baker, 1986; Gebru, 2017). The Cirque Lake Stock was originally proposed as the source of the mineralizing fluids because of its close spatial association with the Mactung mineralization. However, like at Cantung, the causal relationship between the pluton and the mineralization was challenged because of the lack of mineralization in the carbonate units at the contact with the pluton, the weak hydrothermal alteration around the pluton, and the lack of correlation between veining and alteration in the pluton and mineralized locations (Atkinson and Baker, 1986). Recent studies have shown that the skarn mineralization (97.5 ± 0.5 Ma from Re–Os in molybdenite, Selby et al., 2003) is broadly coeval with the crystallization of the Cirque Lake Stock and the Rockslide Mountain Stock (97.6 ± 0.2 Ma from U-Pb in zircon, Gebru, 2017). As at Cantung, the timing of the exposed granitic plutons and skarn mineralization overlap closely.

B.2: SAMPLING

Whole rock samples representative of the local lithologies at Cantung and Mactung were selected to determine their Samarium-neodymium isotope composition. Whole rock samples from Cantung include two granitoids samples (Mine Stock pluton), one sample of aplitic dyke, one sample of lamprophyre dyke, one non-skarnified limestone sample (Swiss-Cheese Limestone), and two argillite samples (Lower Argillite and Upper Argillite). Whole rock samples from Mactung include two granitoids samples (Mactung North pluton and Mactung South pluton) and three argillite samples (Unit 1). Further details about the samples are presented in Table B.1.

Scheelite from Cantung include two samples from an early-stage quartz vein cutting across the Mine stock pluton, two samples from argillite units (Lower Argillite and Upper Argillite), one sample from the garnet-pyroxene skarn (hosted in the Ore Limestone), one sample from the pyroxene skarn (hosted in the Swiss-Cheese Limestone), one sample from the amphibole-rich facies (hosted in the Swiss-Cheese Limestone) and one sample from the biotite-rich facies (hosted in the Ore Limestone). Scheelite from Mactung include one sample from argillite (hosted in Unit 1), one sample from the garnet-pyroxene skarn (hosted in Unit 3E), one sample from the pyroxene skarn (hosted in Unit 3E) and one sample from the amphibole-rich facies (hosted in Unit 3F). Further details about the samples are presented in Tables B.2 & B.3.

B.3: DETAILED METHODS

B.3.1. Whole rock composition

The mineralogy and mineral zonation of samples was determined in thin sections through transmitted and reflected light microscopy and Scanning Electron Microscopy (SEM). Unaltered samples were selected for whole rock analyses and ground in a shatter box using an alumina mill.

Whole rock Samarium-neodymium isotope compositions were determined through mass spectrometry of Sm and Nd fractions separated and measured at the Crustal Re-Os Geochronology Laboratory and CCIM ICPMS facilities at the University of Alberta. Sample powders were weighed and spiked with a known amount of mixed ^{150}Nd-^{149}Sm tracer solution calibrated directly against the Caltech mixed Sm/Nd normal described by Wasserburg et al. (1981). Samarium and neodymium fractions were separated following the procedures described in Creaser et al. (1997) and Unterschutz et al. (2002).

The purified Sm and Nd fractions were analyzed for isotopic composition and concentration using a Nu Plasma™ multi-collector inductively coupled plasma mass spectrometer (MC-ICP-

MS) at CCIM-ICPMS facility at the University of Alberta. All Nd isotope ratios were normalized for variable mass fractionation to a value of ^{146}Nd / ^{144}Nd = 0.7219 using the exponential fractionation law. The ^{143}Nd / ^{144}Nd ratios presented here are relative to a value of 0.511850 for the La Jolla Nd isotopic standard, monitored by use of an in-house Alfa Nd isotopic standard. The value of ^{143}Nd / ^{144}Nd obtained for the JNdi-1 standard following this procedure was 0.512109 ± 8 (2SE) compared to a known value 0.512107 ± 7 (Tanaka et al., 2000). Sm isotopic abundances were normalized for variable mass fractionation to a value of 1.17537 for ^{152}Sm / ^{154}Sm also using the exponential law. The Nd isotope standard "Shin Etsu: J-Ndi-1" (Tanaka et al., 2000) was also analyzed using the same procedures. Using the mixed ^{150}Nd-^{149}Sm tracer, the measured ^{147}Sm / ^{144}Nd ratios for the synthetic BCR-1 standard range from 0.1380 to 0.1382, suggesting reproducibility for ^{147}Sm / ^{144}Nd of ~ ± 0.1% for real rock powders.

B.3.2. Scheelite composition

Chemical homogeneity/heterogeneity in scheelite was tested in thin section through cathodoluminescence imaging at the Scanning Electron Microscope Laboratory at the University of Alberta using a Zeiss EVO LS15 Scanning Electron Microscope and through point mode LA-ICPMS transects perpendicular to growth zones in individual grains.

The Samarium-neodymium isotope compositions of scheelite were determined through solution MC-ICPMS of scheelite separates and through in-situ laser ablation split stream analyses (LASS) ICPMS of thin sections and grain mounts. These two procedures were combined to (1) verify the accuracy of the results and (2) to evaluate compositions in samples where the concentrations of Sm or Nd were too low to obtain meaningful results through LASS.

For solution MC-ICPMS, scheelite grains were separated at the SELFRAG laboratory of the Canadian Centre for Isotopic Microanalysis (CCIM) at the University of Alberta, then handpicked under a binocular microscope under ultraviolet light. Scheelite powders were obtained using an agate mortar. Scheelite dissolution and Sm and Nd fractions separation were performed at the Crustal Re-Os Geochronology Laboratory of the University of Alberta following procedures described by Kempe et al. (2001).

Only four scheelite samples were analyzed via LASS ICP MS: one sample from the Mactung pyroxene skarn, one from the Cantung quartz vein, one from Mactung argillites and one from Cantung argillites. Simultaneous Sm-Nd isotope and trace element (Sm and Nd) measurements were carried out in the Arctic Resources Laboratory at the University of Alberta (Luo et al., 2019). The scheelite samples were ablated using the LASS technique (Yuan et al., 2008; Xie et al. 2008; Fisher et al., 2014). Samples were ablated using a 193 nm Resolution Excimer ArF laser equipped with a Laurin-technic S-155 two-volume ablation cell. Analyses were performed using a laser fluence of 6 J/cm^2 and a repetition rate of 10 Hz. Analysis time consisted of 60 seconds of background followed by 70 seconds of ablation and then 40 seconds of sample washout. The carrier gas was a mixture of ~1.6 L/min Ar and 14 ml/min N_2, which entered tangentially from the top of the S-155 ablation cell funnel and ~800 ml/min He entering from the side of the cell. This yielded a pressure in the ablation cell of ~7.5 KPa. The ablated sample aerosol, He, N_2 and Ar mixture was then split after the laser cell using a Y-piece, diverting the ablation product to a Thermo Neptune Plus using multiple Faraday detectors with 1011 Ω amplifiers operating in static collection mode (for Sm-Nd) and a Thermo Element-XR 2 mass spectrometer using a single secondary electron multiplier detector in peak hopping mode (for trace elements). The length of tubing was equalized such that the ablated sample aerosol arrives simultaneously at both mass spectrometers. Calibration was performed using NIST SRM 612 in conjunction with internal standardization using isotope ^{43}Ca. The results of the measurements of secondary standards (e.g., NIST614) agree with the reference values within relative uncertainties of typically 5–10% or better at the 95% confidence level.

The present-day CHUR values used for the initial εNd (εNd_i) calculation are $^{143}Nd/^{144}Nd$=0.512638 and $^{147}Sm/^{144}Nd$=0.1967.

B.4: DETAILS FOR DATA PRESENTED IN FIGURES

B.4.1. Data presented in Figure 4.1:

1/Basement rocks and faults are from Whitmeyer and Karlstrom (2007) (<2.0 Ga orogens and arcs ,1.9-1.8 Ga reworked Archean crust, and >2.5 Ga Archean crust) and from Esteve et al. (2020) (Mackenzie craton and Canadian shield).

2/εNd data are from Morris and Creaser (2008) for the Canadian Cordillera and from Chapman et al. (2017) for the US Cordillera.

3/Tungsten deposits and classification are from Sinclair et al. (2011) and Sinclair et al. (2014).

B.4.1.1. Compiled data presented in Figure 4.3:

Archean and Early Proterozoic crust fields are from Villeneuve et al. (1993), Grenville-age crust field is from Garzione et al (1997) and references therein.

B.4.1.1.a. Igneous / meta-igneous units

1/Lamprophyre data include: lamprophyres from the Scheelite Dome (Mair et al., 2011), from near the Roy pluton, near the Pelly River pluton, and from the Cantung deposit (Rasmussen, 2013);

2/ Felsic (meta-)igneous rocks data include: Bonnet Plume River intrusions (Northeastern Yukon) (Thorkelson et al., 2001), Fort Simpson magnetic High intrusions (Northeastern BC &

Southern Yukon) (Villeneuve et al., 1991), and intrusions and orthogneiss from the Taltson, Buffalo Head, Chinchaga and Ksituan domains (Northern Alberta) (Theriault and Ross, 1991); 3/ Mafic (meta-)igneous rocks data include: Archean/Early Proterozoic metagabbro from the Buffalo Head domain (Northern Alberta) (Theriault and Ross, 1991), Neoproterozoic basalts/sills from Little Dal basalts and Tsezotene sills (Mackenzie Mtns, NWT) (Dudas and Lustwerk, 1997), and recent to Tertiary basalts from the Iskut-Unuk rivers volcanic field (SW Yukon) (Cousens and Bevier, 1995), from Watson Lake (Abraham et al., 2001), and from the Mount Skukum Volcanic Complex and the Bennett Lake Volcanic Complex (Morris and Creaser, 2003).

B.4.1.1.b. Sedimentary / meta-sedimentary units

1/ Paleozoic metasediments data include data from Garzione et al. (1997) (Yukon and Northwest Territories) and from Cousens (2007) (Eastern Yukon);

2/ Windermere Supergroup (Yukon and NWT) data are from Garzione et al. (1997);

3/Mackenzie Mountains Supergroup (NWT) data are from Rainbird et al. (1997);

4/Wernecke Supergroup (Yukon) data are from Thorkelson et al. (2005).

B.4.1.2. Data from this study presented in Figure 4.3 and in Figure B.1:

Detailed data for this study are presented in Tables B.1, B.2 & B.3.

B.4.1.2.a. Scheelite data

Scheelite from Cantung are from the garnet-pyroxene skarn, the pyroxene skarn, the amphibole-rich facies, the biotite-rich facies, argillite, and a quartz vein in Mine Stock pluton. Scheelite from Mactung are from the garnet-pyroxene skarn, the pyroxene skarn, the amphibole-rich facies, and argillite.

Details about these different facies can be found in Elongo et al. (2020).

B.4.1.2.b. Whole rock data

1/ Lamprophyre: Cretaceous lamprophyre from the Cantung deposit;

2/ Felsic intrusions data include data from the Cretaceous Mine Stock pluton and aplite from Cantung, and from the Cretaceous Mactung North and South plutons;

3/ Metasediments data include data from the Cambrian Swiss-Cheese limestone and argillites from Cantung and the Cambrian argillites from Mactung.

B.4.2. Data presented in Figure 4.4:

The source data from Figure 4.4 are presented in Table B.4.

The oxidation state of the plutons was assessed based on the $\log_{10}$(Fe2O3/FeO) vs FeO_{total} classification scheme from Blevin (2004). Iron oxides and zircon saturation temperatures (ZST) data are taken from Rasmussen (2013) (NWT and Yukon, Canada), Hart et al. (2004), Bateman et al. (1965) and Chapman et al. (2021) (Western USA and Mexico). Chapman et al. (2021) data are a compilation of data from G. Haxel (unpublished), Shaw and Guilbert (1990), Force (1997), Keith and Reynolds (1980), Best et al. (1974), Lee et al. (1981), Lee and Van Loenen (1971), and from John and Wooden (1990). Some units/plutons compiled by Chapman et al. (2021) are represented by several samples with different iron oxides content and different ZST. For these units/plutons, samples with the same oxidation state were lumped together and an average ZST was given for each oxidation state. For each of these units/plutons, the percentage represented by samples with the same oxidation state is also given and presented as a partitioned circle in Figure 4.4.

Zircon saturation temperatures (Watson and Harrison, 1983) presented in these studies are calculated from whole rock compositions based on the concentrations of zirconium, silica, aluminum and alkalies in the rock.

Zircon solubility is a function of temperature and composition of melt as defined by the following equation:

$\ln D^{Zr,zircon/melt} = \{-3.8 - [0.85(M-1)]\} + 12900/T$ (Watson and Harrison, 1983)

where $D^{Zr,zircon/melt}$ is the ratio of Zr concentration in zircon (~496000 ppm) to that in the melt, M is the cation ratio (Na+K+2·Ca)/(Al·Si) accounting for dependence of zircon solubility on SiO_2 and peraluminosity of the melt (Miller et al., 2003), and T is the temperature (Kelvins). Rearranging the equation to yield T provides the zircon saturation temperature geothermometer equation: $T_{Zr}=12900/[2.95 + 0.85M + \ln(496000/Zr_{melt})]$.

Zircon saturation temperatures can be used to estimate initial melt temperatures; however, these estimates are influenced by the inherited zircon content of the melt (Miller et al., 2003). The zircon saturation temperature geothermometer provides a good estimate of initial magma temperature at the source for plutons with abundant inherited zircon and provides an underestimate initial temperature for plutons poor in inherited zircon (Miller et al., 2003). Thus, it provides minimum estimates of initial temperature if the magma was undersaturated, but maximum estimates of initial temperature if the magma was saturated (Miller et al., 2003).

B.5. References

Abraham, A. C., Francis, D., & Polvé, M. (2001). Recent alkaline basalts as probes of the lithospheric mantle roots of the northern Canadian Cordillera. Chemical Geology, 175(3-4), 361-386.

Atkinson, D., & Baker, D.J. (1986). Recent developments in the geologic understanding of Mactung. Mineral Deposits of the Northern Cordillera. Canadian Institute of Mining, Metallurgy and Petroleum, 37, 234-244.

Bateman, P. C., Pakiser, L. C., & Kane, M. F. (1965). Geology and tungsten mineralization of the Bishop district, California, with a section on gravity study of Owens Valley and a section on seismic profile (No. 470). US Govt. Print. Off., 208p.

Best, M. G., & Brimhall, W. H. (1974). Late Cenozoic alkalic basaltic magmas in the western Colorado Plateaus and the Basin and Range transition zone, USA, and their bearing on mantle dynamics. Geological Society of America Bulletin, 85(11), 1677-1690.

Blevin, P. L. (2004). Redox and compositional parameters for interpreting the granitoid metallogeny of eastern Australia: Implications for gold-rich ore systems. Resource Geology, 54(3), 241-252.

Blusson, S. L. (1968). Geology and tungsten deposits near the headwaters of Flat River, Yukon Territory and southwestern district of Mackenzie, Canada (Vol. 67, No. 22). Department of Energy, Mines and Resources

Chapman, J. B., Ducea, M. N., Kapp, P., Gehrels, G. E., & DeCelles, P. G. (2017). Spatial and temporal radiogenic isotopic trends of magmatism in Cordilleran orogens. Gondwana Research, 48, 189-204.

Chapman, J. B., Runyon, S. E., Shields, J., Lawler, B. L., Pridmore, C. J., Scoggin, S. H., Swaim, N.T., Trzinski, A.E., Wiley, H.N., Barth, A.P., & Haxel, G. B. (2021). The North American Cordilleran Anatectic Belt. Earth-Science Reviews, 215, 103576.

Cousens, B. L. (2007). Radiogenic isotope studies of Pb-Zn mineralization in the Howards Pass area, Selwyn Basin. Mineral and Energy Resource Potential of the Proposed Expansion to the Nahanni National Park Reserve, North Cordillera, Northwest Territories: Geological Survey of Canada, Open File, 5344, 14.

Cousens, B. L., & Bevier, M. L. (1995). Discerning asthenospheric, lithospheric, and crustal influences on the geochemistry of Quaternary basalts from the Iskut–Unuk rivers area, northwestern British Columbia. Canadian Journal of Earth Sciences, 32(9), 1451-1461.

Creaser, R. A., Erdmer, P., Stevens, R. A., & Grant, S. L. (1997). Tectonic affinity of Nisutlin and Anvil assemblage strata from the Teslin tectonic zone, northern Canadian Cordillera: Constraints from neodymium isotope and geochemical evidence. Tectonics, 16(1), 107-121.

Dick, L. A., & Hodgson, C. J. (1982). The MacTung W-Cu (Zn) contact metasomatic and related deposits of the northeastern Canadian Cordillera. Economic Geology, 77(4), 845-867.

Dudás, F. Ö., & Lustwerk, R. L. (1997). Geochemistry of the Little Dal basalts: continental tholeiites from the Mackenzie Mountains, Northwest Territories, Canada. Canadian Journal of Earth Sciences, 34(1), 50-58.

Elongo, V., Lecumberri-Sanchez, P., Legros, H., Falck, H., Adlakha, E., Roy-Garand, A., n.d. Paragenetic constraints on the Cantung, Mactung and Lened tungsten skarn deposits, Canada: implications for grade distribution. Ore Geol. Rev.

Estève, C., Audet, P., Schaeffer, A. J., Schutt, D. L., Aster, R. C., & Cubley, J. F. (2020). Seismic evidence for craton chiseling and displacement of lithospheric mantle by the Tintina fault in the northern Canadian Cordillera. Geology, 48(11), 1120-1125.

Fischer, B.J., Martel, E., and Falck, H., (2018). Geology of the Mactung tungsten skarn and area – Review and 2016 field observations; Northwest Territories Geological Survey, NWT Open File 2018-02, 84 pages and appendices.

Fisher, C. M., Vervoort, J. D., & DuFrane, S. A. (2014). Accurate Hf isotope determinations of complex zircons using the “laser ablation split stream” method. Geochemistry, Geophysics, Geosystems, 15(1), 121-139.

Force, E. R. (1997). Geology and mineral resources of the Santa Catalina Mountains, southeastern Arizona: A cross-sectional approach. Earth, Planets and Space, 57(8), 701-715.

Garzione, C. N., Patchett, P. J., Ross, G. M., & Nelson, J. (1997). Provenance of Paleozoic sedimentary rocks in the Canadian Cordilleran miogeocline: a Nd isotopic study. Canadian Journal of Earth Sciences, 34(12), 1603-1618.

Gebru, A. L. (2017). Petrogenesis of Granitoids in the Vicinity of the Mactung Tungsten Skarn Deposit, NE Yukon-Northwest Territories: Characterization of Skarn Mineralization and Causative Plutons through Geological, Petrochemical, Mineralogical, and Geochronological Analysis. Unpublished PhD Thesis, University of New Brunswick, New Brunswick, Canada.

Goldstein, S. L., O'nions, R. K., & Hamilton, P. J. (1984). A Sm-Nd isotopic study of atmospheric dusts and particulates from major river systems. Earth and Planetary Science Letters, 70(2), 221-236.

Gordey, S. P., & Anderson, R. G. (1993). Evolution of the northern Cordilleran miogeocline, Nahanni map area (105I), Yukon and Northwest Territories. Geological Survey of Canada Memoir 428, 214p.

Hart, C. J., Mair, J. L., Goldfarb, R. J., & Groves, D. I. (2004). Source and redox controls on metallogenic variations in intrusion-related ore systems, Tombstone-Tungsten Belt, Yukon Territory, Canada. Earth and Environmental Science Transactions of The Royal Society of Edinburgh, 95(1-2), 339-356.

Jacobsen, S. B., & Wasserburg, G. J. (1980). Sm-Nd isotopic evolution of chondrites. Earth and Planetary Science Letters, 50(1), 139-155.

John, B. E., & Wooden, J. (1990). Petrology and geochemistry of the metaluminous to peraluminous Chemehuevi Mountains Plutonic Suite, southeastern California. The Nature and Origin of Cordilleran Magmatism. Geological Society of America, Memoir, 174, 71-98.

Keith, S. B., & Reynolds, S. J. (1980). Geochemistry of Cordilleran metamorphic core complexes. Cordilleran metamorphic core complexes and their uranium favorability: US Department of Energy Open-File Report GJBX-256 (80), 321.

Kempe, U., Belyatsky, B., Krymsky, R., Kremenetsky, A., & Ivanov, P. (2001). Sm–Nd and Sr isotope systematics of scheelite from the giant Au (–W) deposit Muruntau (Uzbekistan): implications for the age and sources of Au mineralization. Mineralium Deposita, 36(5), 379-392.

Lee, D. E., & Van Loenen, R. E. (1971). Hybrid granitoid rocks of the southern Snake Range, Nevada (pp. 1-46). US Government Printing Office.

Lee, D. E., Kistler, R. W., Friedman, I., & Van Loenen, R. E. (1981). Two-mica granites of northeastern Nevada. Journal of Geophysical Research: Solid Earth, 86(B11), 10607-10616.

Lentz, C. (2020). Genesis of Gold Mineralization at the Cantung W-Cu skarn deposit, N.W.T. Unpublished MSc Thesis, University of New Brunswick, New Brunswick, Canada.

Luo, Y., Pearson, D.G., Scott, J., Palmer, M.C., Fisher, C.M., Sarkar, C., Vezinet, A., Lecumberri-Sanchez, P., 2019. Simultaneous In situ Analysis of Sm-Nd isotopes and

Trace Elements in Scheelite by Laser Ablation Split Stream ICP-MS: Challenges and Emerging Approaches., 2019 North America laser ablation workshop, Austin, p. 34.

Mair, J. L., Farmer, G. L., Groves, D. I., Hart, C. J., & Goldfarb, R. J. (2011). Petrogenesis of postcollisional magmatism at Scheelite Dome, Yukon, Canada: evidence for a lithospheric mantle source for magmas associated with intrusion-related gold systems. Economic Geology, 106(3), 451-480.

Mathieson, G. A., & Clark, A. H. (1984). The Cantung E Zone scheelite skarn orebody, Tungsten, Northwest Territories; a revised genetic model. Economic Geology, 79(5), 883-901.

Miller, C. F., McDowell, S. M., & Mapes, R. W. (2003). Hot and cold granites? Implications of zircon saturation temperatures and preservation of inheritance. Geology, 31(6), 529-532.

Morris, G. A., & Creaser, R. A. (2008). Correlation of mid-Cretaceous granites with source terranes in the northern Canadian Cordillera. Canadian Journal of Earth Sciences, 45(3), 389-403.

Morris, G. A., & Creaser, R. A. (2003). Crustal recycling during subduction at the Eocene Cordilleran margin of North America: a petrogenetic study from the southwestern Yukon. Canadian Journal of Earth Sciences, 40(12), 1805-1821.

Rainbird, R. H., McNicoll, V. J., Theriault, R. J., Heaman, L. M., Abbott, J. G., Long, D. G. F., & Thorkelson, D. J. (1997). Pan-continental river system draining Grenville Orogen recorded by U-Pb and Sm-Nd geochronology of Neoproterozoic quartzarenites and mudrocks, northwestern Canada. The Journal of Geology, 105(1), 1-17.

Rasmussen, K. L., Lentz, D. R., Falck, H., & Pattison, D. R. (2011). Felsic magmatic phases and the role of late-stage aplitic dykes in the formation of the world-class Cantung

Tungsten skarn deposit, Northwest Territories, Canada. Ore Geology Reviews, 41(1), 75-111.

Rasmussen, K.L. (2013) The timing, composition, and petrogenesis of syn- to post-accretionary magmatism in the northern Cordilleran miogeocline, eastern Yukon and southwestern Northwest Territories. Ph.D. Thesis, University of British Columbia, Vancouver, British Columbia, Canada, 788 pp.

Selby, D., Creaser, R. A., Heaman, L. M., & Hart, C. J. (2003). Re-Os and U-Pb geochronology of the Clear Creek, Dublin Gulch, and Mactung deposits, Tombstone Gold Belt, Yukon, Canada: absolute timing relationships between plutonism and mineralization. Canadian Journal of Earth Sciences, 40(12), 1839-1852.

Shaw, A. L., & Guilbert, J. M. (1990). Geochemistry and metallogeny of Arizona peraluminous granitoids with reference to Appalachian and European occurrences. Ore-bearing granite systems: petrogenesis and mineralizing processes. Geological Society of America, Special Paper, 246, 317-356.

Sinclair, W D; Gonevchuck, G A; Korostelev, P G; Semenyak, B I; Rodlonov, S; Seltmann, R; Stemprok, M. (2011). World distribution of tin and tungsten deposits. Geological Survey of Canada, Open File 5482, https://doi.org/10.4095/287906

Sinclair, W D; Gonevchuk, G A; Korostelev, P G; Semenyak, B I; Rodionov, S M; Seltmann, R; Stemprok, M. (2014). Geological Survey of Canada, Open File 7688, https://doi.org/10.4095/295581

Tanaka, T., Togashi, S., Kamioka, H., Amakawa, H., Kagami, H., Hamamoto, T., ... & Kunimaru, T. (2000). JNdi-1: a neodymium isotopic reference in consistency with LaJolla neodymium. Chemical Geology, 168(3-4), 279-281.

Thériault, R. J., & Ross, G. M. (1991). Nd isotopic evidence for crustal recycling in the ca. 2.0 Ga subsurface of western Canada. Canadian Journal of Earth Sciences, 28(8), 1140-1147.

Thorkelson, D. J., Abbott, J. G., Mortensen, J. K., Creaser, R. A., Villeneuve, M. E., McNicoll, V. J., & Layer, P. W. (2005). Early and middle Proterozoic evolution of Yukon, Canada. Canadian Journal of Earth Sciences, 42(6), 1045-1071.

Thorkelson, D. J., Mortensen, J. K., Creaser, R. A., Davidson, G. J., & Abbott, J. G. (2001). Early Proterozoic magmatism in Yukon, Canada: constraints on the evolution of northwestern Laurentia. Canadian Journal of Earth Sciences, 38(10), 1479-1494.

Unterschutz, J. L., Creaser, R. A., Erdmer, P., Thompson, R. I., & Daughtry, K. L. (2002). North American margin origin of Quesnel terrane strata in the southern Canadian Cordillera: Inferences from geochemical and Nd isotopic characteristics of Triassic metasedimentary rocks. Geological Society of America Bulletin, 114(4), 462-475.

Villeneuve, M. E. (1993). Tectonic subdivision and U-Pb geochronology of the crystalline basement of the Alberta Basin, Western Canada (Vol. 447). Geological Survey of Canada.

Villeneuve, M. E., Thériault, R. J., & Ross, G. M. (1991). U–Pb ages and Sm–Nd signature of two subsurface granites from the Fort Simpson magnetic high, northwest Canada. Canadian Journal of Earth Sciences, 28(7), 1003-1008.

Wasserburg, G. J., Jacobsen, S. B., DePaolo, D. J., McCulloch, M. T., & Wen, T. (1981). Precise determination of SmNd ratios, Sm and Nd isotopic abundances in standard solutions. Geochimica et Cosmochimica Acta, 45(12), 2311-2323.

Watson, E. B., & Harrison, T. M. (1983). Zircon saturation revisited: temperature and composition effects in a variety of crustal magma types. Earth and Planetary Science Letters, 64(2), 295-304.

Whitmeyer, S. J., & Karlstrom, K. E. (2007). Tectonic model for the Proterozoic growth of North America. Geosphere, 3(4), 220-259.

Xie, L., Zhang, Y., Zhang, H., Sun, J., & Wu, F. (2008). In situ simultaneous determination of trace elements, U-Pb and Lu-Hf isotopes in zircon and baddeleyite. Chinese Science Bulletin, 53(10), 1565-1573.

Yuan, H. L., Gao, S., Dai, M. N., Zong, C. L., Günther, D., Fontaine, G. H., ... & Diwu, C. (2008). Simultaneous determinations of U–Pb age, Hf isotopes and trace element compositions of zircon by excimer laser-ablation quadrupole and multiple-collector ICP-MS. Chemical Geology, 247(1-2), 100-118.

Table B.1. Samarium-neodymium isotope data for whole rocks from Cantung and Mactung analyzed in this study through solution inductively coupled plasma mass spectrometry (solution ICP MS). Present-day Depleted Mantle parameters used are $^{147}Sm/^{144}Nd$ = 0.2136, $^{143}Nd/^{144}Nd$ = 0.513163 (Goldstein et al., 1984). Present-day CHUR parameters used are $^{147}Sm/^{144}Nd$ = 0.1966 and $^{143}Nd/^{144}Nd$ = 0.512638 (Jacobsen and Wasserburg, 1980). The "0" indice represents the present-day value, and the "t" indice represents initial value (at the time of formation). ~Age t (Ma) represents an average of the age for samples that have age (t) data with errors.

Deposit	Label in Figure 4.3 & Figure B.1	Sample name	Lithology	Sm (ppm)	Nd (ppm)	$^{147}Sm/^{144}Nd$	$^{143}Nd/^{144}Nd_0$	2SE on $^{143}Nd/^{144}Nd_0$	εNd_0	2SE on εNd_0	~Age t (Ma)	$^{143}Nd/^{144}Nd_t$	εNd_t	2SE on εNd_t	T_{DM} (Ga)	CHUR at age t	Age t range (Ma)	Age reference
Mactung	Felsic intrusions	18-MA-13	Granitoid (Mactung North Pluton)	2.05	9.24	0.1344	0.511603	0.000010	-20.2	0.2	97.6	0.511517	-19.4	0.2	3.0	0.512512	97.6 ± 0.2	Gebru (2017)
		18-MA-03	Granitoid (Mactung South Pluton)	3.22	15.74	0.1239	0.511593	0.000010	-20.4	0.2	97.6	0.511514	-19.5	0.2	2.6	0.512512	97.6 ± 0.2	Gebru (2017)
	Metasediments	MS161 322-322.3 A	Argillite (Unit 1)	6.67	37.98	0.1061	0.511656	0.000008	-19.2	0.2	582	0.511252	-12.4	0.2	2.1	0.511888	635-529	Gordey and Anderson (1993)
		MS177 86.2-86.3	Argillite (Unit 1)	7.93	43.88	0.1093	0.511647	0.000010	-19.3	0.2	582	0.511231	-12.8	0.2	2.2	0.511888	635-529	Gordey and Anderson (1993)
		18-MA-10	Argillite (Unit 1)	8.50	51.51	0.0998	0.511320	0.000009	-25.7	0.2	582	0.510939	-18.5	0.2	2.5	0.511888	635-529	Gordey and Anderson (1993)
Cantung	Felsic intrusions	S12-39 913	Granitoid (Mine Stock pluton)	3.45	15.91	0.1309	0.511842	0.000009	-15.5	0.2	98.2	0.511757	-14.7	0.2	2.4	0.512512	98.2 ± 0.4	Rasmussen (2013)
		S13-06 666.5-668	Granitoid (Mine Stock pluton)	4.60	23.71	0.1173	0.511853	0.000007	-15.3	0.1	98.2	0.511778	-14.3	0.1	2.1	0.512512	98.2 ± 0.4	Rasmussen (2013)
		18-CA-11	Aplite dyke	5.91	31.63	0.1129	0.511824	0.000011	-15.9	0.2	98.3	0.511751	-14.8	0.2	2.0	0.512512	97.3 ± 0.3	Rasmussen (2013)
	Lamprophyre	18-CA-37	Lamprophyre dyke	6.06	29.56	0.1240	0.512056	0.000010	-11.4	0.2	96.7	0.511977	-10.5	0.2	1.9	0.512514	96.7 ± 0.8	Rasmussen (2013)
	Metasediments	18-CA-05	Limestone (Swiss-Cheese)	5.41	26.74	0.1222	0.511666	0.000005	-19.0	0.1	525	0.511245	-14.0	0.1	2.5	0.511961	541-509	Blusson (1968)
		U2602-140	Argillite (Upper)	6.06	33.15	0.1105	0.511540	0.000008	-21.4	0.2	525	0.511160	-15.7	0.2	2.4	0.511961	541-509	Blusson (1968)
		18-CA-10	Argillite (Lower)	5.32	30.19	0.1066	0.511601	0.000008	-20.2	0.2	582	0.511195	-13.5	0.2	2.2	0.511888	635-529	Blusson (1968)

Table B.2. Samarium-neodymium isotope data for scheelite from Cantung and Mactung analyzed in this study through solution inductively coupled plasma mass spectrometry (solution ICP MS). Present-day Depleted Mantle parameters used are $^{147}Sm/^{144}Nd = 0.2136$, $^{143}Nd/^{144}Nd = 0.513163$ (Goldstein et al., 1984). Present-day CHUR parameters used are $^{147}Sm/^{144}Nd = 0.1966$ and $^{143}Nd/^{144}Nd = 0.512638$ (Jacobsen and Wasserburg, 1980). The "0" indice represents the present-day value, and the "t" indice represents initial value (at the time of formation). ~Age t (Ma) represents an average of the age for samples that have age (t) data with errors. T_{DM} not calculated for samples with $^{147}Sm/^{144}Nd > 0.14$.

Deposit	**Sample name**	**Facies**	**Sm (ppm)**	**Nd (ppm)**	**$^{147}Sm/^{144}Nd$**	**$^{143}Nd/^{144}Nd_0$**	**2SE on $^{143}Nd/^{144}Nd_0$**	**εNd_0**	**2SE on εNd_0**	**~Age t (Ma)**	**$^{143}Nd/^{144}Nd_t$**	**εNd_t**	**2SE on εNd_t**	**T_{DM} (Ga)**	**CHUR at age t**	**Age t range (Ma)**	**Age reference**
Mactung	MS161 322-322.3 A	Argillite (Unit 1)	10.79	55.77	0.1170	0.511676	0.000005	-18.8	0.1	97.5	0.511602	-17.8	0.1	2.3	0.512513	97.5 ± 0.5	Selby et al. (2003)
	MS231 60-60.3	Pyroxene skarn (Unit 3E)	15.56	80.06	0.1175	0.511839	0.000006	-15.6	0.1	97.5	0.511764	-14.6	0.1	2.1	0.512513	97.5 ± 0.5	Selby et al. (2003)
	18-MA-02	Garnet-pyroxene skarn (Unit 3E)	22.76	100.25	0.1373	0.511608	0.000006	-20.1	0.1	97.5	0.511520	-19.4	0.1	3.1	0.512513	97.5 ± 0.5	Selby et al. (2003)
	MS161 185.6-185.9	Amphibole-rich facies (Unit 3F)	10.79	55.77	0.1170	0.511676	0.000005	-18.8	0.1	97.5	0.511602	-17.8	0.1	2.3	0.512513	97.5 ± 0.5	Selby et al. (2003)
Cantung	18-CA-28	Biotite-rich facies (Ore Limestone)	97.35	252.82	0.2328	0.511646	0.000007	-19.4	0.1	94.6	0.511502	-19.8	0.1	N/A	0.512516	94.6 ± 2.1	*This PhD thesis*
	18-CA-29b	Amphibole-rich facies (Swiss-Cheese Limestone)	6.87	37.17	0.1117	0.512139	0.000006	-9.7	0.1	94.6	0.512070	-8.7	0.1	1.5	0.512516	94.6 ± 2.1	*This PhD thesis*
	18-CA-31a	Pyroxene skarn (Swiss-Cheese Limestone)	92.17	231.88	0.2403	0.511646	0.000006	-19.3	0.1	94.6	0.511498	-19.9	0.1	N/A	0.512516	94.6 ± 2.1	*This PhD thesis*
	18-CA-47	Garnet-pyroxene skarn (Ore Limestone)	25.86	87.81	0.1781	0.511820	0.000009	-15.9	0.2	94.6	0.511710	-15.7	0.2	N/A	0.512516	94.6 ± 2.1	*This PhD thesis*
	18-CA-50	Quartz vein in Mine Stock pluton	227.22	493.94	0.2781	0.511899	0.000005	-14.4	0.1	94.6	0.511727	-15.4	0.1	N/A	0.512516	94.6 ± 2.1	*This PhD thesis*
	18-CA-50	Quartz vein in Mine Stock pluton	237.95	604.48	0.2380	0.511855	0.000006	-15.3	0.1	94.6	0.511708	-15.8	0.1	N/A	0.512516	94.6 ± 2.1	*This PhD thesis*
	18-CA-10	Argillite (Lower)	11.74	38.31	0.1852	0.511700	0.000006	-18.3	0.1	94.6	0.511585	-18.2	0.1	N/A	0.512516	94.6 ± 2.1	*This PhD thesis*
	18-CA-51	Argillite (Upper)	5.13	16.88	0.1837	0.511699	0.000049	-18.3	1.0	94.6	0.511585	-18.2	1.0	N/A	0.512516	94.6 ± 2.1	*This PhD thesis*

Table B.3. Samarium-neodymium isotope data for scheelite from Cantung and Mactung analyzed in this study through laser ablation split stream inductively coupled plasma mass spectrometry (LASS ICP MS). Average values are used for each sample for plotting purposes in figures 4.3 & B.1. Present-day Depleted Mantle parameters used are $^{147}Sm/^{144}Nd$ = 0.2136, $^{143}Nd/^{144}Nd$ = 0.513163 (Goldstein et al., 1984). Present-day CHUR parameters used are $^{147}Sm/^{144}Nd$ = 0.1966 and $^{143}Nd/^{144}Nd$ = 0.512638 (Jacobsen and Wasserburg, 1980). The "0" indice represents the present-day value, and the "t" indice represents initial value (at the time of formation). ~Age t (Ma) represents an average of the age for samples that have age (t) data with errors. T_{DM} not calculated for samples with $^{147}Sm/^{144}Nd$ > 0.14.

Deposit	Sample name	Facies	Sm (ppm)	Nd (ppm)	$^{147}Sm/^{144}Nd$	$^{143}Nd/^{144}Nd_0$	2SE on $^{143}Nd/^{144}Nd_0$	εNd_0	2SE on εNd_0	~Age t (Ma)	$^{143}Nd/^{144}Nd_t$	εNd_t	2SE on εNd_t	T_{DM} (Ga)	CHUR at age t	Age t range (Ma)	Age reference
Mactung	MS231 60-60.3	Pyroxene skarn (Unit 3E)	10.01	47.22	0.1341	0.511980	0.000100	-12.8	2.0	98	0.511894	-12.1	2.0	2.3	0.512513	97.5 ± 0.5	Selby et al. (2003)
	MS231 60-60.3	Pyroxene skarn (Unit 3E)	14.36	79.70	0.1162	0.511957	0.000085	-13.3	1.7	98	0.511883	-12.3	1.7	1.9	0.512513	97.5 ± 0.5	Selby et al. (2003)
	MS231 60-60.3	Pyroxene skarn (Unit 3E)	15.19	75.60	0.1048	0.511950	0.000110	-13.4	2.1	98	0.511883	-12.3	2.1	1.7	0.512513	97.5 ± 0.5	Selby et al. (2003)
	MS231 60-60.3	Pyroxene skarn (Unit 3E)	16.37	78.80	0.1191	0.511890	0.000120	-14.6	2.3	98	0.511814	-13.6	2.3	2.0	0.512513	97.5 ± 0.5	Selby et al. (2003)
	MS231 60-60.3	Pyroxene skarn (Unit 3E)	12.72	58.10	0.1277	0.511890	0.000100	-14.6	2.0	98	0.511809	-13.7	2.0	2.2	0.512513	97.5 ± 0.5	Selby et al. (2003)
	MS161 322-322.3 A	Argillite (Unit 1)	28.45	100.50	0.1581	0.511655	0.000033	-19.2	0.6	98	0.511554	-18.7	0.6	N/A	0.512513	97.5 ± 0.5	Selby et al. (2003)
	MS161 322-322.3 A	Argillite (Unit 1)	14.29	36.28	0.1722	0.511590	0.000100	-20.4	2.0	98	0.511480	-20.1	2.0	N/A	0.512513	97.5 ± 0.5	Selby et al. (2003)
	MS161 322-322.3 A	Argillite (Unit 1)	19.75	67.30	0.1726	0.511620	0.000120	-19.9	2.3	98	0.511510	-19.6	2.3	N/A	0.512513	97.5 ± 0.5	Selby et al. (2003)
	MS161 322-322.3 A	Argillite (Unit 1)	12.23	42.60	0.2505	0.511660	0.000067	-19.1	1.3	98	0.511500	-19.8	1.3	N/A	0.512513	97.5 ± 0.5	Selby et al. (2003)
Cantung	18-CA-50	Quartz vein in Mine Stock pluton	268.70	809.30	0.2000	0.511804	0.000022	-16.3	0.4	95	0.511680	-16.3	0.4	N/A	0.512516	94.6 ± 2.1	*This PhD thesis*
	18-CA-50	Quartz vein in Mine Stock pluton	303.20	874.00	0.2124	0.511807	0.000025	-16.2	0.5	95	0.511676	-16.4	0.5	N/A	0.512516	94.6 ± 2.1	*This PhD thesis*
	18-CA-50	Quartz vein in Mine Stock pluton	284.90	837.00	0.2058	0.511820	0.000028	-16.0	0.5	95	0.511693	-16.1	0.5	N/A	0.512516	94.6 ± 2.1	*This PhD thesis*
	18-CA-50	Quartz vein in Mine Stock pluton	330.00	878.00	0.2276	0.511799	0.000026	-16.4	0.5	95	0.511658	-16.7	0.5	N/A	0.512516	94.6 ± 2.1	*This PhD thesis*
	18-CA-50	Quartz vein in Mine Stock pluton	315.40	798.00	0.2379	0.511857	0.000020	-15.2	0.4	95	0.511710	-15.7	0.4	N/A	0.512516	94.6 ± 2.1	*This PhD thesis*

Table B.3. (continued)

Cantung	18-CA-50	Quartz vein in Mine Stock pluton	307.00	891.00	0.2049	0.511842	0.000028	-15.5	0.5	95	0.511715	-15.6	0.5	N/A	0.512516	94.6 ± 2.1	*This PhD thesis*
	18-CA-50	Quartz vein in Mine Stock pluton	238.00	517.30	0.2761	0.511834	0.000038	-15.7	0.7	95	0.511663	-16.6	0.7	N/A	0.512516	94.6 ± 2.1	*This PhD thesis*
	18-CA-50	Quartz vein in Mine Stock pluton	358.00	1020.00	0.2222	0.511791	0.000029	-16.5	0.6	95	0.511653	-16.8	0.6	N/A	0.512516	94.6 ± 2.1	*This PhD thesis*
	18-CA-50	Quartz vein in Mine Stock pluton	355.40	921.00	0.2299	0.511818	0.000019	-16.0	0.4	95	0.511676	-16.4	0.4	N/A	0.512516	94.6 ± 2.1	*This PhD thesis*
	18-CA-50	Quartz vein in Mine Stock pluton	268.90	768.40	0.2119	0.511826	0.000027	-15.8	0.5	95	0.511695	-16.0	0.5	N/A	0.512516	94.6 ± 2.1	*This PhD thesis*
	18-CA-50	Quartz vein in Mine Stock pluton	287.30	721.20	0.2390	0.511860	0.000027	-15.2	0.5	95	0.511712	-15.7	0.5	N/A	0.512516	94.6 ± 2.1	*This PhD thesis*
	18-CA-50	Quartz vein in Mine Stock pluton	314.10	793.00	0.2359	0.511849	0.000023	-15.4	0.4	95	0.511703	-15.9	0.4	N/A	0.512516	94.6 ± 2.1	*This PhD thesis*
	18-CA-50	Quartz vein in Mine Stock pluton	275.50	677.00	0.2518	0.511837	0.000037	-15.6	0.7	95	0.511681	-16.3	0.7	N/A	0.512516	94.6 ± 2.1	*This PhD thesis*
	18-CA-50	Quartz vein in Mine Stock pluton	261.90	787.00	0.2036	0.511824	0.000029	-15.9	0.6	95	0.511698	-16.0	0.6	N/A	0.512516	94.6 ± 2.1	*This PhD thesis*
	18-CA-50	Quartz vein in Mine Stock pluton	236.60	741.00	0.1948	0.511809	0.000031	-16.2	0.6	95	0.511688	-16.2	0.6	N/A	0.512516	94.6 ± 2.1	*This PhD thesis*
	18-CA-50	Quartz vein in Mine Stock pluton	299.40	785.00	0.2294	0.511834	0.000031	-15.7	0.6	95	0.511692	-16.1	0.6	N/A	0.512516	94.6 ± 2.1	*This PhD thesis*
	18-CA-50	Quartz vein in Mine Stock pluton	201.20	606.10	0.2016	0.511808	0.000034	-16.2	0.7	95	0.511683	-16.3	0.7	N/A	0.512516	94.6 ± 2.1	*This PhD thesis*
	18-CA-50	Quartz vein in Mine Stock pluton	308.50	780.00	0.2356	0.511853	0.000029	-15.3	0.6	95	0.511707	-15.8	0.6	N/A	0.512516	94.6 ± 2.1	*This PhD thesis*
	18-CA-10	Argillite (Lower)	73.00	251.70	0.1814	0.511687	0.000045	-18.6	0.9	95	0.511575	-18.4	0.9	N/A	0.512516	94.6 ± 2.1	*This PhD thesis*
	18-CA-10	Argillite (Lower)	67.60	255.00	0.1648	0.511580	0.000110	-20.6	2.1	95	0.511478	-20.3	2.1	N/A	0.512516	94.6 ± 2.1	*This PhD thesis*

Table B.4. Zircon saturation temperatures and oxidation state of peraluminous granites in the North American Cordillera. Italicized data are data from literature; other data are calculated/inferred in this study. The oxidation state of the plutons was assessed based on the log10(Fe2O3/FeO) vs FeOtotal classification scheme from Blevin (2004). Iron oxides and zircon saturation temperatures (ZST) data are taken from Rasmussen (2013) (NWT and Yukon, Canada), Hart et al. (2004), Bateman et al. (1965) and Chapman et al. (2021) (Western USA and Mexico). Chapman et al. (2021) data are a compilation of data from G. Haxel (unpublished), Shaw and Guilbert (1990), Force (1997), Keith and Reynolds (1980), Best et al. (1974), Lee et al. (1981), Lee and Van Loenen (1971), and from John and Wooden (1990).

State/Province, Country	Unit/ Pluton	Sample name	Latitude	Longitude	Zircon Saturation Temperature (°C)	Fe_2O_3	FeO	FeO(t)	$Log_{10}(Fe_2O_3/FeO)$	Oxidation state	Raw data source
NWT, Canada	O'Grady batholith	KR-05-97b	*62.95*	*-128.71*	*790*	*1.23*	*2.82*	*4.37*	-0.36	Moderately oxidized	Rasmussen (2013)
NWT, Canada	Hole-in-the-Wall batholith	KR-05-198	*61.62*	*-127.18*	*860*	*0.27*	*3.08*	*3.70*	-1.06	Moderately reduced	Rasmussen (2013)
NWT, Canada	Pelly River pluton	KR-05-76	*62.76*	*-129.64*	*786*	*7.20*	*2.37*	*9.84*	0.48	Very strongly oxidized	Rasmussen (2013)
NWT, Canada	Mount Christie pluton	KR-05-62	*62.99*	*-129.48*	*786*	*0.36*	*4.22*	*5.06*	-1.07	Moderately reduced	Rasmussen (2013)
NWT, Canada	Central Nahanni pluton	KR-05-130	*62.69*	*-128.63*	*813*	*0.44*	*3.32*	*4.14*	-0.88	Moderately reduced	Rasmussen (2013)
NWT, Canada	North Nahanni pluton	KR-05-136	*62.77*	*-128.64*	*827*	*0.54*	*2.81*	*3.67*	-0.72	Moderately reduced	Rasmussen (2013)
NWT, Canada	Mount Wilson pluton	KR-05-68	*62.89*	*-129.69*	*851*	*0.20*	*2.56*	*3.05*	-1.11	Strongly reduced	Rasmussen (2013)
NWT, Canada	Jorgensen pluton	KR-05-08	*60.87*	*-126.29*	*781*	*0.35*	*3.27*	*3.99*	-0.97	Moderately reduced	Rasmussen (2013)
NWT, Canada	Park pluton	KR-05-43	*61.47*	*-126.43*	*800*	*1.54*	*2.63*	*4.47*	-0.23	Moderately oxidized	Rasmussen (2013)
NWT, Canada	Coal River batholith	KR-05-196	*61.54*	*-127.24*	*827*	*0.77*	*2.37*	*3.41*	-0.49	Moderately reduced	Rasmussen (2013)
NWT, Canada	Roy pluton	KR-05-22	*61.58*	*-127.66*	*843*	*0.81*	*1.34*	*2.30*	-0.22	Moderately oxidized	Rasmussen (2013)
NWT, Canada	Fish pluton	KR-05-26	*61.63*	*-127.49*	*842*	*0.55*	*1.34*	*2.04*	-0.39	Moderately oxidized	Rasmussen (2013)
NWT, Canada	Faille pluton	0.3M-216	*62.19*	*-127.66*		*0.53*	*2.65*	*3.49*	-0.70	Moderately reduced	Rasmussen (2013)
NWT, Canada	Mount Sir James McBrien pluton	0.3M-217	*62.10*	*-127.69*		*0.83*	*2.34*	*3.44*	-0.45	Moderately reduced	Rasmussen (2013)

Table B.4. (continued)

NWT, Canada	Hole-in-the-Wall batholith	KR-05-164	61.74	-127.36	826	0.16	1.53	1.86	-0.98	Moderately reduced	Rasmussen (2013)
NWT, Canada	Cac pluton	KR-05-110	62.37	-128.55	833	0.22	2.57	3.08	-1.07	Moderately reduced	Rasmussen (2013)
NWT, Canada	Lened pluton	KR-05-175	62.38	-128.65	843	0.29	2.57	2.86	-0.95	Strongly reduced	Rasmussen (2013)
NWT, Canada	Mine Stock (Cantung pluton)	03M-207	61.97	-128.23		0.08	2.39	2.75	-1.48	Strongly reduced	Rasmussen (2013)
NWT, Canada	Circular Stock pluton	KR-05-143	61.96	-128.25	832	0.20	2.06	2.49	-1.01	Moderately reduced	Rasmussen (2013)
NWT, Canada	Little Hyland pluton	KR-05-208	61.62	-127.18	832	0.01	1.92	2.15	-2.28	Strongly reduced	Rasmussen (2013)
NWT, Canada	Rifle Range pluton	KR-05-148	62.00	-128.17	835	0.11	1.80	2.11	-1.21	Strongly reduced	Rasmussen (2013)
Yukon, Canada	Ivo pluton	KR-05-32	61.05	-127.11	871	0.14	1.02	1.28	-0.86	Moderately reduced	Rasmussen (2013)
Yukon, Canada	Marion pluton	KR-05-191	61.39	-127.34	836	0.20	1.93	2.35	-0.98	Moderately reduced	Rasmussen (2013)
Yukon, Canada	Powers pluton	KR-05-10	60.80	-126.08	781	1.13	3.14	4.63	-0.44	Moderately oxidized	Rasmussen (2013)
Yukon, Canada	Coal River batholith	KR-05-194	61.37	-127.24	870	0.34	2.31	2.91	-0.83	Moderately reduced	Rasmussen (2013)
Yukon, Canada	Nahanni Range pluton	KR-05-210	61.92	-128.41	845	0.18	1.41	1.75	-0.89	Moderately reduced	Rasmussen (2013)
Yukon, Canada	Dublin Gulch (main phase)	Main phase	64.02	-135.82	781	0.57	2.50	3.01	-0.64	Moderately reduced	Hart et al. (2004)
Yukon, Canada	Dublin Gulch (Quartz Syenite)	Quartz syenite	64.04	-135.78	790	0.50	1.40	1.85	-0.45	Moderately reduced	Hart et al. (2004)
Yukon, Canada	Mactung	Main phase	63.28	-130.15	797	0.63	2.90	3.47	-0.66	Moderately reduced	Hart et al. (2004)
CA, USA	Inconsolable granodiorite	6	37.12	-118.53		1.86	4.06	5.73	-0.34	Moderately oxidized	Bateman et al. (1965)
CA, USA	Tinemaha granodiorite	10	37.05	-118.43		2.59	3.17	5.50	-0.09	Strongly oxidized	Bateman et al. (1965)
CA, USA	Granodiorite of McMurray Meadows	9	37.41	-118.70		1.90	2.52	4.23	-0.12	Strongly oxidized	Bateman et al. (1965)
CA, USA	Wheeler Crest quartz monzonite	11	37.08	-118.36		1.03	1.38	2.31	-0.13	Moderately oxidized	Bateman et al. (1965)
CA, USA	Round Valley Peak granodiorite	5	37.46	-118.70		2.35	3.25	5.36	-0.14	Strongly oxidized	Bateman et al. (1965)
CA, USA	Lamarck granodiorite	22	37.62	-118.70		1.45	2.52	3.82	-0.24	Moderately oxidized	Bateman et al. (1965)
CA, USA	Tungsten Hills quartz monzonite 1	5	37.36	-118.72		0.89	1.03	1.83	-0.06	Moderately oxidized	Bateman et al. (1965)
CA, USA	Tungsten Hills quartz monzonite 2	52	37.24	-118.56		1.07	1.99	2.95	-0.27	Moderately oxidized	Bateman et al. (1965)
CA, USA	Cathedral Peak quartz monzonite 1	4 (b)	37.35	-118.74		1.00	0.65	1.55	0.19	Strongly oxidized	Bateman et al. (1965)

Table B.4. (continued)

CA, USA	Cathedral Peak quartz monzonite 2	12 (b)	37.26	-118.64		*0.40*	*0.34*	0.70	0.07	Strongly oxidized	Bateman et al. (1965)
CA, USA	Cathedral Peak quartz monzonite 3	23 (a)	37.11	-118.48		*0.60*	*0.88*	1.42	-0.17	Moderately oxidized	Bateman et al. (1965)
CA, USA	Cathedral Peak alaskite 1	37 (b)	37.24	-118.40		*0.90*	*0.81*	1.62	0.05	Strongly oxidized	Bateman et al. (1965)
CA, USA	Cathedral Peak alaskite 2	46 (b)	37.18	-118.42		*0.30*	*0.74*	1.01	-0.39	Moderately reduced	Bateman et al. (1965)
AZ, USA	Artesa Hills	SP152	31.84	-112.71	*698*	*0.21*	*0.14*	*0.33*	0.19	Moderately oxidized	G. Haxel (unpublished)
AZ, USA	Artesa Hills	SP76	31.84	-112.71	*728*	*0.15*	*0.52*	*0.66*	-0.53	Moderately reduced	G. Haxel (unpublished)
AZ, USA	Artesa Hills	SP78	31.84	-112.71	*722*	*0.28*	*0.09*	*0.34*	0.49	Strongly oxidized	G. Haxel (unpublished)
AZ, USA	Comobabi	CB64	32.05	-112.86	*654*	*0.27*	*0.11*	*0.35*	0.39	Strongly oxidized	G. Haxel (unpublished)
AZ, USA	Pan-Tak pluton	CM131B	*32.00*	-111.58	*750*	*0.47*	*0.37*	*0.79*	0.10	Strongly oxidized	G. Haxel (unpublished)
AZ, USA	Pan-Tak pluton	CM131A	*32.00*	-111.58	*771*	*0.66*	*0.59*	*1.18*	0.05	Strongly oxidized	G. Haxel (unpublished)
AZ, USA	Pan-Tak pluton	BG81	*32.00*	-111.58	*763*	*0.61*	*0.58*	*1.13*	0.02	Strongly oxidized	G. Haxel (unpublished)
AZ, USA	Pan-Tak pluton	CM602	*32.00*	-111.58	*668*	*0.11*	*0.32*	*0.42*	-0.46	Moderately reduced	G. Haxel (unpublished)
AZ, USA	Pan-Tak pluton	PR362A	*32.00*	-111.58	*745*	*0.38*	*0.37*	*0.71*	0.01	Strongly oxidized	G. Haxel (unpublished)
AZ, USA	Pan-Tak pluton	BG82	*32.00*	-111.58	*771*	*0.71*	*0.34*	*0.98*	0.32	Strongly oxidized	G. Haxel (unpublished)
AZ, USA	Pan-Tak pluton	CM152	*32.00*	-111.58	*743*	*0.51*	*0.23*	*0.69*	0.35	Strongly oxidized	G. Haxel (unpublished)
AZ, USA	Pan-Tak pluton	BG90	*32.00*	-111.58	*718*	*0.06*	*0.49*	*0.54*	-0.91	Moderately reduced	G. Haxel (unpublished)
AZ, USA	Pan-Tak pluton	PUP14	*32.00*	-111.58	*772*	*0.59*	*0.28*	*0.81*	0.32	Strongly oxidized	G. Haxel (unpublished)
AZ, USA	Pan-Tak pluton	CM117	*32.00*	-111.58	*665*	*0.42*	*0.14*	*0.52*	0.48	Strongly oxidized	G. Haxel (unpublished)
AZ, USA	Pan-Tak pluton	BG85	*32.00*	-111.58	*713*	*0.30*	*0.21*	*0.48*	0.15	Strongly oxidized	G. Haxel (unpublished)
AZ, USA	Pan-Tak pluton	CM601	*32.00*	-111.58	*726*	*0.42*	*0.29*	*0.67*	0.16	Strongly oxidized	G. Haxel (unpublished)
AZ, USA	Pan-Tak pluton	BG84	*32.00*	-111.58	*692*	*0.11*	*0.22*	*0.32*	-0.30	Moderately oxidized	G. Haxel (unpublished)
AZ, USA	Pan-Tak pluton	CM134	*32.00*	-111.58	*696*	*0.14*	*0.12*	*0.25*	0.07	Strongly oxidized	G. Haxel (unpublished)

Table B.4. (continued)

AZ, USA	Kupk Hills	WP104	31.94	-112.77	*748*	*0.77*	*0.18*	*0.87*	0.63	Very strongly oxidized	G. Haxel (unpublished)
AZ, USA	Kupk Hills	GH119	31.94	-112.77	*709*	*0.28*	*0.15*	*0.41*	0.28	Strongly oxidized	G. Haxel (unpublished)
AZ, USA	Morena	SP690	31.59	-111.87	*722*	*0.67*	*0.10*	*0.70*	0.83	Very strongly oxidized	G. Haxel (unpublished)
AZ, USA	Senita Basin pluton	OP109	31.96	-112.85	*707*	*0.24*	*0.27*	*0.49*	-0.05	Moderately oxidized	G. Haxel (unpublished)
AZ, USA	Senita Basin pluton	OP157	31.96	-112.85	*763*	*0.66*	*0.71*	*1.31*	-0.03	Strongly oxidized	G. Haxel (unpublished)
AZ, USA	Senita Basin pluton	OP140	31.96	-112.85	*694*	*0.28*	*0.06*	*0.32*	0.67	Very strongly oxidized	G. Haxel (unpublished)
AZ, USA	Senita Basin pluton	OP167B	31.96	-112.85	*772*	*0.42*	*0.29*	*0.67*	0.16	Strongly oxidized	G. Haxel (unpublished)
AZ, USA	Senita Basin pluton	OP168	31.96	-112.85	*675*	*0.08*	*0.17*	*0.24*	-0.32	Moderately oxidized	G. Haxel (unpublished)
AZ, USA	Senita Basin pluton	OP188	31.96	-112.85	*688*	*0.38*	*0.01*	*0.35*	1.58	Strongly oxidized	G. Haxel (unpublished)
AZ, USA	Senita Basin pluton	OP156	31.96	-112.85	*736*	*0.47*	*0.10*	*0.52*	0.67	Very strongly oxidized	G. Haxel (unpublished)
AZ, USA	Senita Basin pluton	OP177	31.96	-112.85	*721*	*0.16*	*0.09*	*0.23*	0.25	Strongly oxidized	G. Haxel (unpublished)
AZ, USA	Sierra Blanca	PR34	32.11	-112.76	*731*	*0.34*	*0.28*	*0.59*	0.08	Strongly oxidized	G. Haxel (unpublished)
AZ, USA	Sierra Blanca	PR364	32.11	-112.76	*707*	*0.27*	*0.14*	*0.39*	0.29	Strongly oxidized	G. Haxel (unpublished)
AZ, USA	Sierra Blanca	QT125	32.11	-112.76	*699*	*0.37*	*0.14*	*0.48*	0.43	Strongly oxidized	G. Haxel (unpublished)
AZ, USA	Sierra Blanca	PUP6A-B	32.11	-112.76	*733*	*0.30*	*0.16*	*0.43*	0.28	Strongly oxidized	G. Haxel (unpublished)
AZ, USA	Sierra Blanca	QT217	32.11	-112.76	*673*	*0.38*	*0.11*	*0.45*	0.54	Very strongly oxidized	G. Haxel (unpublished)
AZ, USA	Sierra Blanca	QT216	32.11	-112.76	*673*	*0.25*	*0.23*	*0.46*	0.04	Strongly oxidized	G. Haxel (unpublished)
AZ, USA	Sierra Blanca	QT233	32.11	-112.76	*717*	*0.27*	*0.11*	*0.35*	0.39	Strongly oxidized	G. Haxel (unpublished)
AZ, USA	Sierra Blanca	PUP6	32.11	-112.76	*654*	*0.29*	*0.09*	*0.35*	0.51	Very strongly oxidized	G. Haxel (unpublished)
AZ, USA	Sierra Blanca	PR33	32.11	-112.76	*748*	*0.13*	*0.04*	*0.15*	0.50	Very strongly oxidized	G. Haxel (unpublished)
AZ, USA	Sierra Blanca	QT107A	32.11	-112.76	*672*	*0.18*	*0.06*	*0.23*	0.49	Very strongly oxidized	G. Haxel (unpublished)
AZ, USA	Sierra Blanca	QT124A	32.11	-112.76	*699*	*0.27*	*0.09*	*0.33*	0.48	Very strongly oxidized	G. Haxel (unpublished)
AZ, USA	Texas Canyon pluton	TC586	*32.05*	-110.13	*797*	*0.80*	*0.78*	*1.50*	0.01	Strongly oxidized	Shaw and Guilbert (1990)

Table B.4. (continued)

AZ, USA	Dushey Canyon	HQG186	*33.81*	-113.28	*753*	*0.31*	*0.35*	*0.63*	-0.05	Moderately oxidized	Shaw and Guilbert (1990)
AZ, USA	Dushey Canyon	HQG286	*33.81*	-113.28	*1003*	*0.52*	*0.54*	*1.01*	-0.02	Strongly oxidized	Shaw and Guilbert (1990)
AZ, USA	Wilderness pluton	Spencer sill	*32.30*	-111.35		*0.81*	*0.75*	*1.48*	0.03	Strongly oxidized	Force (1997)
AZ, USA	Wilderness pluton	Wildernes Sill	*32.30*	-111.35		*0.51*	*0.40*	*0.86*	0.11	Strongly oxidized	Force (1997)
AZ, USA	Wilderness pluton	Wildernes Sill	*32.30*	-111.35		*0.46*	*0.25*	*0.66*	0.26	Strongly oxidized	Force (1997)
AZ, USA	Wilderness pluton	Wildernes Sill	*32.30*	-111.35		*0.24*	*0.24*	*0.46*	0.00	Strongly oxidized	Force (1997)
AZ, USA	Wilderness pluton	Wildernes Sill	*32.30*	-111.35		*0.48*	*0.35*	*0.78*	0.14	Strongly oxidized	Force (1997)
AZ, USA	Wilderness pluton	Wildernes Sill	*32.30*	-111.35		*0.43*	*0.32*	*0.71*	0.13	Strongly oxidized	Force (1997)
AZ, USA	Wilderness pluton	inclsuion zone	*32.30*	-111.35		*0.52*	*0.21*	*0.68*	0.39	Strongly oxidized	Force (1997)
AZ, USA	Wilderness pluton	inclsuion zone	*32.30*	-111.35		*0.48*	*0.37*	*0.80*	0.11	Strongly oxidized	Force (1997)
AZ, USA	Wilderness pluton	Catnip sill	*32.30*	-111.35		*0.75*	*0.51*	*1.18*	0.17	Strongly oxidized	Force (1997)
AZ, USA	Wilderness pluton	Seven_Falls	*32.30*	-111.35		*0.81*	*1.42*	*2.15*	-0.24	Moderately oxidized	Keith and Reynolds (1980)
AZ, USA	Wilderness pluton	Lower Foliated Bio Granite	*32.30*	-111.35		*1.01*	*0.68*	*1.59*	0.17	Strongly oxidized	Keith and Reynolds (1980)
AZ, USA	Wilderness pluton	Upper 2-mica granite	*32.30*	-111.35		*0.50*	*0.39*	*0.84*	0.11	Strongly oxidized	Keith and Reynolds (1980)
AZ, USA	Wilderness pluton	Lemmon Rock leucogranite	*32.30*	-111.35		*0.29*	*0.20*	*0.46*	0.17	Strongly oxidized	Keith and Reynolds (1980)
AZ, USA	Wilderness pluton	Garnet schlieren	*32.30*	-111.35		*1.51*	*1.39*	*2.75*	0.04	Strongly oxidized	Keith and Reynolds (1980)
AZ, USA	White Tank	WT286	*33.55*	-112.70	*765*	*0.19*	*0.46*	*0.63*	-0.38	Moderately reduced	Shaw and Guilbert (1990)
AZ, USA	White Tank	WT3C86	*33.55*	-112.70	*726*	*0.31*	*0.34*	*0.62*	-0.04	Moderately oxidized	Shaw and Guilbert (1990)
AZ, USA	White Tank	TW586	*33.55*	-112.70	*710*	*0.28*	*0.25*	*0.50*	0.05	Strongly oxidized	Shaw and Guilbert (1990)
AZ, USA	White Tank	WT686	*33.55*	-112.70	*696*	*0.17*	*0.21*	*0.36*	-0.09	Moderately oxidized	Shaw and Guilbert (1990)
AZ, USA	White Tank	WT786	*33.55*	-112.70	*781*	*0.28*	*0.57*	*0.82*	-0.31	Moderately oxidized	Shaw and Guilbert (1990)
AZ, USA	White Tank	WT8A86	*33.55*	-112.70	*735*	*0.46*	*0.29*	*0.70*	0.20	Strongly oxidized	Shaw and Guilbert (1990)
AZ, USA	White Tank	WT8B86	*33.55*	-112.70	*774*	*0.32*	*0.48*	*0.77*	-0.18	Moderately oxidized	Shaw and Guilbert (1990)
AZ, USA	White Tank	WT186	*33.55*	-112.70	*629*	*0.05*	*0.07*	*0.11*	-0.15	Moderately oxidized	Shaw and Guilbert (1990)
AZ, USA	White Tank	WT1186	*33.55*	-112.70	*619*	*0.08*	*0.05*	*0.12*	0.20	Strongly oxidized	Shaw and Guilbert (1990)

Table B.4. (continued)

NV, USA	Tungstonia pluton	8	*39.10*	-114.19		*0.15*	*1.62*	*1.75*	-1.03	Moderately reduced	Best et al. (1974)
NV, USA	Tungstonia pluton	9AB	*39.10*	-114.19		*0.30*	*0.57*	*0.84*	-0.28	Moderately oxidized	Best et al. (1974)
NV, USA	Tungstonia pluton	9B	*39.10*	-114.19		*0.28*	*0.83*	*1.08*	-0.47	Moderately reduced	Best et al. (1974)
NV, USA	Tungstonia pluton	40	*39.10*	-114.19		*0.33*	*0.52*	*0.82*	-0.20	Moderately oxidized	Best et al. (1974)
NV, USA	Tungstonia pluton	244-MW-60	*39.10*	-114.19	*706*	*0.25*	*0.63*	*0.85*	-0.40	Moderately reduced	Lee et al. (1981)
NV, USA	Pole Canyon pluton	88	*39.10*	-114.21	*740*	*0.72*	*0.24*	*0.89*	0.48	Very strongly oxidized	Lee and Van Loenen (1971)
NV, USA	Pole Canyon pluton	89	*39.10*	-114.21	*741*	*1.20*	*0.77*	*1.85*	0.19	Strongly oxidized	Lee and Van Loenen (1971)
NV, USA	Pole Canyon pluton	90	*39.10*	-114.21	*713*	*0.54*	*0.95*	*1.44*	-0.25	Moderately oxidized	Lee and Van Loenen (1971)
NV, USA	Pole Canyon pluton	91	*39.10*	-114.21	*732*	*0.68*	*0.38*	*0.99*	0.25	Strongly oxidized	Lee and Van Loenen (1971)
NV, USA	Pole Canyon pluton	92	*39.10*	-114.21	*710*	*0.78*	*0.38*	*1.08*	0.31	Strongly oxidized	Lee and Van Loenen (1971)
NV, USA	Pole Canyon pluton	93	*39.10*	-114.21	*729*	*0.88*	*0.38*	*1.17*	0.36	Strongly oxidized	Lee and Van Loenen (1971)
NV, USA	Pole Canyon pluton	94	*39.10*	-114.21	*735*	*0.48*	*0.40*	*0.83*	0.08	Strongly oxidized	Lee and Van Loenen (1971)
NV, USA	Pole Canyon pluton	95	*39.10*	-114.21	*756*	*0.85*	*0.32*	*1.08*	0.42	Strongly oxidized	Lee and Van Loenen (1971)
NV, USA	Pole Canyon pluton	96	*39.10*	-114.21	*789*	*2.20*	*0.20*	*2.18*	1.04	Strongly oxidized	Lee and Van Loenen (1971)
CA, USA	Chemehuevi	H80Ch-307	*34.55*	-114.52	*769*	*2.27*	*1.42*	*3.46*	0.20	Strongly oxidized	John and Wooden (1990)
CA, USA	Chemehuevi	H80Ch-305	*34.55*	-114.52	*804*	*2.36*	*2.86*	*4.98*	-0.08	Strongly oxidized	John and Wooden (1990)
CA, USA	Chemehuevi	BJ80CH-194	*34.55*	-114.52		*2.60*	*3.47*	*5.81*	-0.13	Moderately oxidized	John and Wooden (1990)
CA, USA	Chemehuevi	BJ81Ch-72 (1)	*34.55*	-114.52	*811*	*2.56*	*2.06*	*4.36*	0.09	Strongly oxidized	John and Wooden (1990)
CA, USA	Chemehuevi	BJ81Ch-72	*34.55*	-114.52	*798*	*1.86*	*1.98*	*3.65*	-0.03	Strongly oxidized	John and Wooden (1990)
CA, USA	Chemehuevi	BJ82Ch-103	*34.55*	-114.52	*787*	*1.82*	*1.29*	*2.93*	0.15	Strongly oxidized	John and Wooden (1990)
CA, USA	Chemehuevi	BJ81Ch-306	*34.55*	-114.52	*810*	*1.40*	*1.29*	*2.55*	0.04	Strongly oxidized	John and Wooden (1990)
CA, USA	Chemehuevi	BJ82Ch-81	*34.55*	-114.52	*776*	*1.62*	*0.98*	*2.44*	0.22	Strongly oxidized	John and Wooden (1990)
CA, USA	Chemehuevi	BJ80Ch-241^1	*34.55*	-114.52	*777*	*1.06*	*0.78*	*1.73*	0.13	Strongly oxidized	John and Wooden (1990)
CA, USA	Chemehuevi	BJ81Ch-64	*34.55*	-114.52	*774*	*0.76*	*0.74*	*1.42*	0.01	Strongly oxidized	John and Wooden (1990)
CA, USA	Chemehuevi	BJ81Ch-113 (1)	*34.55*	-114.52	*780*	*0.93*	*1.10*	*1.94*	-0.07	Strongly oxidized	John and Wooden (1990)

Table B.4. (continued)

CA, USA	Chemehuevi	BJ81Ch-113 (2)	*34.55*	-114.52	*790*	*0.73*	*1.18*	*1.84*	-0.21	Moderately oxidized	John and Wooden (1990)
CA, USA	Chemehuevi	H80Ch-308^1	*34.55*	-114.52	*764*	*0.49*	*1.05*	*1.49*	-0.33	Moderately oxidized	John and Wooden (1990)
CA, USA	Chemehuevi	BJ80Ch-200^1	*34.55*	-114.52	*761*	*0.77*	*0.57*	*1.26*	0.13	Strongly oxidized	John and Wooden (1990)
CA, USA	Chemehuevi	H81Mh-61	*34.55*	-114.52	*722*	*0.39*	*1.21*	*1.56*	-0.49	Moderately reduced	John and Wooden (1990)
CA, USA	Chemehuevi	H80Mh-310^1	*34.55*	-114.52	*789*	*0.91*	*0.68*	*1.50*	0.13	Strongly oxidized	John and Wooden (1990)
CA, USA	Chemehuevi	P80Ch-55^1	*34.55*	-114.52	*756*	*0.77*	*0.35*	*1.04*	0.34	Strongly oxidized	John and Wooden (1990)
CA, USA	Chemehuevi	BJ81Ch-46	*34.55*	-114.52		*0.52*	*0.46*	*0.93*	0.05	Strongly oxidized	John and Wooden (1990)
CA, USA	Chemehuevi	BJ81Ch-61	*34.55*	-114.52	*766*	*0.45*	*0.45*	*0.85*	0.00	Strongly oxidized	John and Wooden (1990)
CA, USA	Chemehuevi	BJ81Ch-5	*34.55*	-114.52	*755*	*0.45*	*0.31*	*0.71*	0.16	Strongly oxidized	John and Wooden (1990)
CA, USA	Chemehuevi	BJ81Ch-22	*34.55*	-114.52	*708*	*0.20*	*0.25*	*0.43*	-0.10	Strongly oxidized	John and Wooden (1990)
CA, USA	Chemehuevi	BJ84Ch-9	*34.55*	-114.52	*744*	*0.08*	*0.19*	*0.26*	-0.38	Moderately reduced	John and Wooden (1990)
CA, USA	Chemehuevi	MJ82Ch-1	*34.55*	-114.52	*765*	*0.40*	*0.17*	*0.53*	0.37	Strongly oxidized	John and Wooden (1990)
CA, USA	Whale Mtn.	BJ81Ch-103	*34.68*	-114.54	*730*	*2.51*	*5.71*	*7.97*	-0.36	Moderately oxidized	John and Wooden (1990)
CA, USA	Whale Mtn.	BJ81Ch-103	*34.68*	-114.54	*754*	*3.69*	*5.52*	*8.84*	-0.17	Strongly oxidized	John and Wooden (1990)
CA, USA	Whale Mtn.	BJ81Ch-2	*34.68*	-114.54	*702*	*2.62*	*4.96*	*7.32*	-0.28	Moderately oxidized	John and Wooden (1990)
CA, USA	Whale Mtn.	H80Mh-311	*34.68*	-114.54	*635*	*1.76*	*5.14*	*6.72*	-0.47	Moderately oxidized	John and Wooden (1990)
CA, USA	Whale Mtn.	BJ81Ch-106	*34.68*	-114.54	*892*	*2.12*	*3.28*	*5.19*	-0.19	Moderately oxidized	John and Wooden (1990)
CA, USA	Whale Mtn.	BJ81Ch-3	*34.68*	-114.54	*869*	*2.53*	*2.84*	*5.12*	-0.05	Strongly oxidized	John and Wooden (1990)
CA, USA	Whale Mtn.	BJ81Ch-308	*34.68*	-114.54		*1.20*	*3.20*	*4.28*	-0.43	Moderately oxidized	John and Wooden (1990)
CA, USA	Whale Mtn.	BJ80Ch-198^1	*34.68*	-114.54	*809*	*1.52*	*1.47*	*2.84*	0.01	Strongly oxidized	John and Wooden (1990)
SON, Mexico	Mezquital	2H126	*30.90*	-111.88	*729*	*0.42*	*0.71*	*1.09*	-0.23	Moderately oxidized	G. Haxel (unpublished)
SON, Mexico	Presumido Peak pluton	2H12	*31.50*	-111.62	*781*	*0.88*	*0.93*	*1.72*	-0.03	Moderately oxidized	G. Haxel (unpublished)
SON, Mexico	Presumido Peak pluton	SP239B	*31.50*	-111.62	*774*	*1.49*	*0.40*	*1.74*	0.57	Very strongly oxidized	G. Haxel (unpublished)

Table B.4. (continued)

SON, Mexico	Presumido Peak pluton	SP651	*31.50*	-111.62	*785*	*2.04*	*0.91*	*2.75*	0.35	Strongly oxidized	G. Haxel (unpublished)
SON, Mexico	Presumido Peak pluton	2H21	*31.50*	-111.62	*727*	*0.67*	*0.25*	*0.86*	0.43	Strongly oxidized	G. Haxel (unpublished)
SON, Mexico	Presumido Peak pluton	PUP41	*31.50*	-111.62	*761*	*0.92*	*0.36*	*1.19*	0.41	Strongly oxidized	G. Haxel (unpublished)
SON, Mexico	Presumido Peak pluton	GH2-27	*31.50*	-111.62	*699*	*0.57*	*0.37*	*0.88*	0.19	Strongly oxidized	G. Haxel (unpublished)
SON, Mexico	Presumido Peak pluton	2H14	*31.50*	-111.62	*712*	*0.77*	*0.11*	*0.80*	0.84	Very strongly oxidized	G. Haxel (unpublished)
SON, Mexico	Presumido Peak pluton	GH2-26	*31.50*	-111.62	*707*	*0.42*	*0.27*	*0.65*	0.19	Strongly oxidized	G. Haxel (unpublished)
SON, Mexico	Presumido Peak pluton	2H7	*31.50*	-111.62	*674*	*0.59*	*0.14*	*0.68*	0.63	Very strongly oxidized	G. Haxel (unpublished)
SON, Mexico	Presumido Peak pluton	CM178	*31.50*	-111.62	*810*	*0.86*	*0.18*	*0.95*	0.68	Very strongly oxidized	G. Haxel (unpublished)
SON, Mexico	Presumido Peak pluton	SP220	*31.50*	-111.62	*710*	*0.46*	*0.24*	*0.66*	0.29	Strongly oxidized	G. Haxel (unpublished)
SON, Mexico	Presumido Peak pluton	SP240	*31.50*	-111.62	*725*	*0.49*	*0.11*	*0.55*	0.65	Very strongly oxidized	G. Haxel (unpublished)
SON, Mexico	Presumido Peak pluton	CM170	*31.50*	-111.62	*803*	*0.82*	*0.24*	*0.98*	0.54	Very strongly oxidized	G. Haxel (unpublished)
SON, Mexico	Presumido Peak pluton	CM161	*31.50*	-111.62	*694*	*0.02*	*0.25*	*0.27*	-1.05	Strongly reduced	G. Haxel (unpublished)
SON, Mexico	Presumido Peak pluton	SP136A	*31.50*	-111.62	*646*	*0.19*	*0.24*	*0.41*	-0.09	Moderately oxidized	G. Haxel (unpublished)
SON, Mexico	Presumido Peak pluton	CM169	*31.50*	-111.62	*787*	*0.74*	*0.10*	*0.76*	0.87	Very strongly oxidized	G. Haxel (unpublished)
SON, Mexico	Presumido Peak pluton	GH2-28	*31.50*	-111.62	*715*	*0.32*	*0.16*	*0.45*	0.30	Strongly oxidized	G. Haxel (unpublished)
SON, Mexico	Presumido Peak pluton	SP221	*31.50*	-111.62	*705*	*0.24*	*0.30*	*0.51*	-0.10	Moderately oxidized	G. Haxel (unpublished)
SON, Mexico	Presumido Peak pluton	SP217	*31.50*	-111.62	*685*	*0.46*	*0.11*	*0.52*	0.62	Very strongly oxidized	G. Haxel (unpublished)
SON, Mexico	Presumido Peak pluton	2H28	*31.50*	-111.62	*726*	*0.34*	*0.08*	*0.39*	0.63	Very strongly oxidized	G. Haxel (unpublished)
SON, Mexico	Presumido Peak pluton	2H2	*31.50*	-111.62	*724*	*0.31*	*0.17*	*0.45*	0.26	Strongly oxidized	G. Haxel (unpublished)
SON, Mexico	Presumido Peak pluton	SP238	*31.50*	-111.62	*740*	*0.45*	*0.45*	*0.86*	0.00	Strongly oxidized	G. Haxel (unpublished)
SON, Mexico	Presumido Peak pluton	SP239C	*31.50*	-111.62	*721*	*0.39*	*0.13*	*0.48*	0.47	Strongly oxidized	G. Haxel (unpublished)
SON, Mexico	Presumido Peak pluton	2H25	*31.50*	-111.62	*690*	*0.13*	*0.09*	*0.21*	0.16	Strongly oxidized	G. Haxel (unpublished)
SON, Mexico	Presumido Peak pluton	SP128A	*31.50*	-111.62	*702*	*0.45*	*0.11*	*0.51*	0.61	Very strongly oxidized	G. Haxel (unpublished)

Table B.4. (continued)

SON, Mexico	Presumido Peak pluton	SP640	*31.50*	-111.62	*679*	*0.18*	*0.15*	*0.32*	0.09	Strongly oxidized	G. Haxel (unpublished)
SON, Mexico	Presumido Peak pluton	SP130A	*31.50*	-111.62	*614*	*0.58*	*0.07*	*0.59*	0.92	Very strongly oxidized	G. Haxel (unpublished)
SON, Mexico	Presumido Peak pluton	SP661D	*31.50*	-111.62	*656*	*0.19*	*0.10*	*0.27*	0.28	Strongly oxidized	G. Haxel (unpublished)
SON, Mexico	Presumido Peak pluton	GH2-29	*31.50*	-111.62	*784*	*0.75*	*0.02*	*0.69*	1.57	Very strongly oxidized	G. Haxel (unpublished)
SON, Mexico	Presumido Peak pluton	2H29	*31.50*	-111.62	*709*	*0.14*	*0.11*	*0.23*	0.10	Strongly oxidized	G. Haxel (unpublished)
SON, Mexico	Presumido Peak pluton	SP656	*31.50*	-111.62	*663*	*0.25*	*0.11*	*0.33*	0.35	Strongly oxidized	G. Haxel (unpublished)
SON, Mexico	Presumido Peak pluton	SP655	*31.50*	-111.62	*700*	*0.39*	*0.10*	*0.45*	0.59	Very strongly oxidized	G. Haxel (unpublished)
SON, Mexico	Presumido Peak pluton	SP241B	*31.50*	-111.62	*674*	*0.14*	*0.09*	*0.22*	0.19	Strongly oxidized	G. Haxel (unpublished)
SON, Mexico	Presumido Peak pluton	SP135	*31.50*	-111.62	*767*	*0.62*	*0.09*	*0.65*	0.84	Very strongly oxidized	G. Haxel (unpublished)
SON, Mexico	Presumido Peak pluton	SP634	*31.50*	-111.62	*653*	*0.18*	*0.18*	*0.34*	0.00	Strongly oxidized	G. Haxel (unpublished)
SON, Mexico	Presumido Peak pluton	CM155	*31.50*	-111.62	*775*	*0.52*	*0.10*	*0.57*	0.72	Very strongly oxidized	G. Haxel (unpublished)
SON, Mexico	Presumido Peak pluton	SP128C	*31.50*	-111.62	*729*	*0.56*	*0.21*	*0.71*	0.42	Strongly oxidized	G. Haxel (unpublished)
SON, Mexico	Presumido Peak pluton	SP95	*31.50*	-111.62	*694*	*0.29*	*0.24*	*0.50*	0.09	Strongly oxidized	G. Haxel (unpublished)

Figure B.1. εNd at time of formation (t) for scheelite, and local lithologies in the Canadian Tungsten Belt (Blow-up of Figure 4.3, showing on data acquired in this study only). Squares and circles are data acquired in this study with squares representing Nd isotopic compositions of scheelite and circles representing neodymium isotopic compositions of local lithologies associated with the Cantung and Mactung deposits.

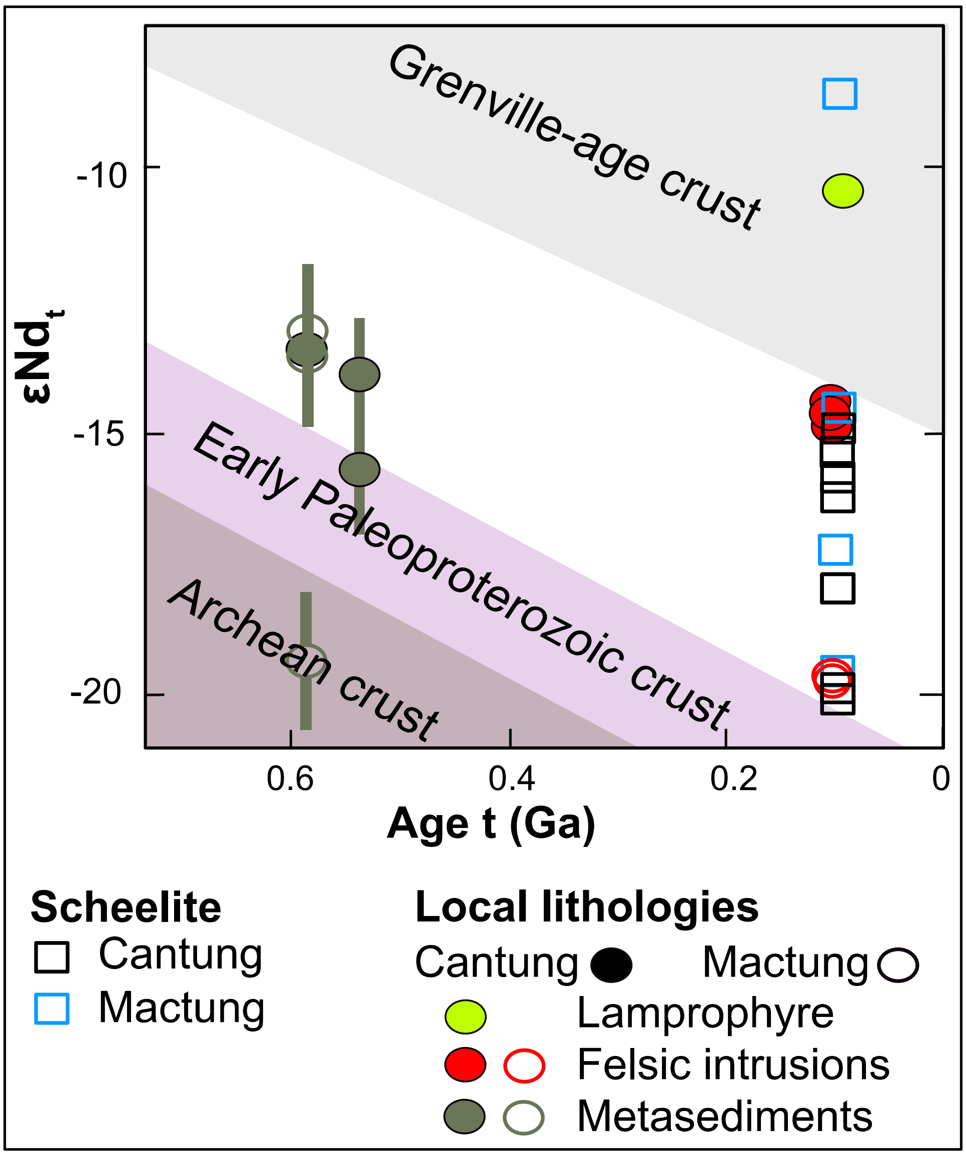

Appendix C: Trace element composition of scheelite

Trace element composition of scheelite from the Cantung, Mactung and Lened deposits were obtained by Laser ablation inductively coupled mass spectrometry (LA-ICPMS) analyses on thin sections in a Thermo Scientific ICAP-Q quadrupole ICPMS coupled to a New Wave UP-213 Nd YAG laser ablation system at the CCIM-ICPMS facility of the University of Alberta using spot sizes of 25 or 30µm. Analyses were run on transects perpendicular to growth zones in individual scheelite grains. No matrix-matched standard is currently available for scheelite, therefore NIST 612 was used as an external standard cycled prior to and at the end of each sample analysis and after every 8 or 10 spot analyses. Calcium (^{43}Ca) was used as internal standard assuming a stoichiometric composition for scheelite with Ca 13.92 weight %. Data reduction was carried out using Igor Pro and Iolite software. The results presented (Tables C.1, C.2 and C.3) represent analyses on individual spots on scheelite grains.

Table C.1. Trace element composition of scheelite from the Cantung deposit. *All values are in ppm. NA= not analyzed; LOD= limit of detection.*

Sample name	Scheelite host	Ti_ m47	Mn_ m55	Fe_ m57	Cu_ m63	As_ m75	Rb_ m85	Sr_ m88	Y_ m89	Zr_ m90	Nb_ m93	Mo_ m95	Ag_ m107	Cs_ m133	Ba_ m137	La_ m139	Ce_ m140	Pr_ m141	Nd_ m146
18-CA-50	Quartz-vein in Mine Stock pluton	<LOD	NA	NA	<LOD	NA	<LOD	60.5	1115.0	0.2	589.4	14.3	NA	<LOD	<LOD	68.0	305.7	74.3	504.6
		<LOD	NA	NA	1.1	NA	<LOD	56.0	1023.0	0.6	632.0	13.7	NA	<LOD	<LOD	99.8	386.0	76.7	437.9
		<LOD	NA	NA	0.9	NA	<LOD	62.9	1117.0	0.3	885.0	18.0	NA	<LOD	<LOD	69.5	283.5	67.0	488.4
		<LOD	NA	NA	<LOD	NA	<LOD	61.2	1307.0	0.9	1019.0	16.7	NA	<LOD	0.3	100.0	424.6	99.3	675.7
		<LOD	NA	NA	<LOD	NA	<LOD	61.2	1012.0	0.7	1129.0	17.4	NA	<LOD	<LOD	113.0	470.8	108.9	733.0
		<LOD	NA	NA	1.0	NA	<LOD	63.0	1132.0	0.6	994.0	18.0	NA	<LOD	0.3	139.7	585.0	124.0	810.0
		<LOD	NA	NA	0.9	NA	<LOD	64.5	1293.0	0.2	924.0	18.5	NA	<LOD	<LOD	130.4	507.0	108.9	729.0
		<LOD	NA	NA	<LOD	NA	<LOD	66.7	1796.0	0.5	1137.0	15.6	NA	<LOD	0.3	196.0	761.0	159.8	980.0
		<LOD	NA	NA	<LOD	NA	<LOD	65.2	1443.0	0.3	1166.0	14.8	NA	0.1	<LOD	168.5	701.0	139.8	864.0
		<LOD	NA	NA	<LOD	NA	<LOD	63.7	1334.0	0.1	1158.0	16.1	NA	<LOD	<LOD	136.6	586.2	124.4	836.0
		<LOD	NA	NA	<LOD	NA	<LOD	63.2	1674.0	0.2	1104.0	15.8	NA	0.0	<LOD	152.0	653.7	134.0	904.0
		<LOD	NA	NA	<LOD	NA	<LOD	62.6	1305.0	0.2	1147.0	17.1	NA	<LOD	<LOD	118.6	521.4	114.0	812.0
		<LOD	NA	NA	<LOD	NA	<LOD	64.4	1438.0	0.2	1101.0	16.0	NA	<LOD	<LOD	118.9	529.0	111.8	795.0
		<LOD	NA	NA	<LOD	NA	<LOD	61.2	1424.0	0.1	1021.0	15.7	NA	<LOD	<LOD	108.7	507.3	106.9	743.0
		<LOD	NA	NA	<LOD	NA	<LOD	61.6	1837.0	0.1	1265.0	14.7	NA	<LOD	<LOD	119.7	582.4	126.0	893.0
		<LOD	NA	NA	0.7	NA	<LOD	63.3	1447.0	0.4	1227.0	15.1	NA	<LOD	<LOD	126.2	559.1	115.3	797.0
		<LOD	NA	NA	<LOD	NA	<LOD	59.9	1225.0	0.1	1090.0	14.5	NA	0.1	<LOD	125.9	553.1	105.1	642.4
		3.3	NA	NA	<LOD	NA	0.6	58.5	7000.0	0.5	2170.0	16.5	NA	0.0	<LOD	198.1	984.0	209.0	1540.0
		<LOD	NA	NA	<LOD	NA	<LOD	58.2	1816.0	0.1	1188.0	14.7	NA	<LOD	<LOD	129.1	654.2	133.8	836.4
		<LOD	NA	NA	<LOD	NA	<LOD	59.1	1767.0	0.1	1481.0	18.2	NA	<LOD	<LOD	131.5	622.1	132.6	930.0
		<LOD	NA	NA	0.7	NA	<LOD	54.8	2055.0	0.4	1378.0	21.4	NA	<LOD	0.1	199.2	879.0	166.4	930.0
		<LOD	NA	NA	<LOD	NA	0.2	53.5	2021.0	0.5	1523.0	21.2	NA	0.0	0.4	176.0	806.0	162.7	966.0
		<LOD	NA	NA	1.3	NA	<LOD	55.1	1084.0	0.2	1103.0	7.5	NA	<LOD	0.1	155.0	733.0	151.0	906.0
		<LOD	NA	NA	<LOD	NA	0.5	57.7	1746.0	0.3	1389.0	23.1	NA	0.3	0.4	149.6	713.0	152.0	941.0
		<LOD	NA	NA	<LOD	NA	<LOD	51.8	1978.0	0.1	1543.0	21.4	NA	<LOD	<LOD	148.5	709.8	157.1	1013.0

Table C.1. (continued)

		<LOD	NA	NA	<LOD	NA	<LOD	53.5	1811.0	0.2	1529.0	22.2	NA	<LOD	0.1	132.3	635.7	145.4	958.0
		11.1	NA	NA	8.7	NA	1.8	56.4	1535.0	3.9	1216.0	17.7	NA	0.1	4.7	156.9	700.0	136.1	756.0
		<LOD	NA	NA	1.0	NA	<LOD	55.2	1357.0	0.5	1144.0	17.7	NA	<LOD	0.1	153.1	682.1	138.6	779.0
		<LOD	NA	NA	<LOD	NA	<LOD	55.6	1793.0	0.1	1382.0	17.5	NA	<LOD	<LOD	117.1	562.0	130.8	847.0
		<LOD	NA	NA	<LOD	NA	<LOD	54.0	1686.0	0.1	1088.0	16.2	NA	<LOD	<LOD	168.7	689.0	136.2	708.7
		<LOD	NA	NA	<LOD	NA	0.3	55.0	1849.0	0.1	1539.0	17.2	NA	0.2	<LOD	116.8	542.0	132.5	913.0
		<LOD	NA	NA	<LOD	NA	<LOD	53.8	1447.0	0.1	1080.0	15.4	NA	<LOD	<LOD	166.3	661.0	125.5	692.0
		<LOD	NA	NA	<LOD	NA	<LOD	53.5	1666.0	0.2	1703.0	18.4	NA	<LOD	0.1	106.1	519.0	127.3	869.0
		<LOD	NA	NA	<LOD	NA	<LOD	56.9	2010.0	0.1	1513.0	14.9	NA	<LOD	<LOD	112.7	528.5	125.0	815.0
		<LOD	NA	NA	<LOD	NA	<LOD	58.0	1813.0	0.1	1497.0	14.3	NA	<LOD	<LOD	106.3	520.7	127.4	831.0
		<LOD	NA	NA	<LOD	NA	0.3	65.5	1608.0	0.1	1345.0	16.1	NA	0.1	<LOD	99.1	471.1	115.3	770.0
		<LOD	NA	NA	<LOD	NA	<LOD	64.1	1655.0	0.0	1333.0	17.3	NA	<LOD	<LOD	101.3	477.0	115.0	767.7
		<LOD	NA	NA	<LOD	NA	<LOD	67.6	1996.0	0.3	2224.0	15.7	NA	0.0	0.2	132.1	617.0	136.7	832.0
		<LOD	NA	NA	<LOD	NA	0.6	68.5	1323.0	0.1	1340.0	16.9	NA	1.6	0.2	101.7	475.0	108.2	732.0
		<LOD	NA	NA	<LOD	NA	<LOD	59.9	1951.0	0.1	1574.0	16.8	NA	<LOD	<LOD	109.6	535.7	128.5	860.0
		<LOD	NA	NA	<LOD	NA	<LOD	60.0	1803.0	1.3	1530.0	17.9	NA	0.0	0.1	115.1	539.3	123.6	816.0
		<LOD	NA	NA	<LOD	NA	<LOD	61.5	1066.0	0.3	695.0	21.4	NA	0.0	<LOD	178.0	718.0	116.0	482.0
		<LOD	NA	NA	<LOD	NA	<LOD	77.6	1823.0	0.1	2287.0	16.3	NA	<LOD	<LOD	229.7	780.0	124.4	545.4
		<LOD	NA	NA	<LOD	NA	<LOD	59.1	1055.0	0.1	799.0	20.3	NA	<LOD	<LOD	101.8	442.8	84.7	444.0
		<LOD	NA	NA	<LOD	NA	<LOD	58.1	1888.0	0.1	1646.0	19.1	NA	0.0	<LOD	143.4	650.0	138.9	909.0
		<LOD	NA	NA	<LOD	NA	<LOD	61.2	1171.0	0.1	937.0	14.8	NA	<LOD	0.2	118.7	488.4	89.7	496.5
		<LOD	NA	NA	<LOD	NA	<LOD	66.7	1419.0	0.1	1287.0	14.1	NA	0.1	<LOD	92.8	459.5	106.3	757.0
		<LOD	NA	NA	<LOD	NA	<LOD	61.9	1463.0	0.1	1093.0	17.3	NA	0.0	<LOD	83.5	454.3	110.9	844.0
		<LOD	NA	NA	<LOD	NA	<LOD	64.0	1222.0	1.3	1065.0	16.0	NA	0.0	0.4	52.9	285.2	70.3	528.3
		<LOD	NA	NA	<LOD	NA	<LOD	57.1	776.0	0.0	452.5	13.9	NA	<LOD	0.1	63.3	300.3	61.6	353.8
		NA	67.0	710.0	<LOD	3.1	1.5	85.3	1014.0	NA	NA	40.2	<LOD	NA	NA	NA	268.0	45.3	214.0
		NA	15.0	52.8	<LOD	3.4	<LOD	103.3	929.0	NA	NA	43.7	<LOD	NA	NA	NA	117.6	27.2	168.2
		NA	16.8	46.9	<LOD	2.4	<LOD	88.0	100.7	NA	NA	69.3	<LOD	NA	NA	NA	31.6	6.9	40.5
18-CA-10	Lower Argillite	NA	32.6	340.0	<LOD	3.4	9.0	72.6	973.0	NA	NA	46.1	<LOD	NA	NA	NA	142.2	29.6	176.2
		NA	140.0	1040.0	<LOD	2.7	42.2	78.2	1024.0	NA	NA	44.1	0.39	NA	NA	NA	134.4	28.5	168.0
		NA	13.6	40.5	1.2	2.5	<LOD	91.6	514.0	NA	NA	44.5	<LOD	NA	NA	NA	58.4	14.2	99.1
		NA	43.2	133.0	1.6	2.4	<LOD	114.1	92.8	NA	NA	71.6	<LOD	NA	NA	NA	9.8	1.9	12.1

Table C.1. (continued)

		NA	225.0	2780.0	129.0	<LOD	30.5	118.6	65.1	NA	NA	65.9	205.0	NA	NA	NA	8.3	1.7	9.7
		NA	16.1	57.3	<LOD	<LOD	<LOD	78.8	596.0	NA	NA	58.9	<LOD	NA	NA	NA	129.7	24.0	126.1
		NA	955.0	7280.0	<LOD	<LOD	0.8	86.7	58.0	NA	NA	79.2	<LOD	NA	NA	NA	14.7	2.8	17.5
		NA	6030.0	79200.0	12.4	<LOD	395.0	518.0	50.9	NA	NA	22.9	<LOD	NA	NA	NA	7.7	1.2	5.6
		NA	666.0	930.0	8.9	<LOD	<LOD	3.9	320.3	NA	NA	0.5	<LOD	NA	NA	NA	76.7	13.0	61.3
		NA	17.5	46.4	<LOD	<LOD	<LOD	74.0	110.5	NA	NA	82.6	<LOD	NA	NA	NA	10.9	3.1	23.4
		NA	13.5	40.3	<LOD	2.1	<LOD	48.2	359.4	NA	NA	84.1	<LOD	NA	NA	NA	115.3	19.2	103.8
		NA	21.0	68.3	<LOD	<LOD	<LOD	83.6	148.1	NA	NA	72.6	<LOD	NA	NA	NA	27.6	7.0	49.6
		NA	15.7	53.5	<LOD	<LOD	<LOD	49.2	335.9	NA	NA	59.5	<LOD	NA	NA	NA	144.9	19.9	83.7
		NA	12.7	44.9	<LOD	<LOD	<LOD	76.2	332.3	NA	NA	46.8	<LOD	NA	NA	NA	78.4	16.0	82.1
		NA	23.6	89.0	<LOD	<LOD	1.4	130.1	360.5	NA	NA	45.4	<LOD	NA	NA	NA	30.9	8.9	62.1
		NA	20.5	58.0	<LOD	<LOD	<LOD	98.9	500.0	NA	NA	44.6	<LOD	NA	NA	NA	99.5	20.1	109.1
		NA	249.0	3780.0	<LOD	<LOD	84.0	98.1	538.0	NA	NA	55.4	<LOD	NA	NA	NA	127.0	21.7	99.9
		NA	15.8	77.0	<LOD	2.9	0.8	71.5	792.0	NA	NA	53.0	<LOD	NA	NA	NA	195.3	36.3	194.2
		NA	43.5	102.0	<LOD	<LOD	<LOD	91.9	250.4	NA	NA	65.2	<LOD	NA	NA	NA	33.3	6.7	37.5
		NA	16.1	56.6	<LOD	<LOD	<LOD	114.6	321.0	NA	NA	74.5	<LOD	NA	NA	NA	58.9	11.7	71.4
		NA	16.9	50.0	<LOD	<LOD	<LOD	68.2	96.4	NA	NA	97.0	<LOD	NA	NA	NA	30.4	5.8	34.1
		NA	12.4	44.4	<LOD	<LOD	<LOD	69.9	540.0	NA	NA	62.5	<LOD	NA	NA	NA	158.8	27.8	148.4
		NA	12.6	47.3	<LOD	<LOD	<LOD	88.2	63.9	NA	NA	125.4	<LOD	NA	NA	NA	18.7	2.7	14.8
		NA	22.5	56.0	<LOD	<LOD	<LOD	74.4	118.9	NA	NA	83.5	<LOD	NA	NA	NA	38.8	7.4	41.3
		NA	534.0	1124.0	4.5	<LOD	<LOD	5.4	500.0	NA	NA	0.9	<LOD	NA	NA	NA	39.1	8.5	49.9
		NA	11.9	50.0	1.1	2.3	<LOD	73.5	440.0	NA	NA	80.4	<LOD	NA	NA	NA	67.0	14.2	83.2
		NA	701.0	8090.0	3.8	<LOD	7.8	129.9	193.0	NA	NA	52.3	<LOD	NA	NA	NA	19.8	3.2	17.8
18-CA-47	Garnet-pyroxene skarn	NA	53.4	88.0	NA	NA	<LOD	35.4	59.0	NA	NA	349.4	NA	NA	NA	NA	44.6	7.5	38.2
		NA	18.6	93.9	NA	NA	<LOD	60.1	74.4	NA	NA	547.0	NA	NA	NA	NA	41.7	7.3	37.9
		NA	24.8	89.5	NA	NA	<LOD	45.0	188.9	NA	NA	319.0	NA	NA	NA	NA	165.9	21.9	80.2
		NA	31.2	93.6	NA	NA	<LOD	30.6	78.9	NA	NA	374.0	NA	NA	NA	NA	75.8	10.8	44.6
		NA	22.1	91.5	NA	NA	<LOD	41.7	313.9	NA	NA	379.3	NA	NA	NA	NA	164.0	30.1	153.6
		NA	92.0	1180.0	NA	NA	<LOD	38.8	93.3	NA	NA	383.0	NA	NA	NA	NA	57.2	8.8	41.2
		NA	21.3	95.9	NA	NA	<LOD	60.0	112.5	NA	NA	651.0	NA	NA	NA	NA	72.3	10.8	52.8
18-CA-31a	Pyroxene skarn	NA	17.3	81.0	NA	NA	<LOD	51.9	7.1	NA	NA	254.5	NA	NA	NA	NA	25.7	3.2	10.8
		NA	28.2	102.0	NA	NA	<LOD	59.4	58.1	NA	NA	197.4	NA	NA	NA	NA	78.6	10.1	43.3

Table C.1. (continued)

		NA	34.1	91.8	NA	NA	<LOD	59.2	42.7	NA	NA	350.3	NA	NA	NA	NA	17.1	4.6	35.7
		NA	31.5	87.4	NA	NA	<LOD	60.1	49.4	NA	NA	390.9	NA	NA	NA	NA	46.7	7.5	39.0
18-CA-29b	Amphibole-rich facies	NA	22.6	228.0	NA	NA	<LOD	41.0	54.2	NA	NA	509.2	NA	NA	NA	NA	138.2	24.5	117.0
		NA	26.4	93.2	NA	NA	<LOD	49.3	21.8	NA	NA	629.6	NA	NA	NA	NA	93.5	12.9	50.3
		NA	34.2	67.5	NA	NA	<LOD	34.7	15.0	NA	NA	616.0	NA	NA	NA	NA	75.2	9.9	36.9
		NA	27.3	79.0	NA	NA	<LOD	75.6	24.5	NA	NA	1287.0	NA	NA	NA	NA	111.1	16.8	88.9
		NA	140.0	1120.0	NA	NA	<LOD	68.0	28.6	NA	NA	1211.0	NA	NA	NA	NA	111.5	17.6	87.8
18-CA-40B	Biotite-Amphibole rich facies	NA	11.4	167.0	NA	NA	<LOD	62.7	371.1	NA	NA	123.9	NA	NA	NA	NA	119.8	21.3	125.1
		NA	46.4	920.0	NA	NA	9.9	70.1	151.0	NA	NA	72.9	NA	NA	NA	NA	153.1	20.9	70.2
		NA	16.4	223.0	NA	NA	0.2	54.2	144.6	NA	NA	108.2	NA	NA	NA	NA	78.3	12.3	61.5
18-CA-28	Biotite-rich facies	NA	37.8	98.2	NA	NA	0.5	77.4	660.5	NA	NA	43.2	NA	NA	NA	NA	261.7	38.1	161.4
		NA	16.4	65.0	NA	NA	<LOD	77.3	497.0	NA	NA	74.2	NA	NA	NA	NA	47.6	11.8	85.6
		NA	40.0	75.0	NA	NA	<LOD	82.5	1166.0	NA	NA	47.8	NA	NA	NA	NA	230.1	46.8	273.0
		NA	33.3	81.0	NA	NA	<LOD	84.6	1073.0	NA	NA	42.4	NA	NA	NA	NA	211.4	43.0	260.0
18-CA-40B	Quartz vein in Biotite-Amphibole rich facies	NA	50.4	140.1	NA	NA	<LOD	69.2	528.6	NA	NA	56.4	NA	NA	NA	NA	767.0	96.3	309.5
		NA	45.1	142.5	NA	NA	<LOD	62.3	467.9	NA	NA	58.7	NA	NA	NA	NA	847.0	96.9	284.2
		NA	48.3	124.8	NA	NA	<LOD	72.4	275.0	NA	NA	51.4	NA	NA	NA	NA	471.4	52.7	146.7
		NA	51.1	121.0	NA	NA	<LOD	70.4	637.3	NA	NA	55.8	NA	NA	NA	NA	1020.0	121.2	373.7
18-CA-51	Upper Argillite	<LOD	NA	NA	<LOD	NA	<LOD	45.4	89.0	<LOD	27.0	59.9	NA	<LOD	<LOD	0.3	1.4	0.3	3.5
		<LOD	NA	NA	<LOD	NA	<LOD	57.4	153.3	<LOD	121.5	32.5	NA	<LOD	<LOD	0.7	3.6	1.1	12.2
		<LOD	NA	NA	<LOD	NA	<LOD	47.6	237.2	<LOD	122.6	45.0	NA	<LOD	<LOD	5.1	25.1	5.9	40.6
		<LOD	NA	NA	0.4	NA	0.9	63.5	592.0	0.0	318.1	23.9	NA	0.7	0.8	1447.0	1910.0	154.0	583.0
		<LOD	NA	NA	<LOD	NA	<LOD	52.5	536.1	0.0	213.7	34.9	NA	0.1	<LOD	22.6	81.4	13.5	63.6
		<LOD	NA	NA	<LOD	NA	<LOD	65.2	397.9	<LOD	188.8	53.9	NA	<LOD	<LOD	10.8	48.6	9.9	55.7
		<LOD	NA	NA	0.7	NA	0.9	68.7	1534.0	0.0	1085.0	49.0	NA	0.5	1.3	12.9	63.3	15.4	104.8
		<LOD	NA	NA	<LOD	NA	<LOD	58.8	256.3	<LOD	122.5	88.5	NA	<LOD	<LOD	5.3	30.4	7.0	46.5
		<LOD	NA	NA	0.4	NA	<LOD	54.3	521.0	0.0	357.3	65.1	NA	<LOD	<LOD	8.9	46.1	10.2	62.0
		<LOD	NA	NA	<LOD	NA	<LOD	53.4	334.9	<LOD	169.6	124.5	NA	<LOD	<LOD	10.0	46.4	10.2	67.1
		<LOD	NA	NA	<LOD	NA	<LOD	58.3	437.7	0.0	318.1	94.2	NA	0.0	<LOD	9.9	59.2	13.9	89.0
		<LOD	NA	NA	8.3	NA	<LOD	59.0	433.5	0.1	205.0	56.1	NA	0.1	<LOD	92.0	157.0	19.1	80.2
		<LOD	NA	NA	<LOD	NA	<LOD	57.8	608.5	<LOD	286.8	59.2	NA	<LOD	<LOD	33.1	113.8	17.4	76.0
		<LOD	NA	NA	<LOD	NA	<LOD	59.0	978.0	0.0	429.5	37.5	NA	<LOD	<LOD	39.5	166.3	29.6	160.5

Table C.1. (continued)

		<LOD	NA	NA	<LOD	NA	<LOD	60.3	1067.0	0.1	401.6	28.9	NA	<LOD	<LOD	112.0	306.2	45.4	212.9
		<LOD	NA	NA	<LOD	NA	<LOD	60.3	944.0	0.1	400.2	32.6	NA	0.0	<LOD	89.9	254.0	38.0	178.7
		<LOD	NA	NA	<LOD	NA	<LOD	61.2	1171.0	0.0	476.0	32.4	NA	<LOD	<LOD	109.4	294.7	43.1	202.4
		<LOD	NA	NA	2.4	NA	<LOD	62.4	1167.0	0.1	623.0	30.8	NA	0.1	<LOD	820.0	1000.0	104.0	427.0
		<LOD	NA	NA	<LOD	NA	0.2	61.0	1675.0	0.1	1223.0	31.6	NA	0.0	<LOD	73.8	226.0	38.5	237.8
		<LOD	NA	NA	8.4	NA	0.2	60.7	773.0	<LOD	452.4	35.7	NA	0.1	0.0	53.3	137.8	19.4	96.8
		<LOD	NA	NA	<LOD	NA	<LOD	57.5	505.5	<LOD	249.5	49.3	NA	<LOD	<LOD	34.4	122.6	17.6	80.1
		<LOD	NA	NA	<LOD	NA	<LOD	52.8	466.0	<LOD	269.5	101.6	NA	0.0	<LOD	7.0	56.1	12.6	70.8
		<LOD	NA	NA	<LOD	NA	<LOD	53.8	339.1	0.0	160.6	162.3	NA	<LOD	<LOD	1.7	19.4	5.9	44.6
		<LOD	NA	NA	<LOD	NA	<LOD	66.8	228.5	0.0	150.1	136.7	NA	<LOD	<LOD	2.0	18.6	5.5	41.4
		<LOD	NA	NA	<LOD	NA	<LOD	58.7	1183.0	0.1	538.8	49.7	NA	<LOD	<LOD	124.0	303.0	38.6	158.3
		<LOD	NA	NA	<LOD	NA	<LOD	57.1	1197.0	0.0	507.1	50.4	NA	<LOD	<LOD	107.8	267.8	35.4	148.7
		<LOD	NA	NA	<LOD	NA	<LOD	57.1	1282.0	<LOD	533.6	57.3	NA	<LOD	<LOD	106.8	271.0	36.1	146.0
		<LOD	NA	NA	<LOD	NA	<LOD	55.7	1130.0	0.1	465.7	61.6	NA	<LOD	<LOD	87.6	214.8	28.6	120.9
		<LOD	NA	NA	<LOD	NA	<LOD	55.4	1051.0	0.0	439.7	63.1	NA	<LOD	<LOD	76.5	194.4	25.9	112.5
		<LOD	NA	NA	1.0	NA	<LOD	59.2	1209.0	0.5	364.5	56.7	NA	0.0	0.6	2400.0	2800.0	280.0	920.0
		<LOD	NA	NA	<LOD	NA	<LOD	53.2	1158.0	0.1	406.2	61.5	NA	0.0	<LOD	71.8	181.7	25.1	111.8
		<LOD	NA	NA	<LOD	NA	0.4	58.0	1063.0	0.1	406.4	67.4	NA	0.3	0.6	191.0	290.0	33.0	140.0
		<LOD	NA	NA	<LOD	NA	0.7	60.1	896.0	0.0	356.5	63.2	NA	0.4	1.1	75.6	161.0	21.8	91.5
		<LOD	NA	NA	<LOD	NA	0.2	55.8	963.0	<LOD	298.3	70.9	NA	0.1	<LOD	79.6	171.0	21.4	85.7
		<LOD	NA	NA	0.5	NA	<LOD	54.9	901.0	0.0	315.8	68.8	NA	0.2	<LOD	47.6	131.1	17.9	76.4
		<LOD	NA	NA	<LOD	NA	0.2	58.0	809.0	0.1	278.4	78.6	NA	0.2	0.0	136.0	232.0	25.2	99.5
		<LOD	NA	NA	2340.0	NA	<LOD	59.8	375.2	0.0	221.6	45.5	NA	0.2	0.3	11.1	36.5	5.8	33.3
		<LOD	NA	NA	6200.0	NA	<LOD	88.7	251.1	0.0	214.3	51.4	NA	22.0	0.2	7.4	24.1	3.7	19.3
		<LOD	NA	NA	0.6	NA	<LOD	56.6	509.7	0.0	250.3	72.2	NA	0.2	0.4	13.6	52.2	9.1	43.9
		<LOD	NA	NA	<LOD	NA	<LOD	54.6	458.4	0.1	263.4	66.9	NA	0.1	<LOD	16.0	58.2	9.5	44.4
		<LOD	NA	NA	<LOD	NA	<LOD	60.0	660.0	0.1	291.8	65.3	NA	0.0	<LOD	77.0	190.0	22.2	78.5
		<LOD	NA	NA	<LOD	NA	<LOD	55.0	643.0	0.0	315.9	61.4	NA	0.0	<LOD	27.6	89.5	13.3	56.6
		488.0	NA	NA	532.0	NA	6.6	318.0	23000.0	27.5	9.3	72.0	NA	6.2	20.4	9140.0	18700.0	1849.0	5730.0
		<LOD	NA	NA	<LOD	NA	<LOD	52.7	289.6	<LOD	241.7	25.5	NA	<LOD	<LOD	5.7	18.6	3.1	19.6
		<LOD	NA	NA	<LOD	NA	<LOD	55.8	559.7	0.0	283.1	72.3	NA	<LOD	<LOD	71.4	138.6	17.4	66.6

Table C.1. (continued)

Sample name	Scheelite host	Sm_ m147	Eu_ m153	Gd_ m157	Tb_ m159	Dy_ m163	Ho_ m165	Er_ m166	Tm_ m169	Yb_ m172	Lu_ m175	Hf_ m178	Ta_ m181	Au_ m197	Pb_ m206	Pb_ m208	Bi_ m209	Th_ m232	U_ m238
18-CA-50	Quartz-vein in Mine Stock pluton	193.8	12.6	214.9	31.8	217.0	40.0	122.1	14.8	70.0	7.6	0.2	7.8	NA	12.6	12.4	0.0	0.9	0.8
		154.0	12.3	198.2	33.4	240.4	45.2	133.3	14.9	67.2	6.6	0.2	8.2	NA	13.0	12.9	0.0	1.1	1.2
		240.3	10.0	333.8	49.6	323.0	52.7	132.1	12.0	48.1	4.7	0.3	9.6	NA	12.4	12.3	0.0	0.7	0.7
		284.9	13.6	341.9	50.9	331.9	54.6	146.4	14.8	62.8	6.2	0.3	10.1	NA	14.7	14.4	0.0	1.4	1.4
		316.3	14.3	364.7	52.4	319.8	49.0	117.2	11.0	43.8	4.5	0.2	9.8	NA	14.1	14.2	0.0	1.4	2.0
		312.9	17.5	353.3	50.0	321.2	52.9	135.7	13.7	58.8	6.3	0.2	11.0	NA	37.7	32.6	0.0	1.4	1.4
		309.0	14.9	375.7	52.4	343.6	57.6	143.9	14.4	63.2	6.3	0.3	9.2	NA	14.6	14.0	0.0	1.0	0.8
		350.0	15.8	402.0	61.8	440.0	80.7	221.0	23.0	110.9	11.3	0.4	15.1	NA	15.6	15.3	0.0	2.1	1.2
		298.4	14.7	353.2	54.8	386.2	70.4	182.9	18.8	84.2	8.7	0.3	14.7	NA	15.0	14.5	0.1	1.9	1.4
		311.5	13.5	364.1	54.2	369.9	65.2	168.7	16.9	77.3	7.9	0.3	13.8	NA	14.7	13.7	0.0	1.5	1.1
		334.1	14.5	399.2	60.1	414.1	76.4	203.4	21.5	99.0	10.6	0.4	13.4	NA	13.9	12.8	0.0	1.5	0.9
		322.8	11.1	381.6	55.1	357.3	62.6	156.7	15.7	71.8	7.5	0.3	13.3	NA	13.1	12.9	0.0	1.2	1.0
		312.2	11.9	381.1	57.1	381.6	68.7	170.4	17.6	84.9	8.8	0.3	12.0	NA	13.5	12.9	0.0	1.4	0.8
		295.5	10.7	349.5	53.8	361.1	66.5	166.8	18.0	86.7	9.0	0.3	11.9	NA	13.0	12.5	0.0	1.2	0.7
		369.3	11.8	469.2	73.1	479.1	87.5	213.7	22.4	107.2	11.1	0.4	12.8	NA	13.2	12.9	0.0	1.8	0.9
		336.1	12.5	432.1	67.0	427.9	77.4	182.9	18.8	85.8	9.0	0.4	13.3	NA	16.5	14.6	0.0	1.6	1.2
		230.8	12.2	325.8	53.2	349.1	68.2	165.3	17.1	74.7	8.2	0.3	14.1	NA	14.2	14.2	0.0	2.1	0.9
		746.0	20.6	1207.0	217.0	1540.0	315.0	826.0	95.9	481.0	49.9	1.4	26.8	NA	14.7	13.5	0.0	15.0	5.4
		301.1	12.4	333.2	56.2	361.0	68.8	174.8	21.6	104.0	10.9	0.3	10.7	NA	13.3	12.9	0.0	2.4	1.0
		380.4	11.0	457.6	71.1	425.5	77.4	177.8	19.8	86.7	8.5	0.3	12.4	NA	12.8	12.6	0.0	1.9	0.9
		290.5	14.5	310.6	56.2	375.5	75.2	200.6	26.4	129.6	13.4	0.3	13.5	NA	11.4	10.3	0.0	3.2	1.4
		334.3	14.4	366.6	63.4	399.7	78.5	201.8	26.4	123.6	13.0	0.4	14.3	NA	11.2	10.5	0.2	2.6	1.0
		298.7	11.9	292.2	45.0	255.0	45.4	96.2	10.9	45.5	4.1	0.2	6.9	NA	11.0	10.1	0.0	0.3	0.4
		335.4	12.0	377.9	62.0	377.6	72.0	177.4	21.2	93.8	9.4	0.2	11.9	NA	10.4	9.7	0.0	1.7	0.8
		392.1	12.2	452.4	73.6	440.3	81.2	193.4	23.6	106.6	10.6	0.4	12.7	NA	10.3	9.3	0.0	2.0	1.0
		392.0	11.1	456.4	73.0	431.8	78.5	178.8	20.5	90.3	8.9	0.4	12.1	NA	10.4	10.4	0.0	2.0	0.9
		250.6	12.9	285.5	50.0	324.8	64.8	165.1	20.0	93.6	10.0	0.5	10.3	NA	20.1	16.4	0.1	2.6	1.5
		261.4	13.0	296.2	49.1	304.6	57.2	136.2	16.3	71.9	7.4	0.3	9.3	NA	15.8	14.8	0.1	1.7	1.1
		339.6	10.6	406.8	68.3	420.0	77.1	178.6	21.3	98.7	9.6	0.3	11.0	NA	12.7	11.9	0.0	1.7	0.8
		215.8	12.6	254.1	46.0	315.9	63.7	167.5	21.4	103.7	10.6	0.3	10.2	NA	13.5	11.8	0.1	1.7	0.8
		411.8	9.9	498.0	78.1	458.3	77.6	172.0	19.3	85.7	8.0	0.4	12.1	NA	14.7	12.9	0.1	1.7	0.9

Table C.1. (continued)

		228.3	11.7	298.6	52.1	350.2	65.8	158.5	17.3	78.0	7.6	0.3	9.2	NA	14.4	12.8	<LOD	1.1	0.5
		373.6	9.0	471.7	73.1	447.1	76.9	168.3	16.8	69.8	6.8	0.4	14.1	NA	12.8	11.6	0.0	2.1	1.2
		334.3	9.4	427.8	70.8	467.2	84.4	199.5	22.0	103.6	9.9	0.4	11.3	NA	13.9	12.0	0.0	2.4	1.2
		375.0	10.6	444.5	71.3	445.3	76.0	175.8	18.8	87.8	8.3	0.4	11.9	NA	12.5	11.5	0.0	2.3	1.1
		344.5	10.1	405.9	65.6	425.6	71.5	167.4	17.8	83.6	8.1	0.4	11.6	NA	14.1	12.3	0.0	1.9	0.9
		346.3	10.0	415.2	67.5	438.6	73.6	175.7	19.2	92.5	8.6	0.3	12.0	NA	12.7	11.8	0.0	2.1	1.0
		336.1	11.6	380.0	65.8	457.2	79.8	207.6	25.1	131.5	13.1	0.4	20.4	NA	12.0	10.7	0.0	16.8	7.0
		380.6	8.7	468.0	74.3	454.7	67.2	148.0	15.1	69.6	6.2	0.4	11.5	NA	15.3	14.4	0.2	1.9	1.3
		381.5	9.7	456.7	72.3	473.6	79.6	191.1	20.2	92.7	9.2	0.3	11.3	NA	13.0	12.5	0.0	2.5	1.2
		341.0	10.7	395.4	64.5	436.9	75.2	188.4	20.1	98.0	9.6	0.5	12.7	NA	14.4	13.5	0.0	2.1	1.8
		128.0	9.8	108.2	20.5	156.8	30.1	93.7	13.1	76.3	8.2	0.1	7.0	NA	11.3	10.9	0.0	1.2	0.9
		144.3	13.5	139.0	28.1	236.1	48.3	166.8	25.9	168.3	19.8	0.2	22.7	NA	18.7	18.3	0.2	9.6	5.2
		145.3	8.8	151.3	26.5	194.2	35.6	101.6	12.6	67.1	6.8	0.1	6.4	NA	12.9	12.6	<LOD	1.2	0.6
		387.4	10.4	456.0	73.0	489.0	79.6	189.3	19.3	86.1	8.4	0.4	14.1	NA	14.0	13.1	<LOD	2.0	1.2
		160.1	9.3	190.0	33.3	254.0	47.1	131.2	16.1	82.3	8.5	0.2	11.0	NA	11.1	10.8	0.0	2.2	1.0
		336.0	9.4	426.4	64.1	426.6	73.9	170.9	17.6	78.5	7.8	0.3	11.6	NA	11.8	12.3	0.0	1.7	0.8
		346.4	11.3	427.8	60.6	394.3	68.5	162.9	16.9	74.5	7.2	0.3	9.9	NA	11.7	10.7	0.0	1.2	0.7
		250.1	10.4	330.9	50.9	338.0	58.8	136.3	13.2	52.8	4.5	0.2	9.7	NA	10.7	10.9	0.0	0.5	3.2
		106.9	11.5	103.5	17.0	123.1	23.6	69.8	9.3	51.0	5.0	0.1	4.6	NA	10.4	10.1	0.0	1.1	0.7
		60.8	7.6	73.8	16.3	135.7	32.7	114.4	18.7	116.9	15.1	NA	NA	6.3	4.5	4.6	0.1	NA	0.7
		66.8	5.2	92.7	20.0	158.9	37.8	119.8	15.4	82.3	9.5	NA	NA	5.9	5.6	5.7	0.1	NA	0.5
		12.7	5.1	16.8	2.9	19.6	4.3	11.9	1.3	7.5	1.0	NA	NA	6.1	6.2	6.3	0.1	NA	0.1
		71.0	7.1	104.3	22.1	176.1	40.7	122.9	16.5	84.0	9.8	NA	NA	6.2	4.7	5.0	0.1	NA	0.4
		65.7	6.5	93.5	20.8	170.5	40.0	126.6	17.8	91.7	10.7	NA	NA	6.0	5.5	5.4	2.9	NA	0.3
		43.9	3.4	64.7	13.1	103.1	22.9	67.7	8.9	45.7	5.3	NA	NA	6.2	6.3	6.1	11.2	NA	0.2
		6.1	1.9	9.4	2.0	16.1	3.8	11.8	1.5	8.4	1.0	NA	NA	5.8	8.3	7.8	25.6	NA	1.8
18-CA-10	Lower Argillite	4.1	1.3	6.9	1.4	11.4	2.8	8.2	1.1	5.9	0.7	NA	NA	8.7	12.0	12.0	92000.0	NA	1.0
		44.3	8.2	58.7	12.0	94.8	22.1	71.5	10.6	65.5	8.8	NA	NA	5.8	6.7	5.9	1.1	NA	3.7
		5.9	2.8	7.8	1.3	9.9	2.2	7.1	1.0	5.8	0.7	NA	NA	4.8	5.4	4.9	<LOD	NA	7.8
		2.6	1.2	5.1	1.0	9.2	2.1	5.4	0.7	3.2	0.3	NA	NA	1.9	13.7	13.1	0.5	NA	0.2
		21.9	24.7	26.5	5.4	45.1	10.0	32.5	5.3	40.3	6.2	NA	NA	0.8	3.6	1.0	0.8	NA	54.2
		11.2	3.2	16.7	3.3	23.6	4.7	12.8	1.5	6.4	0.7	NA	NA	5.4	6.6	6.7	0.0	NA	0.0
		41.4	25.1	49.8	8.7	60.2	12.8	37.9	5.9	42.7	6.9	NA	NA	5.4	4.7	4.9	0.0	NA	3.7
		17.2	5.8	22.5	4.0	29.2	6.1	16.7	2.1	11.5	1.3	NA	NA	5.0	7.8	7.6	0.0	NA	0.1
		32.0	18.6	33.9	6.3	47.4	10.1	34.2	6.0	51.0	8.0	NA	NA	5.6	5.5	5.4	0.0	NA	2.9

Table C.1. (continued)

		27.3	7.7	29.3	6.0	47.2	10.8	36.0	5.8	36.2	4.2	NA	NA	5.2	5.8	5.5	0.1	NA	0.1
		27.3	4.3	39.2	8.0	65.7	15.5	47.7	6.8	36.1	4.0	NA	NA	5.0	10.7	10.4	0.1	NA	0.4
		39.9	7.2	46.6	9.6	77.1	17.3	57.7	9.2	58.0	7.1	NA	NA	4.8	8.8	8.6	0.0	NA	1.4
		34.5	10.5	38.6	8.3	71.2	17.6	62.5	10.9	78.2	10.7	NA	NA	5.2	8.2	7.5	0.1	NA	2.8
		70.4	11.6	85.0	16.8	129.4	29.9	94.1	13.6	82.5	10.4	NA	NA	5.2	5.1	5.3	0.1	NA	2.0
		17.0	4.8	23.3	4.8	39.3	9.6	30.9	4.8	29.5	3.7	NA	NA	4.2	6.5	6.4	0.1	NA	1.9
		27.4	4.8	37.0	7.2	57.0	12.6	40.4	5.5	32.5	4.2	NA	NA	4.7	6.7	6.9	0.1	NA	0.5
		12.2	7.9	14.8	2.5	18.1	3.8	10.6	1.5	9.3	1.1	NA	NA	5.0	6.7	6.8	0.0	NA	0.0
		53.0	14.1	62.4	11.8	92.5	21.4	67.3	9.7	60.7	7.7	NA	NA	4.6	5.2	5.3	0.1	NA	0.9
		4.7	1.3	5.6	1.3	9.7	2.5	7.8	1.2	8.0	1.0	NA	NA	4.4	5.9	6.5	0.1	NA	0.1
		14.5	5.2	18.4	3.4	23.6	5.2	14.0	1.8	10.1	1.3	NA	NA	4.9	6.1	6.4	0.2	NA	0.1
		27.9	17.5	37.5	9.1	77.0	17.0	54.7	8.5	57.5	6.6	NA	NA	0.5	3.8	1.2	0.7	NA	42.8
		32.7	4.5	44.1	9.4	77.1	18.3	56.4	7.3	42.2	4.3	NA	NA	4.7	5.4	5.2	1.3	NA	0.2
		8.6	4.0	17.8	3.9	32.8	8.0	22.0	3.3	21.3	2.7	NA	NA	4.1	7.7	7.7	46.1	NA	10.0
18-CA-47	Garnet-pyroxene skarn	12.6	3.4	12.9	2.1	12.1	2.4	6.3	0.7	3.8	0.4	NA	NA	NA	1.9	2.3	NA	<LOD	0.1
		13.4	2.1	14.2	2.4	14.2	2.8	7.4	0.9	5.2	0.5	NA	NA	NA	1.7	1.9	NA	<LOD	0.1
		23.5	4.0	22.9	4.5	31.1	6.4	19.3	3.0	21.0	2.4	NA	NA	NA	3.8	3.5	NA	0.2	0.9
		13.0	2.4	10.7	2.2	13.2	2.6	6.8	1.0	6.8	0.6	NA	NA	NA	2.3	2.5	NA	<LOD	0.1
		53.6	8.7	55.0	11.4	75.8	14.6	38.9	4.8	25.0	2.5	NA	NA	NA	3.2	3.4	NA	0.1	0.7
		14.3	2.1	14.6	2.6	17.5	3.4	9.2	1.3	7.8	0.8	NA	NA	NA	5.2	5.1	NA	<LOD	0.2
		18.5	2.7	17.8	3.2	20.3	4.0	10.7	1.5	8.0	0.8	NA	NA	NA	2.8	2.5	NA	<LOD	0.0
18-CA-31a	Pyroxene skarn	1.5	15.8	1.4	0.2	1.0	0.1	0.2	<LOD	<LOD	<LOD	NA	NA	NA	2.7	2.4	NA	<LOD	1.1
		7.6	15.1	7.2	1.0	5.9	1.4	3.7	0.5	2.3	0.1	NA	NA	NA	4.0	3.4	NA	0.2	1.5
		11.4	9.2	14.6	2.0	10.3	2.0	3.7	0.2	0.3	<LOD	NA	NA	NA	3.8	3.6	NA	<LOD	1.5
		9.6	5.5	11.7	1.7	9.3	1.8	3.7	0.2	0.5	0.0	NA	NA	NA	3.3	3.3	NA	0.1	0.9
18-CA-29b	Amphibole-rich facies	25.8	2.1	17.6	2.8	15.4	2.6	6.0	0.7	3.8	0.4	NA	NA	NA	3.6	3.8	NA	<LOD	<LOD
		9.1	1.5	5.7	0.9	5.0	0.9	2.1	0.3	1.5	0.1	NA	NA	NA	4.3	3.9	NA	0.0	0.0
		6.5	1.3	4.6	0.7	3.4	0.6	1.3	0.2	0.7	0.1	NA	NA	NA	2.9	2.8	NA	<LOD	<LOD
		14.0	1.5	10.7	1.2	6.0	1.0	2.3	0.2	1.1	0.1	NA	NA	NA	3.0	2.9	NA	0.3	0.4
		15.8	1.5	11.4	1.3	6.5	1.0	2.5	0.3	1.4	0.1	NA	NA	NA	3.9	3.1	NA	0.1	0.2
18-CA-40B	Biotite-Amphibole rich facies	57.5	9.8	81.5	14.2	86.3	17.1	41.3	4.9	26.6	3.2	NA	NA	NA	4.6	4.6	NA	1.6	0.8
		16.3	9.8	15.6	2.9	19.8	4.4	15.0	2.8	21.6	3.2	NA	NA	NA	5.8	5.5	NA	0.9	0.6
		22.1	7.1	27.7	4.9	28.7	5.7	14.9	1.9	11.2	1.3	NA	NA	NA	4.5	4.5	NA	1.0	0.3
18-CA-28	Biotite-rich facies	43.8	13.4	42.6	9.2	68.8	15.5	52.9	9.5	68.1	8.4	NA	NA	NA	5.2	4.7	NA	0.2	0.2
		48.8	5.5	80.7	16.7	125.0	28.5	74.4	8.8	43.8	5.3	NA	NA	NA	7.3	6.8	NA	<LOD	0.1

Table C.1. (continued)

		109.2	16.8	146.5	32.3	242.6	54.1	156.5	22.0	129.9	15.0	NA	NA	NA	8.5	8.2	NA	0.2	0.4
		107.8	14.9	137.9	29.7	211.7	47.8	135.7	19.1	109.6	12.3	NA	NA	NA	8.7	9.1	NA	0.2	0.5
18-CA-40B	Quartz vein in Biotite-Amphibole rich facies	59.2	22.2	39.5	8.5	64.4	13.9	48.8	10.4	86.4	11.4	NA	NA	NA	7.7	7.4	NA	4.7	2.3
		51.0	18.2	33.1	7.2	54.8	11.8	43.4	9.1	77.3	10.1	NA	NA	NA	7.2	6.9	NA	2.8	1.2
		24.6	22.1	16.0	3.7	27.7	6.4	24.8	5.8	54.7	7.6	NA	NA	NA	7.8	7.5	NA	2.8	1.5
		71.7	20.9	46.6	10.5	76.0	16.1	57.7	12.1	97.4	12.6	NA	NA	NA	7.4	7.6	NA	3.5	1.7
18-CA-51	Upper Argillite	2.8	1.2	6.9	1.6	13.2	3.3	10.8	1.5	8.9	1.3	<LOD	0.2	NA	3.6	3.3	0.0	<LOD	0.0
		14.4	1.7	29.8	5.9	37.5	6.4	14.8	1.5	7.1	0.7	<LOD	10.5	NA	2.5	2.4	<LOD	<LOD	0.0
		24.0	6.9	32.0	6.4	43.3	8.4	24.1	3.3	20.7	2.4	0.0	21.0	NA	4.6	4.4	0.0	0.2	0.2
		85.2	16.8	73.9	13.3	96.6	19.7	62.5	10.0	64.6	7.6	0.1	53.4	NA	6.8	6.1	0.1	1.5	2.2
		30.4	16.8	34.6	8.7	67.8	14.6	51.0	9.1	63.1	7.0	0.0	28.5	NA	5.9	5.3	0.0	0.2	0.4
		26.0	9.2	31.8	7.2	55.5	11.9	38.5	6.0	39.3	4.7	0.1	6.9	NA	5.2	4.5	0.0	0.1	0.3
		67.1	16.1	98.6	26.7	225.2	49.9	165.8	25.4	155.0	16.0	0.2	147.9	NA	7.0	6.3	0.1	0.4	1.2
		24.6	8.8	31.3	6.4	47.5	9.0	26.9	3.8	23.9	3.2	0.0	3.6	NA	4.8	4.6	0.0	0.1	0.3
		35.9	10.1	48.3	11.6	89.9	17.8	55.5	8.0	48.0	5.0	0.1	25.0	NA	5.2	4.9	0.0	0.2	0.6
		35.5	8.5	46.0	9.6	66.7	13.2	37.1	5.0	28.3	3.6	0.0	6.0	NA	4.9	4.5	0.0	0.1	0.3
		44.8	8.8	57.2	12.2	88.7	17.2	50.7	6.8	37.5	4.6	0.0	14.4	NA	5.3	4.9	0.0	0.1	0.4
		28.4	13.2	33.5	7.7	61.3	12.4	43.0	7.5	58.1	7.0	0.1	21.4	NA	10.1	8.6	0.1	0.7	1.8
		29.7	14.0	36.9	9.2	76.8	16.1	58.0	10.7	76.8	9.5	0.1	37.7	NA	5.6	5.7	0.0	0.9	0.7
		69.4	14.4	82.5	18.9	151.4	29.6	98.5	16.2	105.2	12.6	0.1	65.1	NA	5.8	5.5	0.0	1.7	0.8
		76.5	19.1	85.7	18.9	147.7	29.3	102.0	18.1	127.4	15.5	0.1	63.7	NA	6.9	6.7	0.0	2.9	0.9
		71.1	18.8	84.6	18.2	139.0	27.3	89.2	16.2	119.1	14.2	0.1	70.6	NA	7.9	7.7	0.0	3.3	1.0
		81.7	19.6	91.1	20.6	162.8	32.3	109.8	19.5	132.2	16.9	0.1	82.3	NA	7.8	6.9	0.0	3.6	1.0
		122.5	18.0	152.5	31.4	226.9	43.1	129.5	19.2	121.4	14.6	0.2	113.6	NA	7.1	6.6	0.1	5.0	1.7
		164.0	15.4	260.0	55.2	393.0	71.0	193.0	25.6	149.9	16.3	0.4	136.2	NA	7.8	7.3	0.1	2.9	1.4
		54.7	15.1	76.5	18.0	139.4	26.4	81.7	13.4	92.8	11.6	0.1	94.7	NA	7.7	6.9	0.1	3.7	1.6
		33.0	20.6	39.7	9.1	74.5	14.5	48.1	9.4	74.7	10.0	0.0	43.6	NA	5.8	5.4	0.1	4.6	1.2
		28.0	12.3	36.2	8.7	73.2	14.4	50.1	8.4	56.4	7.0	0.1	16.3	NA	3.4	3.3	0.1	0.3	1.1
		23.8	7.9	33.1	7.8	61.3	11.9	37.6	5.7	35.3	4.5	0.1	6.4	NA	3.2	3.2	0.0	0.2	0.8
		24.0	9.5	33.8	6.8	51.1	8.9	25.9	3.5	21.2	2.6	0.0	5.3	NA	4.5	4.3	0.0	0.2	0.4
		60.0	30.1	69.7	16.9	145.2	28.7	105.8	21.2	172.8	23.7	0.1	98.7	NA	7.2	6.8	0.1	7.9	2.6
		59.1	35.5	73.0	17.4	150.3	30.0	107.4	21.2	173.7	24.0	0.1	90.5	NA	7.1	6.7	0.1	8.9	3.2
		60.4	35.7	74.7	18.3	158.6	31.4	115.5	23.4	186.0	25.6	0.1	86.7	NA	7.3	7.1	0.1	7.9	3.2
		51.5	35.1	68.0	16.3	144.2	28.1	102.5	20.4	169.3	22.9	0.1	75.6	NA	7.4	6.7	0.1	6.0	2.9
		50.6	32.5	64.4	15.9	136.9	26.4	94.3	18.3	150.4	20.2	0.1	72.7	NA	7.0	6.1	0.1	3.8	2.4

Table C.1. (continued)

		161.0	50.3	133.0	23.4	175.4	30.1	102.5	18.2	141.0	18.7	0.2	56.3	NA	8.1	7.7	0.4	6.9	7.1
		52.6	41.0	70.4	17.3	154.4	29.6	108.4	21.3	175.6	24.5	0.1	64.5	NA	6.7	6.4	0.1	5.3	3.8
		51.3	37.8	67.3	16.4	143.5	27.4	100.2	19.7	158.0	22.4	0.1	62.7	NA	6.6	6.3	0.1	4.2	3.8
		42.5	34.5	58.3	14.0	122.7	23.5	84.4	16.3	128.8	17.8	0.1	53.5	NA	6.1	5.6	0.1	2.7	2.6
		37.2	38.6	50.5	12.7	116.5	22.8	86.6	18.1	156.3	22.1	0.1	46.5	NA	6.2	5.7	0.1	3.4	3.3
		37.6	41.4	51.0	13.0	118.8	23.1	85.9	17.5	146.7	21.8	0.1	47.7	NA	7.0	7.0	0.2	3.9	4.3
		37.0	40.0	49.9	12.0	108.9	21.0	74.9	15.2	131.3	19.3	0.1	40.0	NA	6.3	6.1	0.4	3.6	4.7
		21.3	19.5	35.2	8.1	65.6	11.6	36.9	6.3	44.0	6.1	<LOD	24.7	NA	36.0	33.7	69.0	1.1	2.7
		10.8	8.9	17.8	4.2	38.4	7.4	26.6	5.1	40.5	5.8	<LOD	22.1	NA	10.8	10.1	48.7	0.9	2.2
		21.7	29.2	27.2	7.1	65.9	12.4	47.7	10.0	80.5	12.3	0.0	38.5	NA	5.2	4.7	0.0	1.9	2.6
		21.7	24.3	28.3	6.9	64.4	11.8	42.6	8.2	65.1	9.4	<LOD	39.5	NA	5.5	5.6	0.1	1.8	1.6
		31.6	34.5	38.0	9.4	85.5	14.9	55.2	10.8	87.7	12.6	0.1	46.7	NA	6.6	5.7	0.1	3.1	2.4
		25.3	34.8	34.7	8.7	81.2	15.2	58.2	12.4	101.2	15.1	0.0	50.8	NA	6.6	6.6	0.0	3.4	2.8
		2090.0	621.0	2050.0	430.0	3190.0	474.0	1424.0	231.0	1690.0	221.0	3.2	2.1	NA	225.0	103.0	12.7	145.0	1310.0
		14.9	6.2	33.0	7.4	64.4	11.6	34.2	4.2	23.4	2.6	0.1	9.5	NA	4.6	3.9	0.0	0.1	0.2
		26.0	30.8	34.1	8.0	75.3	13.7	51.2	10.4	82.3	12.1	0.1	43.5	NA	5.8	5.6	0.1	2.5	2.1

Table C.2. Trace element composition of scheelite from the Mactung deposit. *All values are in ppm. NA= not analyzed; LOD= limit of detection.*

Sample name	Scheelite host	Ti_ m47	Mn_ m55	Fe_ m57	Cu_ m63	As_ m75	Rb_ m85	Sr_ m88	Y_ m89	Zr_ m90	Nb_ m93	Mo_ m95	Ag_ m107	Cs_ m133	Ba_ m137	La_ m139	Ce_ m140	Pr_ m141	Nd_ m146
MS161 322-322.3A	Argillite (Unit 1)	NA	8.4	57.7	<LOD	<LOD	<LOD	93.4	169.5	NA	NA	44.7	<LOD	NA	NA	NA	25.3	6.5	64.1
		NA	14.4	341.0	<LOD	<LOD	6.3	88.5	164.4	NA	NA	29.2	<LOD	NA	NA	NA	105.2	25.5	162.8
		NA	18.3	239.0	<LOD	<LOD	<LOD	93.3	94.9	NA	NA	35.0	<LOD	NA	NA	NA	28.2	6.9	52.3
		NA	16.4	254.0	<LOD	<LOD	<LOD	138.2	66.1	NA	NA	39.8	<LOD	NA	NA	NA	18.1	4.4	37.7
		NA	14.6	131.0	<LOD	<LOD	1.4	91.7	133.4	NA	NA	39.7	<LOD	NA	NA	NA	27.8	7.0	58.5
		NA	13.0	105.0	1.5	<LOD	<LOD	91.4	60.1	NA	NA	33.2	<LOD	NA	NA	NA	30.6	6.5	48.3
		NA	3700.0	160000.0	<LOD	<LOD	2320.0	118.5	54.6	NA	NA	33.0	<LOD	NA	NA	NA	24.0	5.1	35.0
		NA	58.4	959.0	<LOD	<LOD	<LOD	96.2	83.1	NA	NA	40.2	<LOD	NA	NA	NA	37.9	7.9	58.6
		NA	14.3	210.0	<LOD	<LOD	2.3	97.0	80.4	NA	NA	49.1	<LOD	NA	NA	NA	19.0	4.5	41.9
		NA	10.9	82.0	<LOD	<LOD	0.5	95.1	56.2	NA	NA	44.3	<LOD	NA	NA	NA	30.9	5.7	38.5
		NA	8.7	168.0	<LOD	<LOD	0.5	108.0	88.1	NA	NA	34.5	<LOD	NA	NA	NA	26.9	6.2	53.8
		NA	32.8	678.0	<LOD	<LOD	<LOD	97.1	218.0	NA	NA	40.7	<LOD	NA	NA	NA	26.7	7.7	85.7
		NA	9.3	275.0	<LOD	<LOD	1.1	98.8	115.8	NA	NA	63.7	<LOD	NA	NA	NA	39.7	12.2	103.6
		NA	15.5	185.0	<LOD	<LOD	<LOD	96.6	114.4	NA	NA	42.3	<LOD	NA	NA	NA	49.9	10.6	70.8
MS231 60-60.3	Pyroxene skarn	NA	8.8	48.3	<LOD	0.9	<LOD	90.5	37.0	NA	NA	282.9	<LOD	NA	NA	NA	46.0	6.5	36.0
		NA	10.3	42.4	<LOD	<LOD	<LOD	25.7	94.9	NA	NA	503.0	<LOD	NA	NA	NA	184.1	25.4	122.2
		NA	8.4	39.0	<LOD	<LOD	<LOD	38.7	58.0	NA	NA	569.0	<LOD	NA	NA	NA	148.3	20.6	101.6
		NA	15.6	50.9	<LOD	<LOD	<LOD	35.6	61.5	NA	NA	611.0	<LOD	NA	NA	NA	154.7	22.1	104.0
		NA	15.8	42.9	<LOD	<LOD	<LOD	40.2	69.9	NA	NA	569.0	<LOD	NA	NA	NA	178.6	25.0	118.0
		NA	13.3	43.7	<LOD	<LOD	<LOD	37.4	67.7	NA	NA	747.0	<LOD	NA	NA	NA	167.6	23.3	101.6
		NA	11.6	48.0	<LOD	1.2	<LOD	47.2	42.6	NA	NA	629.0	<LOD	NA	NA	NA	95.3	13.2	62.1
		NA	11.2	92.0	<LOD	1.7	2.6	96.9	45.4	NA	NA	455.0	<LOD	NA	NA	NA	52.0	8.4	43.7
		NA	11.6	48.7	<LOD	<LOD	<LOD	32.7	101.0	NA	NA	612.0	<LOD	NA	NA	NA	187.3	29.4	142.9
		NA	19.8	51.3	<LOD	<LOD	<LOD	34.5	70.8	NA	NA	659.0	<LOD	NA	NA	NA	129.9	20.9	102.7
		NA	19.5	46.3	<LOD	<LOD	<LOD	34.8	55.7	NA	NA	591.0	<LOD	NA	NA	NA	103.2	16.7	80.8
		NA	20.1	51.8	<LOD	<LOD	<LOD	34.9	42.9	NA	NA	588.0	<LOD	NA	NA	NA	72.8	12.3	61.3
		NA	15.2	51.2	<LOD	<LOD	<LOD	32.7	52.2	NA	NA	567.0	<LOD	NA	NA	NA	102.2	16.7	79.7
		NA	13.3	211.0	<LOD	2.3	<LOD	66.3	55.7	NA	NA	483.0	<LOD	NA	NA	NA	111.7	17.4	71.3
		NA	7.3	57.6	<LOD	1.2	<LOD	38.9	52.8	NA	NA	506.0	<LOD	NA	NA	NA	106.6	16.0	69.6
		NA	6.4	41.5	<LOD	<LOD	<LOD	36.6	51.2	NA	NA	544.4	<LOD	NA	NA	NA	104.5	15.2	65.1
		NA	5.9	41.5	<LOD	1.4	<LOD	50.8	46.0	NA	NA	650.0	<LOD	NA	NA	NA	77.7	12.1	59.1

Table C.2. (continued)

		NA	7.3	44.5	<LOD	<LOD	<LOD	50.4	40.0	NA	NA	634.0	<LOD	NA	NA	NA	67.4	10.8	54.2
		NA	20.5	144.7	<LOD	1.5	<LOD	101.3	33.7	NA	NA	359.0	<LOD	NA	NA	NA	27.2	4.7	24.4
		NA	16.0	62.9	<LOD	1.0	<LOD	42.5	101.4	NA	NA	454.6	<LOD	NA	NA	NA	120.0	20.6	98.9
		NA	7.8	43.3	<LOD	1.4	<LOD	40.9	71.4	NA	NA	441.9	<LOD	NA	NA	NA	88.0	13.7	63.3
		NA	10.8	47.9	<LOD	<LOD	<LOD	36.6	61.0	NA	NA	604.4	<LOD	NA	NA	NA	109.3	14.7	59.2
		NA	11.8	54.3	<LOD	<LOD	<LOD	34.8	73.6	NA	NA	397.0	<LOD	NA	NA	NA	152.8	19.7	74.7
		NA	16.6	51.4	<LOD	<LOD	<LOD	28.9	73.7	NA	NA	349.8	<LOD	NA	NA	NA	140.8	20.4	81.7
		NA	17.7	39.7	<LOD	<LOD	<LOD	24.6	72.6	NA	NA	305.5	<LOD	NA	NA	NA	206.9	27.1	95.8
		NA	17.2	50.3	<LOD	<LOD	<LOD	22.8	55.5	NA	NA	301.5	<LOD	NA	NA	NA	200.8	24.3	80.7
		NA	17.6	58.8	<LOD	<LOD	<LOD	23.7	49.9	NA	NA	286.6	<LOD	NA	NA	NA	207.4	23.9	81.4
		NA	17.7	51.1	<LOD	<LOD	<LOD	22.8	39.2	NA	NA	279.6	<LOD	NA	NA	NA	160.0	18.4	62.2
		NA	17.5	45.5	<LOD	<LOD	<LOD	22.3	35.5	NA	NA	281.0	<LOD	NA	NA	NA	142.7	16.0	52.4
		NA	2.0	168.0	3.0	<LOD	<LOD	53.6	15.9	NA	NA	26.7	<LOD	NA	NA	NA	5.0	1.2	6.8
		NA	17.1	56.4	<LOD	<LOD	<LOD	31.9	58.1	NA	NA	351.7	<LOD	NA	NA	NA	50.6	7.7	35.1
		NA	16.9	63.0	<LOD	<LOD	<LOD	29.5	54.2	NA	NA	330.7	<LOD	NA	NA	NA	85.2	11.0	42.4
		NA	15.7	51.7	<LOD	<LOD	<LOD	20.8	70.2	NA	NA	258.4	<LOD	NA	NA	NA	172.6	21.5	76.1
		NA	21.1	48.5	<LOD	<LOD	<LOD	19.9	65.9	NA	NA	259.2	<LOD	NA	NA	NA	135.9	18.6	75.3
		NA	19.3	76.8	0.6	<LOD	<LOD	21.7	106.8	NA	NA	285.5	<LOD	NA	NA	NA	226.9	30.1	120.3
		NA	18.5	55.9	<LOD	<LOD	<LOD	19.7	54.3	NA	NA	242.0	<LOD	NA	NA	NA	137.5	17.3	65.8
		NA	17.5	49.4	<LOD	<LOD	<LOD	41.4	38.8	NA	NA	420.5	<LOD	NA	NA	NA	90.2	11.2	48.8
		NA	9.7	48.6	<LOD	<LOD	<LOD	37.7	35.7	NA	NA	302.6	<LOD	NA	NA	NA	67.2	9.9	44.3
		NA	10.4	57.0	<LOD	<LOD	<LOD	54.5	32.3	NA	NA	404.6	<LOD	NA	NA	NA	57.6	8.5	38.4
		NA	12.4	48.7	<LOD	<LOD	<LOD	22.5	69.3	NA	NA	260.3	<LOD	NA	NA	NA	190.7	21.9	79.7
		NA	10.1	51.7	<LOD	1.2	<LOD	37.2	70.5	NA	NA	570.4	<LOD	NA	NA	NA	111.7	15.3	68.9
		NA	21.2	48.4	<LOD	<LOD	<LOD	29.3	67.7	NA	NA	502.3	<LOD	NA	NA	NA	179.7	21.9	84.3
		NA	22.2	68.3	<LOD	1.5	0.3	28.5	48.7	NA	NA	538.6	<LOD	NA	NA	NA	110.6	14.1	59.0
		NA	21.1	49.6	<LOD	<LOD	<LOD	26.3	67.5	NA	NA	495.0	<LOD	NA	NA	NA	163.8	21.8	91.5
		NA	19.6	47.3	<LOD	<LOD	<LOD	28.3	63.6	NA	NA	502.6	<LOD	NA	NA	NA	210.9	25.4	92.6
		NA	14.0	44.9	<LOD	<LOD	<LOD	36.4	44.1	NA	NA	558.8	<LOD	NA	NA	NA	111.2	14.9	62.4
		NA	74.0	1880.0	<LOD	1.4	<LOD	89.3	41.8	NA	NA	593.0	<LOD	NA	NA	NA	56.8	8.1	36.9
		NA	21.1	743.0	<LOD	1.2	0.4	36.7	38.1	NA	NA	561.0	<LOD	NA	NA	NA	82.0	11.2	50.1
		NA	9.1	37.8	<LOD	1.4	<LOD	89.5	41.2	NA	NA	509.0	<LOD	NA	NA	NA	52.5	7.8	36.5
		NA	13.1	45.1	<LOD	<LOD	<LOD	31.8	57.9	NA	NA	636.0	<LOD	NA	NA	NA	131.0	16.4	71.5
		NA	19.3	93.0	<LOD	<LOD	<LOD	28.1	76.2	NA	NA	472.0	<LOD	NA	NA	NA	140.0	18.4	75.3
		NA	23.9	38.5	<LOD	<LOD	<LOD	28.1	69.9	NA	NA	448.3	<LOD	NA	NA	NA	66.4	11.3	58.9
		NA	26.0	52.0	<LOD	<LOD	<LOD	28.9	70.6	NA	NA	444.7	0.2	NA	NA	NA	77.8	12.4	62.2
		NA	27.8	41.6	<LOD	<LOD	<LOD	29.0	75.4	NA	NA	454.0	<LOD	NA	NA	NA	51.1	10.9	61.2
		NA	27.5	46.0	<LOD	<LOD	<LOD	29.2	97.9	NA	NA	458.7	<LOD	NA	NA	NA	223.0	33.7	136.0
		NA	26.4	39.4	<LOD	<LOD	<LOD	27.5	88.2	NA	NA	581.0	<LOD	NA	NA	NA	183.0	26.7	127.1
		NA	24.9	40.8	<LOD	<LOD	<LOD	30.2	86.0	NA	NA	585.0	<LOD	NA	NA	NA	106.1	20.0	106.5

Table C.2. (continued)

		NA	22.9	40.4	<LOD	<LOD	<LOD	30.3	75.0	NA	NA	499.8	<LOD	NA	NA	NA	97.6	17.7	93.5
		NA	28.5	136.0	<LOD	<LOD	3.0	38.5	59.7	NA	NA	472.0	<LOD	NA	NA	NA	77.6	14.0	74.4
		NA	22.5	46.2	<LOD	<LOD	<LOD	39.2	45.7	NA	NA	600.0	<LOD	NA	NA	NA	60.6	11.1	58.0
		NA	21.1	69.0	<LOD	1.2	<LOD	38.4	49.4	NA	NA	617.0	<LOD	NA	NA	NA	61.7	11.1	57.6
		NA	19.4	42.8	<LOD	<LOD	<LOD	34.3	72.6	NA	NA	600.0	<LOD	NA	NA	NA	82.8	13.5	67.7
		NA	52.7	184.0	<LOD	<LOD	<LOD	38.7	47.6	NA	NA	583.0	<LOD	NA	NA	NA	55.4	9.6	52.6
		NA	19.2	41.2	<LOD	<LOD	<LOD	37.7	46.0	NA	NA	634.0	<LOD	NA	NA	NA	60.6	9.9	53.2
		NA	20.1	42.2	<LOD	<LOD	<LOD	35.3	55.1	NA	NA	650.3	<LOD	NA	NA	NA	82.8	12.8	61.6
		NA	20.5	38.2	<LOD	<LOD	<LOD	31.9	45.7	NA	NA	626.5	<LOD	NA	NA	NA	83.9	12.1	52.2
		NA	20.7	48.0	<LOD	1.0	<LOD	31.3	44.5	NA	NA	658.4	<LOD	NA	NA	NA	86.5	11.8	50.1
		NA	22.8	37.6	<LOD	<LOD	<LOD	29.9	41.9	NA	NA	626.8	<LOD	NA	NA	NA	77.7	10.3	46.5
		NA	22.8	40.8	<LOD	<LOD	<LOD	34.4	51.9	NA	NA	697.0	<LOD	NA	NA	NA	92.2	12.7	58.8
		NA	21.5	44.7	<LOD	<LOD	<LOD	37.8	107.4	NA	NA	779.0	<LOD	NA	NA	NA	182.5	25.9	121.0
		NA	15.4	38.6	<LOD	1.2	<LOD	33.8	132.9	NA	NA	627.4	<LOD	NA	NA	NA	268.4	37.1	163.6
		NA	9.8	46.8	<LOD	<LOD	<LOD	54.6	64.5	NA	NA	670.5	<LOD	NA	NA	NA	168.0	20.2	81.0
		NA	6.7	78.0	<LOD	1.3	<LOD	69.1	81.3	NA	NA	474.0	<LOD	NA	NA	NA	91.3	14.8	80.2
		NA	5.6	40.2	0.8	<LOD	<LOD	39.0	45.8	NA	NA	725.0	<LOD	NA	NA	NA	94.1	14.2	69.9
		NA	796.0	7670.0	2.4	1.3	0.5	57.6	37.7	NA	NA	616.0	<LOD	NA	NA	NA	67.9	8.9	35.9
		NA	10.6	43.0	1.0	<LOD	<LOD	56.2	105.6	NA	NA	489.3	<LOD	NA	NA	NA	195.5	23.5	93.6
		NA	10.2	43.5	<LOD	<LOD	<LOD	33.1	86.0	NA	NA	664.0	<LOD	NA	NA	NA	242.0	30.6	121.3
		NA	9.9	78.0	<LOD	0.9	<LOD	77.6	50.1	NA	NA	828.0	<LOD	NA	NA	NA	62.5	10.3	54.5
18-MA-02	Garne-pyroxene skarn	NA	65.4	1610.0	NA	NA	<LOD	85.9	25.2	NA	NA	351.3	NA	NA	NA	NA	31.5	4.6	19.3
		NA	10.6	103.1	NA	NA	<LOD	33.8	34.1	NA	NA	2360.0	NA	NA	NA	NA	124.8	14.3	59.7
		NA	14.3	100.7	NA	NA	<LOD	28.9	9.1	NA	NA	2961.0	NA	NA	NA	NA	85.3	7.7	25.5
		NA	36.0	1380.0	NA	NA	<LOD	85.4	56.9	NA	NA	746.0	NA	NA	NA	NA	43.2	7.2	33.8
		NA	12.2	169.0	NA	NA	<LOD	53.0	57.8	NA	NA	1257.0	NA	NA	NA	NA	64.1	7.8	26.6
MS161 185.6-185.9	Amphibole-rich facies	NA	19.7	88.1	NA	NA	<LOD	36.8	65.6	NA	NA	918.0	NA	NA	NA	NA	94.8	13.4	60.5
		NA	19.7	85.8	NA	NA	<LOD	25.8	60.2	NA	NA	776.0	NA	NA	NA	NA	94.7	13.4	61.0
		NA	23.7	81.0	NA	NA	<LOD	24.2	42.1	NA	NA	706.0	NA	NA	NA	NA	68.6	9.9	44.6
		NA	26.0	90.0	NA	NA	<LOD	24.2	51.0	NA	NA	702.0	NA	NA	NA	NA	115.0	14.3	62.3
		NA	23.7	87.2	NA	NA	<LOD	30.2	55.0	NA	NA	867.0	NA	NA	NA	NA	85.2	12.1	55.7
MS05 155 - 80.35-80.5	Pyroxene skarn	NA	26.1	239.0	NA	NA	<LOD	50.8	39.0	NA	NA	767.0	NA	NA	NA	NA	112.7	9.6	26.2
		NA	7.1	58.0	NA	NA	<LOD	76.0	27.0	NA	NA	552.0	NA	NA	NA	NA	42.9	4.6	15.3
		NA	14.0	70.0	NA	NA	<LOD	57.4	25.9	NA	NA	795.0	NA	NA	NA	NA	74.2	6.8	18.9
		NA	8.3	76.0	NA	NA	<LOD	53.7	35.5	NA	NA	695.0	NA	NA	NA	NA	86.3	8.6	24.3
		NA	14.2	70.0	NA	NA	<LOD	55.7	47.8	NA	NA	675.0	NA	NA	NA	NA	109.2	10.9	30.6

Table C.2. (continued)

Sample name	Scheelite host	Sm_ m147	Eu_ m153	Gd_ m157	Tb_ m159	Dy_ m163	Ho_ m165	Er_ m166	Tm_ m169	Yb_ m172	Lu_ m175	Hf_ m178	Ta_ m181	Au_ m197	Pb_ m206	Pb_ m208	Bi_ m209	Th_ m232	U_ m238
MS161 322-322.3A	Argillite (Unit 1)	29.1	2.6	50.7	7.2	47.0	9.9	26.0	2.6	11.4	1.7	NA	NA	3.7	4.8	4.4	<LOD	NA	0.1
		34.8	29.4	37.0	5.4	35.0	7.3	21.0	2.4	12.3	2.3	NA	NA	3.9	4.2	4.3	0.0	NA	0.3
		16.8	4.8	24.3	3.8	23.7	5.0	13.2	1.5	6.7	1.2	NA	NA	3.7	4.6	4.2	<LOD	NA	0.0
		13.5	2.5	21.5	3.1	19.3	4.0	10.2	1.1	4.6	0.8	NA	NA	2.7	5.2	4.5	<LOD	NA	0.1
		25.1	3.3	43.3	6.6	39.7	8.3	21.5	2.0	9.6	1.4	NA	NA	3.6	4.1	3.9	<LOD	NA	0.5
		14.4	7.0	20.4	3.0	17.7	3.6	9.4	1.0	4.4	0.8	NA	NA	3.2	4.0	4.0	0.0	NA	0.3
		10.9	2.9	15.2	2.5	14.4	2.9	8.3	0.7	3.8	0.8	NA	NA	4.2	7.3	5.1	<LOD	NA	0.3
		19.7	13.2	23.0	3.5	21.5	4.4	11.2	1.3	5.4	0.8	NA	NA	3.2	4.1	4.0	<LOD	NA	0.2
		22.5	2.1	37.5	5.9	32.6	6.1	13.6	1.3	5.8	1.0	NA	NA	3.1	4.3	3.5	<LOD	NA	4.3
		13.2	5.8	18.9	2.8	16.7	3.2	8.2	0.8	4.7	0.7	NA	NA	3.6	4.6	4.7	<LOD	NA	0.1
		23.2	4.3	37.8	5.6	31.9	6.3	14.9	1.5	5.4	0.9	NA	NA	3.3	4.6	4.3	<LOD	NA	0.1
		49.5	4.5	84.2	13.2	78.6	15.9	35.9	3.2	13.2	1.8	NA	NA	3.5	4.1	4.0	<LOD	NA	0.1
		33.7	10.4	36.2	5.5	32.4	6.7	16.4	1.7	7.5	1.2	NA	NA	3.9	4.2	3.9	<LOD	NA	0.1
		25.5	38.0	26.1	4.3	25.8	5.4	14.0	1.8	9.2	1.1	NA	NA	4.0	5.2	4.6	<LOD	NA	1.1
MS231 60-60.3	Pyroxene skarn	9.2	1.7	10.5	1.3	8.1	1.5	3.6	0.5	2.5	0.3	NA	NA	4.1	4.8	4.9	0.0	NA	0.0
		24.2	5.4	23.1	3.0	19.7	3.8	9.5	1.4	8.4	1.2	NA	NA	4.2	7.2	6.6	0.0	NA	1.1
		18.9	3.2	19.0	2.2	13.5	2.5	6.5	0.8	4.4	0.7	NA	NA	4.1	8.1	7.3	0.0	NA	0.1
		19.7	3.5	18.2	2.2	13.5	2.6	6.4	0.9	4.7	0.7	NA	NA	4.4	7.9	6.9	0.0	NA	0.2
		23.5	4.4	23.0	2.7	16.4	2.9	7.3	1.0	5.2	0.7	NA	NA	4.2	8.1	7.4	0.0	NA	0.2
		18.8	5.7	15.9	2.1	14.0	2.6	7.0	1.0	5.8	0.7	NA	NA	4.2	8.1	6.9	0.0	NA	0.4
		13.7	1.9	13.2	1.5	9.3	1.6	4.0	0.6	3.3	0.4	NA	NA	3.9	7.4	6.5	<LOD	NA	0.1
		10.7	1.5	11.5	1.6	9.1	1.6	4.7	0.6	2.9	0.4	NA	NA	3.6	6.4	5.4	0.0	NA	0.3
		29.8	3.9	27.6	3.4	20.3	3.8	9.6	1.2	6.4	0.8	NA	NA	3.8	7.9	6.8	0.0	NA	0.6
		21.2	3.2	20.3	2.4	14.5	2.7	6.6	0.8	4.2	0.6	NA	NA	3.9	8.0	7.3	0.1	NA	0.4
		16.3	2.8	14.0	1.8	10.7	2.2	5.5	0.7	3.8	0.5	NA	NA	3.7	7.5	7.2	0.0	NA	0.3
		12.4	3.1	12.3	1.5	8.7	1.7	4.3	0.5	2.7	0.4	NA	NA	3.6	8.3	7.4	0.0	NA	0.1
		14.9	4.5	13.1	1.6	10.4	1.8	5.6	0.7	3.6	0.5	NA	NA	3.7	8.5	7.7	0.0	NA	0.3
		13.6	3.3	11.1	1.5	9.3	1.8	5.2	0.7	4.5	0.6	NA	NA	3.5	7.0	6.3	0.1	NA	3.0
		12.7	4.0	10.0	1.4	8.5	1.8	5.1	0.7	4.2	0.5	NA	NA	3.6	6.1	5.7	0.0	NA	1.5
		12.6	2.7	11.1	1.4	9.1	1.6	4.9	0.6	4.1	0.5	NA	NA	3.3	6.7	6.3	0.0	NA	0.3
		13.4	1.9	12.8	1.6	9.0	1.7	4.4	0.5	3.1	0.4	NA	NA	3.6	5.4	5.1	<LOD	NA	0.0
		14.3	1.9	12.8	1.6	8.5	1.5	3.8	0.4	2.2	0.3	NA	NA	3.5	6.4	5.8	0.0	NA	0.0

Table C.2. (continued)

		7.9	1.2	8.0	1.1	6.8	1.2	3.0	0.3	2.2	0.2	NA	NA	3.5	4.9	5.0	0.0	NA	0.1
		22.8	5.7	21.7	3.1	19.3	3.5	10.9	1.3	8.8	1.2	NA	NA	3.4	6.1	6.2	0.0	NA	2.0
		14.6	5.0	14.1	2.1	12.7	2.4	7.2	0.9	5.5	0.7	NA	NA	3.4	6.5	6.6	0.0	NA	0.3
		12.0	4.6	10.6	1.6	9.7	1.8	6.0	0.8	4.9	0.6	NA	NA	3.4	6.8	6.9	<LOD	NA	0.1
		15.0	6.1	13.5	1.9	12.2	2.4	7.2	0.8	5.0	0.6	NA	NA	3.3	7.0	6.8	<LOD	NA	0.6
		15.5	7.9	13.5	2.0	12.0	2.4	7.6	1.0	5.8	0.6	NA	NA	3.5	6.8	6.8	0.0	NA	1.1
		13.9	6.2	10.4	1.5	10.2	2.0	7.3	1.0	6.6	0.9	NA	NA	3.3	7.7	7.2	0.0	NA	2.2
		11.2	4.5	7.9	1.1	7.2	1.6	5.3	0.8	5.3	0.7	NA	NA	3.4	8.0	7.3	0.0	NA	2.0
		11.0	4.4	8.1	1.1	7.0	1.5	5.2	0.7	4.8	0.6	NA	NA	3.4	7.9	7.5	0.0	NA	1.2
		8.8	3.3	6.5	0.8	5.5	1.2	3.8	0.5	3.6	0.5	NA	NA	3.5	7.6	7.5	0.0	NA	0.4
		7.5	2.1	5.2	0.7	5.1	1.0	3.6	0.5	3.6	0.5	NA	NA	3.4	8.0	7.2	0.0	NA	0.4
		2.2	0.8	2.7	0.3	2.8	0.6	1.8	0.2	1.2	0.1	NA	NA	3.5	3.4	3.2	0.4	NA	0.0
		7.9	2.2	7.6	1.3	8.5	1.6	5.2	0.8	4.7	0.7	NA	NA	3.3	8.0	7.1	0.0	NA	0.1
		8.0	2.3	7.2	1.1	7.6	1.5	5.1	0.8	5.0	0.7	NA	NA	3.4	8.8	8.0	0.0	NA	0.1
		13.2	3.1	10.4	1.5	10.8	2.0	6.4	0.9	6.5	0.9	NA	NA	3.6	8.6	7.9	0.0	NA	0.3
		13.5	5.1	12.9	1.8	11.8	2.2	6.2	0.8	5.0	0.6	NA	NA	3.5	10.5	9.4	0.0	NA	1.8
		21.2	7.7	18.1	2.7	18.5	3.3	9.8	1.3	8.8	1.2	NA	NA	3.4	12.8	11.0	0.2	NA	9.1
		10.6	7.2	8.9	1.3	8.8	1.7	5.1	0.7	4.9	0.7	NA	NA	3.2	9.3	8.4	0.0	NA	2.2
		8.5	2.1	9.2	1.1	6.9	1.3	3.3	0.4	2.7	0.3	NA	NA	3.3	7.1	6.6	<LOD	NA	0.1
		8.9	2.4	7.6	1.0	6.3	1.2	3.3	0.4	2.3	0.3	NA	NA	3.4	5.8	5.6	<LOD	NA	0.1
		7.4	2.0	7.2	0.9	5.7	1.2	3.1	0.4	1.9	0.2	NA	NA	3.4	6.6	6.1	<LOD	NA	0.0
		12.3	7.3	10.8	1.5	10.4	2.0	6.0	1.0	7.6	1.2	NA	NA	3.3	9.7	8.9	0.0	NA	7.8
		13.9	3.0	14.2	2.0	13.8	2.6	7.4	1.0	6.7	0.8	NA	NA	3.5	6.5	6.1	0.0	NA	0.6
		14.3	5.4	11.0	1.7	11.1	2.0	5.8	1.0	7.1	0.8	NA	NA	3.7	9.3	8.0	0.0	NA	4.8
		10.9	3.0	11.1	1.5	9.3	1.7	4.6	0.6	4.0	0.5	NA	NA	3.3	8.2	7.5	0.0	NA	0.6
		15.5	6.3	12.9	1.7	11.4	2.2	6.5	0.9	6.1	0.8	NA	NA	3.4	8.0	6.9	0.1	NA	5.2
		14.0	5.6	10.1	1.4	9.4	1.9	5.9	1.0	6.6	0.8	NA	NA	3.5	9.2	8.4	0.0	NA	5.6
		11.9	3.0	10.1	1.3	8.1	1.5	4.0	0.6	3.8	0.5	NA	NA	3.4	8.0	7.1	0.0	NA	3.0
		8.3	1.9	8.6	1.2	7.9	1.5	3.8	0.5	3.1	0.4	NA	NA	3.4	10.6	9.6	0.1	NA	0.1
		9.3	2.1	8.3	1.1	6.6	1.3	3.7	0.5	3.2	0.4	NA	NA	3.2	9.8	9.4	1.6	NA	0.1
		8.1	1.8	8.3	1.2	7.3	1.5	4.3	0.5	3.2	0.4	NA	NA	3.5	6.3	5.9	0.0	NA	0.0
		13.8	2.1	13.2	1.7	10.4	2.2	5.6	0.7	4.9	0.6	NA	NA	3.4	7.4	6.8	0.0	NA	0.2
		14.4	5.9	12.2	2.0	11.9	2.4	7.4	1.0	6.8	1.0	NA	NA	3.4	8.7	8.5	0.1	NA	2.3

Table C.2. (continued)

		13.7	6.9	12.6	2.0	12.3	2.6	7.0	0.9	5.4	0.6	NA	NA	3.4	9.1	8.4	0.1	NA	2.1
		14.1	7.5	13.6	2.2	13.8	2.7	7.9	0.9	5.5	0.7	NA	NA	3.5	9.5	8.8	0.1	NA	2.0
		15.2	8.6	13.5	2.1	12.7	2.8	7.8	1.0	6.2	0.8	NA	NA	3.5	9.2	8.4	0.0	NA	2.7
		25.2	6.8	22.3	3.0	18.2	3.6	10.2	1.3	7.4	0.9	NA	NA	3.4	8.8	8.2	0.0	NA	2.1
		25.5	4.7	22.9	3.0	17.5	3.4	9.3	1.1	6.1	0.7	NA	NA	3.4	8.7	8.0	0.0	NA	1.2
		23.7	4.5	21.8	2.8	16.2	3.2	8.7	1.0	5.6	0.7	NA	NA	3.5	9.0	8.1	0.0	NA	0.8
		19.1	4.3	16.4	2.3	13.1	2.6	7.5	1.0	5.4	0.6	NA	NA	3.3	8.2	8.0	0.1	NA	1.4
		15.8	3.5	13.6	1.7	10.5	2.1	6.0	0.7	3.9	0.5	NA	NA	2.9	10.5	9.6	0.2	NA	0.6
		12.3	2.8	11.2	1.5	8.6	1.7	4.5	0.5	3.0	0.3	NA	NA	3.3	7.5	7.1	0.0	NA	0.1
		13.2	2.7	12.0	1.5	8.6	1.7	4.9	0.6	3.5	0.4	NA	NA	3.3	7.6	7.0	0.0	NA	0.1
		16.6	2.7	14.4	2.0	12.2	2.6	7.4	1.0	7.1	0.9	NA	NA	3.3	7.3	6.7	0.1	NA	0.1
		13.0	2.4	11.6	1.6	8.6	1.7	4.8	0.6	3.2	0.4	NA	NA	3.2	7.7	6.9	0.0	NA	0.2
		11.9	2.3	10.6	1.4	8.3	1.7	4.6	0.5	3.4	0.4	NA	NA	3.3	6.6	6.1	0.0	NA	0.1
		13.1	2.4	10.1	1.5	8.4	1.7	5.2	0.7	4.5	0.5	NA	NA	3.2	6.4	6.2	0.0	NA	0.1
		11.3	2.4	8.8	1.2	7.5	1.5	4.3	0.5	3.5	0.5	NA	NA	3.5	6.9	6.2	0.0	NA	0.1
		9.3	2.2	6.9	1.1	6.7	1.4	4.2	0.6	4.0	0.4	NA	NA	3.5	6.7	6.2	0.0	NA	0.2
		9.3	2.3	8.0	1.1	6.3	1.4	4.0	0.5	3.3	0.4	NA	NA	3.5	6.8	6.6	0.0	NA	0.3
		13.0	2.0	12.0	1.5	9.0	1.9	4.8	0.6	3.6	0.4	NA	NA	3.3	7.1	6.8	0.0	NA	0.2
		26.2	3.9	22.0	3.0	18.9	3.9	10.2	1.2	7.3	0.9	NA	NA	3.5	9.0	8.0	0.0	NA	4.4
		32.7	5.6	25.1	3.7	22.9	4.4	11.8	1.6	9.2	1.1	NA	NA	3.3	9.7	8.9	0.0	NA	1.2
		15.0	3.4	12.5	1.7	10.5	2.2	6.1	0.8	5.4	0.6	NA	NA	3.5	8.2	7.5	0.0	NA	0.3
		19.6	5.1	18.6	2.6	17.2	3.5	9.4	1.2	7.6	1.0	NA	NA	3.2	5.6	5.0	0.0	NA	5.2
		14.5	3.0	11.9	1.6	9.9	1.9	5.0	0.7	3.7	0.4	NA	NA	3.2	6.0	5.7	<LOD	NA	0.1
		7.9	2.0	6.5	0.9	6.5	1.3	3.7	0.5	3.4	0.4	NA	NA	3.0	6.5	6.2	0.0	NA	0.3
		17.1	6.2	13.4	2.0	13.5	3.0	9.2	1.6	12.4	1.6	NA	NA	3.6	9.5	8.2	0.1	NA	16.6
		19.5	10.6	13.5	1.9	12.8	2.7	8.2	1.4	10.1	1.3	NA	NA	3.3	9.7	7.9	0.5	NA	25.7
		13.6	2.1	13.2	1.8	11.6	2.1	4.9	0.6	3.3	0.4	NA	NA	3.3	7.7	6.7	0.1	NA	0.1
18-MA-02	Garne-pyroxene skarn	5.3	1.4	4.3	0.8	4.5	0.9	2.4	0.4	2.6	0.3	NA	NA	NA	7.6	7.0	NA	<LOD	0.1
		10.2	4.1	9.7	1.2	6.3	1.3	2.6	0.4	2.6	0.3	NA	NA	NA	6.2	5.6	NA	1.5	2.2
		3.2	1.1	2.9	0.3	1.6	0.2	0.6	0.1	0.5	0.0	NA	NA	NA	3.1	3.1	NA	0.1	0.2
		9.4	2.0	9.2	1.7	11.3	2.3	6.7	1.0	6.4	0.7	NA	NA	NA	6.7	6.4	NA	<LOD	0.1
		6.4	4.4	5.4	1.3	8.8	1.8	6.3	1.2	8.9	1.1	NA	NA	NA	7.4	7.2	NA	0.0	1.2
		12.7	3.3	13.4	1.7	10.8	2.2	5.5	0.7	3.8	0.5	NA	NA	NA	8.2	8.2	NA	0.1	0.5

Table C.2. (continued)

MS161 185.6-185.9	Amphibole-rich facies	11.8	2.5	12.0	1.6	9.2	1.9	4.7	0.7	3.9	0.5	NA	NA	NA	9.3	8.8	NA	0.2	0.3
		9.0	2.4	8.8	1.2	6.5	1.4	3.6	0.5	2.9	0.4	NA	NA	NA	8.6	8.6	NA	0.1	0.3
		11.3	2.8	11.3	1.4	7.9	1.6	4.2	0.6	4.0	0.6	NA	NA	NA	9.0	8.9	NA	0.3	0.3
		12.1	2.4	13.4	1.7	9.5	2.0	4.6	0.5	2.8	0.3	NA	NA	NA	8.6	8.0	NA	0.1	0.3
MS05 155 - 80.35-80.5	Pyroxene skarn	3.8	6.7	3.6	0.5	4.0	1.1	3.5	0.6	6.1	0.9	NA	NA	NA	9.6	10.8	NA	5.0	6.1
		3.1	2.5	3.0	0.5	3.5	0.9	2.5	0.4	2.4	0.3	NA	NA	NA	4.7	5.6	NA	0.2	0.2
		2.6	3.1	2.2	0.4	2.7	0.7	2.2	0.4	3.2	0.4	NA	NA	NA	7.0	8.4	NA	0.2	0.4
		3.2	6.4	2.5	0.5	3.5	0.9	3.2	0.5	5.1	0.7	NA	NA	NA	7.2	8.2	NA	1.8	2.5
		4.9	6.2	3.9	0.7	5.0	1.2	4.5	0.8	6.9	1.0	NA	NA	NA	6.9	7.8	NA	1.4	1.8

Table C.3. Trace element composition of scheelite from the Lened deposit. *All values are in ppm. NA= not analyzed; LOD= limit of detection.*

Sample name	Scheelite host	Ti_ m47	Mn_ m55	Fe_ m57	Cu_ m63	As_ m75	Rb_ m85	Sr_ m88	Y_ m89	Zr_ m90	Nb_ m93	Mo_ m95	Ag_ m107	Cs_ m133	Ba_ m137	La_ m139	Ce_ m140	Pr_ m141	Nd_ m146
18-LE-03	Pyroxene skarn	NA	<LOD	59.1	NA	NA	<LOD	126.5	2.7	NA	NA	2600.0	NA	NA	NA	NA	22.1	2.1	6.6
		NA	<LOD	63.0	NA	NA	<LOD	111.9	2.0	NA	NA	2365.0	NA	NA	NA	NA	19.9	1.6	4.6
		NA	<LOD	74.0	NA	NA	<LOD	121.5	8.7	NA	NA	2818.0	NA	NA	NA	NA	38.0	5.5	26.2
		NA	<LOD	81.0	NA	NA	<LOD	131.9	10.2	NA	NA	2724.0	NA	NA	NA	NA	56.4	8.3	35.4
		NA	<LOD	68.0	NA	NA	<LOD	117.5	8.1	NA	NA	2806.0	NA	NA	NA	NA	38.8	5.9	23.9
18-LE-13	Biotite-rich facies	NA	42.4	240.0	NA	NA	<LOD	46.6	36.2	NA	NA	129.8	NA	NA	NA	NA	16.3	3.8	24.8
		NA	10.9	65.0	NA	NA	<LOD	46.9	17.1	NA	NA	5.3	NA	NA	NA	NA	11.6	2.5	14.4
		NA	12.5	89.0	NA	NA	<LOD	43.9	15.4	NA	NA	364.0	NA	NA	NA	NA	9.0	2.2	17.0

Sample name	Scheelite host	Sm_ m147	Eu_ m153	Gd_ m157	Tb_ m159	Dy_ m163	Ho_ m165	Er_ m166	Tm_ m169	Yb_ m172	Lu_ m175	Hf_ m178	Ta_ m181	Au_ m197	Pb_ m206	Pb_ m208	Bi_ m209	Th_ m232	U_ m238
18-LE-03	Pyroxene skarn	0.9	0.4	0.4	0.1	0.5	0.1	0.2	0.0	<LOD	<LOD	NA	NA	NA	0.7	0.8	NA	<LOD	<LOD
		0.6	0.3	0.4	0.0	0.2	0.0	0.2	<LOD	0.2	<LOD	NA	NA	NA	1.2	1.1	NA	<LOD	0.0
		4.3	1.4	3.2	0.4	1.8	0.4	0.9	<LOD	0.2	<LOD	NA	NA	NA	1.2	0.8	NA	<LOD	<LOD
		5.2	1.4	4.1	0.5	2.5	0.4	0.9	0.1	0.3	0.0	NA	NA	NA	1.4	1.0	NA	<LOD	<LOD
		4.0	1.2	3.2	0.4	2.1	0.4	0.8	<LOD	0.2	<LOD	NA	NA	NA	1.2	0.9	NA	<LOD	<LOD
18-LE-13	Biotite-rich facies	14.0	1.1	16.4	2.6	11.7	1.4	2.6	0.2	0.8	0.1	NA	NA	NA	7.3	6.7	NA	<LOD	0.0
		8.0	1.5	8.2	1.2	5.4	0.7	1.3	0.1	0.5	0.1	NA	NA	NA	6.2	5.7	NA	<LOD	<LOD
		9.6	0.5	11.8	1.6	6.8	0.9	1.3	0.1	0.3	0.0	NA	NA	NA	5.4	5.3	NA	<LOD	0.0